DEVELOPMENT AND ANALYSIS OF A HIGH-EFFICIENCY CONCENTRATING SOLAR POWER TOWER PLANT CONCEPT

by

Alireza Javanshir

A dissertation submitted to the faculty of
The University of North Carolina at Charlotte
in partial fulfillment of the requirements
for the degree of Doctor of Philosophy in
Mechanical Engineering

Charlotte

2018

Approved by:

_____
Dr. Nenad Sarunac

_____
Dr. Gloria Elliott

_____
Dr. Jeffrey Phillips

_____
Dr. Russell Keanini

_____
Dr. Shen-En Chen

ABSTRACT

ALIREZA JAVANSHIR. Development and analysis of a high-efficiency concentrating solar power tower plant concept. (Under the direction of DR. NENAD SARUNAC)

Emissions of greenhouse gases (GHGs) are one of the main problems of using fossil energy sources such as coal and natural gas. Thus, decarbonization of the energy sector, i.e., the increased use of the lower carbon intensity and carbon-free energy sources and technologies, such as solar and wind, is needed to meet increasing energy demand and reduce emissions. Although the Sun's energy falling on Earth has the capacity of being the largest source of electricity by the mid-century, efficiency, intermittency, and cost are the challenges for the solar and other renewable energy technologies.

Concentrating solar power tower (CSP-T) technology is one of the technologies for converting solar energy to electric energy (electricity). In a CSP-T plant, the large number of mirrors or lenses is used to concentrate incoming solar energy to a small area. Thus, solar energy is first converted to the thermal energy in the solar receiver, and then to the mechanical and electrical energy in a plant power block.

This study focuses on the CSP-T technology integrated with power cycles such as Rankine and Brayton. Selection of the power cycles, working fluids, and heat rejection systems was analyzed in this research study with the objective to improve conversion (mirror-to-electric generator) efficiency and reduce the cost.

The selection of the best working fluid for a power cycle is traditionally performed by conducting a large number of parametric calculations over a range of cycle operating parameters for a number of candidate working fluids. A novel and systematic multi-step

method was developed in this study for the selection of the best working fluid(s) for the commonly considered power cycles and specified (selected) cycle operating conditions (maximum temperature and pressure, and heat rejection temperature). The best working fluid gives the highest thermal efficiency, or the highest net power output of the power cycle. The power cycle modeling and design analysis were performed by employing EBSILON Professional Version 11 (EPV-11) software.

Thermo-physical and environmental properties of the working fluids, and construction and operating cost of the CSP-T plant were the main criteria considered in the working fluid and power cycle selection procedure.

To alleviate the negative effects of dry cooling in arid areas, where most CSP-T plans are (and will be) built, a direct air-cooled cooling tower (CT) with the “cold energy” thermal storage system (CE-TES), and a closed-loop hybrid-cooled CT are proposed. The effects of both cooling methods on cycle performance (net power output and electricity generation) were analyzed and compared.

DEDICATION

To my parents, my sisters, and my girlfriend. Without their support and love, none of this would be possible.

ACKNOWLEDGEMENTS

My research would not have been possible, if I did not get encouragement and support from a number of people. I would like to take this opportunity to recognize them. Somehow, all of them have left an indelible mark on me.

First and foremost, I would like to express my deepest gratitude to my graduate advisor, Dr. Nenad Sarunac. There is no doubt that I would not be able to complete this work without his support and guidance. I am deeply grateful for having the opportunity to collaborate with him during my PhD at the University of North Carolina at Charlotte.

I would also like to express my gratitude to Dr. Tony Schmitz, the graduate coordinator of Mechanical Engineering PhD program and Dr. Mike Mazzola, the director of Energy Production and Infrastructure Center (EPIC) at UNC Charlotte, for supporting me during my PhD.

I am also grateful to Dr. Gloria Elliott, Dr. Jeffrey Phillips, Dr. Russell Keanini, and Dr. Shen-En Chen for accepting to be on my doctoral committee and generously sharing their knowledge with me.

I would also like to express my gratitude to graduate school at UNC Charlotte for supporting me by tuition scholarship (GASP) during my PhD program.

TABLE OF CONTENTS

LIST OF FIGURES

LIST OF TABLES

NOMENCLATURE

C	Cost
C_p	Specific heat capacity
C_P^0	Purchase cost
CF	Capacity factor
CI	Confidence interval
CN	Sensitivity coefficient
C_{TCI}	Total capital investment
d	Discount rate
DNI	Direct normal irradiance
F	factor
FOM	Figure of merit
h	Enthalpy
h_{fg}	Latent heat (enthalpy) of evaporation
ITD	Initial temperature difference
Ja	Jacob number
$LCOE$	Levelized cost of electricity
$\dot{m}$	Mass flow rate
MRE	Mean relative error
OH	Annual operation hours
P	Pressure
$\dot{Q}$	Heat input rate
$\dot{q}$	Specific heat input rate
r	Inflation rate
r_p	Pressure ratio
s	Entropy
$SDRE$	Standard deviation of the relative error

SM	Solar multiple
T	Temperature
$\dot{W}$	Power output
$\dot{w}$	Specific work

GREEK SYMBOLS

ε	Effectiveness
η	Efficiency

SUBSCRIPTS

amb	Ambient
BM	Bare module
c	Compressor
cond	Condensation
cr	Critical
DMC	Direct manufacturing cost
f	Working fluid
Fix	fixed
gen	Generator
in	Input
max	Maximum
min	Minimum
OM	Operation and maintenance cost
opt	Optimum
out	Output
p	Pump
r	Dimensionless

ref	Reference
reg	Regenerative
T	Turbine
th	Thermal

ACRONYMS

ACC	Air-cooled condenser
CE-TES	Cold energy thermal storage system
EPV-11	EBSILON Professional Version 11
GUI	Graphical user interface
GWP	Global warming potential
HEX	Air-to-water heat exchanger
HP	High pressure
LP	Low pressure
ODP	Ozone depletion potential
ORC	Organic Rankine cycle
RBC	Regenerative Brayton cycle
RBCR	Regenerative Brayton cycle with recompression
RSRC	Regenerative steam Rankine cycle with reheat
TIT	Turbine inlet temperature
V	Valve

CHAPTER 1: INTRODUCTION AND PROBLEM STATEMENT

1.1. Overview

This study focuses on the concentrating solar power tower (CSP-T) technology using a Rankine, ORC, Brayton, or combined cycle as a power block integrated with the solar power tower and heliostat field.

A detailed design, analysis, and optimization of thermodynamic power cycles: Rankine, Organic Rankine cycle (ORC), Brayton, or combined cycles integrated with the solar power tower technology is the main focus of this study. The results of the analysis were used to develop a systematic method for selection of the optimal working fluid(s) considering the cycle operating conditions and thermo-physical properties of the working fluids.

Also, the methods for improved heat rejection were investigated and analyzed to help achieve better thermal efficiency and lower system cost. The analyzed heat rejection methods included the dry and closed-loop hybrid cooling systems. System modeling and design analysis were performed by employing EBSILON Professional software [1].

1.2. Background and Motivation

According to the International Energy Agency (IEA) analysis [2], the solar energy has the capacity to be the largest source of electricity by the mid-century. According to this analysis, the two IEA roadmaps show solar energy could provide one-third of world's energy demand. This amount is larger than other kinds of primary energy sources such as fossil fuels, nuclear and wind. The roadmaps show that by 2050 solar photovoltaic (PV) and concentrated solar power (CSP) could produce 16% and 11% of world's electricity,

respectively. Additionally, solar energy can reduce the emission more than 6 billion tons of carbon dioxide (CO_2) per year by 2050.

Listed below are the most important advantages of solar energy.

- Solar energy is free, but there is a cost for the equipment.
- Solar energy does not produce any pollution.
- Solar energy can provide the energy for many devices that require a small amount of energy, such as calculators.
- In comparison with fossil fuels, the solar energy source is infinite.

However, solar energy has disadvantages, such as:

- Solar energy is available only when it is daytime and sunny. Thus, in many areas, such as the UK, where the number of sunny days is smaller compared to the number of cloudy days, or at geographical locations of higher latitude, building solar energy stations might be difficult to justify. Figure 1.1 shows the global resources of solar energy [2].
- The magnitude of the solar flux, reaching Earth's surface is very much dependent on atmospheric conditions and position of the sun in the sky. On a clear sunny day and the Sun at the zenith, the solar flux is equal to 1,000 W/m^2, i.e., 1 Sun. Figure 1.2 shows the effect of atmospheric conditions on solar flux.
- The equipment used to harness solar energy is expensive.
- Solar energy uses a significant amount of land.

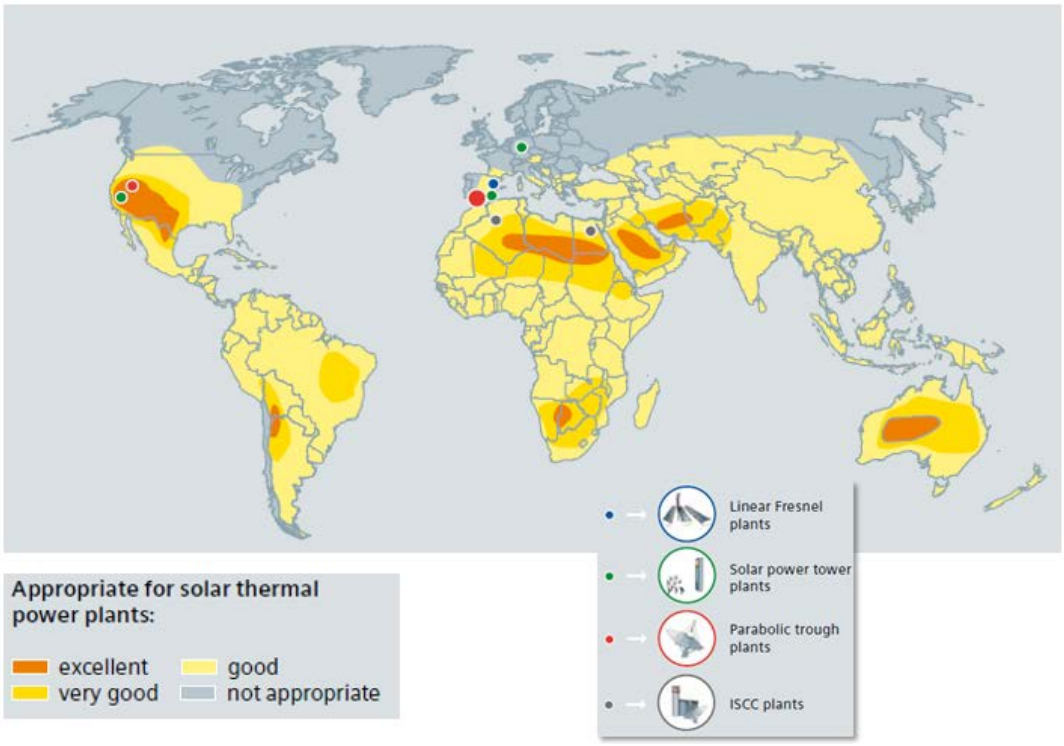

Figure 1.1. The global resources of solar energy [2].

Atmospheric conditions	Chilly, clear, blue sky	Thick smog	Sun is coming out	Sun = yellow disc	Sun = white disc	Sun just discernible	High smog	Overcast weather
global	1000 W/m²	600 W/m²	500 W/m²	400 W/m²	300 W/m²	200 W/m²	100 W/m²	50 W/m²
diffus	10%	50%	30%	50%	60%	100%	100%	100%

Figure 1.2. The effect of atmospheric conditions on solar flux [2].

One of the objectives of the U.S. Department of Energy (DOE) SunShot Initiative [3] is to make the cost of solar energy comparable to the traditional energy sources by the 2020's. The main goals of the Initiative are to make renewable and clean energy sources more affordable, accessible, and efficient.

1.3. Solar Power Technologies

In last 10 to 20 years, a rapid increase in energy consumption fueled by the increase in global energy demand and GDP has raised concerns concerning greenhouse gas (GHG) and non-GHG emissions from the energy (and other sectors) and associated immediate and future consequences. The issue of GHG emissions is the main concern related to the traditional energy hydrocarbon sources such as coal and natural gas. Also, the non-GHG pollution by sulfur dioxide (SO_2), nitrous oxide (NO_x), and particular matter ($PM_{2.5}$ especially) from the traditional energy sources such as coal and natural gas is causing serious air pollution-related problems in some regions of the world.

The spent nuclear fission fuel is highly radioactive with a long half-life of some of the fission fragments. The spent fuel can either be re-processed (closed fuel cycle) or disposed into a permanent geological storage (open fuel cycle) after use. There is a strong public opposition against the permanent geological storage. On the other hand, nuclear nations view spent fuel processing (i.e., a closed fuel cycle) as a potential path to nuclear weapon proliferation since Plutonium can be produced by this process. Finite fossil fuel resources are also a matter of concern, however not a major concern for next several centuries).

If properly deployed, renewable energy could be one of the solutions for these issues [2].

Hydroelectric energy, wind energy, solar energy, wave and tidal power, biomass energy and geothermal energy are forms of renewable energy. However, solar energy is the most important source of energy that can have a significant role in future [2]. There are two energy conversion technologies for producing electricity from solar energy. The first energy conversion technology is concentrating solar power (CSP), and the second one is solar photovoltaic (PV).

In the CSP applications, the large number of mirrors or lenses are used to concentrate incoming solar flux (solar energy) to a small area. This concentration of solar influx to a small area allows for efficient conversion of solar energy to thermal energy (heat), and results in a high temperature of the heat transfer and working fluids, and thus, in a high thermal efficiency of the power block. The power block typically employs a heat engine (Rankine, Brayton, or a combined cycle, or Stirling engine [4, 5]) to convert heat into mechanical, and electrical energy. The CSP technology is also known as Solar Thermal Electric (STE).

CSP can be divided into four groups:

1.3.1. Parabolic trough (PT)

Parabolic Trough systems use through-shaped mirrors to focus sunlight onto an absorber tube (receiver) placed in the trough's focal line. The troughs are designed to track the sun along one axis, predominantly north-south. The receiver contains a heat transfer fluid (e.g. synthetic thermal oil, molten salt) which is heated by the focused sunlight. The

heat transfer fluid (HTF) is circulated through the tubes and pumped through the heat exchangers to produce steam. The parabolic trough technology is currently the best proven and most used technology, even though the live steam parameters are lower compared to the solar power tower plants [3]. In this system, thermal oil, heated up to 390°C, is used to produce steam to drive a steam turbine. Alternatively, water may be used as a heat transfer and working fluid in a Direct Steam system configuration [6]. Figure 1.3 shows a schematic of the parabolic trough system.

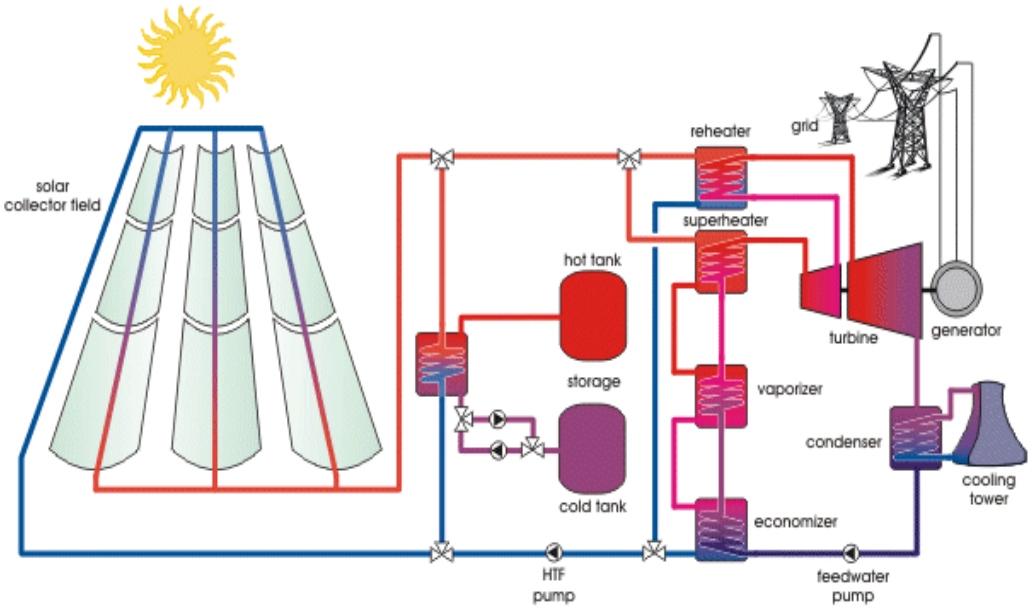

Figure 1.3. Schematic of a concentrated solar thermal trough power plant with thermal storage [7].

The state-of-the-art commercial CSP technology consists of parabolic trough collectors, and receivers using a synthetic oil as a heat transfer fluid (HTF) to deliver heat at ~370°C, to a steam Rankine cycle, with a design thermal-to-electric conversion efficiency of ~38% [3]. A thermal energy storage (TES) system employing molten salt may be incorporated into the system to improve its capacity factor at times the incoming solar flux is low and variable (cloudy days), or zero (night time).

1.3.2. Linear Fresnel technology

The linear Fresnel technology uses long, flat or slightly curved mirrors to focus sunlight onto a linear receiver located at a common focal point of the reflectors. The receiver runs parallel to and above the reflectors and collects (absorbs) the heat to boil water in the tubes, generating high-pressure steam to power the steam turbine (water-direct steam generation, no need for heat exchangers). The reflectors make use of the Fresnel lens effect, which allows for a concentrating mirror with a large aperture and short focal length. This reduces the plant costs since sagged-glass parabolic reflectors are typically much more expensive [8]. Figure 1.4 shows schematic of a linear Fresnel system.

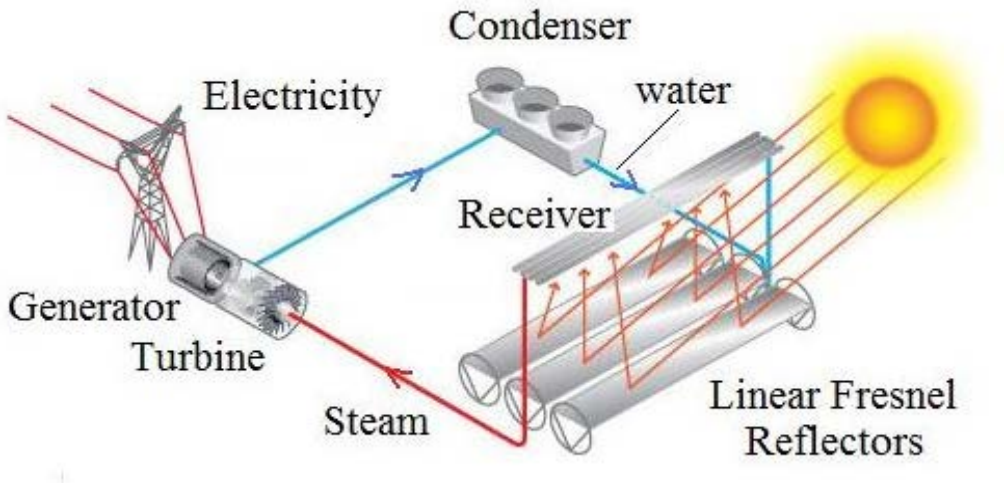

Figure 1.4. The linear Fresnel system [7].

1.3.3. Dish system

Dish system consists of a stand-alone parabolic reflector that concentrates light onto a receiver positioned at the reflector's focal point. The reflector tracks the Sun along two axes. The working fluid in the receiver is heated to 200–700°C and is then used in a Stirling engine to generate power and electricity [9]. A Stirling engine converts heat to

mechanical energy, which is then converted to electricity. This engine compresses and expands air or other gases by a cycle at different temperatures [10]. Figure 1.5 shows schematic of a dish system.

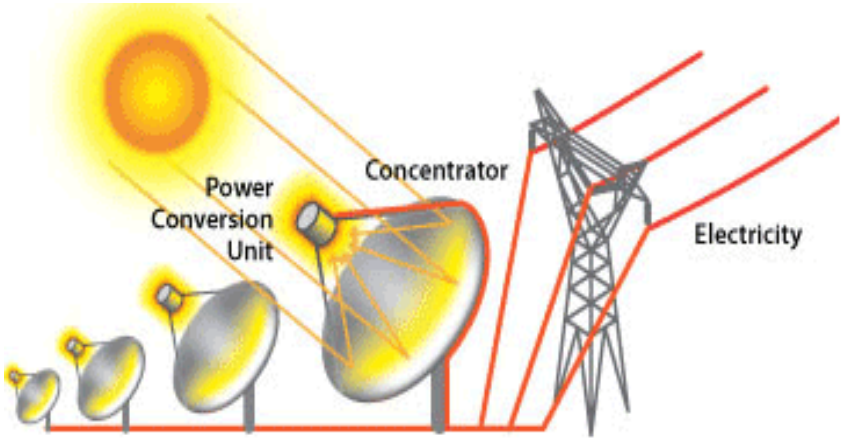

Figure 1.5. The dish system [7].

1.3.4. Solar power tower (SPT)

The Solar Power Tower includes an array of sun-tracking reflectors (heliostats) that focus sunlight on a central receiver located at the top of a centrally located tower. The solar tower contains a heat exchanger where the concentrated solar energy is transferred to an HTF [11]. The HTF transfers the absorbed heat to the working fluid (water) to generate superheated steam. The advantage of the solar tower over the parabolic trough is that the sunlight, reflected to the central receiver, is focused to a smaller area, resulting in much higher HTF temperature (up to 1,000^{o}C), and therefore, higher working fluid temperatures (superheated steam), and thus higher thermal efficiency. Also, the HTF does not have to be piped around the large solar field as is the case with parabolic troughs. For the central tower technologies, the power block can be operated by employing all currently available heat

transfer media such as air, water/ steam, molten salt, and liquid metals. Figure 1.6 shows a schematic of the solar power tower system.

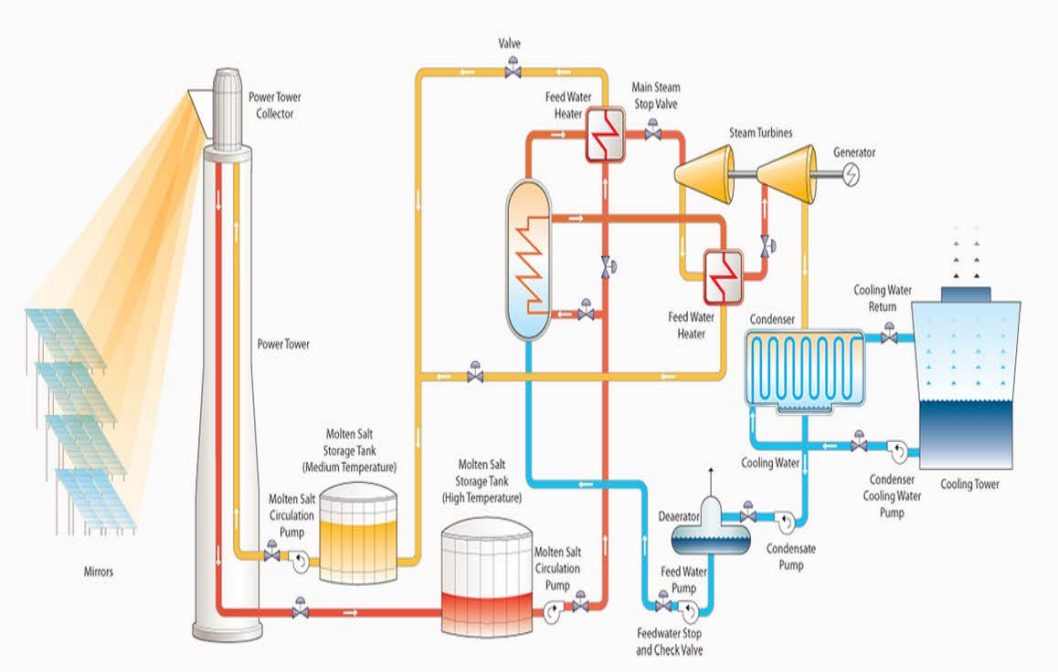

Figure 1.6. The solar power tower system [7].

The current lowest-cost, the state-of-the-art commercial standard for Solar Power Tower utilizes a molten salt HTF, coupled with 10 hours of thermal storage, to deliver heat at ~550 °C to a steam Rankine power cycle, with a designed thermal-to-electric conversion efficiency of ~41% [3].

1.3.5. Photovoltaics (PV)

In a PV system**,** light (photon) absorption leads to the photo-generation and separation of the positive and negative charge carriers. Mass is exchanged across the system /surroundings boundary in the form of electrons, along with the energy imparted from the absorbed photons. Useful energy is delivered initially in the form of direct current electrical power (W_{dc}), or converted into alternating current power (W_{ac}) to supply power

to the grid and /or our buildings [12]. Figure 1.7 shows the systems-surroundings diagram for a photovoltaic (PV) energy conversion device.

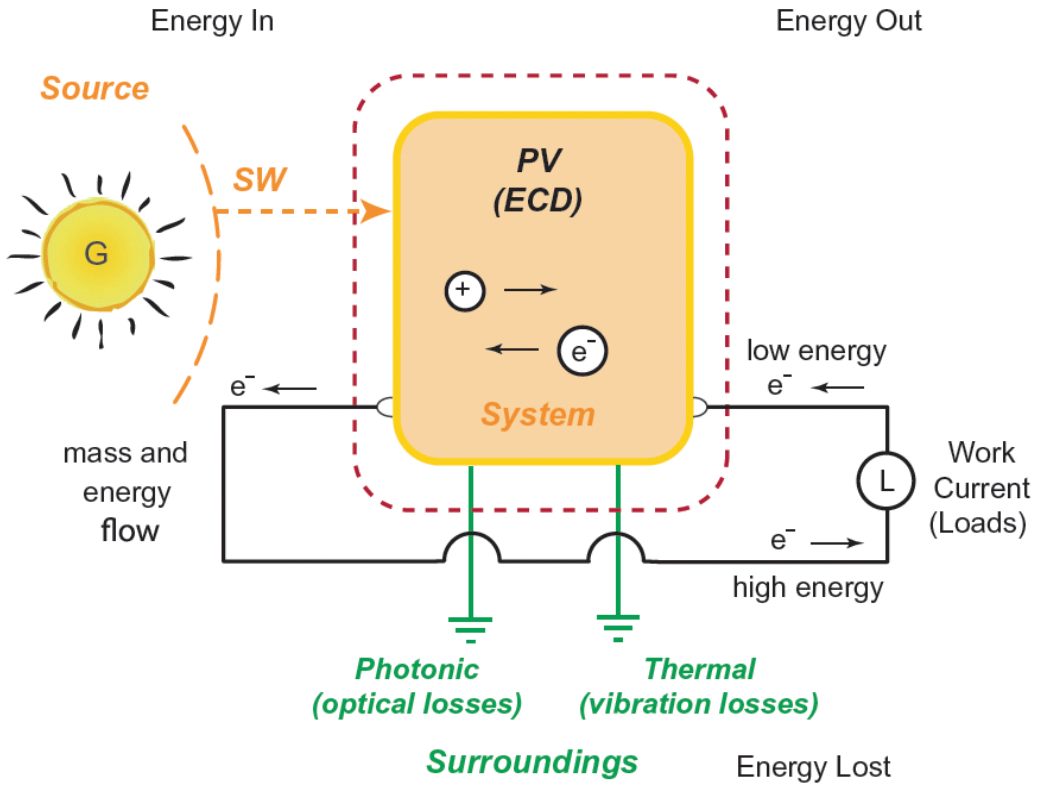

Figure 1.7. The systems-surroundings diagram for a photovoltaic (PV) energy conversion device [7].

1.3.6. Concentrating Photovoltaics (CPV)

In the Concentrating Photovoltaics System, incoming sun light is focused by the mirrors or lenses on the solar cell. Thus, the system uses smaller solar cell area compared to the photovoltaic systems. Concentrating photovoltaics has advantages, such as requiring less photovoltaic material and having higher efficiency than photovoltaic systems [13]. However, this system is expensive and it needs a direct rather than diffuse light. Figure 1.8 shows a schematic of the concentrating photovoltaic system.

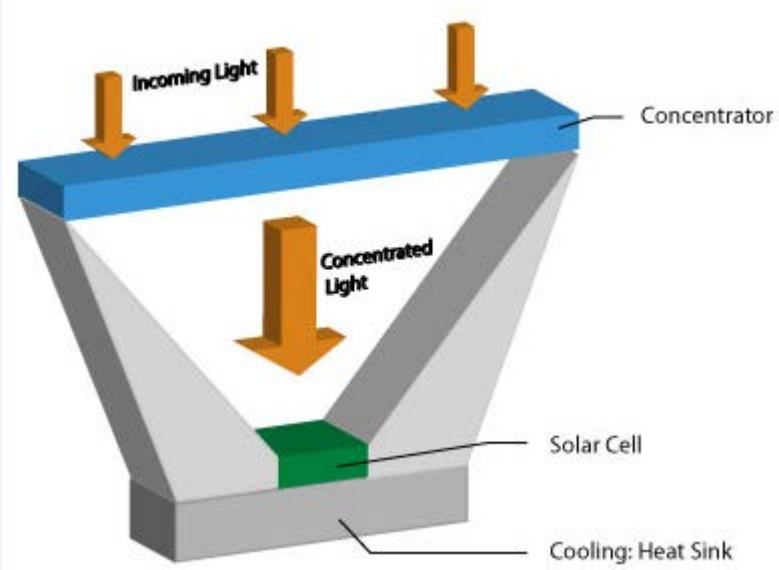

Figure 1.8. The schematic of concentrating photovoltaic system [7].

1.4. Power Cycles

The simple (basic) and combined thermodynamic power (work) cycles of interest are reviewed in this section. Their efficiency, output range, and advantages and disadvantages are discussed. Also, the state-of-the-art of each cycle is presented.

1.4.1. Carnot cycle

The Carnot is an ideal power cycle where heat is added at a constant upper temperature (T_{max}) and rejected at a constant lower temperature (T_{min}). This cycle includes two isothermal processes and two isentropic processes (Figure 1.9a). The thermal efficiency of the Carnot cycle may be expressed as:

$$\eta = 1 - \frac{T_{min}}{T_{max}} \qquad (1.1)$$

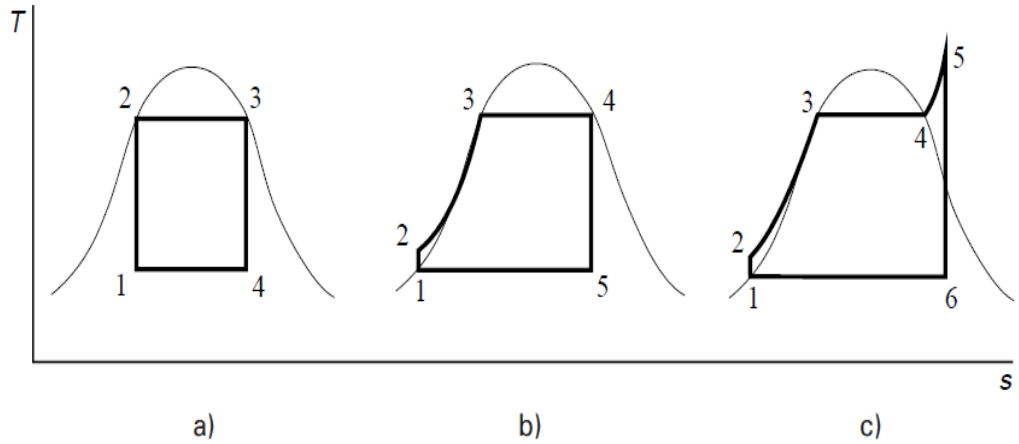

Figure 1.9. a) The Carnot cycle. b) The Rankine cycle. c) The Rankine cycle with superheat.

By increasing the difference between the upper (heat addition) and lower (heat rejection) temperatures, the thermal efficiency of the cycle is increased. No real heat engine that works between upper and lower temperatures can reach Carnot efficiency, in other words, Carnot efficiency is the highest efficiency that could be achieved for the specified upper and lower temperatures. The Carnot cycle is often used as a "measure" of the actual power system's thermal efficiency.

1.4.2. Rankine cycle

The Clausius-Rankine cycle (from now on referred to as the Rankine cycle), includes four thermodynamic processes (Figure 1.9b): The working fluid is pumped from the low to high pressure. Because the working fluid is in a liquid state at this stage, pumping work is small. In the second process, the high-pressure liquid is heated in a boiler and converted to a dry saturated or superheated vapor (steam). In the third process, the working fluid is expanded in a turbine, generating mechanical work, which is converted to electricity in an electric generator. The wet steam is condensed in a condenser at a constant

pressure (condenser back pressure), where latent heat of condensation is rejected to the ambient air or water.

The modern Rankine cycle operates with a superheated steam (Figure 1.9c) and employs steam reheat to improve thermal efficiency of the cycle. If the pressure and temperature of the superheated steam are higher than critical conditions (21.8 MPa and 374.15°C), the cycle is referred to as a supercritical cycle. The efficiency of the Rankine cycle may be increased by increasing the steam pressure and temperature, and reducing the condenser back pressure.

Also, thermal efficiency of the Rankine cycle can be increased by employing regeneration, i.e., increasing temperature of the feedwater into the boiler. The feedwater temperature is increased by using a series of feedwater heaters (FWHs) and steam extracted from the steam turbine at different pressures.

When a supercritical Rankine cycle is used in a solar plant such as Solar One and Solar Energy Generating Systems (SEGS) in California, the reported efficiency is between 37-42% [14, 15]. Higher steam pressure and temperature, as mentioned above, improve thermal efficiency of the Rankine cycle. With the currently available materials (austenitic steels), the Rankine cycle efficiency can be increased up to 45% [16-18].

Rankine cycle is the most developed work cycle and it can operate at reduced (part) load, although with reduced efficiency. However, a relatively high pressure and high temperature are needed for efficient operation. Rankine cycle may operate between 100-600°C (100°C for an ORC, and 600°C for an advanced supercritical steam Rankine Cycle).

1.4.3. Organic Rankine cycle (ORC)

ORC is a Rankine cycle utilizing an organic working fluid with low-temperature phase change instead of water-steam. The operating principles of the Organic Rankine cycle (ORC) and Rankine cycle are the same. Organic Rankine cycle (ORC) has a potential to play a significant role in energy conversion, especially in the low-temperature and Combined Heat and Power (CHP) applications. In the U.S., approximately 60% of the heat derived from the primary energy sources is rejected to the environment as a waste heat [19]. An ORC offers power generation from the renewable, waste heat and low- and medium-grade heat sources such as a geothermal, solar, biomass, and waste heat from the industry, primary movers, and thermal power plants. Refrigerants and hydrocarbons are considered as suitable working fluids for the ORC.

Many papers and studies are dedicated to a solar-powered ORC and working fluid selection [20-24]. Also, many researchers are working on the ORC using geothermal heat source [25-29]. Chen et al. [30] considered pure working fluids for the subcritical and supercritical ORC. Shengjun et al. [31] performed parametric optimization and comparison of different working fluids for the subcritical and transcritical ORC using geothermal heat source. He also studied selection criteria for evaluation of different working fluids. Saleh et al. [29] evaluated 31 different working fluids suitable for a geothermal ORC, studied different work cycle configurations, and compared different working fluids in terms of thermal efficiency. Lakew and Bolland [32] analyzed the effect different working fluids on thermal efficiency of a simple subcritical ORC operating in the 80-160°C temperature range.

Numerous criteria are considered during the working fluid selection procedure. Also, international protocols and agreements stipulate the use of working fluids that are not harmful to the environment. Thus, the criteria such as ozone depletion potential, flammability, toxicity and global warming potential (GWP) need to be considered during the working fluid selection process. Papadopoulos et al. [33] used 15 criteria for the fluid selection; with environmental, safety, physical, chemical and economical properties being the five main groups. The best working fluid is selected based on the cycle thermal efficiency. Details are provided in [34].

There is no working fluid that satisfies all selection criteria [35], thus the fluid selection method balancing the environmental, safety, physical, and chemical properties of a working fluid, capital investment (system cost), manufacturing, maintenance requirements, and cost should be used. The selection processes may be divided into two groups: elimination and ranking [36]. In the first step, elimination is used to reject unsuitable working fluids before the ranking process is applied. Roedder et al. [37] considered 22 criteria divided into six main groups, and then used a combination of the elimination and ranking methods for selection of the working fluid. Different weights were considered for each property of a working fluid. The approach was applied to a two-stage ORC, and Iso-butane was identified as the best working fluid.

A number of scholars have recently conducted research concerning performance optimization of the ORC. Roy et al. [38] presented a parametric optimization process for a regenerative ORC, while He et al. [39] presented a theoretical analysis for determining the optimum evaporation temperature. Wang et al. [40] developed a theoretical model for thermal efficiency in terms of the Jacob number. Also, Kuo et al. [41] proposed a Figure

of Merit (FOM) and showed that efficiency of a subcritical ORC decreases with an increase in FOM. However, the relationship between thermal efficiency and FOM was not presented, and Kuo's definition of FOM is applicable to the subcritical ORC cycle only.

The improvement of a regenerative ORC (ORC with a recuperator) in conjunction with the simple ORC (ORC without a recuperator) to improve its performance has been a focus of the recent research work [42].

Algieri et al. [43]studied sub-, trans- and supercritical ORC using dry working fluids and the effect of internal heat recovery. A study by Mago et al. [44] based on combined first and second law of thermodynamics analysis shows that using a dry working fluid for the regenerative ORC would not only reduce the required amount of waste heat needed to generate specified power output, but would also lower the irreversibility by increasing cycle efficiency, compared to the simple ORC. The energy and exergy analysis for the reheat-regenerative Rankine cycle was performed by Acar [45] indicating that, although energy and exergy efficiencies of the closed cycle are the same, a better understanding of the losses in the system is gained by the exergy analysis. Ying et al. [46] proposed a new approach of utilizing solar heat as a heat source to heat the feedwater in the regenerative ORC. Wang et al. [47] evaluated characteristics of five different types of ORC. Their analysis proves that the regenerative ORC has the lowest rate of exergy destruction, since a portion of the heat from the turbine exhaust is recovered in the recuperator and beneficially used, instead of being rejected in the condenser.

Hung et al. [48] reported that implementing a regenerator does not result in a significant thermal efficiency improvement (up to 2-% points) for the ORCs using wet and

isentropic working fluids. However, for dry working fluids, the thermal efficiency improvement can be higher than 9%-points.

Solar energy driven regenerative ORC has been studied during the past few years. Wang et al. [49] evaluated the effect of thermodynamic characteristics of working fluids on performance of a low temperature solar regenerative ORC power generation system using a flat plate collector for four organic working fluids: R245fa, R123, isobutene, and R134a. A numerical simulation of the heat transfer and power conversion for a low temperature solar thermal electric generation systems was carried out by Gang et al. [50]. Thermal efficiency of about 8.6% and 4.9% for irradiance 750 W/m^2 was reported for the ORC systems with and without regeneration, respectively. However, not many investigations have been conducted on the effect of parameters such as intermediate pressure on performance of the regenerative ORC system. In addition, only a few operating points have been taken into account while investigating an engine waste heat recovery system performance.

1.4.4. Brayton cycle

Brayton cycle is similar to the Rankine cycle. However, in the Brayton cycle the working fluid remains in a gas phase or a supercritical state at all state points. Thus, Brayton cycle is classified as a gas cycle.

An ideal Brayton cycle, presented in Figure 1.10a, consists of four processes: isentropic compression of the working fluid, isobaric heat addition (heat addition at constant pressure), isentropic expansion, and, for a closed cycle, isobaric heat rejection. For the open cycle, temperature of the working fluid at the turbine exhaust is in the 400 to 600°C range – high enough to be used in the bottoming cycle, such a steam Rankine cycle.

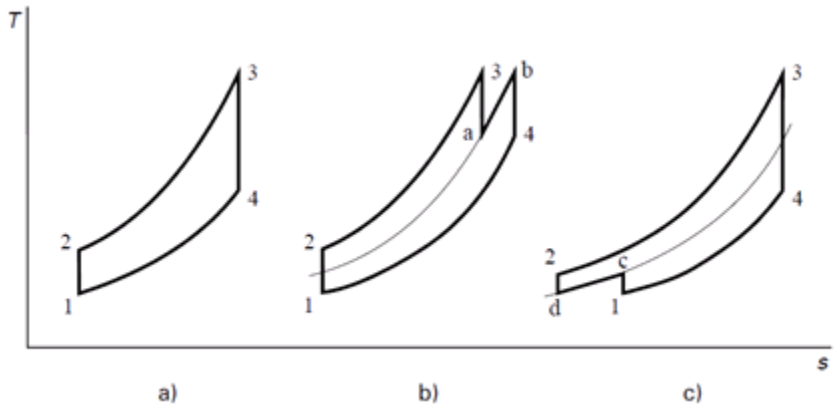

Figure 1.10. a) Bryton cycle, b) reheating, c) intercooling.

The efficiency of the Brayton cycle may be improved by modifications such as reheating and intercooling. The expansion work can be increased by reheating (Figure 1.10b), while the compression work can be reduced by intercooling (Figure 1.10c).

The real Brayton cycle approximates the ideal one, however, compression and expansion are not isentropic due to the losses associated with fluid friction, secondary flows, and heat transfer. Also, there is a pressure loss during heat addition and heat rejection. Thus, thermodynamic efficiency of the real Brayton cycle is lower, compared to the efficiency of the ideal cycle.

Since modern receivers in solar towers may achieve temperature of the HTF higher than 1,000^{o}C [51, 52], the Brayton is a suitable cycle for the solar tower CSP plants. Efficiencies of the order of 50% are reported for high-power, advanced helium Brayton cycles [17]. In these cycles, the turbine inlet temperature (TIT) is between 750 to 850°C.

A literature review concerning the use of the supercritical CO_2 (sCO_2) as a working fluid in the Brayton cycle was performed. According to the reported results [53], a sCO_2 Brayton cycle has higher efficiency, compared to other working fluids. Also, due to its high

molecular weight, the volumetric flow rate of sCO_2 is smaller compared to helium and other working fluids, resulting in a much smaller turbomachinery size.

According to [54-56], the sCO_2 Brayton cycle has the following advantages, compared to the other working fluids: (a) higher cycle efficiency at the same turbine inlet temperature since the compressor work is reduced around the critical point (i.e., in the "liquid-like" region), (b) smaller turbomachinery and heat transfer equipment, (c) higher heat transport capacity (at constant pressure), and (d) lower and more constant cycle exhaust temperature compared to conventional Brayton cycles. In the "liquid-like" region, supercritical fluids behave like liquids in terms of compressibility and heat transfer characteristics. This reduces compressor work and also leads to the more efficient regenerative heat exchange [10].

Thermodynamic analysis of different configurations of the sCO_2 Brayton power cycle shows that the sCO_2 power cycle is a good candidate for the CSP applications [57-61]. Chacartegui et al. [62] proposed three different configurations for the use of supercritical and trans-critical CO_2 cycles. Their results, based on the First Law of Thermodynamics analysis, show these cycles are promising technologies for the solar power tower plants. The use of recompression CO_2 Brayton cycle for the solar thermal power plants was investigated by Iverson et al. [63] showing the efficiency benefits of the system at maximum operating temperatures above 600°C. Studies by Angelino [56] show that single-heated sCO_2 cycles operating at maximum temperature above 650°C have higher thermodynamic efficiency compared to the reheat steam Rankine cycles. Studies by Dostal et al. [54] report thermal efficiency of 46.07% of the sCO_2 Brayton cycle with the turbine inlet temperature (TIT) of 550°C, and 49.25% for the Helium Brayton cycle with

the TIT of 880°C. Garg et al. [64] showed that to achieve specified value of thermal efficiency with a lower maximum temperature and, therefore, lower operating costs, power cycle needs to operate in the supercritical regime. Turchi et al. [65] developed benchmark results for different configurations of the sCO_2 cycle in nuclear applications.

Nitrogen, Helium and Nitrous Oxide are other choices of the working fluids for the Brayton cycle [60].

The Brayton cycle using Nitrogen has been developed in France under the ASTRID (Advanced Sodium Technological Reactor for Industrial Demonstration) project [66]. Alpy et al. [66] provide a comparison of the thermodynamic performance of Nitrogen and sCO_2 cycle for the ASTRID. The sCO_2 cycle achieves higher thermal efficiency (about 44%), compared to the Nitrogen cycle (about 38%).

Current high-concentration solar tower technology makes it possible for the Helium Brayton cycles to operate with a turbine inlet temperature ranging from 750 to 850°C which is significantly higher than that of the subcritical steam Rankine cycles. Operating at such conditions, multiple-reheat Helium Brayton cycles are predicted to achieve thermal efficiencies of the order of 50% [17]. Angelino and Invernizzi [67] concluded that, with Helium having favorable heat transfer characteristics, it is beneficial to add a closed Brayton cycle with high-temperature rejected heat for the cogeneration applications.

Jeong et al. [68] have performed performance analysis of the Brayton cycle for different working fluids including sCO_2, and sCO_2 mixtures with N_2, O_2, He and Ar. The results indicated that the CO_2–He binary mixture has the highest cycle efficiency of all analyzed mixtures.

Sarkar [69] performed thermodynamic analysis of the recompression Brayton cycle using N_2O as a working fluid for the next generation (Gen IV) of advanced nuclear reactors. The optimization of pressure ratio and mass split flow fraction was performed over a range of operating conditions.

Brayton cycle with a regenerator placed ahead of the cooler to recover heat and thus, improve the cycle efficiency is referred to as a regenerative Brayton cycle. Memon et al. [70] performed optimization of the high temperature simple and regenerative gas turbine cycle power plants and concluded that the regenerative cycle has smaller exergy destruction compared to the simple cycle.

1.4.5. Combined cycles

In a combined power cycle, two simple (basic) thermodynamic cycles are combined to achieve higher efficiency and power output. Based on the temperature range, the cycles are divided into the topping and bottoming cycles. The basic characteristics and efficiency of combined cycles, suitable for the CSP are presented. Because of the working temperature range (100-600°C) of the Rankine cycle, it can be used as a topping and a bottoming cycle. The Brayton cycle is mostly used as a topping cycle because the high turbine inlet temperature (TIT) is needed to achieve high thermal efficiency, which makes it compatible with high-temperature solar tower CSP plant. Although the capital cost of combined cycles is higher than for simple cycles, thermal efficiency is considerably higher, which justifies higher cost [71, 72]. Figure 1.11 shows the T-s diagram of the Brayton/Rankine cycle.

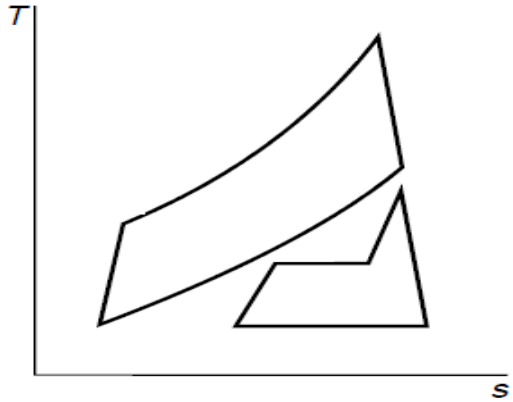

Figure 1.11. T-S Diagram Of combined Brayton/Rankine cycle.

With a low exhaust temperature of the topping cycle, ORC could be a more suitable choice for the bottoming cycle over the steam Rankine cycle [73]. Despite the numerous research studies in incorporating ORC as a bottoming cycle, such as [74, 75], a combination of the regenerative Brayton cycle as a topping cycle and ORC as a bottoming cycle at large scale power plants has not been evaluated to the sufficient level of detail, and the combined regenerative Brayton/simple ORC cycle (from now on referred to as the combined Brayton/ORC cycle) needs more investigation.

Another suitable choice for CSP applications where the exit temperature from the topping cycle is in the 80 to 150°C range, is the Rankine/ORC combined cycle, where a steam Rankine cycle is used as the topping cycle and an ORC as the bottoming cycle. The exit temperature from the topping cycle depends on the choice of the working fluid in the bottoming ORC.

1.5. Research Objectives

The performance improvement of the concentrating solar power tower plant (CSP-T) is the focus of this thesis. As presented in Figure 1.12, the CSP-T plant components may be divided into four groups: a) Collectors, b) Receiver, c) Thermal Energy Storage and

Heat Transfer Fluid (HTF), and d) Power Block. This work is primarily concerned with the Power Block and the Thermal Storage System (TES), and its integration with the receiver. The solar field, i.e., the collectors and its operating conditions, such as concentration ratio are not part of this study. The required information for that part of the system was obtained from the published literature.

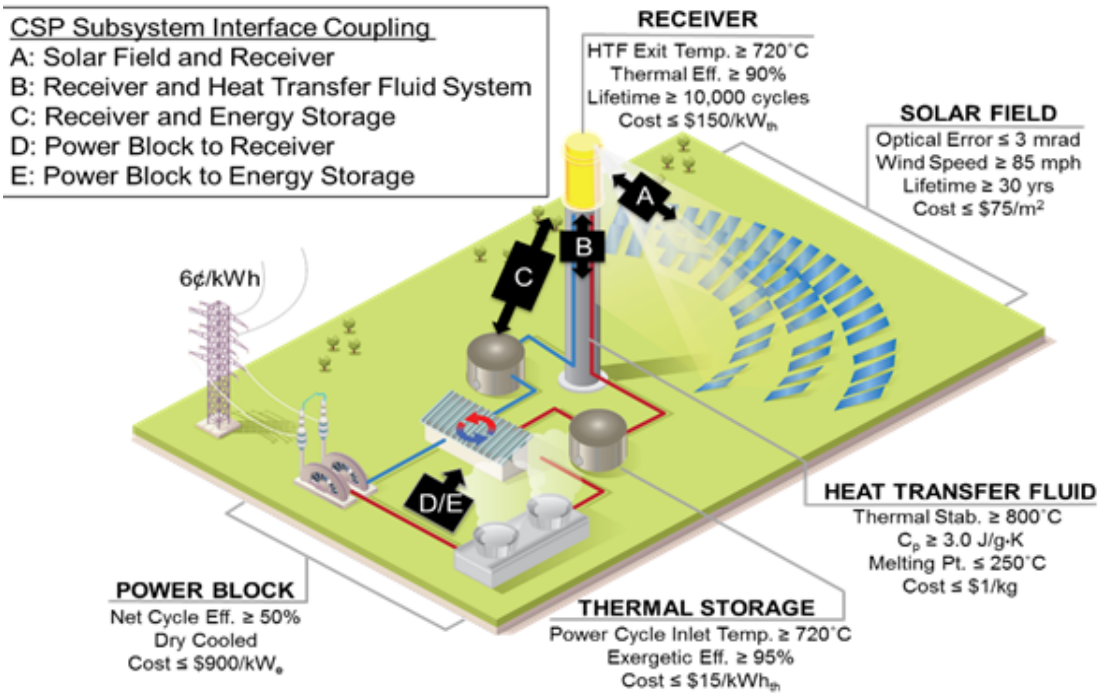

Figure 1.12. Schematic illustration of a CSP-T plant [3].

As mentioned above, CSPs have two main issues. The first one is the efficiency, and the second one is the cost. Thus, in order to improve the efficiency and lower the cost, the three main objectives of this work include the following:

1. Determine thermal efficiency of a single or combined power cycle employing different working fluids and operating conditions.

2. Develop a methodology for selecting working fluid or a combination of working fluids resulting in the highest thermal efficiency of a power cycle for the selected (prescribed or given) operating conditions (such as maximum and minimum temperature and pressure of the topping and bottoming cycles).

3. Investigate options for improving heat rejection from the power block assuming dry cooling. Investigate and analyze the methods for improving the efficiency of a dry cooling system and determine the effect on thermal efficiency and cost.

Higher thermal efficiency and a systematic procedure (methodology) for the selection of working fluids and operating conditions of the simple and combined cycles are expected outcomes of this research work.

1.5.1. Selection of working fluid(s)

Selection of the working fluid(s) and operating parameters, such as temperature and pressure of the working and heat transfer fluids (HTF) for a CSP-T has a dramatic effect on the plant efficiency and environment. For example, exotic fluids are used in the CSP-T plants to store heat at a low pressure. However, these fluids could be hazardous in case of the leaks. Also, global climate change, emission of CO_2 and ozone depletion are of main concern for power plants and selection of working and heat transfer and storage fluids [76].

The selection of working fluids (for simple cycles), and combination of working fluids (for combined cycles) has been traditionally performed based on thermodynamic efficiency calculated for the candidate working fluids or combinations of fluids over a range of operating conditions. That is, cycle analysis was performed by employing a number of working fluids and a range of operating conditions to determine cycle

performance parameters, such as thermal efficiency, specific net work output, and mass flow rate of the working fluid.

A methodology for selection of working fluids best suitable for the CSP-T plant over a range of maximum temperatures achievable by the current, state-of-the-art, and future receiver technologies and choices of HTFs (water, molten salt, liquid metals, or air) was developed in this work. Thermal efficiency and size of the power generation equipment were selected as the main evaluation criteria, followed by the equipment cost and development status.

Performance maps were developed as guidance for selection of the best working fluid for specific operating conditions for selected candidate power cycles. The maps of the power cycle thermal efficiency and power output, i.e., the performance maps were developed to enable selection of best working fluids for the number of power cycles. For the selected power cycle, these performance maps show which working fluid results in highest efficiency or power output for a given set of operating conditions.

1.5.2. Selection of power cycles

Based on the characteristics and performance of the work cycles described in the previous section, several cycles were selected for analysis.

Cycle selection was based on the following criteria:

- Thermal efficiency
- Suitability for integration with the solar power CSP
- Complexity of the equipment
- Construction and operating cost

- Development status

The selected cycles are divided into the two main categories:

Category A: One simple cycle. It can either be an advanced high-temperature Brayton or an advanced Rankine cycle. Although combined cycles have higher efficiency compared to the simple cycles, simple Rankine, ORC, and Brayton cycles are less complex, and, thus, less expensive to construct and operate. Also, these cycles are well developed (except for non-conventional working fluids) and more suitable for cycling.

Category B: A combined Brayton/Rankine cycle. High thermal efficiency is the main advantage of a combined cycle.

The combined Brayton/ORC cycle is especially suitable for the solar power CSP-T plant since: (a) heat rejection from the bottoming Rankine cycle only is needed (the bottoming Rankine typically delivers one third of the power output), (b) Brayton cycle is more suitable for a complete turndown over the night hours compared to the Rankine cycle. However, for efficient operation this cycle requires high TIT.

The effects of modifications to the topping and/or bottoming cycles, such as regeneration were also studied, although the main objectives of this study are: selection of the power cycles, operating parameters, and working fluids.

1.5.3. Heat rejection improvement

Since it is expected that the concentrating solar tower power plants will be built in deserts and other arid areas, the heat rejection will be accomplished by employing a mechanical draft dry cooling tower (CT). Unlike a wet CT, where temperature of the cooled water leaving the tower (entering steam condenser) depends on the wet bulb temperature

of the ambient air, for a dry CT temperature of the cooled water leaving the tower is a function of the dry bulb ambient air temperature [77]. Because the dry bulb temperature is higher compared to the wet bulb temperature, the use of dry cooling results in higher temperature of the cooled water leaving the CT, higher condenser back pressure, lower power output, and lower thermal efficiency of the power block compared to the wet CT system. Therefore, thermal efficiency of the power cycle rejecting heat via a dry CT is, approximately 2%-points lower compared to the wet CT [78-80].

Dry cooling system can be divided into two groups: direct or indirect. In a direct dry cooling system, the exhaust flow from the turbine is sent to an air-cooled-condenser (ACC). Figure 1.13 shows the schematic of a direct dry cooling system. Heat rejection to the environment is performed in a single step, where steam is condensed inside the finned tube cooled by the ambient air. In the indirect dry cooling system, steam is condensed in a conventional surface condenser or a contact condenser in a cooling water loop. The latent heat of condensation is rejected in a dry CT.

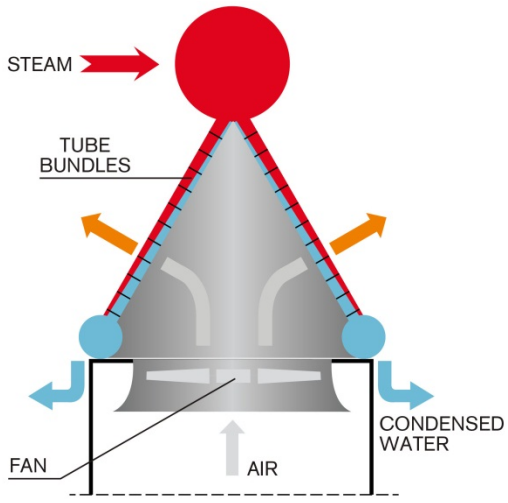

Figure 1.13. Schematics of the air-cooled condenser.

To alleviate negative effects of dry cooling, a direct air-cooled mechanical draft CT with the "cold energy" thermal storage system (CE-TES) is proposed, as presented in Figures 1.14 and 1.15.

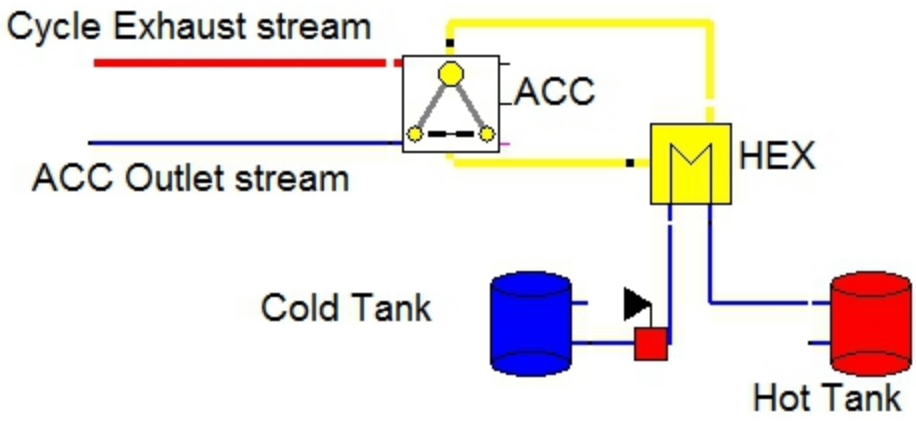

Figure 1.14. Day-time operation of the cooling tower system**.**

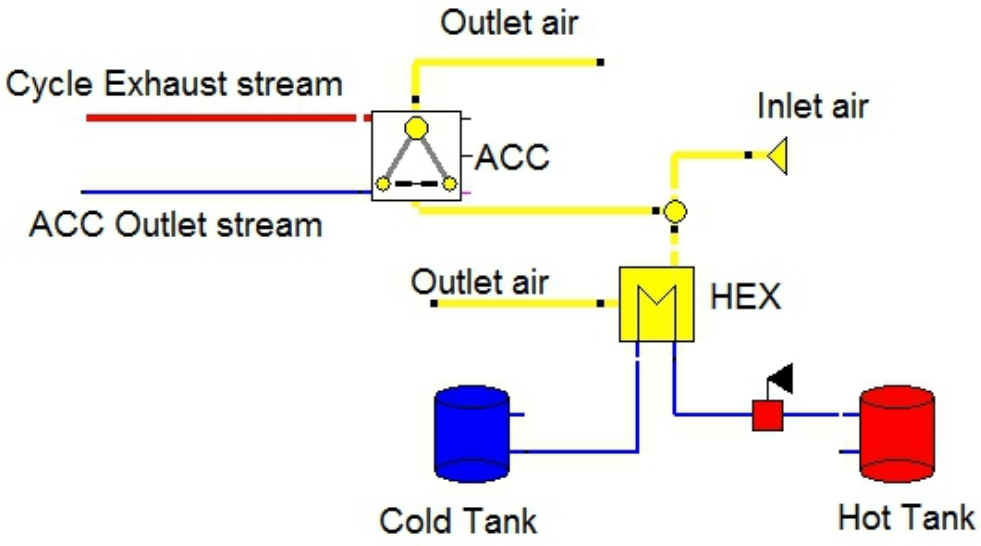

Figure 1.15. Night time-operation of the cooling tower system.

As shown in Figures 1.14 and 1.15, the CE-TES system includes the Warm and Cold Tanks. During the night, when the ambient air temperature is much lower compared to the day-time temperature (especially in deserts and arid regions), the thermal energy storage fluid from the Warm Tank is cooled by the cold air and stored in the Cold Tank. The CT will be cooled by the ambient cold air bypassing the air-to-water heat exchanger (HEX) as presented in Figure 1.15. During the hottest period of the day, the hot air will be cooled by the cold fluid from the Cold Tank prior to entering the CT as presented in Figure 1.14.

Water-glycol mixture is proposed to be used for the cold energy storage due to its low cost. Performance of the cold energy storage system may be improved by using encapsulated phase change materials (PCHs) immersed in the Cold Tank.

In the direct dry cooling method with CE-TES, there is a high overall temperature difference between the ambient air, air in the Cold Tank, and the discharge stream to the condenser. A closed-loop hybrid method is proposed to alleviate the negative effect of temperature difference in a dry cooling method. In the closed-loop hybrid method, cold energy form Cold Tank can be transferred directly to the tube bundles in ACC. Thus, the steam can be condensed directly by the cooling water. Figure 1.16 shows the schematics of air-cooled condenser and tube bundles.

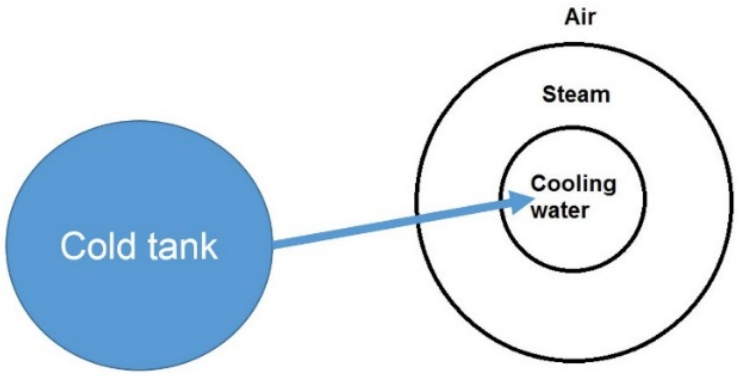

Figure 1.16. Schematic of tube bundles in ACC.

1.6. Organization of the Thesis

This thesis is organized into eight chapters as follows:

In Chapter 2, thermodynamic and techno-economic models of different power cycles integrated with CSP-T plants are presented. Theoretical equations used to calculate the performance parameters (thermal efficiency, net work output, and etc.) of power cycles are developed and presented.

In Chapter 3, thermo-physical properties of different working fluids are listed and different types of working fluids are presented. Environmental properties such as ozone depletion potential (ODP) or global warming potential (GWP) are discussed.

In Chapter 4, the results of parametric calculations performed over a range of cycle operating conditions for the previously described simple and combined power cycles operating with different working fluids are presented. The results were analyzed to determine the effect of thermo-physical properties of the working fluids on thermodynamic performance of the cycle (efficiency and specific net work output). A statistical regression analysis was used to correlate the results and develop correlations for cycle thermal

efficiency, specific net work output, and specific heat input in terms of the relevant cycle operating parameters. Performance maps were developed for the analyzed power cycles as guides for the selection of the best working fluid(s) for the specified (selected or given) cycle operating conditions.

In Chapter 5, the thermodynamic models of different power cycles are validated by using data form the published literature.

In Chapter 6, the effect of operating conditions on performance of a number of selected power cycles is presented. The best power cycle having the highest thermal efficiency or net power output for specified operating conditions was identified.

In Chapter 7, techno-economic analysis of the CSP-T plants is presented. Selection of the best working fluid and the best power cycle is the main focus of this chapter.

In Chapter 8, the effects of using CE-TES system with the dry cooling are analyzed. Also, the proposed closed-loop hybrid cooling method is described and analyzed, and the effect of both cooling methods on cycle performance are analyzed and compared.

The research contributions and accomplishments of this thesis work are presented and future research needs are discussed in Chapter 9.

CHAPTER 2: TERMODYNAMIC AND TECHNO-ECONOMIC MODELING OF CSP-T PLANTS

2.1. Overview

Thermodynamic and techno-economic models of the power cycles considered for integration with a CSP-T plant are presented in Chapter 2. Theoretical equations used to calculate performance parameters (thermal efficiency, net work output, and etc.) of the selected power cycles are developed.

2.2. EBSILON Professional Modeling Code

EBSILON Professional Version 11 (EPV-11) is a commercial software developed by STEAG Energy Services company for detailed modeling of thermodynamic processes [1]. It is used for the modeling, design, and optimization of power generation systems. The code is used by major European universities and power companies for research, design, and optimization purposes. Thermo-physical properties of the working fluids used in the analysis are determined by REFPROP [81] developed by NIST. The main EPV-11 features include are the following:

- The code has an embedded scripting language that gives user access to input, output and calculation capabilities and to combine these with the user-written codes.
- Powerful calculation module and robust solution algorithm.
- Extensive component library.
- Material properties library for fuels and working fluids.
- Intelligent error analysis and online user help.

The REFPROP library, used to obtain the thermo-physical properties of the working fluids, was integrated with EPV-11 to simulate the thermodynamic power cycles [81, 82]. The EPV-11 workspace is presented in Figure 2.1.

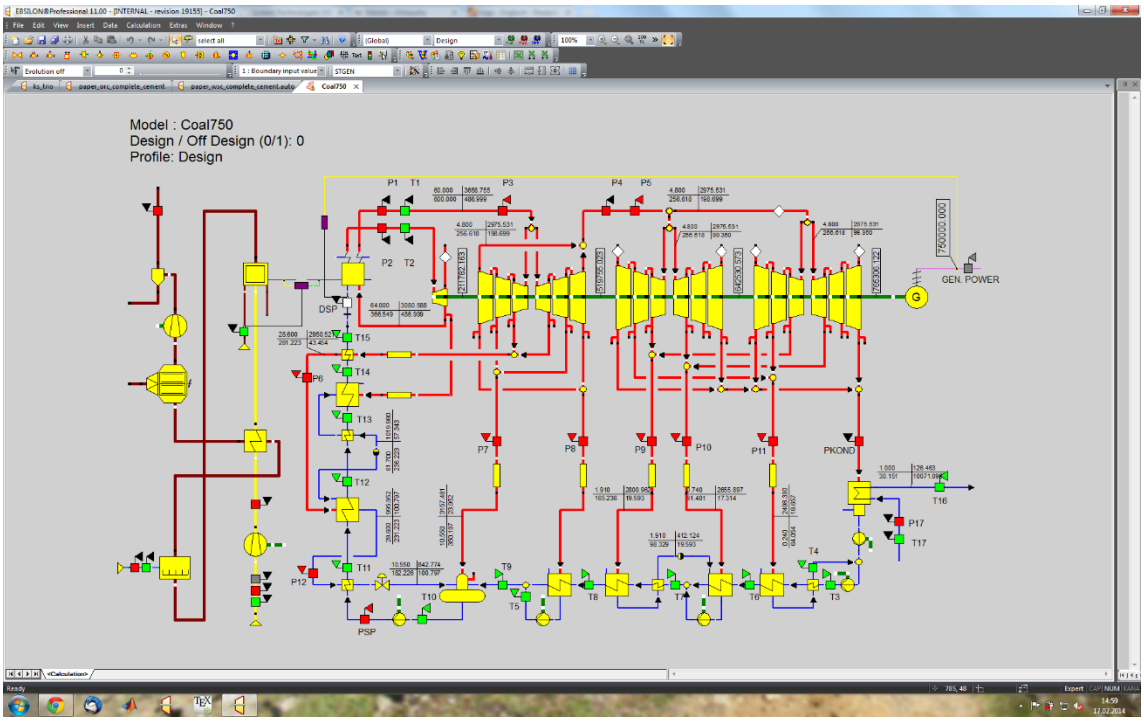

Figure 2.1. The workspace of the EPV-11 software.

2.3. Thermodynamic Analysis of a CSP-T Plant (Theoretical Model)

Selection of working fluids resulting in best performance (thermodynamic efficiency or net specific work output) of the simple and combined power cycles, such as Brayton, ORC, Brayton/ORC, and Rankine/ORC for the specified operating conditions (maximum temperature and pressure, heat rejection temperature, and others) is typically a time-consuming and arduous task. The commonly used approach involves performing a large number of parametric calculations which are carried out over a range of operating

parameters for a number of candidate working fluids for the power cycle under consideration.

A novel and systematic multi-step method was developed for the selection of best working fluids for the commonly considered power cycles. The first step involves development of a thermodynamic cycle model using the semi-perfect gas assumption (defined in Section 3.3 in Chapter 3) to develop theoretical expressions for thermal efficiency, heat input, and net specific work. The detailed models of the power cycles are developed in the second step using EBSILON Professional version 11 (EPV-11) power systems modeling code. The EPV-11 models are exercised over a range of operating conditions and a multitude of working fluids to generate results on cycle performance parameters. The statistical regression analysis is used in the third step to develop correlations for the cycle efficiency and net specific work of the same form as theoretical expressions developed in Step 1.

For the transcritical and supercritical cycles, the region near the critical point needs to be treated separately due to the large variation in thermo-physical properties, yielding to the set of correlations applicable for the Critical Zone.

The last step in the process involves construction of performance maps, where performance parameters, such as thermodynamic efficiency and net specific work output are presented as functions of the cycle operating conditions. The performance maps are constructed by using an extremum seeking algorithm which, for the specified cycle operating conditions, identifies the working fluid resulting in the best cycle performance from the results generated by the EPV-11 cycle models. The maps typically contain several zones and identify the best working fluid for each zone.

The first step of the working fluid selection method: development of the theoretical thermodynamic model of the selected power cycles (simple and regenerative ORC, simple and regenerative Brayton cycle, regenerative Brayton cycle with recompression, combined Brayton/ORC cycle, steam Rankine cycle with reheat, and combined Rankine/ORC cycle) is presented in this section. The second, third, and fourth steps of the working fluid selection method are described and discussed in Chapter 4.

2.3.1. Simple ORC

As described previously, the operating principles of the ORC and Rankine cycle are the same: compression of the liquid, phase change (evaporation) in the evaporator (primary heat exchanger), expansion in the turbine (expander), and phase change (condensation) in the condenser. The main components of a simple ORC (feed pump, evaporator (primary heat exchanger), turbine, and condenser) are presented in Figure 2.2. The feed pump delivers working fluid at the elevated pressure to the evaporator (primary heat exchanger) where the working fluid is evaporated at approximately constant pressure using the externally supplied heat. A superheater is used in some ORC designs to superheat the working fluid. The saturated or superheated working fluid is expanded in the turbine (expander), which is driving an electric generator. The low-pressure, low-temperature working fluid leaving the turbine is condensed in the condenser. The pressure of the working fluid leaving the condenser as a saturated (or slightly subcooled liquid) is increased by the feed pump, completing the power cycle. Depending on the type of the working fluid, a recuperator may be placed ahead of the condenser to recover heat and transfer it to the working fluid leaving the feed pump. Such configuration is referred to as

the recuperated (regenerated) ORC. Schematic of a regenerated ORC is presented in Figure 2.5.

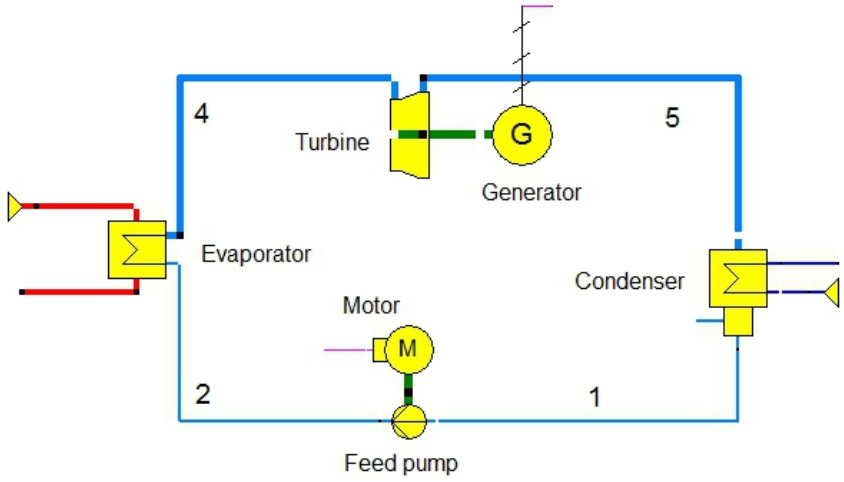

Figure 2.2. Schematic of a simple ORC.

The T-s diagrams of the simple subcritical and transcritical ORCs are presented in Figure 2.3. In the subcritical cycle, the working fluid undergoes a phase change in the evaporator. In the case of a superheated subcritical cycle, working fluid is superheated in the superheater prior to entering the turbine. There is no phase change in a supercritical cycle where the working fluid remains as a homogeneous supercritical fluid throughout the entire power cycle. However, in a transcritical cycle, the minimum cycle temperature and pressure are lower than the critical point conditions, thus a phase change occurs. In both transcritical and supercritical cycles, the maximum cycle temperature and pressure are higher than critical temperature and pressure, respectively.

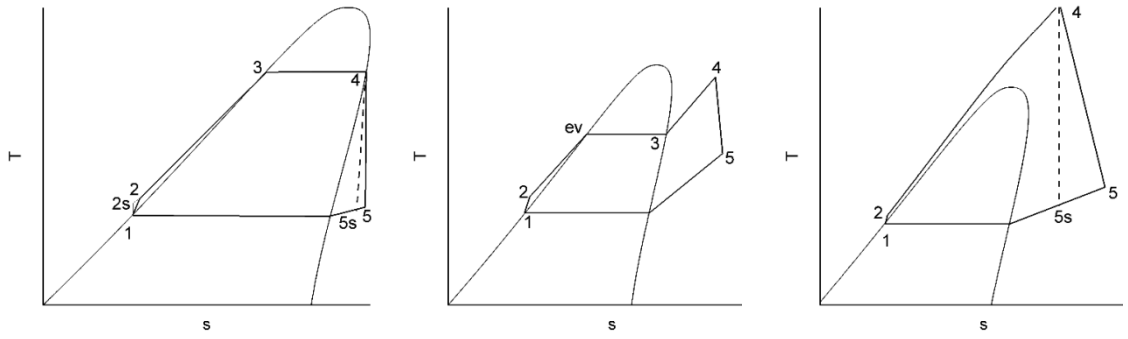

A) Subcritical B) Subcritical with superheat C) Transcritical

Figure 2.3. T-s diagram for the simple ORC.

The analysis of the cycle performance was performed by neglecting the friction and heat losses in the pipes and heat exchangers, and assuming adiabatic turbine and feed pump. An ORC is a considerably simpler and smaller power cycle compared to the steam Rankine cycle with significantly smaller heat exchangers and considerably simpler connecting piping. Also, the molar mass of most organic fluids and their density is higher compared to steam, resulting in comparatively smaller volumetric flows and, thus smaller equipment size. Thus, friction in the pipes and heat exchangers, and the resulting pressure drop does not have a significant effect on cycle performance and can be neglected (more details can be found in Section 4.3.4 of Chapter 4).

In terms of the heat losses, turbomachinery is typically assumed to be adiabatic since any heat exchange with the surroundings is several orders of magnitude smaller compared to the energy flux through the turbomachine.

For a subcritical cycle without the superheat (Figure 2.3A), heat input to the cycle includes the sensible heat and latent heat (process 2-4):

$$\dot{Q}_{in} = \dot{m}_f \dot{q}_{in} = \dot{Q}_{24} \approx \dot{Q}_{14} = \dot{m}_f (h_4 - h_1) = \dot{m}_f ((h_3 - h_1) + h_{fg}) = \dot{m}_f (\bar{C}_{P,13} (T_4 - T_1) + h_{fg}) \quad (2.1)$$

where $\bar{C}_{P,13}$ represents the average specific heat capacity calculated from the State Point (SP) 1 to SP 3, T_1 is the temperature at the feed pump inlet, T_4 is the maximum temperature (turbine inlet temperature, TIT), h_{fg} is the latent heat (enthalpy) of evaporation (vaporization), $\dot{q}_{in}$ is the specific heat input, and $\dot{m}_f$ is the mass flow rate of the working fluid.

The entropy change of the working fluid from SP 1 to 4 is:

$$s_4 - s_1 = \int_{T_1,P_4}^{T_4,P_4} \frac{C_p}{T} dT + \frac{h_{fg}}{T_4} \tag{2.2}$$

$$s_4 - s_1 = \bar{C}_{P,13}\, ln\left(\frac{T_4}{T_1}\right) + \frac{h_{fg}}{T_4} \tag{2.3}$$

The heat rejected from the cycle is equal to:

$$\dot{Q}_{out} = \dot{m}_f \dot{q}_{out} = \dot{m}_f((s_5 - s_1)T_{eq,c}) \approx \dot{m}_f((s_4 - s_1)T_{eq,c}) \tag{2.4}$$

where $T_{eq,c}$ denotes the average of the turbine outlet temperature and condensation temperatures. The net work output is:

$$\dot{W}_{net} = \dot{m}_f \dot{w}_{net} = \dot{m}_f(\dot{q}_{in} - \dot{q}_{out})\eta_t \tag{2.5}$$

$$\dot{W}_{net} = \eta_t \dot{m}_f \left\{\bar{C}_{P,13}(T_4 - T_1) + h_{fg} - \left(\bar{C}_{P,13}\, ln\left(\frac{T_4}{T_1}\right) + \frac{h_{fg}}{T_4}\right) T_{eq,c}\right\} \tag{2.6}$$

where η_t denotes turbine isentropic efficiency. The thermal efficiency of the cycle η_{th} is defined as:

$$\eta_{th} = \frac{\dot{W}_{net}}{\dot{Q}_{in}} \tag{2.7}$$

$$\eta_{th} = \dot{W}_{net}/\dot{Q}_{in} = \eta_t \frac{Ja+1-\frac{T_{eq,c}}{T_1}\left(\frac{Ja\, ln(T_{EC})}{T_{EC}-1}+\frac{1}{T_{EC}}\right)}{Ja+1} \tag{2.8}$$

where:

$$Ja = \frac{\bar{C}_{P,13}(T_4 - T_1)}{h_{fg}}, \qquad T_{EC} = \frac{Evaporation\ temperature}{Condensation\ temperature} = \frac{T_4}{T_1} \tag{2.9}$$

The quantity *Ja* is the Jacob number defined as the ratio of sensible and latent heats. For the wet and isentropic fluids $(T_{eq,c}/T_1) \approx 1$, while for the dry fluids the ratio is greater than one. The properties and definition of wet, dry, and isentropic fluids are defined in Chapter 3. However, if the fluid is not too dry, this ratio can be equal to 1. Figure 2.4 shows thermal efficiency for the ORC employing the ideal (isentropic) and actual (non-isentropic) turbine in terms of the Jacob number for $T_{eq,c}/T_1 = 1$. The results show that η_{th} decreases as the Jacob number increases. Details are provided in [40].

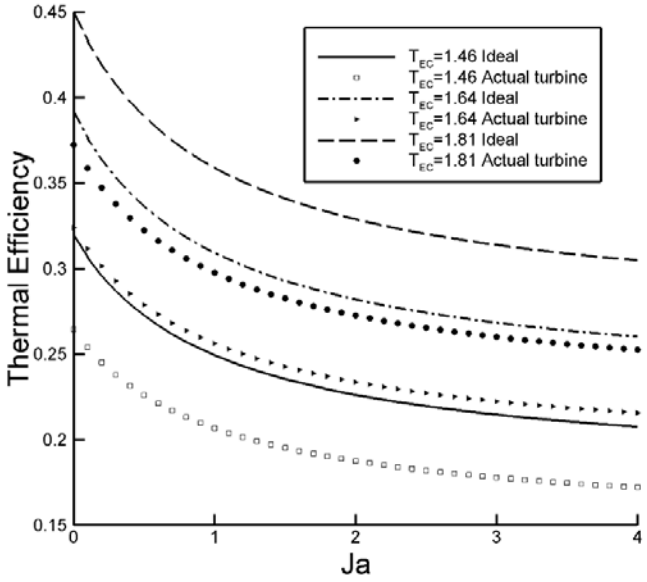

Figure 2.4. Thermal efficiency for the ORC employing the ideal and actual turbine in terms of the Jacob number.

For a superheated subcritical ORC (Figure 2.3B), the procedure for obtaining the expression for η_{th} is similar - the difference is, we have to account for the superheat. The heat input provided to the cycle includes the sensible heat and latent heat (process 2-4):

$$\dot{Q}_{in} = \dot{m}_f \dot{q}_{in} = \dot{Q}_{24} = \dot{Q}_{14} = \dot{m}_f(\bar{C}_{P,1ev}(T_{ev} - T_1) + h_{fg} + \bar{C}_{P,34}(T_4 - T_{ev})) \qquad (2.10)$$

The heat rejected from the cycle is equal to:

$$\dot{Q}_{out} = \dot{m}_f \dot{q}_{out} = \dot{m}_f((s_5 - s_1)T_{eq,c}) \approx \dot{m}_f((s_4 - s_1)T_{eq,c}) \quad (2.11)$$

The entropy change of the working fluid from SP 1 to 4 is:

$$s_4 - s_1 = \bar{C}_{P,1ev}\, ln\left(\frac{T_{ev}}{T_1}\right) + \bar{C}_{P,34}\, ln\left(\frac{T_4}{T_{ev}}\right) + \frac{h_{fg}}{T_{ev}} \quad (2.12)$$

The thermal efficiency is defined as:

$$\eta_{th} = \frac{\dot{W}_{net}}{\dot{W}_{in}} = \eta_t \frac{Ja + Ja_S + 1 - \frac{T_{eq,c}}{T_1}\left(\frac{Ja\, ln(T_{EC})}{T_{EC} - 1} + \frac{Ja_S ln(\frac{T_4}{T_1 T_{EC}})}{\frac{T_4}{T_1} - T_{EC}} + \frac{1}{T_{EC}}\right)}{Ja + Ja_s + 1} \quad (2.13)$$

where *Ja* is the Jacob number and Ja_s is the superheat Jacob number.

$$Ja = \frac{\bar{C}_{P,1ev}(T_{ev} - T_1)}{h_{fg}}, Ja_s = \frac{\bar{C}_{P,34}(T_4 - T_{ev})}{h_{fg}} \quad (2.14)$$

The results show that thermal efficiency decreases as the Jacob number *Ja* and superheat Jacob number Ja_s increase. By removing the superheat, the maximum temperature T_4 becomes equal to the evaporation temperature T_{ev}. Thus $Ja_s = 0$ and Eqn. (2.13) simplifies to Eqn. (2.8).

For a transcritical cycle (Figure 2.4C), the similar procedure is used to determine the expression for thermal efficiency – the difference is, there is no phase change, thus latent heat of evaporation is equal to zero.

$$\dot{Q}_{in} = \dot{m}_f \dot{q}_{in} = \dot{m}_f \dot{q}_{24} = \dot{m}_f \dot{q}_{14} = \dot{m}_f \bar{C}_{P,14}(T_4 - T_1) \quad (2.15)$$

$$\dot{Q}_{out} = \dot{m}_f \dot{q}_{out} = \dot{m}_f((s_5 - s_1)T_{eq,c}) \approx \dot{m}_f((s_4 - s_1)T_{eq,c}) \quad (2.16)$$

$$s_4 - s_1 = \bar{C}_{P,14}\, ln\left(\frac{T_4}{T_1}\right) \quad (2.17)$$

$$\dot{W}_{net} = \dot{m}_f \dot{w}_{net} = \dot{m}_f(q_{in} - q_{out})\eta_t \quad (2.18)$$

$$\dot{W}_{net} = \eta_t \dot{m}_{wf} \bar{C}_{P,14}\left\{(T_4 - T_1) - ln\left(\frac{T_4}{T_1}\right) T_{eq,c}\right\} \quad (2.19)$$

$$\eta_{th} = \eta_t \left(1 - \frac{ln(T_{EC}) \frac{T_{eq,c}}{T_1}}{(T_{EC}-1)} \right) \quad (2.20)$$

In the supercritical region, thermal efficiency is a function of the ratio of the maximum (T_4) and minimum temperatures (T_1). The cycle efficiency increases, as this ratio is increased ($d\eta_{th}/dT_{EC} > 0$).

$$\frac{d\eta_{th}}{dT_{EC}} = \eta_t \frac{T_{eq,c}}{T_1 (T_{EC}-1)^2} \left(\frac{1}{T_{EC}} + ln(T_{EC}) \right) > 0 \quad (2.21)$$

2.3.2. Regenerative ORC

Both the regenerative ORC and regenerative Rankine cycles employ five thermodynamic processes: pressure increase of the evaporator inlet, evaporation in the primary heat exchanger, expansion in the turbine (expander), condensation, and preheating of the pump outlet by the turbine outlet (regeneration). Figure 2.5 is an illustration of the regenerative ORC presenting the main system components: feed pump, evaporator (primary heat exchanger), turbine, condenser, and regenerator. The feed pump delivers working fluid at the elevated pressure to the regenerator to be preheated by the turbine exhaust flow stream and sends it to the approximately constant pressure evaporator to be evaporated using the externally supplied heat. Some ORC designs might also implement a superheater to superheat the working fluid before it is expanded in the turbine (expander) driving an electric generator. The low-pressure, low-temperature working fluid leaving the turbine is cooled in the regenerator and condensed in the condenser to reach the saturated liquid (or slightly subcooled) state. The pressure of the working fluid leaving the condenser is increased by the feed pump, completing the work cycle.

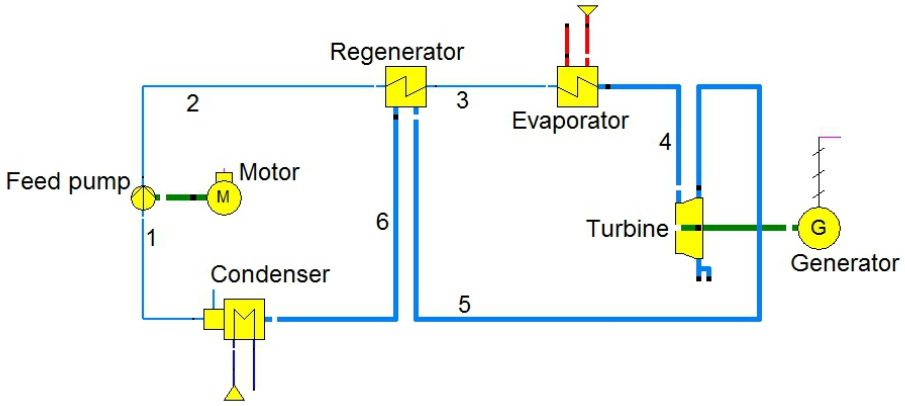

Figure 2.5. Schematic of a regenerative ORC.

The analysis of the cycle performance was performed by neglecting the friction and heat losses in the pipes and heat exchangers, and assuming adiabatic turbine and feed pump.

The heat input to the cycle is calculated as:

$$\dot{Q_{in}} = \dot{m_f}(h_4 - h_3) \tag{2.22}$$

The net power output is:

$$\dot{W}_{net} = \dot{W}_T - \dot{W}_P = \dot{m_f}(h_4 - h_5 + h_1 - h_2) \tag{2.23}$$

For perfect gas (defined in Section 3.3 in Chapter 3):

$$\dot{W}_{net} = \dot{m_f} C_p (T_4 - T_5 + T_1 - T_2) \tag{2.23a}$$

The temperature at State Point 3 and 5 are calculated by:

$$T_3 = T_2 + (T_5 - T_6) \tag{2.24}$$

$$T_5 = T_6 + (T_5 - T_2)\varepsilon_{reg} \tag{2.25}$$

$$T_3 = T_2 + (T_5 - T_2)\varepsilon_{reg} \tag{2.26}$$

where ε_{reg} denotes regenerator effectiveness.

The thermal efficiency of the cycle η_{th} is defined as:

$$\eta_{th} = \frac{\dot{W}_{net}}{\dot{Q}_{in}} \quad (2.27)$$

2.3.3. Simple Brayton cycle

Figure 2.6 shows the main thermodynamic processes and components of a simple Brayton cycle. Compressed working fluid discharged from the compressor at State Point 2 (SP2) is heated by the heater (primary heat exchanger) at approximately constant pressure to SP3. Mechanical work is generated by expanding the high temperature and pressure working fluid in the turbine (expander) from SP3 to SP4. The low temperature and pressure working fluid discharged from the turbine at SP4 is cooled by the cooler to SP1 prior being compressed in the compressor to SP2 to complete the cycle.

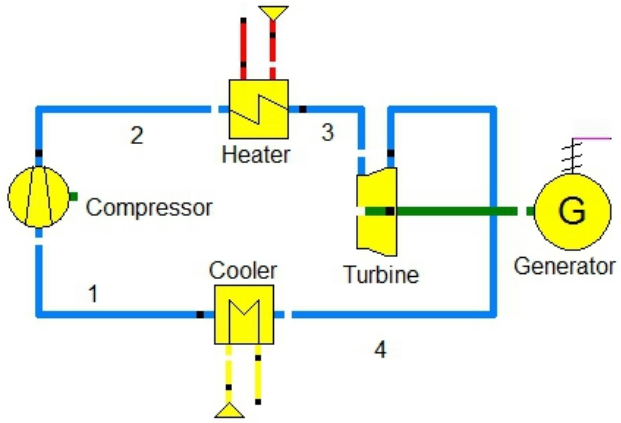

Figure 2.6. Schematic of a simple Brayton cycle.

The T-s diagrams of a simple transcritical and supercritical Brayton cycle are presented in Figure 2.7. As shown in Figure 2.7A, the compression work of the supercritical cycle having the compressor inlet in the “liquid-like” region is greatly reduced, compared to the case where the compressor inlet is in the “gas-like” region (Figure 2.7B).

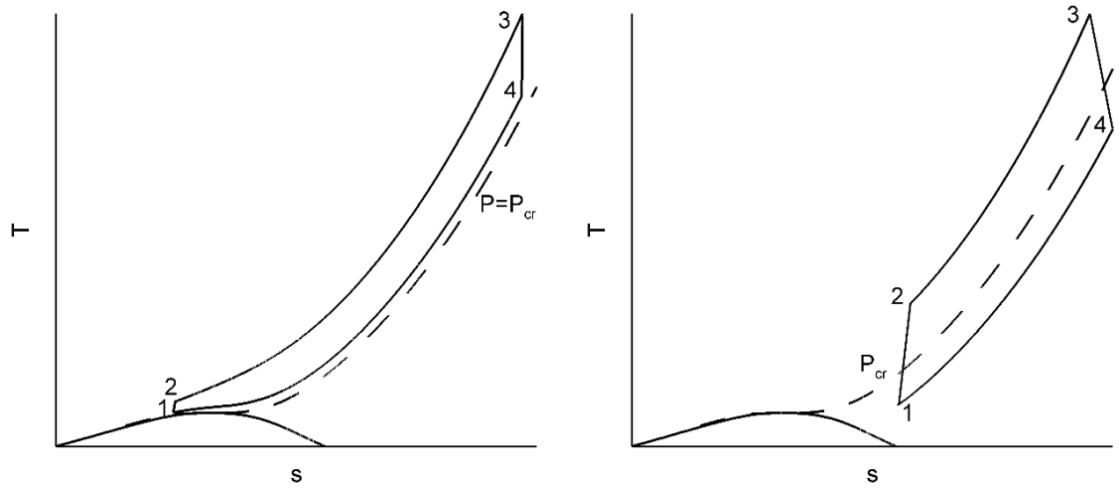

A) Supercritical B) Transcritical

Figure 2.7. T-s diagrams for the simple supercritical and transcritical Brayton cycle.

The thermodynamic analysis of the cycle performance was performed by neglecting the friction and heat losses in the pipes and heat exchangers, and assuming adiabatic turbine and feed pump (compressor).

The rate of turbine work output in a simple Brayton cycle may be determined as:

$$\dot{W}_T = \dot{m}_f \int_{T_4}^{T_3} c_p(T) dT \qquad (2.28)$$

where $\dot{m}$ is the mass flow rate of the working fluid and $c_p(T)$ is the specific heat of the gas (working fluid) at constant pressure; a function of temperature *T*.

Since for the monatomic gases such as Helium and Argon (except when highly compressed, at very low temperatures and high pressures) specific heat is constant and independent of temperature, to simplify the analysis, the constant specific heat value was assumed. However, for the diatomic gases such as air and N_2 and triatomic gases such as CO_2 the specific heat varies (increases) with temperature. Thus, in the following analysis,

for the diatomic and triatomic gases, c_p should be replaced by $\bar{c}_p$. Thus, The Eqn. (2.28) can be written as:

$$\dot{W}_T = \dot{m}_f c_p (T_3 - T_4) \tag{2.29}$$

For the perfect or semi-perfect gases (defined in Section 3.3 in Chapter 3), Eqn. (2.29) can be expressed in terms of the pressure ratio across the turbine and compressor r_P [83]:

$$r_P = \frac{P_3}{P_4} = \frac{P_{max}}{P_{min}} \tag{2.30}$$

The pressure ratio r_P can be used to determine the absolute temperature ratio across the turbine:

$$\frac{T_3}{T_{4s}} = r_p^{(k-1)/k} \tag{2.31}$$

where *k* is defined as the ratio of specific heats at constant pressure and constant volume.

$$k = \frac{c_p}{c_v} \tag{2.32}$$

Expressing the gas constant *R* as a function of specific heat values gives:

$$R = c_p - c_v \tag{2.33}$$

Eqns. (2.29) and (2.31) can be combined to yield the expression for the turbine power output:

$$\dot{W}_T = \dot{m}_f \eta_T c_p T_3 \left(1 - \frac{1}{r_p^{\frac{k-1}{k}}}\right) \tag{2.34}$$

where η_T is the turbine isentropic efficiency.

Using the same approach for the compressor power input leads to:

$$\dot{W}_c = \frac{\dot{m}_f c_p T_1}{\eta_c} \left(r_p^{\frac{k-1}{k}} - 1\right) \tag{2.35}$$

where η_c is the compressor isentropic efficiency.

The net work rate (power) output of the cycle is given by:

$$\dot{W}_{net} = \dot{W}_T - \dot{W}_c = \dot{m}_f c_p T_1 \left[\left(\eta_T \frac{T_3}{T_1} - \frac{r_p^{\frac{k-1}{k}}}{\eta_c} \right) \left(1 - \frac{1}{r_p^{\frac{k-1}{k}}} \right) \right] \quad (2.36)$$

The optimum pressure ratio for real cycles can be determined by differentiating Eqn. (2.36) with respect to r_p and setting the derivative to zero.

$$\frac{d}{dr_p}\left(\dot{W}_{net}\right) = 0 \quad (2.37)$$

The optimum pressure ratio can be expressed as:

$$r_{p_{opt}} = (\eta_t \eta_c \frac{T_3}{T_1})^{\frac{k}{2(k-1)}} \quad (2.38)$$

Since the quantity *k/2(k-1)* decreases as *k* increases, for the fixed minimum and maximum cycle temperatures the optimum pressure ratio for the monatomic gases (such as He) is, in general, lower than for the diatomic gases (such N_2, and Air), and the triatomic gases (CO_2) [83].

For the real gas assumption, Eqn. (2.38) can be written as:

$$r_{p_{opt}} = c_1(\eta_t \eta_c \frac{T_3}{T_1})^{\frac{kc_2}{2(k-1)}} = c_1 a^{\frac{kc_2}{2(k-1)}} \quad (2.39)$$

where the quantity “a” is defined as:

$$a = \eta_t \eta_c \frac{T_3}{T_1} \quad (2.40)$$

Figure 2.8 represents simulated (calculated by EPV-11) results for the optimum pressure ratio for different working fluids. Numerical values of constants c_1 and c_2 for different real gases are presented in Table 2.1.

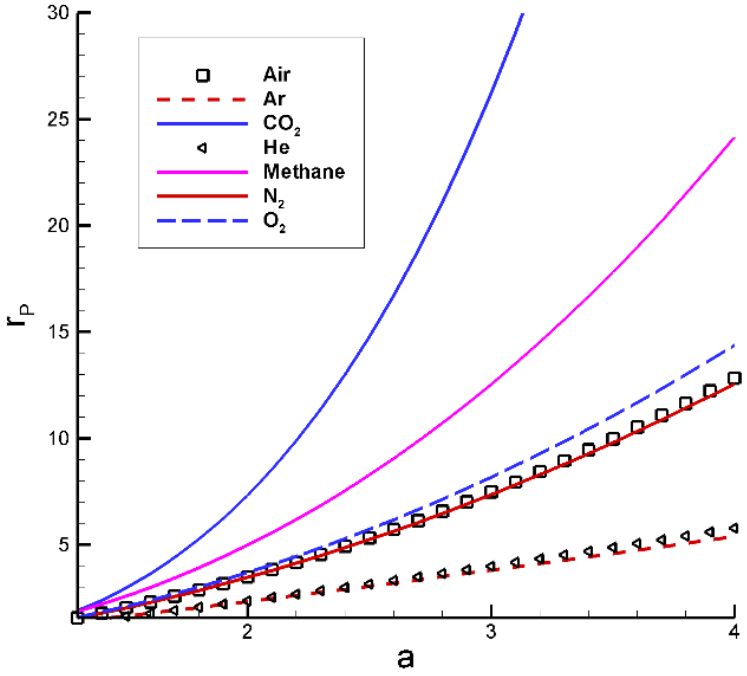

Figure 2.8. Optimum pressure ratio for real gasses.

Table 2.1. $c_1 and\ c_2$ Values for real gases.

Fluid	c_1	c_2
O_2	1.102	0.9658
Air	1.0953	0.9516
N_2	1.09494	0.9473
Methane	1.381265	0.8423
Ne	0.961943	1.0289
Kr	1.266174	0.8116
Ar	1.083395	0.9647
He	0.957433	1.0238
CO_2	1.727543	0.8642

Figure 2.8 shows that values of the optimum pressure ratio for all analyzed monatomic gasses are low and, as expected, approximately the same. The optimum pressure ratio for the diatomic gases is higher, with CO_2 (triatomic gas) having the highest value of r_p of all analyzed gases. Thus, to achieve the maximum power output, the power cycle using CO_2 as a working fluid needs to operate with much higher optimum pressure ratio, compared to other working fluids. For all working fluids, the optimal pressure ratio

increases as the maximum temperature is increased, which is consistent with the conventional thermodynamic analysis of the Brayton cycle performance.

The specific net work output of the cycle at the optimum pressure ratio, i.e., the maximum specific net work output $\dot{w}_{net,max}$ can be expressed as:

$$\dot{w}_{net,max} = \frac{\dot{W}_{net,max}}{\dot{m}_f} = \frac{c_p}{\eta_c}\left[(\eta_c \eta_T T_3)^{0.5} - {T_1}^{0.5}\right]^2 \tag{2.41}$$

The heat input to the simple Brayton cycle is:

$$\dot{Q}_{in} = \dot{m}_f c_p[(T_3 - T_1) - \left(T_1 \frac{r_p^{\frac{k-1}{k}} - 1}{\eta_c}\right)] \tag{2.42}$$

The specific heat input at the optimum pressure ratio can be written as:

$$\dot{q}_{net,max} = \frac{\dot{Q}_{net,max}}{\dot{m}_f} = c_p \left[(T_3 - T_1) - \left(\frac{T_3 T_1 \eta_T}{\eta_c}\right)^{0.5} + \frac{T_1}{\eta_c}\right] \tag{2.43}$$

By dividing Eqn. (2.41) by Eqn. (2.43), thermal efficiency of the simple Brayton cycle at the optimum pressure ratio can be expressed as:

$$\eta_{th} = \frac{\dot{W}_{net,max}}{\dot{Q}_{in,max}} = \frac{\left[(\eta_c \eta_T T_3)^{0.5} - {T_1}^{0.5}\right]^2}{(T_3 - T_1) - \left(\frac{T_3 T_1 \eta_T}{\eta_c}\right)^{0.5} + \frac{T_1}{\eta_c}} \tag{2.44}$$

Based on the Eqn. (2.44), thermal efficiency of a simple Brayton cycle at the optimum pressure ratio does not depend on the working fluid properties.

The turbine and compressor discharge temperatures at the optimum pressure ratio can be determined from:

$$T_4 = \left[(1 - \eta_T)T_3 + \frac{\eta_T T_3}{r_p^{\frac{k-1}{k}}}\right] \tag{2.45}$$

$$T_2 = \frac{(\eta_T \eta_c T_1 T_3)^{0.5} - T_1}{\eta_c} + T_1 \tag{2.46}$$

2.3.4. Regenerative Brayton cycle

Depending on the type of the working fluid (dry, wet, or isentropic), a regenerative Brayton cycle with a regenerator placed ahead of the cooler to recover heat from the turbine exhaust and thus, improve the cycle efficiency may be chosen instead of a simple Bryton cycle. Figure 2.9 presents the main components of a regenerative Brayton cycle: the compressor, heater (primary heat exchanger), turbine, cooler, and regenerator. The working fluid discharged from the turbine at SP4 passes through the recuperator where its temperature is reduced to SP5. The heat recovered by the recuperator is transferred to the working fluid discharged from the compressor, increasing its temperature from SP2 to SP6. The preheated working fluid is then heated by the heater to SP3.

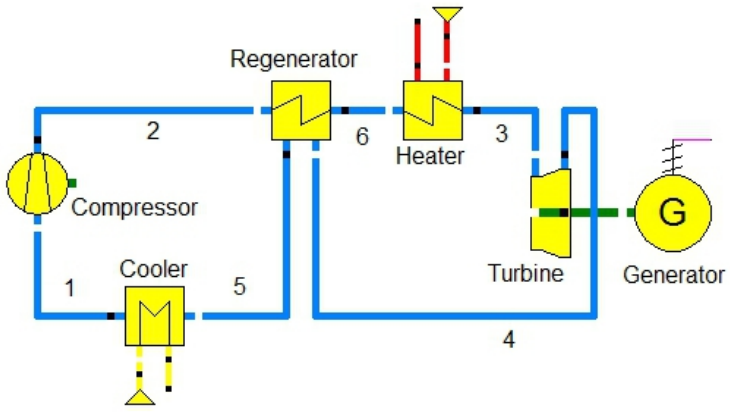

Figure 2.9. Schematic of the regenerative Brayton cycle.

Regeneration is defined as the internal exchange of heat within the cycle. Due to the lower value of temperature T_2 at SP2 compared to temperature T_4 at SP4, regeneration is used to preheat the compressor discharge by the turbine exhaust gases in a surface type heat exchanger referred to as the regenerator. The regenerator effectiveness ε_{reg}, is defined as the ratio of the actual to maximum possible temperature difference. In other words:

$$\varepsilon_{reg} = \frac{T_6 - T_2}{T_4 - T_2} \tag{2.47}$$

The heater inlet temperature T_6 can be calculated as:

$$T_6 = \left[T_2 + \varepsilon_{reg}(T_4 - T_2)\right] \tag{2.48}$$

The cooler inlet temperature T_5 can be determined from:

$$T_5 = \left[T_4 - \varepsilon_{reg}(T_4 - T_2)\right] \tag{2.49}$$

The heat input to the regenerative cycle is:

$$\dot{Q}_{in,reg,max} = \dot{m}_f c_p (T_3 - T_6) = \dot{m}_f c_p \left[T_3 - T_2 - \varepsilon_{reg}(T_4 - T_2)\right] \tag{2.50}$$

Adding regeneration to the cycle does not change the net work output and the optimum pressure ratio, thus thermal efficiency of the regenerative Brayton cycle at the optimum pressure ratio can be expressed as:

$$\eta_{th} = \frac{\dot{W}_{net,max}}{\dot{Q}_{in,reg,max}} = \frac{\left[(\eta_C \eta_T T_3)^{0.5} - T_1{}^{0.5}\right]^2}{T_3 - T_2 - \varepsilon_{reg}(T_4 - T_2)} \tag{2.51}$$

Based on Eqn. (2.51), at the optimum pressure ratio, properties of the working fluid do not affect thermal efficiency of a regenerative Brayton cycle.

2.3.5. Regenerative Brayton cycle with recompression

The main thermodynamic processes and components of a regenerative Brayton cycle with recompression (RBCR), also known as the Feher cycle, are shown in Figure 2.10. In the RBCR, a portion (20-40%) of the hot stream is returned to the minimum cycle temperature while the remaining stream detours the cooler and is recompressed to the maximum cycle pressure from the higher temperature [84]. Due to the high variation of C_p with pressure near the critical point of CO_2 (see Section 3.3 of Chapter 3), having one

heat exchanger results in a pinch-point[1] limitation in the recuperator due to unfavorable capacity rate ratio (C_R) [85]. Thus, dividing the recuperation duty into the high-temperature (HT) and low-temperature (LT) recuperators, splitting the flow leaving the LT recuperator, compressing it, and circulating it through the HT recuperator shifts the capacity rate ratio and avoids the pinch-point limitation [85]. Therefore, recompression results in better performance of the Brayton cycle. Moreover, lower heat duty of each heat exchanger combined with larger pinch-point and more favorable capacity rate ratio results in a smaller heat exchanger size.

Therefore, the use of a supercritical CO_2 (sCO_2) as the working fluid has been mainly the focus of the research concerning the recompression Brayton cycle. Operation of the compressor in the "liquid-like" region where density is high reduces the compressor work and increases the thermal efficiency. Having two smaller heat exchangers rather than one large heat exchanger in a recompression cycle can prevent instability of the CO_2 cycle when the cycle operates near the CO_2 critical point. However, matching the pressure at SP 9, where discharge streams from the LT regenerator and re-compressor (Compressor 2) mix, is a challenge.

1. The pinch-point is defined as the point where temperature difference between the two streams in the heat exchanger is minimum.

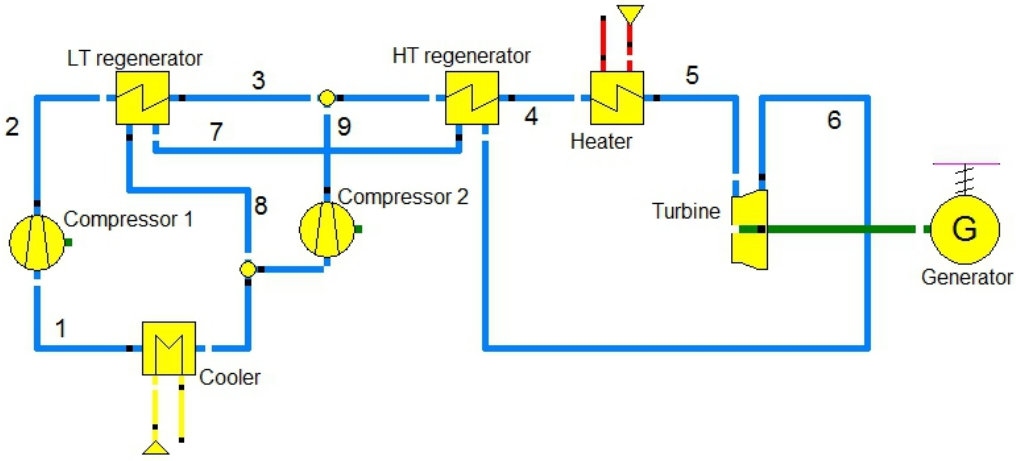

Figure 2.10. Schematic of the regenerative Brayton cycle with recompression.

2.3.6. Combined Brayton/ORC cycle

In a combined power cycle, two or more thermodynamic cycles are combined to achieve higher efficiency and power output. Based on the operating temperature range, the cycles are divided into the topping and bottoming cycles. The Brayton cycle was selected as a topping cycle because the high turbine inlet temperature (TIT) is needed to achieve high thermal efficiency, which makes it compatible with the high-temperature CSP-T plant. The exhaust temperature of a simple Brayton cycle (above 400°C) is higher than the maximum allowed ORC operating temperature; thus, a regenerative Brayton cycle, having lower exhaust temperature, needs be used as a topping cycle in a combined Brayton/ORC cycle. The main components of a combined Brayton/simple ORC are shown in Figure 2.11.

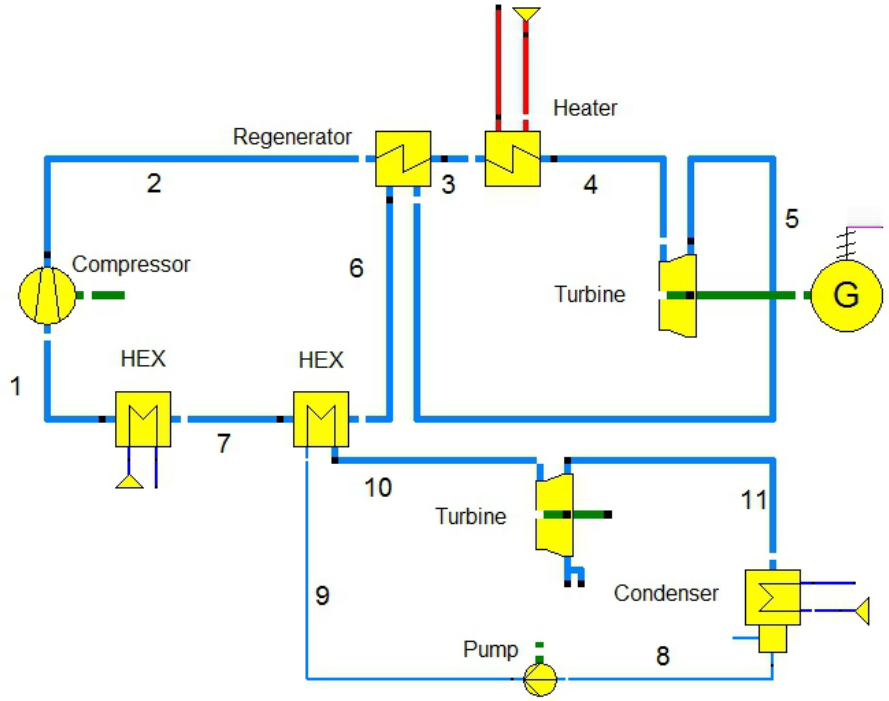

Figure 2.11. Schematic representation of a combined Brayton/ORC cycle.

Thermal efficiency of a combined cycle may be calculated as:

$$\eta_{combined} = \frac{\dot{W}_{net,Brayton} + \dot{W}_{net,ORC}}{\dot{Q}_{in,Brayton}} = \eta_{th,Brayton} + A \qquad (2.52)$$

Eqn. (2.52) provides insight into why combined cycles are more efficient compared to the simple cycles: efficiency of the combined cycle is a sum of the Brayton (topping) cycle efficiency and a positive quantity *A* representing the improvement in thermal efficiency due to the net power output of the bottoming cycle. As it will be shown later, the value of quantity *A* depends on a selection of the working fluid for the bottoming (ORC) cycle.

2.3.7. Regenerative steam Rankine cycle with a reheat

A regenerative steam Rankine cycle with a reheat (RSRC), described in this section, employs eight thermodynamic processes: pressure increase at the evaporator inlet, phase

change in the evaporator, expansion in the high pressure (HP) turbine, reheat in a reheater, expansion in the low pressure (LP) turbine, condensation, pressure increase of the condensate leaving the condenser using the LP and HP feed pumps, placed upstream and downstream from the deaerator (open feedwater heater), and use of energy from a steam extracted from the HP turbine exhaust IP turbine inlet) to preheat the condensate flow leaving the LP pump (regeneration).

Figure 2.12 is an illustration of the RSRC presenting the main system components: LP and feed pumps, evaporator and HP turbine, reheater and LP turbine, and a deaerator (open feedwater heater). The steam leaving the evaporator is referred to as the live or main steam.

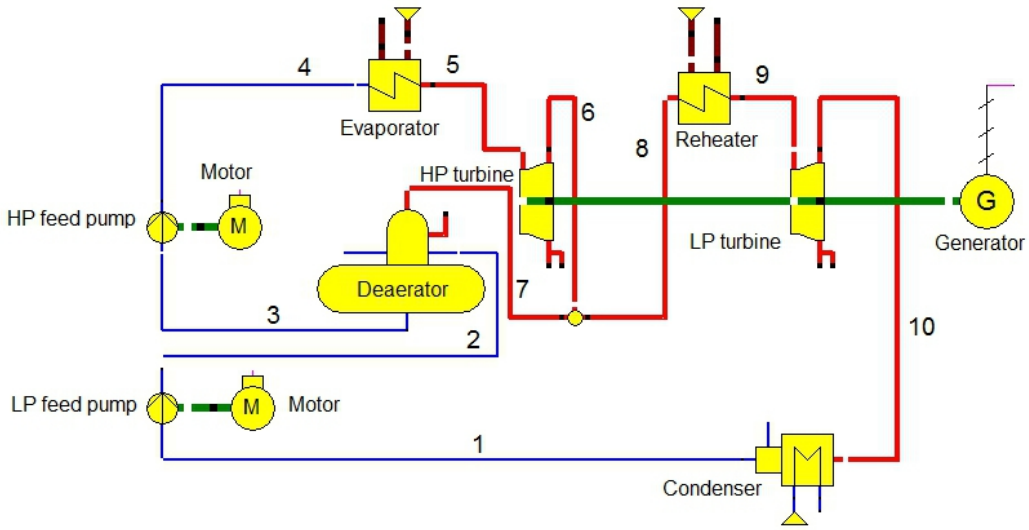

Figure 2.12. Schematic of the RSRC.

2.3.8. Combined Rankine/ORC cycle

As shown in Figure 2.13, RSRC was selected as a topping cycle, while a simple ORC was selected as a bottoming cycle.

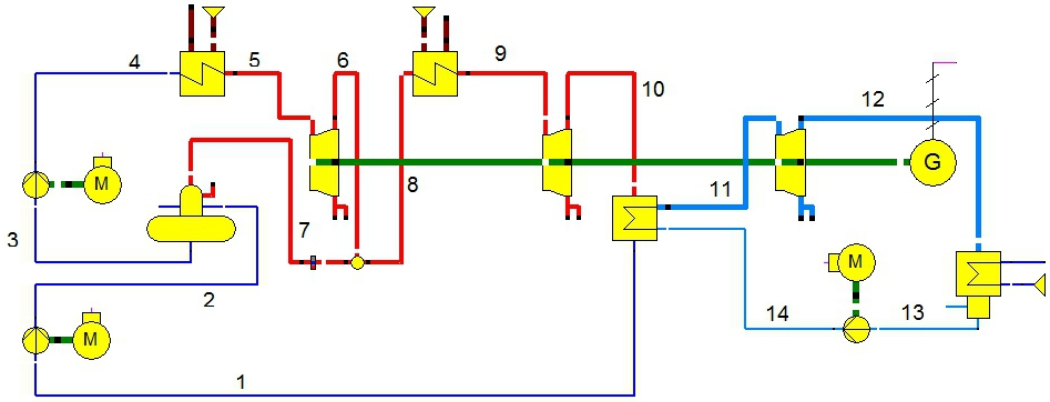

Figure 2.13. Schematic of the combined Rankine/ORC cycle.

2.4. Techno-economic Analysis of a CSP-T Plant (Theoretical Model)

2.4.1. Estimation of a power block cost

The capital cost of a power block consists of the purchased cost of the equipment, the labor and materials needed for the installation, such as the piping, the foundations and structural supports, the electrical equipment, the instrumentation and controls, and the indirect expenses. The indirect expenses cover the transportation costs for shipping equipment to the plant site and salaries for the project personnel.

Table 2.2 shows components of the total capital investment cost considered in this study. More details can be found in [86].

Table 2.2**.** Components of the total capital investment for a power block.

	Components of total capital investment	**Formula**
C_{TCI}	Total capital investment	$C_{TCI} = C_{TDC}+C_{land}+C_{royal}+C_{startup}$
$C_{startup}$	Cost of plant startup	$C_{startup} = 0.1*C_{TDC}$
C_{royal}	Cost of royalties	0
C_{land}	Cost of land	$C_{land} = 45*10\text{^}4*(P/100MWNET)\text{^}0.7$
C_{TDC}	Total depreciable capital	$C_{TDC} = 1.18*C_{DPI}$
C_{DPI}	Total direct permanent investment	$C_{DPI} = 1.1*C_{TBM}$
C_{TBM}	Total bare module cost	$C_{TBM} = \sum C_{BM}+C_{spare}+C_{wf}$
C_{wf}	working fluid	C_{wf}
C_{SPARE}	Cost for spares	$2.1C_{BM}^{pump}$

The bare module cost, C_{BM}, is the sum of direct and indirect costs for each unit as described in Turton et al. [87] and can be calculated by Eqn. (2.53).

$$C_{BM} = C_P^0 F_{BM} \tag{2.53}$$

C_P^0 is the purchase cost of the equipment in the base condition. The base condition represents the case where the equipment is made of the most common material, usually carbon steel, and is operating at the ambient pressure. F_{BM} is the bare module factor.

The data for the purchase cost of the equipment, described by Turton et al. [87], were obtained based on the average CEPCI (Chemical Engineering Plant Cost Index) value of 397. The updated value of CEPCI of 556.8 for the year of 2015 was utilized for the present economic estimate.

The purchased equipment cost for the base conditions, C_P^0 may be determined by employing Eqn. (2.54).

$$log_{10} C_P^0 = K_1 + K_2 * log_{10} AA + K_3 (log_{10} AA)^2 \tag{2.54}$$

where *AA* is the size parameter for the equipment, and K_1, K_2, and K_3 are the constants given in Table 2.3. For the Brayton cycle analyzed in this work, the primary heat exchanger and recuperator was assumed to be a printed-circuit heat exchanger (PCHE). The high-pressure gas (such as sCO_2) on the cold side of the PCHE, and a high-viscosity fluid (liquid metal) on its hot side were used.

To represent the power density of different working fluids, the compressor data were modified by the density ratio ρ_{air}/ρ_{fluid}. The A-frame, finned-tube air coolers were considered for the all cooling (heat rejection) processes.

Table 2.3. Coefficients used to calculate the price of different components in a power block.

Equipment	K_1	K_2	K_3	C_1	C_2	C_3	B_1	B_2	F_M	F_{BM}	AA
ORC turbine	2.2476	1.4965	-0.1618	**	**	**	**	**	**	6.1	kW
ORC pump	3.3892	0.0536	0.1538	-0.393	0.3957	-0.0022	1.89	1.35	1.5	**	kW
ORC HEX	4.3247	-0.0303	0.1634	0.0388	-0.1127	0.0818	1.63	1.66	1	**	Area(m2)
Motor pump	2.4604	1.4191	-0.1798	**	**	**	**	**	**	1.5	kW
ORC ACC HEX	4.0336	0.2341	0.0497	0.0388	-0.1127	0.0818	0.96	1.21	1	**	Area(m2)
ORC ACC fan	3.1761	-0.1373	0.3414	**	**	**	**	**	2.5	5	Q(m3/s)
motors fans	2.4604	1.4191	-0.1798	**	**	**	**	**	**	1.5	kW
Brayton HEX	0.9420	0.8778	0	**	**	**	**	**	**	**	UA(W/K)
Brayton turbine	3.5195	0.5886	0	**	**	**	**	**	**	**	kW
regenerator	0.716	0.8933	0	**	**	**	**	**	**	**	UA(W/K)
Brayton cooler	1.4843	0.8919	0	**	**	**	**	**	**	**	UA(W/K)
compressor	3.1093	0.9142	0	**	**	**	**	**	**	**	kW
Generator	**	**	**	**	**	**	**	**	**	1.5	kW
Working fluid	**	**	**	**	**	**	**	**	**	1.25	**

The purchased equipment cost of the electrical generator, $C^0_{P,gen}$ is calculated according to Eqn. (2.55) as presented in Ref. [88]

$$C^0_{P,gen} = 690(\dot{W}_{gen})^{0.95} \tag{2.55}$$

The bare module factor, F_{BM} was calculated from:

$$F_{BM} = B_1 + B_2 * F_M * F_P \tag{2.56}$$

$$log_{10} F_P = C_1 + C_2 * log_{10} P + C_3 (log_{10} P)^2 \tag{2.57}$$

where B_1 and B_2 are the constants given in Table 2.3; F_M is the equipment material factor listed in Table 2.3; while F_P is the operating pressure factor. The relative pressure with unit of bar gauge (1 bar=0.0 barg) is used in Eqn. (2.57), where the pressure factors are always greater than unity. The constants C_1, C_2 and, C_3 are given in Table 2.3. Since the ORC is running at temperatures lower than 350°C, material changes were not considered for the components operating at different temperatures. The Brayton cycle is operating in a temperature range between 300 to 1,000°C, thus different materials of construction such as carbon steel, stainless steel, nickel alloys 625, 718, etc. should be used for different operating temperatures. The material selection method for the expanders and heat exchanges is discussed in Ref. [89]. Table 2.4 to Table 2.6 show F_{BM} values for components of the Brayton cycle operating at different maximum temperatures and pressures. The materials and material factors used for tempture higher than 800°C are not practical today, however it is unticipated that these material factors can be feasible in next decade by the development in material science. Thus, the analysis in this study will be done for maximum tempetures up to 1000°C.

Table 2.4**.** Material selection for the primary heat exchanger and compressor in a Brayton cycle.

T_{max}(°C)<	P_{max}<10 MPa		P_{max}<20 MPa		P_{max}<30 MPa	
	Material	F_{BM}	**Material**	F_{BM}	**Material**	F_{BM}
500	Carbon steel	1	Carbon steel	1	Carbon steel	1
650	Stainless steel (347)	2.5	Stainless steel (347)	2.5	Stainless steel (347)	2.5
700	Stainless steel (347)	2.5	Stainless steel (347)	2.5	Nickel alloy(625)	3
750	Stainless steel (347)	2.5	Nickel alloy (625)	3	Nickel alloy (625)	3
900	Nickel alloy (625)	3	Nickel alloy (625)	3	Nickel alloy (625)	3

Table 2.5**.** Material selection for the turbine in a Brayton cycle.

T_{max}(°C)<	P_{max}<10 MPa		P_{max}<20 MPa		P_{max}<30 MPa	
	Material	F_{BM}	**Material**	F_{BM}	**Material**	F_{BM}
500	Stainless steel (347)	2.5	Stainless steel (347)	2.5	Stainless steel (347)	2.5
650	Stainless steel (347)	2.5	Nickel alloy (625)	3	Nickel alloy (625)	3
900	Nickel alloy (625)	3	Nickel alloy (625)	3	Nickel alloy (625)	3

Table 2.6. Material selection for the air-cooled cooler in a Brayton cycle.

T_{max}(°C)<	P_{max}<10 MPa		P_{max} <20 MPa		P_{max}<30 MPa	
	Material	**F_{BM}**	**Material**	**F_{BM}**	**Material**	**F_{BM}**
500	Carbon steel	1	Carbon steel	1	Carbon steel	1
650	Carbon steel	1	Stainless steel (347)	2.5	Stainless steel (347)	2.5
900	Stainless steel (347)	2.5	Stainless steel (347)	2.5	Stainless steel (347)	2.5

Pumps are typically inexpensive but require regular maintenance to prevent leaks, therefore it is often recommended to provide funds for the spares, C_{spare}, for the pumps [86].

The cost of land, C_{land}, is related to the size of the power block [90] and is assumed to be 2.47\$/m^2 in southern California while the cost of royalties, C_{royal}, is neglected in the present work.

The cost of the working fluid, C_{wf} should be considered as the capital cost for an ORC. According to Ref. [91], the amount of the working fluid is expected as the liquid amount to fill the whole ORC system. Toffolo et al. [91], showed that for an ORC, about 370 kg of Iso-butane is needed for each kg/s of the working fluid. More details can be found in [91]. For a Brayton cycle, the cost of the working fluid does not play a major role on the cost of the power block. Table 2.7 shows the price of working fluids for ORC and Brayton cycles.

Table 2.7**.** Price of different working fluids.

Fluid	**Price(\$/kg)**
Air	0
Butane	1.195
CO_2	0.1
Ethanol	0.53
Helium	42.553
Iso-butane	0.86
R11	3.60
R141b	1.75

The total operation and maintenance (O&M) cost, C_{OM} is the sum of the direct manufacturing cost C_{DMC} and fixed costs, C_{Fix}.

$$C_{OM} = C_{DMC} + C_{Fix} \tag{2.58}$$

$$C_{DMC} = C_{Main} + C_{UT} \tag{2.59}$$

The sum of the maintenance and utilities costs, which includes wages and benefits, salaries and benefits, materials and services, and manufacturing overhead is called the direct manufacturing cost.

As defined in Ref. [86], maintenance cost C_{Main} can be calculated as:

$$C_{Main} = 0.0805 C_{TCI} \tag{2.60}$$

Utilities cost is related to the dry cooling tower [90] and it is calculated as:

$$C_{UT} = 2.1795 * (\dot{W}_{net}(MW))^{0.7} \tag{2.61}$$

Fixed cost includes the cost of the property taxes and liability insurance, and is equal to:

$$C_{Fix} = 0.02 C_{TDC} \tag{2.62}$$

Annual operation hours and electricity generation is:

$$OH_{Annual} = CF * 24 * 365 \tag{2.63}$$

$$E_{net} = \dot{W}_{net} * OH_{Annual} \tag{2.64}$$

where CF is the capacity factor of the power block and it is assumed to be 0.8. The Levelized Cost of Electricity (LCOE) of the project is calculated according to Eqn. (2.65), as described in Ref. [90]:

$$LCOE = \frac{C_{TCI} + \sum_{n=1}^{N} \frac{C_{OM,n}}{(1+d_{nominal})^{n}}}{\sum_{n=1}^{N} \frac{E_{net,n}}{(1+d_{real})^{n}}} \tag{2.65}$$

$$d_{nominal} = \left(\left(1 + \frac{d_{real}}{100}\right) * \left(1 + \frac{r}{100}\right) - 1\right) * 100 \quad (2.66)$$

where *d* is the discount rate and *r* is the inflation rate. The real discount and interest rates were assumed to be 0.055 and 0.025, respectively. *N* is the economical lifetime of the plant set to be 20 years, while *n* is the year of operation.

2.4.2. CSP-T plant cost estimation

This section discusses properties and the cost of the concentrated solar tower and its integration with the power block.

A concentrated solar power tower system includes: 1) solar field system, 2) tower and receiver system, 3) thermal storage system (TES), 4) power block system, and 5) site improvements. Table 2.8 shows components of each subsystem.

Table 2.8. List of the CSP-T plant components.

Solar field	**Tower/ receiver**	**Thermal storage**	**Power block**	**Site improvements**
Mirrors	Tower	Cold Tank	Turbomachinery	Site Preparation
Drivers	Receiver	Hot tank	Heat exchangers	Clearing and Grubbing
Pedestal, Mirror Support, Foundation Controls and Wired Connections	Riser and Downcomer Piping and Insulation	Piping, Insulation, Valves, & Fittings	Cooling system	Grading, Drainage, Remediation, Retention, & Detention
Field Wiring & Foundation Labor	Horizontal Piping & Insulation	Instrumentation Controls		Roads, Parking and Fencing
Installation and Checkout	Controls, Instruments, Heat trace	Foundations & Support Structures		Water Supply Infrastructure
	Cold Salt Pumps	Media		
	Space Part			

Figure 2.14 shows the schematic of the concentrated solar tower power plant with direct “two-tank” thermal energy storage system using molten salt as a heat transfer media. Adding thermal storage to a CSP-T plant with annual direct normal irradiance (DNI) higher than 2000 kWh/m²/y can increase the capacity factor of the system to 50% [92]. Nine hours of thermal storage and the capacity factor of 50% for a CSP-T plant integrated with

different power block configurations were assumed in this study. Basic characteristics of a CSP-T plant are summarized in Table 2.9.

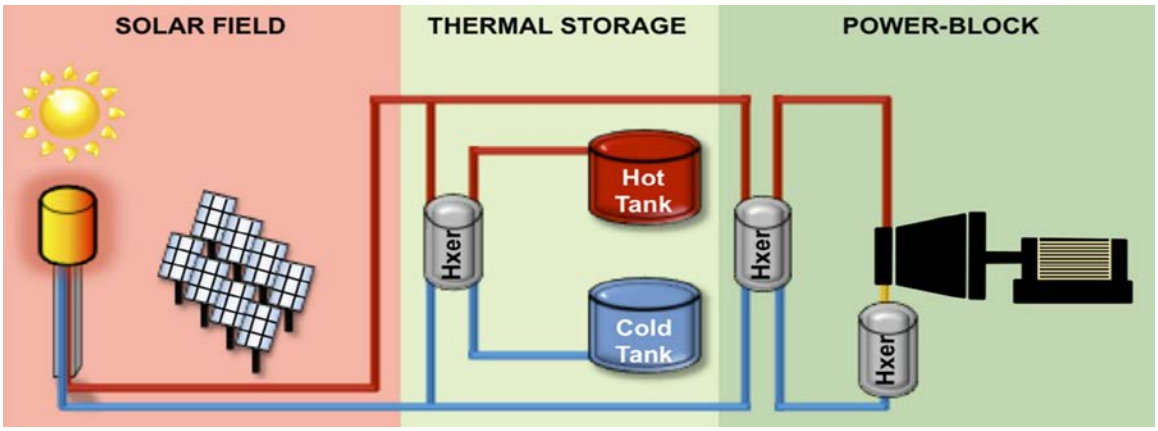

Figure 2.14. Schematic of a CSP-T plant [93].

Table 2.9. Properties of the CSP-T plant.

Parameter	Assumption
Thermal storage	9 hr
Solar multiple	2.1
Storage and heat transfer fluid	Molten salt
Thermal storage system	Direct " two-tank" system
Location	Southern California
Currency	2015 U.S Dollar
Cooling system	Dry cooling
Area of a single heliostat	12.2m*12.2m=148.84 m^2
Annual DNI(kWh/m2/yr)	2792
Capacity factor	0.5

The power plant is assumed to be located in Southern California and the labor rates at that location were considered in the calculations. These costs were evaluated according to the System Advisor Model (SAM) [94] provided by the National Renewable Energy Laboratory (NREL).

The total capital investment of a power plant includes direct costs (DC) and indirect costs (IDC). Data for the economic analysis for the DC and IDC are shown in Table 2.10 and Table 2.11, respectively.

Table 2.10. List of direct costs.

Direct cost (DC) Category	Unit	Value	Comment
Site improvements	$/m^2	16	Total heliostat reflective area
Solar Field	$/m^2	93	Total heliostat reflective area
Storage	$/kWh$_{th}$	Calculated by Ref. [95]	Storage capacity
Tower and Receiver	$/kW$_{th}$	Calculated by Eqns. 17 and 18	Receiver thermal power
Power block	$/MW	Calculated	Gross turbine capacity

Table 2.11. List of indirect costs.

Indirect cost (IDC) Category	Unit	Value	Comment
Contingency	% of DC	10	**
EPC and owner cost	% of DC	10	**
Land	$/acre	10,000	Total Land area
Sales tax	Applied to 80% of DC	7.75%	California tax

Total tower cost and receiver cost are calculated by Eqns. (2.67) and (2.68).

$$Total\ tower\ cost = 3{,}000{,}000 \times e^{(0.0113 * (Tower\ height - 0.5 * Reciever\ height + 0.5 * heliostat\ height))} \quad (2.67)$$

$$Total\ receiver\ cost = 103{,}000{,}000 \times \left(\frac{Reciever\ area}{1571}\right)^{0.7} * F_M \quad (2.68)$$

For maximum temperatures higher and lower than 650°C, F_M is equal to 1 and 1.5, respectively. Tower height, receiver height, heliostat height, receiver area, shape of the heliostat field, and the number of heliostats are calculated by SAM. The total heliostat reflective area, storage capacity, cycle heat input, receiver thermal power, and total land area are calculated by:

$$Total\ heliostat\ reflective\ area = Number\ of\ heliostats \times Area\ of\ a\ single\ heliostat \quad (2.69)$$

$$Storage\ capacity = Cycle\ heat\ input \times Hours\ of\ storage \quad (2.70)$$

$$Cycle\ heat\ input = \frac{Turbine\ gross\ power}{Cycle\ gross\ efficiency} \quad (2.71)$$

$$Receiver\ thermal\ power = Solar\ multiple \times Cycle\ heat\ input \quad (2.72)$$

Total land area= Solar field land area+ Non-solar field land (2.73)

The solar multiple (SM) expresses the solar field aperture area as a function of the power cycle capacity. A solar multiple of 1 is the aperture area required to deliver enough thermal energy to the power block to drive it at its nameplate capacity under the design conditions. A CSP-T plant with and without thermal energy storage has a solar multiple of equal to or greater than one, respectively.

The operation and maintenance (O&M) cost includes the fixed and variable costs which are listed in Table 2.12.

Table 2.12. Operation and maintenance costs for CSP-T plant.

C_{OM} cost Category	**Unit**	**Value**	**Comments**
Fixed annual cost	$/year	0	**
Fixed cost by capacity	$/kW/year	65	Net power output
Variable cost by generation	$/MWh	1	Annual net electrical output
Fossil fuel cost	$/MMBTU	0	**

LCOE of the CSP-T plant can be calculated by using Eqn. (2.65). Finally, it should be mentioned that the effect of the natural convection and radiation heat loss of the solar receiver is considered by the SAM software. This heat loss is dependent on the location of the power plant and also on the maximum temperature of the cycle. The calculated heat loss is the sum of convection and radiation heat losses from the receiver.

CHAPTER 3: WORKING FLUID PROPERTIES

3.1. Overview

In this chapter, thermo-physical properties of the selected working fluids are listed, and different types (categories) of working fluids are presented. Environmental properties such as ozone depletion potential (ODP) or global warming potential (GWP) are discussed.

3.2. Physical Properties of Working Fluids

The choice of the working fluid for an ORC has a significant effect on the cycle performance. Different working fluids were evaluated to determine the best working fluid and establish the procedure for its selection for a simple ORC. Depending on the slope of the saturated vapor curve in the T-s diagram, working fluids are divided into the three main categories: dry, wet and isentropic. The positive, negative and infinite slope refers to the dry, wet, and isentropic fluids, respectively. Figure 3.1 shows saturation curves of the three types of the working fluids in the T-s diagram. The slope of the saturated vapor curve is one of the most important thermo-physical properties of the working fluid in an ORC [96], having a significant effect on its thermal efficiency and equipment arrangement [48]. In order to maintain the maximum allowed wetness at the turbine outlet and prevent erosion damage to the blading, the wet working fluid has to be superheated prior to its expansion in the turbine [97]. For the isentropic fluids, previous studies [97] have shown that there is a weak relation between the cycle efficiency and turbine inlet temperature (TIT). For the dry fluids, the highest cycle efficiency is achieved by maintaining saturated steam conditions at the turbine inlet [44, 98, 99]. Superheating the dry fluid will increase the

turbine exit temperature and condenser loading without having a significant effect on the turbine power output.

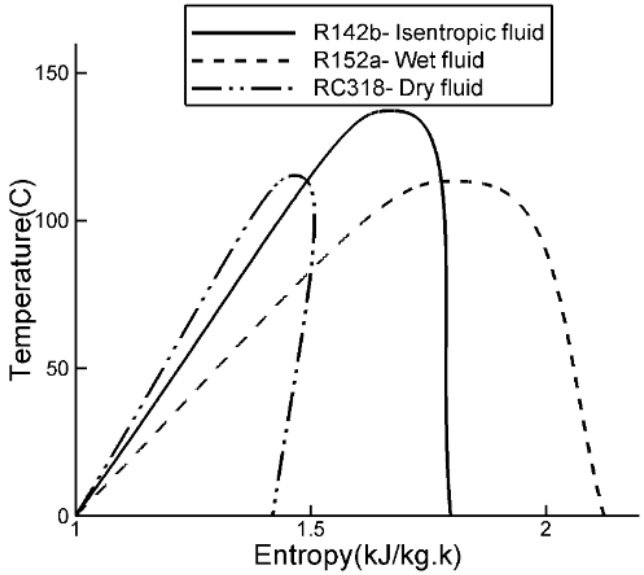

Figure 3.1. Comparison of wet, dry and isentropic fluids.

Physical properties of the working fluids play a significant role on the ORC performance. Therefore, it is essential to carefully select the appropriate working fluid. Table 3.1 shows the properties of working fluids used in this study. It can be seen that organic fluids have a significantly lower critical pressure and temperature compared to water (21.8 MPa and 374 °C). Also, the molar mass of organic fluids is higher compared to water.

Table 3.1. Physical, safety and environmental data of the working fluids used in a simple and regenerative ORC.

		Physical Data				Environmental and Safety Data				
	Fluid	**Molar mass (kg/kmol)**	**T_{cr} (°C)**	**P_{cr} (MPa)**	**Type**	**GWP**	**ODP**	**Toxicity**	**Flammability**	**Corros - iveness**
1	RC318	200.3	115.23	2.77	Dry	8200	0	NO	NO	NO
2	Butane	58.122	151.98	3.79	Dry	3	0	NO	YES	NO
3	Isobutane	58.122	134.66	3.62	Dry	3	0	NO	YES	NO
4	Ammonia	17.03	132.25	11.33	Wet	0	0	YES	NO	YES
5	R11	137.37	197.96	4.40	Isentropic	4000	1	NO	NO	NO
6	R141b	116.95	204.35	4.21	Isentropic	600	0.11	YES	NO	NO
7	R152a	66.051	113.26	4.51	Wet	140	0	NO	YES	NO
8	R142b	100.5	137.11	4.05	Isentropic	1800	0.06	YES	YES	NO
9	R134a	102.03	101.06	4.05	Wet	1300	0	NO	NO	NO
10	R245fa	134.05	154.01	3.65	Dry	1030	0	NO	NO	NO
11	R236ea	152.04	139.29	3.50	Dry	9810	0	NO	NO	NO
12	R236fa	152.04	124.92	3.20	Dry	1300	0	NO	NO	NO
13	Ethanol	46.068	240.75	6.14	Wet	n.a.	n.a.	NO	YES	NO
14	Methanol	32.042	239.45	8.10	Wet	n.a.	n.a.	YES	YES	NO
15	R12	120.91	111.97	4.13	Isentropic	10890	1	NO	NO	NO
16	Pentane	72.149	196.55	3.37	Dry	5	0	YES	YES	NO
17	R227ea	170.03	101.75	2.92	Dry	3220	0	NO	NO	NO
18	R123	152.93	183.68	3.66	Dry	77	0.02	YES	NO	NO
19	R22	86.468	96.145	4.99	Wet	1700	0.05	NO	NO	NO
20	R32	52.024	78.105	5.78	Wet	675	0	NO	YES	NO
21	R113	187.38	214.06	3.39	Dry	6130	1	NO	NO	NO
22	Isopentane	72.149	187.2	3.37	Dry	5	0	YES	YES	NO
23	R114	170.92	145.68	3.25	Dry	10.04	1	NO	NO	NO
24	n-Hexane	86.18	234.45	3.02	Dry	900	0	YES	YES	NO
25	R245ca	134.047	174.42	3.94	Dry	693	0	YES	YES	NO

n.a., non-available.

To increase thermal efficiency of an ORC employing dry fluids, a regenerator located downstream of the turbine is commonly used to lower the temperature of the working fluid into the condenser. As discussed in Chapter 2, the recovered heat is used to increase the temperature of the working fluid entering the evaporator (primary heat exchanger). This cycle modification is referred to as the regenerative ORC [100]. Hung et al. [48] reported that implementing a regenerator does not result in a significant thermal efficiency improvement (up to 2%- points) for the ORCs using wet and isentropic working fluids. Therefore, the wet and isentropic fluids were not analyzed for regenerative ORC. For the dry fluids, regeneration may improve thermal efficiency by more than 9%-points.

Table 3.1 presents properties of 14 dry working fluids investigated for a regenerative ORC. The first nine working fluids listed in Table 3.1 have the potential to be used in a regenerative ORC as they are not toxic. Butane and Iso-butane they are, despite their flammability, used as working fluids in geothermal cycles; R113 and R114 are chlorofluorocarbons (CFCs) with a strong ozone depletion potential. The remaining five dry working fluids are flammable or toxic.

Table 3.2 presents properties of the nine working fluids used in a Brayton cycle. As can be seen in Table 3.2, critical temperature of CO_2 is near the ambient temperature, thus the CO_2 can be used under its supercritical condition.

Table 3.2. Physical, safety and environmental data of the working fluids used in Brayton cycle.

		Physical Data			**Environmental and Safety Data**				
	Fluid	**Molar mass (kg/kmol)**	**T_{cr} (°C)**	**P_{cr} (MPa)**	**GWP**	**ODP**	**Toxicity**	**Flammability**	**Corrosiveness**
1	O_2	31.999	-118.57	5.04	0	0	NO	YES	NO
2	Air	28.965	-140.62	3.78	0	0	NO	NO	NO
3	N_2	28.013	-146.96	3.39	0	0	NO	NO	NO
4	Methane	16.043	-82.586	4.59	21	0	NO	YES	NO
5	Ne	20.179	-228.66	2.67	0	0	NO	NO	NO
6	Kr	83.798	-63.67	5.52	0	0	NO	NO	NO
7	Ar	39.948	-122.46	4.86	0	0	NO	NO	NO
8	He	4.0026	-267.95	0.22	0	0	NO	NO	NO
9	CO_2	44.01	30.978	7.37	1	0	NO	NO	NO

All working fluids listed in Table 3.2 were considered in this study to develop correlations for the cycle thermal efficiency and work output valid over a wide range of thermo-physical properties of the working fluids.

3.3. Perfect, Semi-perfect, and Real Gases

In this study, a perfect gas is a gas having constant specific heat capacity (independent of temperature) at a constant pressure. The specific heat capacity of a semi-

perfect gas is a function of temperature at a constant pressure. The specific heat capacity of a real gas is a function of both temperature and pressure.

3.4. Supercritical Fluids: CO_2

The properties of a supercritical fluid vary between those of a gas and those of a liquid. The largest variation in thermo-physical properties is occurring near the critical (cr) or pseudo-critical (pc) points. The pseudo-critical temperature T_{pc} of the fluid is defined as the point along a line of where the specific heat capacity of the fluid reaches its maximum value. Figure 3.2 shows properties of CO_2 near its critical point. As the data show, there is a dramatic change in fluid properties near the critical point. Also, the specific heat capacity and thermal conductivity of CO_2 tend to infinity as the fluid reaches its critical point.

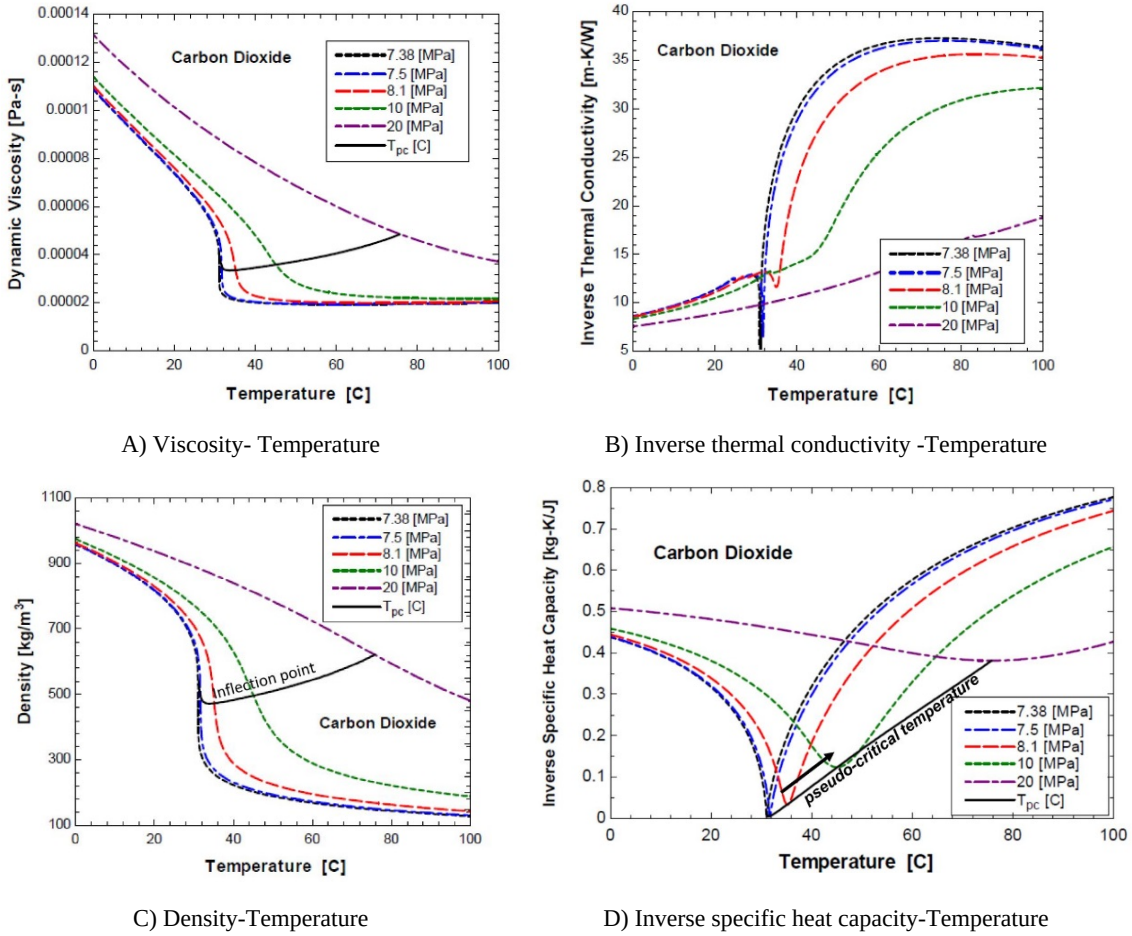

A) Viscosity- Temperature

B) Inverse thermal conductivity -Temperature

C) Density-Temperature

D) Inverse specific heat capacity-Temperature

Figure 3.2. Properties of CO_2.

The T-s diagram for the CO_2 is shown in Figure 3.3. On the right side of the pseudo-critical line, the fluid is more “vapor-like” and the densities are 15 to 30% of the density of water. However, on the left side of the pseudo-critical line, the fluid is more “liquid-like”, and the densities are 65 to 80% of the density of water. This large difference in density results in a considerable difference in compression work, as indicated by the length of the compression lines (red lines) in Figure 3.3, and the mass of working fluid required to fill the pilot-scale recompression Brayton cycle operated by the Sandia National Laboratory [101].

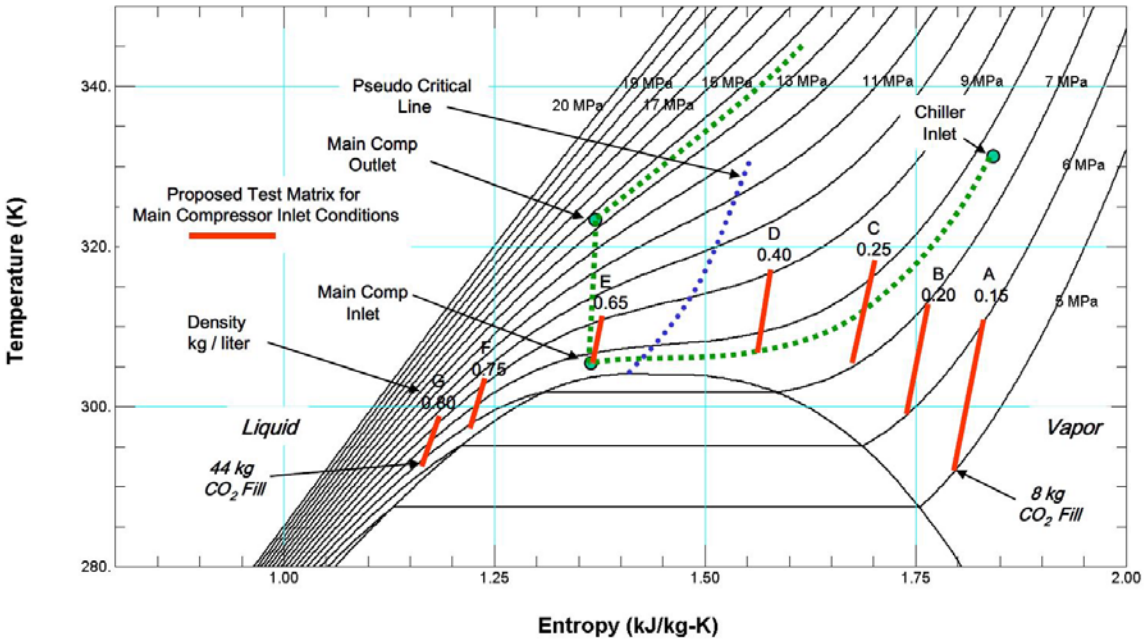

Figure 3.3. T-s diagram of CO_2 [101].

3.5. Environmental Properties of Working Fluids

Environmental and safety characteristics of the working fluids need also to be considered during the plant design because of their effect on plant operators' health and on the environment. Tables 3.1 and 3.2 show some environmental and safety data for the selected working fluids. The global warming potential (GWP), ozone depletion potential (ODP), toxicity, flammability, and corrosiveness are the properties of working fluids considered in this study. The GWP of a working fluid is a measure of its effect on Global Warming. Carbon dioxide (CO_2) has been assigned a GWP of 1. Thus, a fluid with GWP of 2 will have the effect on global warming two times stronger compared to the CO_2. Working fluids with ODP higher than zero cannot be considered for a power generation applications due to restrictions on their use imposed by the Montreal and the Kyoto protocols [102, 103]. The properties in Tables 3.1 and 3.2 were obtained from the GESTIS

database [104]. As it can be seen in Table 3.1, due to its toxicity, flammability, and corrosiveness, ammonia is not a good choice of the working fluid for power generation.

CHAPTER 4: WORKING FLUID SELECTION FOR CSP-T PLANTS

The results of parametric calculations performed over a range of cycle operating conditions corresponding to the CSP-T plant for a number of selected working fluids are presented in Chapter 4. The analysis was performed by using the EPV-11 models and comparing the results to the results from theoretical thermodynamic models developed in Chapter 2 to determine the effect of thermo-physical properties of the working fluids on thermodynamic performance of the cycle (efficiency and specific net work output). A statistical regression analysis was used to correlate simulation results and develop correlations for cycle thermal efficiency, specific net work output, and specific heat input in terms of the relevant cycle operating parameters. Performance maps were developed for the analyzed power cycles as guides for the selection of the best working fluid(s) for the specified (selected or given) set of cycle operating conditions.

The sensitivity analysis of the developed correlations was performed and the results are presented.

4.1. Simple ORC

4.1.1. The effect of operating conditions on simple ORC performance

Thermal efficiency of a simple ORC, determined over a range of operating conditions for twelve selected working fluids (working fluids 1 to 12 listed in Table 3.1), are presented in this section. A schematic representation of a simple ORC is presented in Figure 4.1.

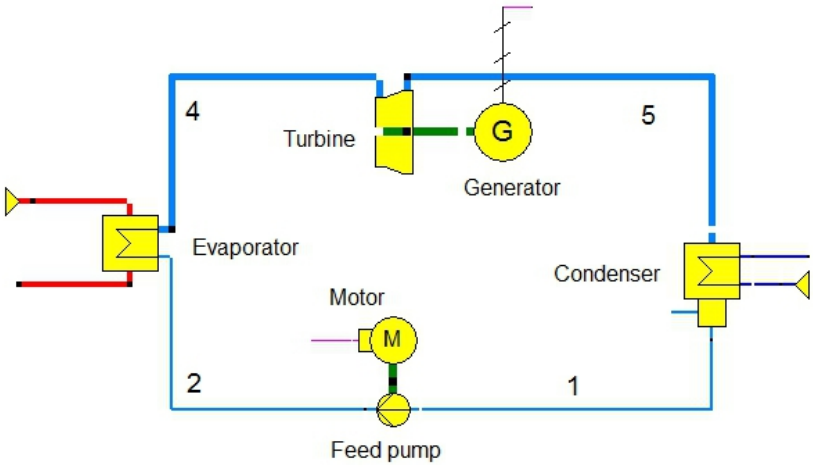

Figure 4.1. Schematic of a simple ORC.

The cycle parameters used in the calculations are summarized in Table 4.1. Based on the previous studies [105, 106], for the operating conditions used in this study, the temperature difference between the turbine inlet temperature (TIT) and the heat source temperature (the primary heat exchanger inlet temperature) is in the range of 5 to 25°C. Thus, the temperature difference of 10°C was selected for this study.

Table 4.1. Simple ORC parameters.

Parameter	Value
Minimum temperature, T_1 (°C)	15
Maximum temperature, T_4 (°C)	50-250
Turbine isentropic efficiency, η_t (%)	0.85
Pump isentropic efficiency (%)	0.8
Evaporator pressure drop (bar)	0.05
Mass flow rate, $\dot{m}_f$ (kg/s)	75
Generator efficiency (%)	0.975
Turbine mechanical efficiency (%)	0.99
Minimum pressure (bar)	Saturation pressure at 15°C

The effect of the cycle operating conditions and a working fluid on thermal efficiency of a simple ORC is presented in Figure 4.2. The contour graphs are plotted in

terms of the dimensionless pressure (P_r) and dimensionless temperature (T_r), defined by the following equations:

$$P_r = \frac{P_{max}}{P_{cr}} \quad , \quad T_r = \frac{T_{max}}{T_{cr}} \tag{4.1}$$

where P_{cr} and T_{cr} are critical pressure and temperature of the working fluid, respectively.

For the wet working fluids (Ammonia, R152a, and R134a), calculations were performed for $T_r = 0.8$ to 1.3 and $P_r = 0.1$ to 1.2, while for the isentropic fluids (R141b, R11, and R142b), the analysis was conducted for $T_r = 0.7$ to 1.15 and $P_r = 0.1$ to 1.2. The dry working fluids (R236ea, R236fa, and R245fa) were analyzed over the $T_r = 0.8$ to 1.2 and $P_r = 0.1$ to >1 ranges, and over the $T_r = 0.8$ to 1 and $P_r = 0.1$ to 0.8 - 0.1 ranges. As the results show, isentropic fluids have higher thermal efficiency in comparison to the dry and wet working fluids. The isentropic fluid R11 gives the highest cycle efficiency, while the dry working fluid R236fa provides the lowest efficiency.

Of all working fluids analyzed for a simple ORC, dry fluids RC318, R236ea, and R245fa have the lowest thermal efficiency. For the range of P_{cr} and T_{cr} analyzed in this study, the maximum value of η_{th} for these working fluids is 18% (Butane has the highest thermal efficiency). For instance, at $T_1 = 14°C, T_{ev} = 60°C$ and $T_4 = 94°C$, thermal efficiency of a simple ORC, determined for twelve working fluids, is presented in Table 4.2. As the results show, the dry working fluids have the lowest efficiency in comparison to other working fluids. Thus, considering thermal efficiency alone, dry working fluids are not a good choice for a simple ORC (especially subcritical ORC with a superheat).

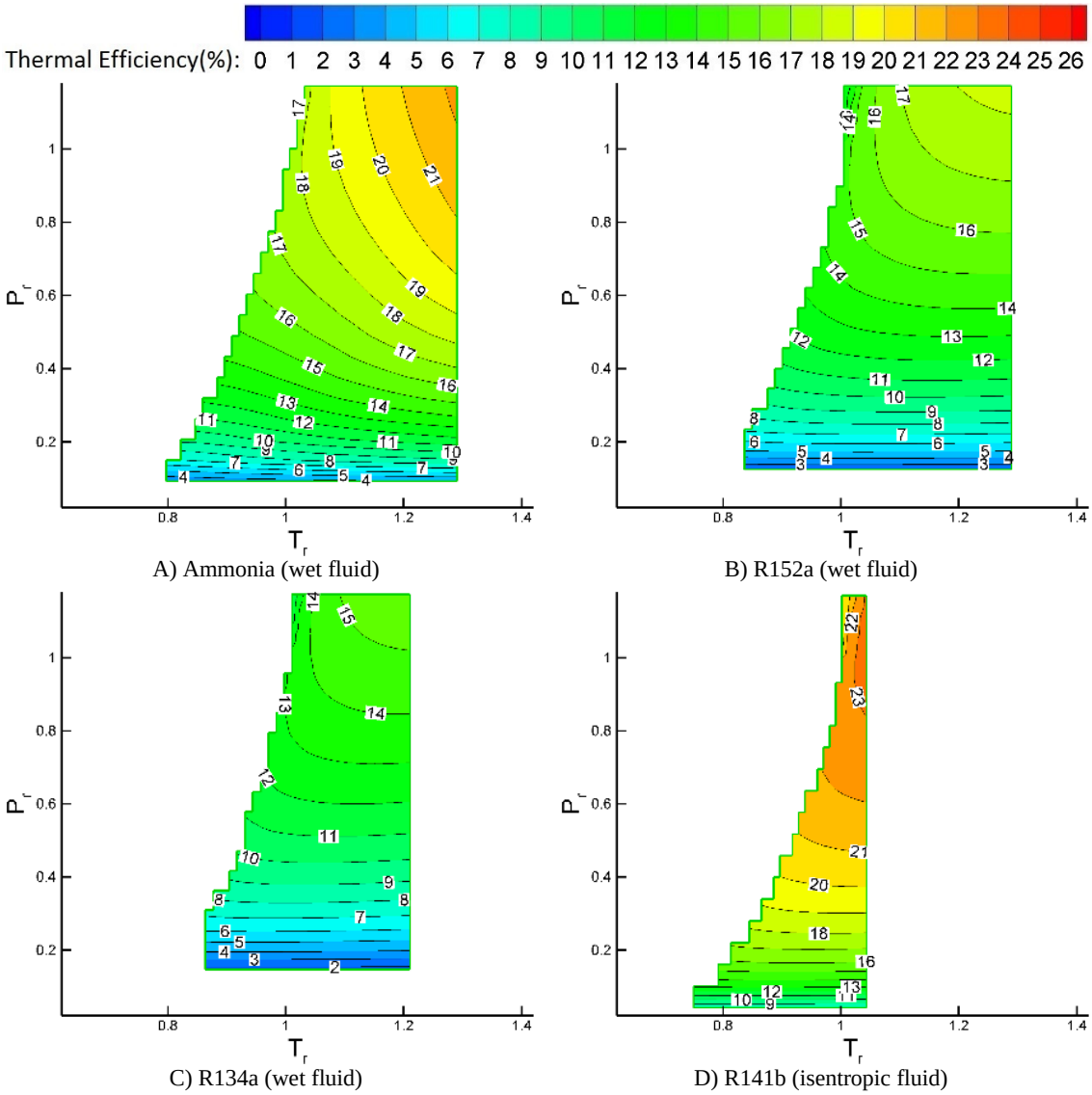

Figure 4.2. Thermal efficiency results for different working fluids used in a simple ORC.

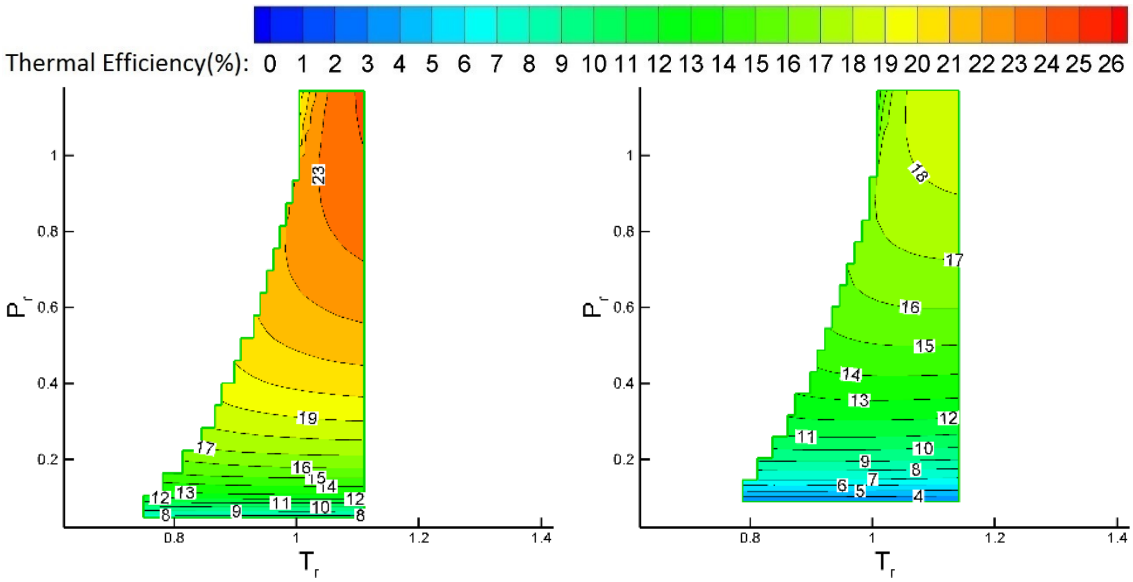

E) R11(isentropic fluid)

F) R142b (isentropic fluid)

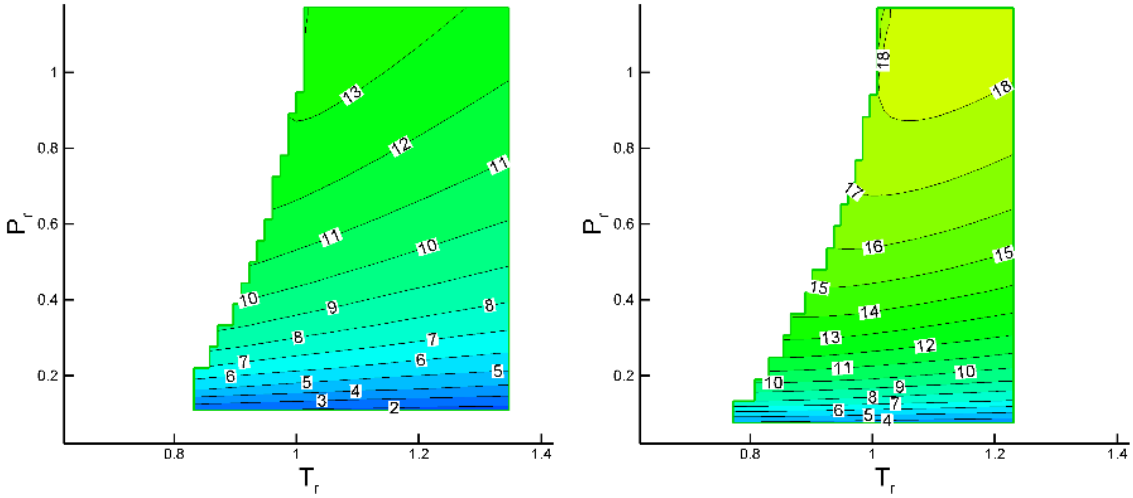

G) RC318 (dry fluid)

H) Butane (dry fluid)

Figure 4.2. Continued.

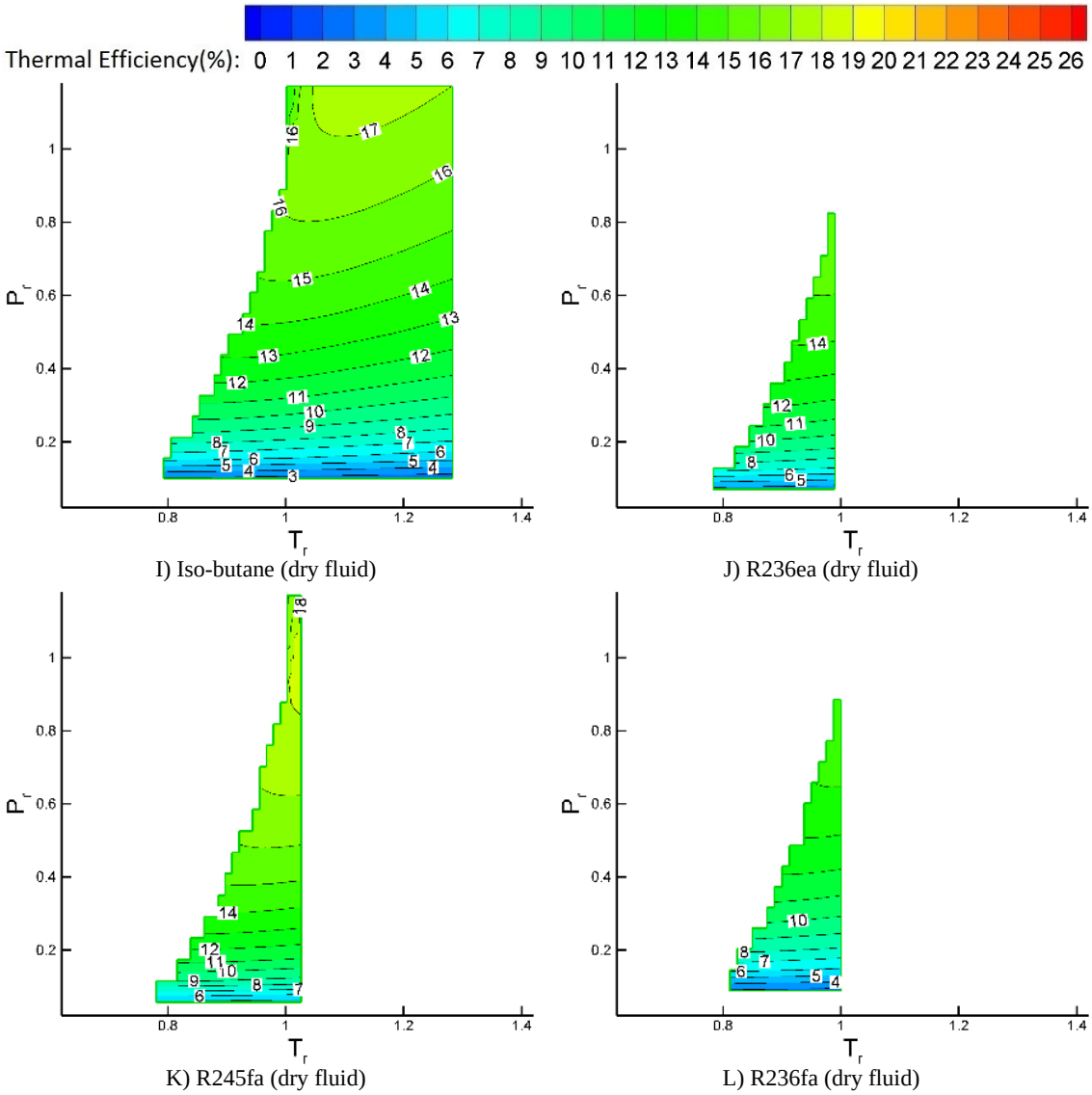

I) Iso-butane (dry fluid)

J) R236ea (dry fluid)

K) R245fa (dry fluid)

L) R236fa (dry fluid)

Figure 4.2. Continued.

For the maximum cycle temperature lower than 60°C, thermal efficiency of a simple ORC is lower than 10% for all analyzed working fluids, with a wet fluid R134a being the best choice, giving efficiency of 8.62%. For the maximum temperature in the 100 to 250°C range, η_{th} is substantially higher, with isentropic fluids R11 and R141b giving the highest efficiency (24% for R11).

Table 4.2. Thermal efficiency for a subcritical ORC with superheat.

Working fluids	Fluid type	Thermal efficiency (%)
R11	Isentropic	10.70
R141B	Isentropic	10.44
Ammonia	wet	10.33
R152A	wet	10.29
R142B	isentropic	10.05
R134A	wet	9.88
R245FA	dry	9.77
Butane	dry	9.77
Iso-butane	dry	9.63
R236ea	dry	9.39
R236fa	dry	8.82
RC318	dry	8.56

For the wet and isentropic fluids, η_{th} increases as the maximum temperature (T_{max}, or TIT) is increased at a constant maximum pressure. The dry fluids exhibit a different behavior; depending on the operating conditions, thermal efficiency of the dry fluids can increase or decrease as T_{max} is increased. For instance, as it can be seen in Figure 4.2, when the operating conditions are in the subcritical region, thermal efficiency of Butane decreases as the maximum temperature is increased. However, in the supercritical region, thermal efficiency increases initially, reaches a maximum, and then decreases. The maximum in thermal efficiency for most of the analyzed dry fluids is close to the critical point ($T_r = 1$). However, some dry fluids (R236ea for example) cannot be used in the EPV-11 model for temperatures above the critical temperature. Therefore, the maximum in η_{th} is not shown for all dry fluids in Figure 4.2.

The difference in the efficiency trends for different types of working fluids may be explained by the slope of the isobaric lines in the superheated region of the T-s diagram. If the slope is steeper in the high-pressure area compared to the low-pressure area, an increase in maximum temperature (T_{max}, TIT) will result in a higher thermal efficiency [107]. The expression for the slope T_s can be determined from the second Gibbs equation [108]:

$$c_p = T(\frac{\partial s}{\partial T})_p \qquad (\frac{\partial T}{\partial s})_p = \frac{T}{c_p} \tag{4.2}$$

$$T_r = \frac{T}{T_{cr}} \qquad s_r = \frac{s}{s_{cr}} \tag{4.3}$$

$$T_s = (\frac{\partial T_r}{\partial s_r})_p = \frac{T}{c_p}\frac{s_{cr}}{T_{cr}} \tag{4.4}$$

Figure 4.3 shows the slope T_s calculated from Eqn. (4.4) for the analyzed working fluids as a function of dimensionless pressure P_r.

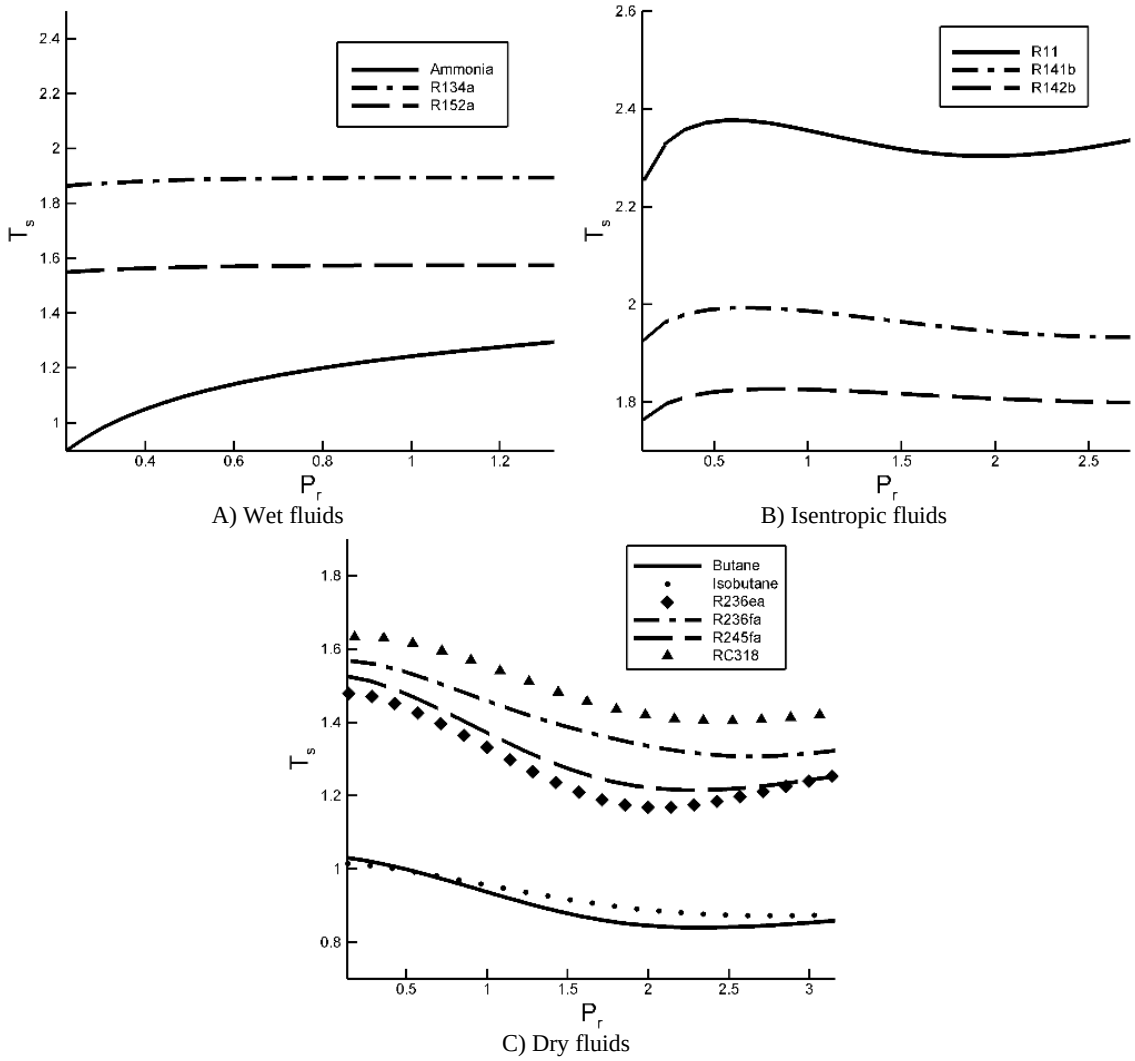

A) Wet fluids

B) Isentropic fluids

C) Dry fluids

Figure 4.3. Slope T_s of the isobaric curves for working fluids analyzed in this work.

For the wet fluids (Figure 4.3A), the slope increases as pressure is increased; however, for the maximum cycle pressure higher than the critical pressure, the slope becomes nearly constant. Thus, for the wet fluids, the constant pressure lines diverge, and an increase in T_{max} (TIT) results in a higher turbine power output and, therefore, higher cycle efficiency.

For the isentropic fluids (Figure 4.3B), there is a maximum in the slope T_s below the critical pressure, followed by the approximately constant slope region. As a consequence, the cycle thermal efficiency increases or remains approximately constant as the maximum cycle temperature (T_{max}, TIT) is increased. For the dry fluids (Figure 4.3C), the slope decreases as P_{max} is increased and reaches a minimum around $P_r = 2$. In the region of the negative slope, isobaric lines converge resulting in a decrease in thermal efficiency with an increase in T_{max} (TIT). The same explanation concerning efficiency trends with T_{max} (TIT) for different types of working fluids is presented in [96].

The specific net work output determined for nine working fluids over the range of operating conditions is presented in Figure 4.4.

In many applications such as solar or geothermal where ORC is chosen as a bottoming cycle, the cycle power output is more important than its thermal efficiency. As the results show, the ORC using Ammonia as a working fluid has the highest specific net work output, followed by Butane and Iso-butane. For TIT below 90°C, Butane produces specific net work output higher than 63 kJ/kg, while for the TIT above 100°C an Ammonia ORC produces net power output between 125 and 400 kJ/kg. At 250°C, the difference between the specific net work output of an Ammonia and RC318 ORC is higher than 360 kJ/kg. However, since Ammonia is toxic to humans, Butane and Iso-butane are often used.

As it can be seen from Eqn. (2.6) and in Figure 4.4, working fluids with higher C_p, such as Ammonia and Butane, produce higher net work output.

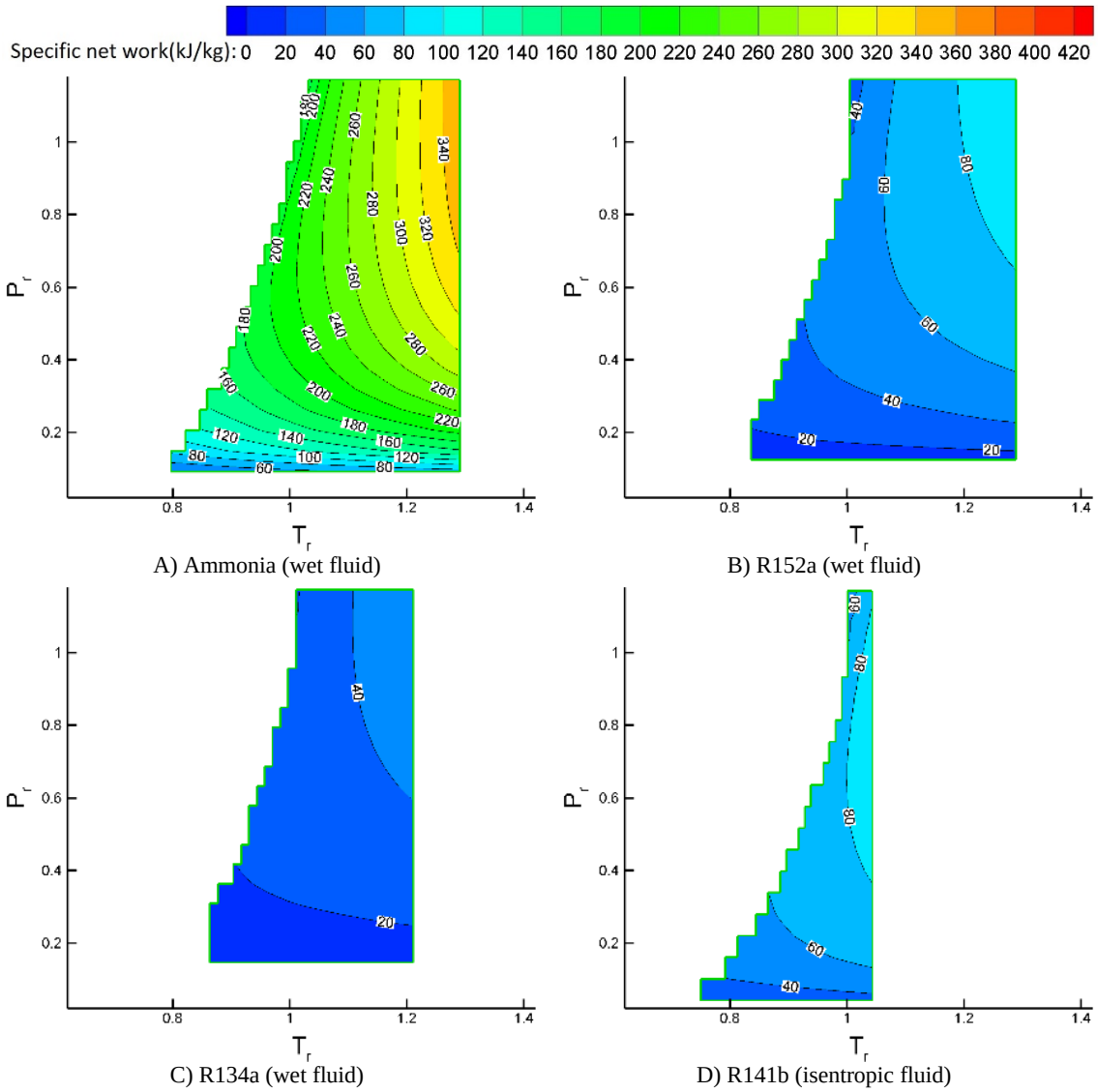

A) Ammonia (wet fluid)

B) R152a (wet fluid)

C) R134a (wet fluid)

D) R141b (isentropic fluid)

Figure 4.4. Specific net work results for working fluids analyzed in this work.

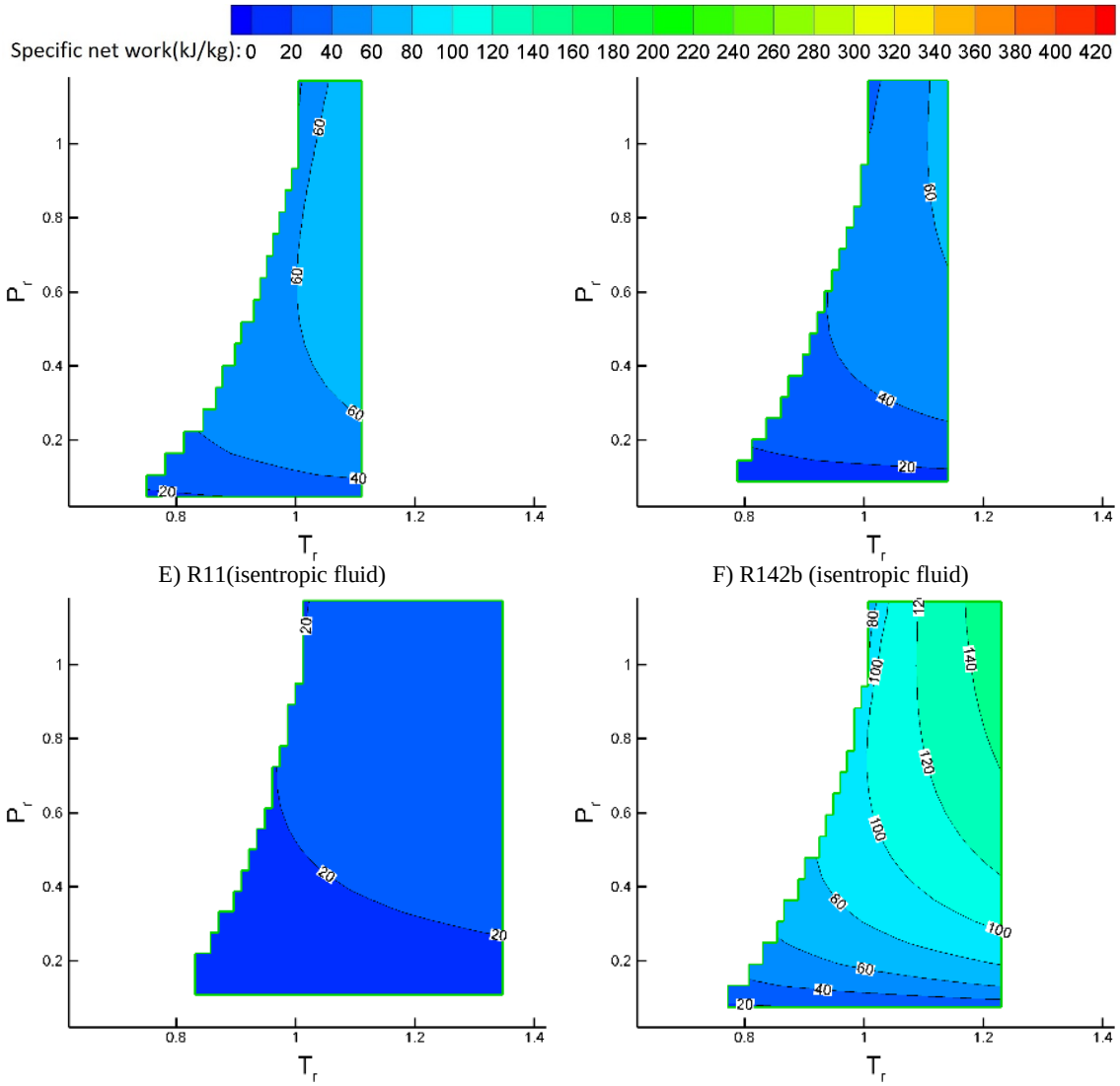

E) R11(isentropic fluid) F) R142b (isentropic fluid)

G) RC318(dry fluid) H) Butane (dry fluid)

Figure 4.4. Continued.

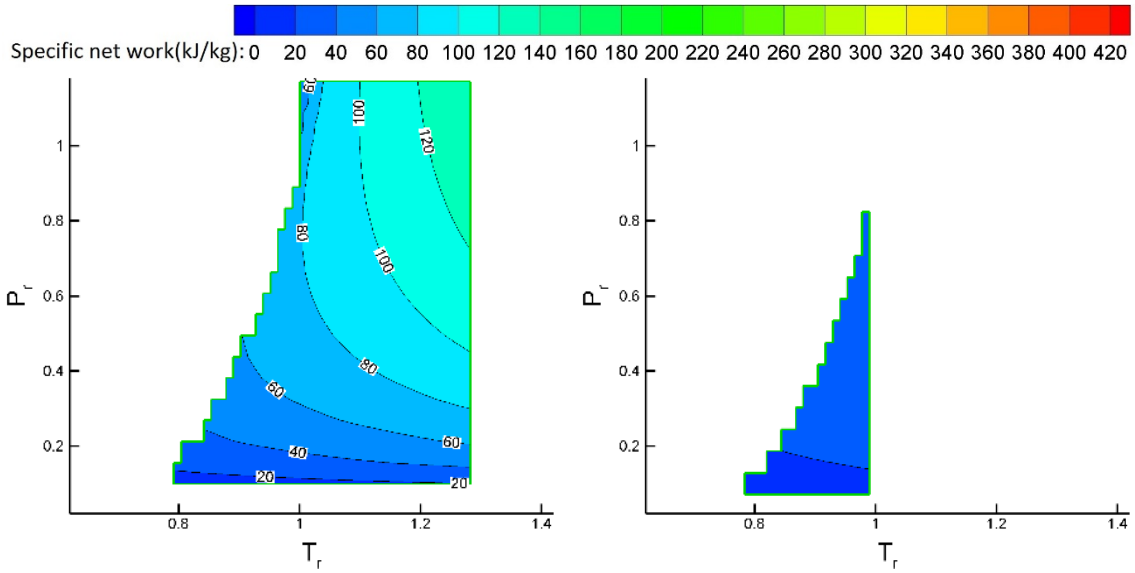

I) Iso-butane (dry fluid)

J) R236ea (dry fluid)

K) R245fa (dry fluid)

L) R236fa (dry fluid)

Figure 4.4. Continued.

4.1.2. Correlations for thermal efficiency of a simple ORC

4.1.2.1. Subcritical ORC without the Superheat

Based on the expression for thermal efficiency developed for a subcritical ORC without the superheat, presented by Eqn. (2.8), η_{th} is a function of the Jacob number, *Ja*.

As the results show, η_{th} decreases as *Ja* is increased. Kuo et al. [41] showed that *Ja* may be used to compare performance of an ORC operating with different working

fluids. However, this approach is not applicable to an ORC using the same working fluid operating at different operating conditions. Therefore, the account for different operating conditions, Kuo et al. proposed the figure of merit (FOM) defined as:

$$FOM = Ja^{0.1}(\frac{1}{T_{EC}})^{0.8} \quad (4.5)$$

Kuo's results show that thermal efficiency of a simple ORC decreases as FOM is increased.

A comparison between the correlation given by Eqn. (2.8) and the results of the ORC performance simulations performed by the EPV-11 modeling code for $T_{EC} = 1.29$ and $\eta_t = 0.85$ is given in Figure 4.5, where thermal efficiency is presented as a function of the Jacob number. As the figure shows, simulation results are in a very good agreement with the theoretical model.

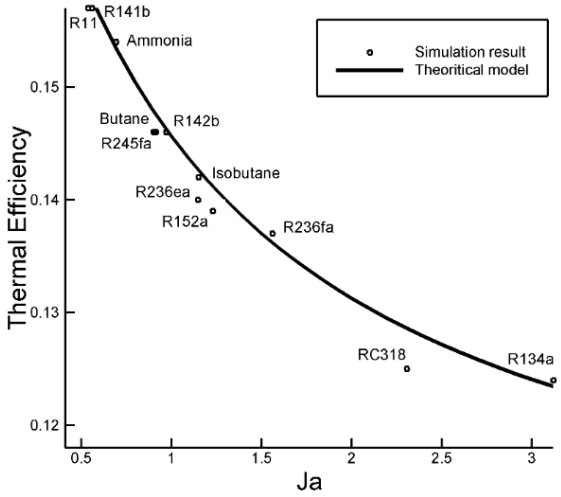

Figure 4.5. Thermal efficiency is presented as a function of the Jacob number for a subcritical ORC without a superheat.

Thermal efficiency determined by using the EBSILON Professional (EPV-11) model of a simple ORC is presented in Figure 4.6 as a function of the FOM. The linear relationship between FOM and η_{th} may be represented by Eqn. (4.6):

$$\eta_{th} = \eta_t(c_1 * FOM + c_2) \tag{4.6}$$

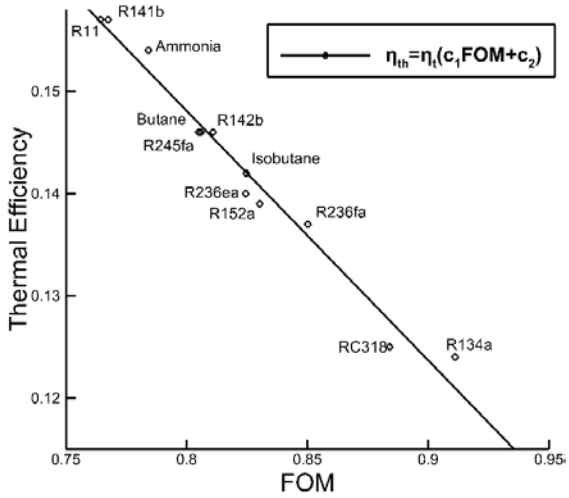

Figure 4.6. Thermal efficiency determined by the EPV-11 model of a simple ORC without superheat as a function of the FOM.

To determine numerical values of coefficients c_1 and c_2, performance of a simple ORC was calculated for 25 working fluids (listed in Table 3.1), 31 evaporation temperatures (40 to 100 °C), and 15 condensation temperatures (2 to 30 °C), for the total of 11,625 cases. The coefficients c_1 and c_2 are presented in Figures 4.7A and 4.7B as functions of T_{EC}. The statistical regression analysis gives the quadratic relationship for coefficients c_1 and c_2 in terms of T_{EC} of the following form:

$$c_1 = 1.207{T_{EC}}^2 - 3.9737T_{EC} + 2.831 \tag{4.7}$$

$$c_2 = -1.862{T_{EC}}^2 + 5.824T_{EC} - 4.009 \tag{4.8}$$

The average relative error is 0.010342.

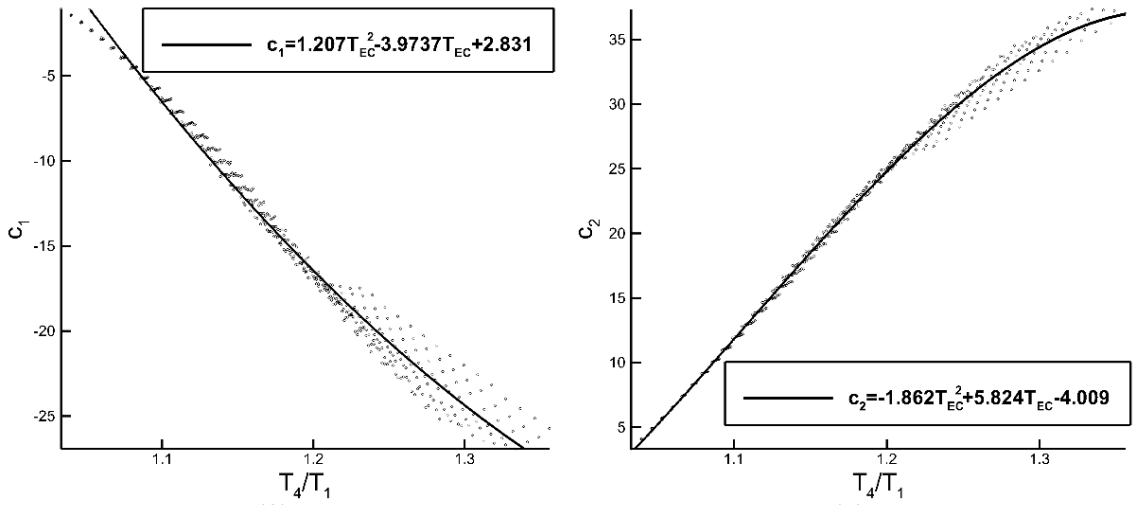

(A) (B)

Figure 4.7. Coefficients for thermal efficiency (Eqn. 4.6) for a subcritical ORC without the superheat.

Following a similar approach, the following expression for the specific heat input for a subcritical ORC without a superheat was developed:

$$\dot{q}_{in} = \frac{\dot{Q}_{in}}{\dot{m}_f} = h_{fg}(Ja + 1) \tag{4.9}$$

where $\dot{m}_f$ is the mass flow rate of the working fluid.

4.1.2.2. Subcritical ORC with the Superheat

Kuo et al. [41] developed a relation for thermal efficiency of a simple subcritical ORC without a superheat. The relations for a subcritical ORC with a superheat and for a transcritical ORC were developed in this study.

Compared to the subcritical cycle without a superheat, thermal efficiency of a superheated subcritical cycle is affected by an additional variable; the superheat temperature. To incorporate the effect of this additional parameter, the number of test cases was increased as follows: 25 working fluids (listed in Table 3.1), 8 condensation temperatures (2 to 30°C), 11 evaporation temperatures (40 to 60°C), and 9 maximum

temperatures (62 to 94°C), for the total of 19,800 cases. Based on the results, the statistical regression analysis gives the following expression for thermal efficiency of the superheated ORC:

$$\eta_{th} = \eta_t(c_1 Ja_t + c_2) \tag{4.10}$$

$$Ja_t = (Ja + k * Ja_s)^{1.45} \tag{4.11}$$

where for the wet and isentropic fluids *k=1*, while for the dry fluids *k=1.5*. Figure 4.8 shows the thermal efficiency versus the proposed modified Jacob number Ja_t. As it can be seen, there is a linear relationship between η_{th} and Ja_t The statistical regression analysis gives the following expressions for coefficients c_1 and c_2 and c_{11}, c_{12}, c_{21}, and c_{22} as functions of T_1, T_{ev}, and T_4:

$$c_1 = \frac{\left(c_{11}*\frac{T_4}{T_1}+c_{12}+\left(\frac{T_{ev}}{T_1}\right)^{11}\right)}{82.875\left(\frac{T_4}{T_{ev}}\right)^{1.46Tev-41.9199}} \quad , \quad c_2 = \frac{\left(c_{21}*\frac{T_4}{T_1}+c_{22}+\left(\frac{T_{ev}}{T_1}\right)^{0.1}\right)}{82.875\left(\frac{T_4}{T_{ev}}\right)^{-0.44}} \tag{4.12}$$

$$c_{11} = -0.5195T_1 + 121.44 \quad , \quad c_{12} = 0.5953T_1 - 146.88 \tag{4.13}$$

$$c_{21} = -0.5157T_1 + 225.92 \quad , \quad c_{22} = 0.5179T_1 - 243.95 \tag{4.14}$$

with the average relative error of 0.0399.

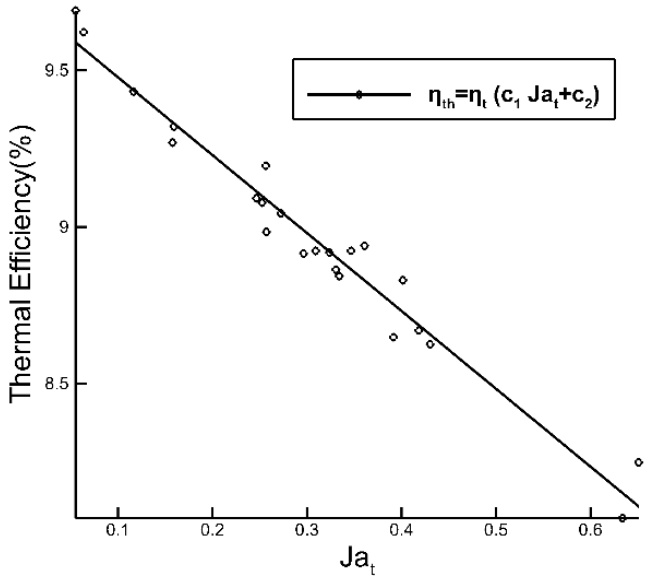

Figure 4.8. Thermal efficiency of a simple ORC with the superheat versus the modified Jacob number Ja_t.

Based on the results, and following a similar approach as for thermal efficiency, the following expression for the specific heat input of a subcritical ORC with a superheat was developed:

$$\dot{q}_{in} = \frac{\dot{Q}_{in}}{\dot{m}_f} = h_{fg}(Ja + Ja_s + 1) \tag{4.15}$$

4.1.2.3. Transcritical ORC

As can be seen from Figure 4.2, for $P_r>1$ thermal efficiency remains approximately constant. Thus, for a transcritical cycle, $P_r=1$ was assumed. As shown in Figure 4.9 and by Eqn. (4.16), at the critical point of the analyzed working fluids, thermal efficiency is a linear function of the dimensionless temperature T_t. The correlation between thermal efficiency and dimensionless temperature T_t is of the following form:

$$\eta_{th} = \eta_t(c_1 T_t + c_2) \tag{4.16}$$

where the dimensionless temperature T_t is defined as:

$$T_t = ln(T_{EC}) - 0.8 * k(T_r - 1) \quad (4.17)$$

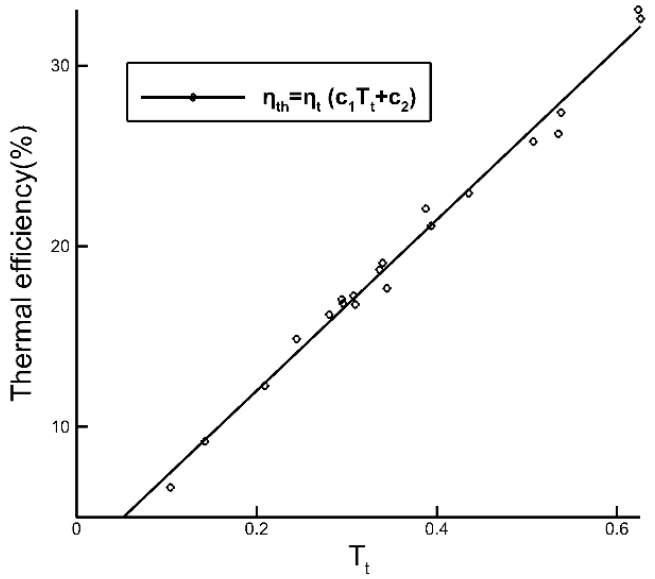

Figure 4.9. Thermal efficiency as a function of T_t for a transcritical cycle.

The constant *k* has the same value as for the subcritical ORC with a superheat case. Calculations of thermal efficiency were performed for 25 working fluids (listed in Table 3.1), 41 values of T_r (1 to 1.2), and 15 condensation temperatures (2 to 30°C), for the total of 15,375 cases. The statistical regression analysis was applied to determine expressions for coefficients c_1 and c_2. As shown in Figure 4.10, c_1 and c_2 are functions of T_r, which can be expressed by the following third order polynomials:

$$c_1 = 5.421{T_r}^3 - 18.332{T_r}^2 + 20.901T_r - 7.483 \quad (4.18)$$

$$c_2 = 3.272{T_r}^3 - 11.065{T_r}^2 + 12.454T_r - 4.639 \quad (4.19)$$

The average relative error is 0.05.

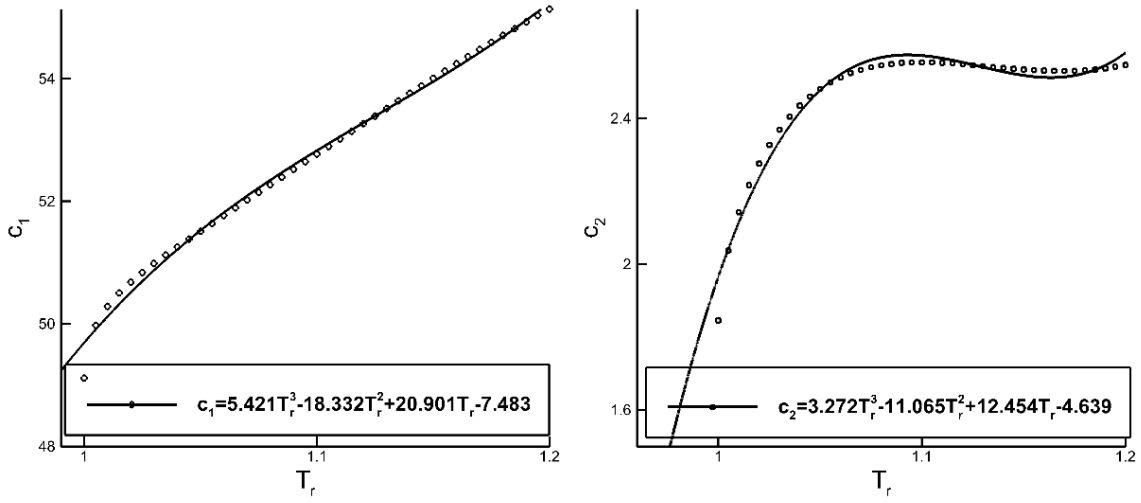

(A) (B)

Figure 4.10. Coefficients in the thermal efficiency correlation for a transcritical ORC.

Based on the results, and using statistical regression analysis, the following expression for specific heat input for a transcritical ORC with a superheat was developed:

$$\dot{q}_{in} = \frac{\dot{Q}_{in}}{\dot{m}_f} = c_{p14}(T_4 - T_1) \tag{4.20}$$

The total net work output for all types of simple ORC can be calculated as:

$$\dot{W}_{net} = \eta_{th}\dot{Q}_{in} \tag{4.21}$$

4.1.3. Effect of the working fluid properties on performance of a simple ORC

Correlations for thermal efficiency developed and presented in the preceding subsections were used to investigate the effects of the working fluid properties on performance of a simple ORC. Eqns. (4.6) and (4.10) show that in a subcritical region, thermal efficiency is a function of the specific heat capacity and the latent heat of evaporation.

It can be shown that the first derivative of Eqns. (4.6) and (4.10) with respect to C_P in the subcritical region is negative (Eqn. (4.22)), meaning that at the constant maximum

and minimum temperatures, working fluids with higher specific heat capacity give lower thermal efficiency.

$$\frac{\partial \eta_{th}}{\partial C_P} < 0 \tag{4.22}$$

However, the first derivative of Eqns. (4.6) and (4.10) with respect to h_{fg} in the subcritical region is positive (Eqn. (4.23)), meaning that at the constant maximum and minimum temperatures, working fluids with higher latent heat of evaporation give higher thermal efficiency.

$$\frac{\partial \eta_{th}}{\partial h_{fg}} > 0 \tag{4.23}$$

Since the first derivatives of the expression for the net work output $\dot{W}_{net}$ (Eqn. (4.21)) with respect to the specific heat capacity C_P and latent heat of evaporation h_{fg} are positive in the subcritical region, Eqn. (4.24), working fluids with higher C_P or h_{fg} produce higher net power output.

$$\frac{\partial \dot{W}_{net}}{\partial C_p} > 0, \frac{\partial \dot{W}_{net}}{\partial h_{fg}} > 0 \tag{4.24}$$

The effect of the critical temperature on thermal efficiency (Eqns. (4.6) and (4.10)) and the net power output (Eqn. (4.21)) is presented in Figure 4.11 for T_{min}=*2*°C and T_{max}=*100*°C. As the results show, η_{th} and $\dot{W}_{net}$ increase as the latent heat of evaporation is increased. An increase in the specific heat C_p, results in a higher net power output and lower thermal efficiency.

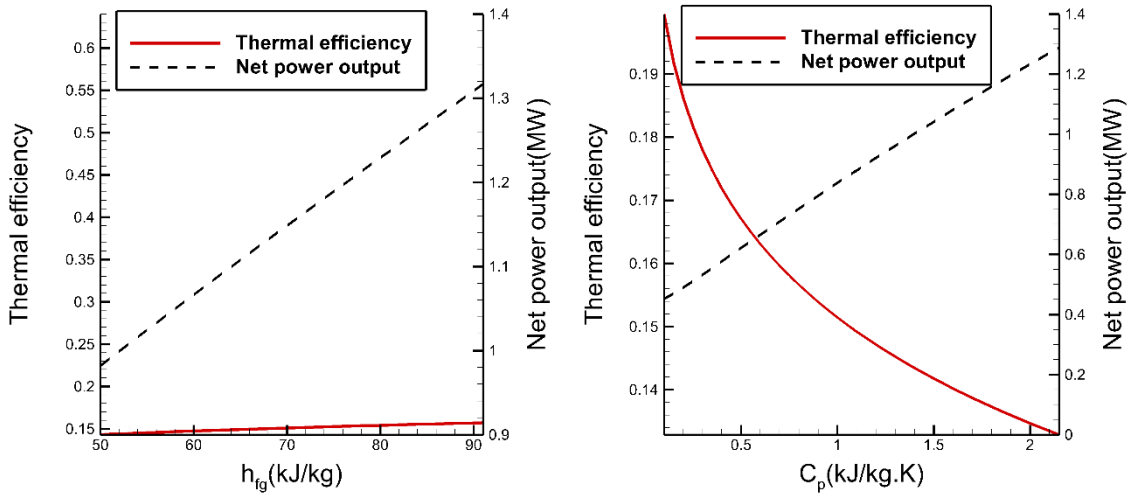

A) h_{fg} B) C_p

Figure 4.11. Effect of latent heat of evaporation and specific heat capacity on thermal efficiency and net power output of a simple ORC in the subcritical region.

Depending on the application of a simple subcritical ORC, there is an optimum specific heat capacity representing a tradeoff between thermal efficiency and net power output. The optimal value of C_p may be determined by developing a relationship between the levelized cost of electricity (LCOE) and C_p and finding its minimum.

Eqn. (4.16) shows that in the supercritical region, thermal efficiency is affected by the critical temperature. It can be shown that the first derivative of Eqn. (4.16) with respect to the critical temperature in the supercritical region is positive (Eqn. (4.25)), meaning that at constant maximum and minimum temperatures, working fluids with higher critical temperature give higher thermal efficiency.

$$\frac{\partial \eta_{th}}{\partial T_{cr}} > 0 \qquad (4.25)$$

Since the first derivatives of the expression for net power output (Eqn. (4.21)) with respect to the specific heat C_p and critical temperature T_{cr} (expressed in dimensionless form

as T_r) are positive, Eqn. (4.26), working fluids with higher C_p or T_{cr} produce higher net power output.

$$\frac{\partial \dot{W}_{net}}{\partial C_p} > 0, \frac{\partial \dot{W}_{net}}{\partial T_{cr}} > 0 \tag{4.26}$$

Also, the first derivative of Eqns. (4.10), (4.16) and (4.21) with respect to k in the superheated subcritical and supercritical region is negative (Eqn. (4.27)), meaning that at constant maximum and minimum temperatures, the wet and isentropic working fluids give higher thermal efficiency and net power output, compared to the dry fluids.

$$\frac{\partial \eta_{th}}{\partial k} < 0, \frac{\partial \dot{W}_{net}}{\partial k} < 0 \tag{4.27}$$

The effect of the critical temperature on thermal efficiency (Eqn. (4.16)) and net power output (Eqn. (4.21)) is presented in Figure 4.12 for T_{min}=*2*°C and T_{max}=*200*°C. As the results show, both η_{th} and $\dot{W}_{net}$ increase as the critical temperature is increased.

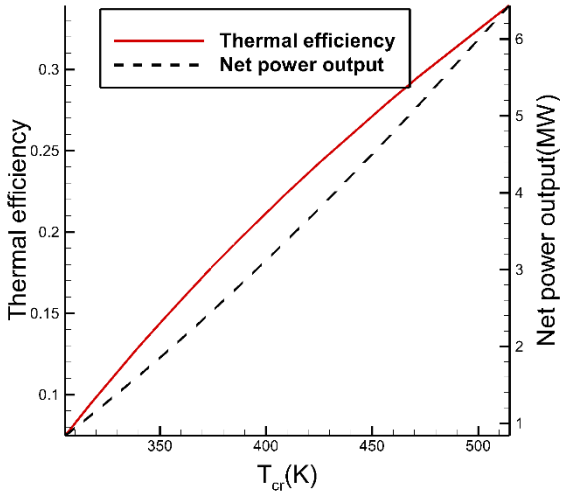

Figure 4.12. Effect of critical temperature on thermal efficiency and net power output of a simple ORC in the supercritical region.

4.2. Regenerative ORC

4.2.1. The effect of operating conditions on performance of a regenerative ORC

Thermal efficiency of a regenerative ORC was determined over a range of operating conditions for the first nine dry working fluids listed in Table 3.1. A schematic representation of a regenerative ORC is presented in Figure 4.13.

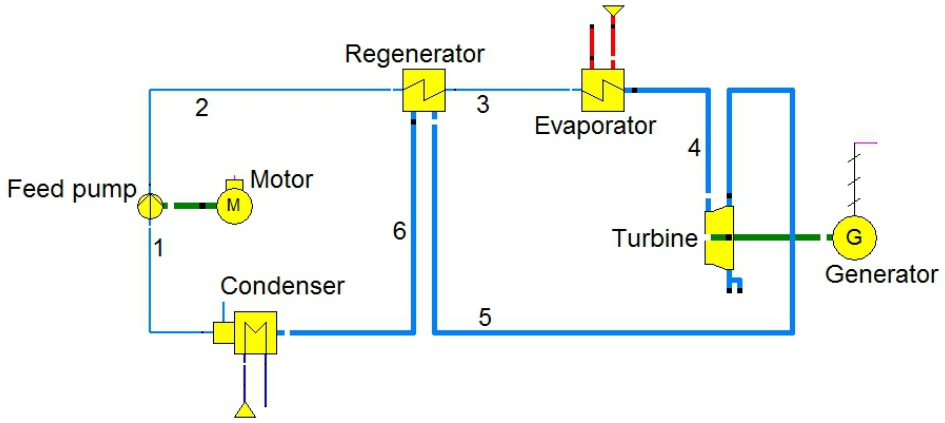

Figure 4.13. Schematic of a regenerative ORC.

The cycle operating parameters used in the calculations are presented in Table 4.3. The temperature difference of 10°C between the turbine inlet temperature (TIT) and the heat source temperature was used in the analysis. The maximum pressure of the cycle was set to 2 MPa, which is lower than the critical pressure of all working fluids used in the analysis. Thus, the regenerative ORC is operating as a subcritical cycle with and without the superheat.

Table 4.3. Regenerative ORC parameters.

Parameter	Value
Maximum pressure, P_4 (MPa)	2
Maximum temperature, T_4 (°C)	85-250
Minimum temperature, T_1 (°C)	2-30
Turbine isentropic efficiency, η_t (%)	0.85
Pump isentropic efficiency (%)	0.8
Regenerator effectiveness	0.85
Mass flow rate, $\dot{m}_f$ (kg/s)	35
Generator efficiency (%)	0.975
Turbine mechanical efficiency (%)	0.99
Minimum pressure (MPa)	Saturation pressure at minimum temperature

The maximum cycle temperature was varied between the saturation temperature at the maximum pressure of 2MPa and 250°C. However, since the upper temperature limit for some working fluids (R236ea for example) is lower than 250°C, cycle analysis for these fluids was performed at lower maximum temperature. The steady state conditions and negligible pressure drop in heat exchangers have been assumed in this study.

Thermal efficiency of a regenerative ORC for nine working fluids is presented in Figure 4.14. The contour graphs are plotted in terms of the minimum and maximum cycle temperature, T_{min} and T_{max} for P_{max} = 2 MPa.

The results show that the regenerative ORCs operating with R113 and R227ea have the highest and lowest thermal efficiencies, respectively compared to the regenerative ORCs using other working fluids. For example, a regenerative ORC operating with R113 and R227ea at T_{min}=*10°C* and T_{max}=*180°C*, has thermal efficiency of 25% and 18%, respectively. For the maximum temperature lower than 175°C, η_{th} is lower than 23%, while for the maximum temperature in the 175 °C to 250°C range, η_{th} reaches 29%. Working fluids R113 and R114 are giving the highest thermal efficiency of 29% and 23%, respectively. However, R113 and R114 are chlorofluorocarbons (CFCs) and they have

been phased-out and prohibited for use in power generation [103]. Regeneration may result in a smaller difference in thermal efficiency between different working fluids. For example, at 150°C thermal efficiency of a regenerative ORC operating with R245fa is just 1%-point higher compared to the regenerative ORC operating with RC318. For a simple ORC, this difference is larger than 5%-points [109].

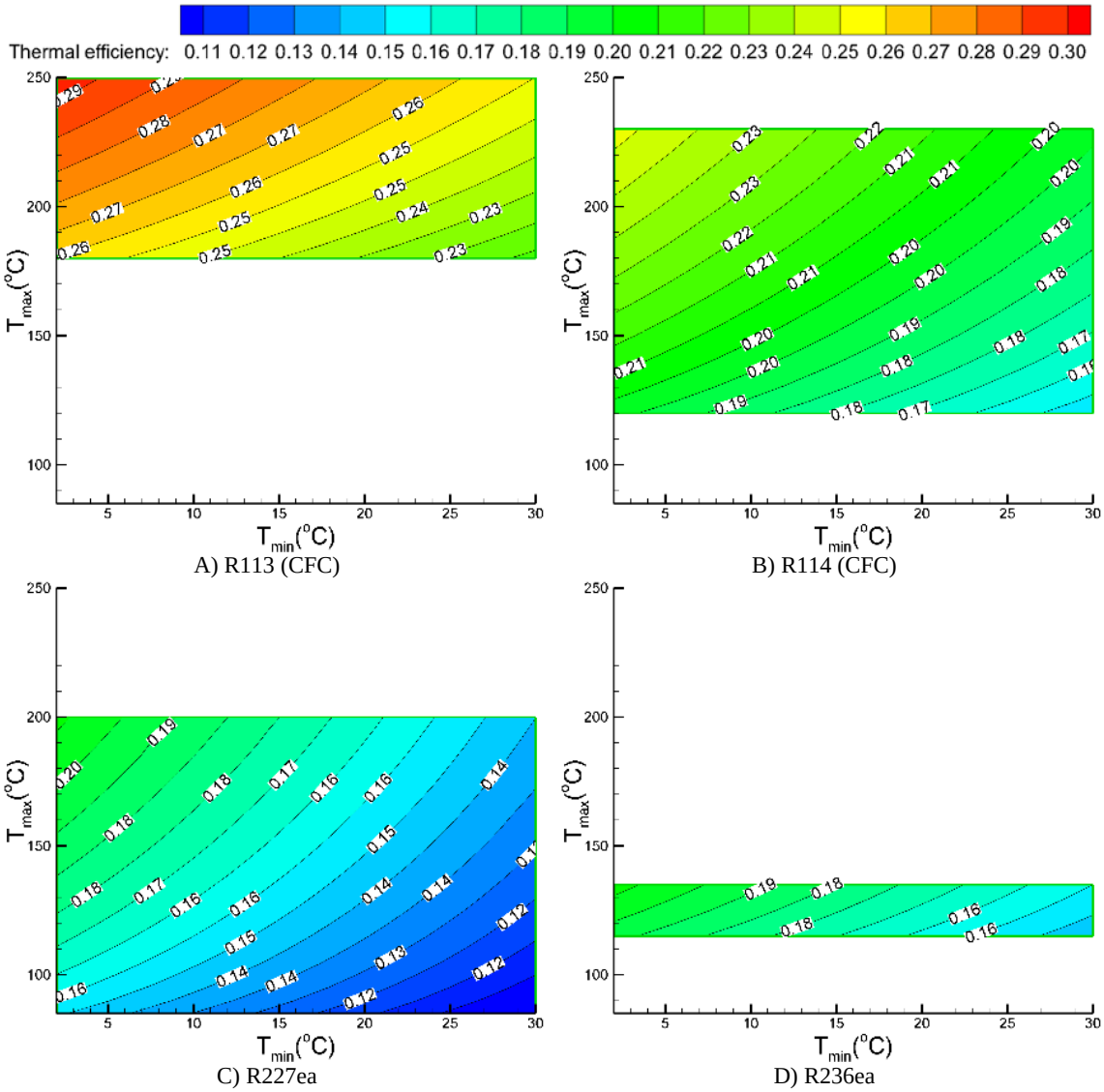

Figure 4.14. Thermal efficiency of a regenerative ORC for nine working fluids analyzed in this work and P_{max} = 2 MPa.

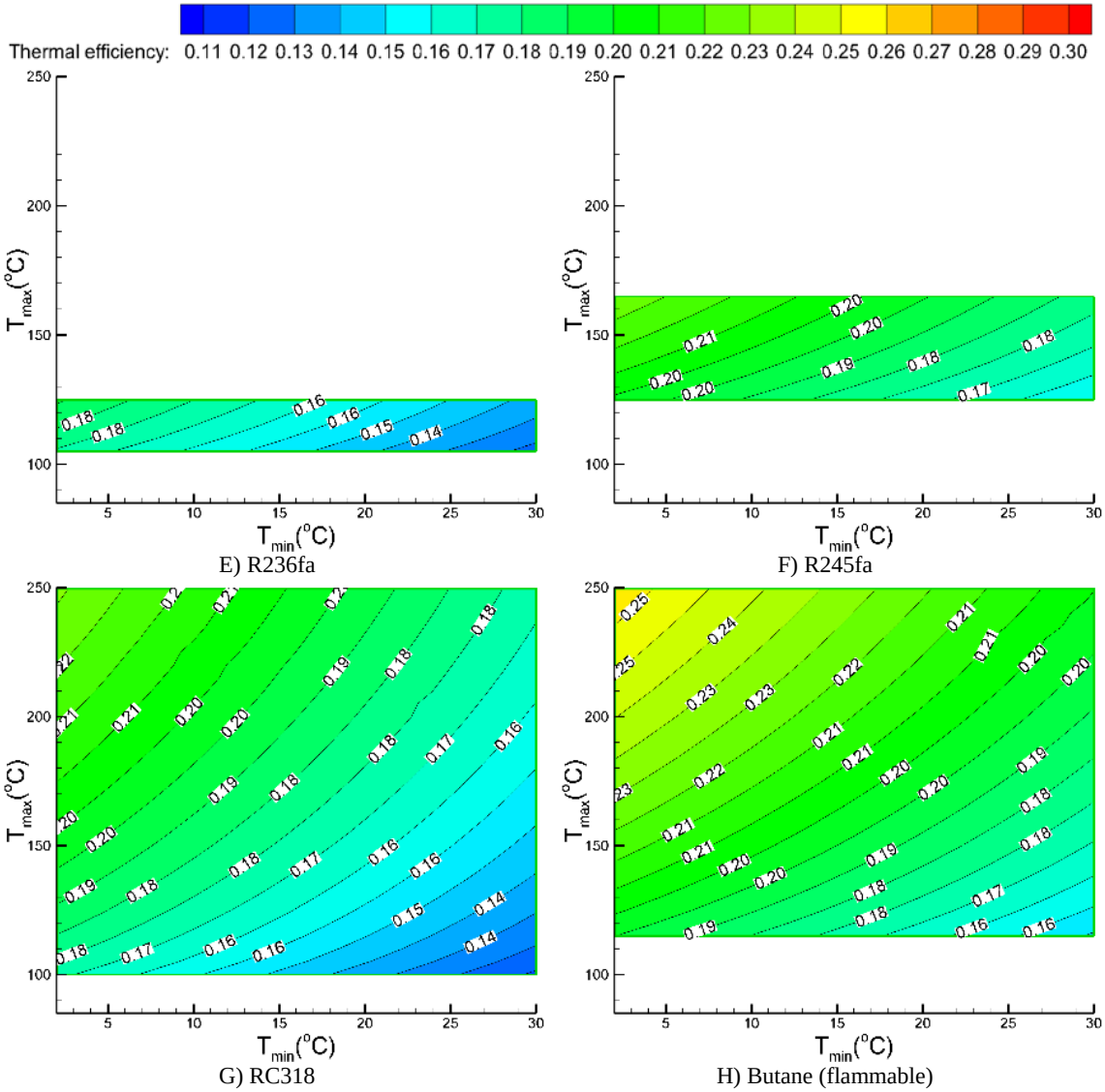

E) R236fa F) R245fa

G) RC318 H) Butane (flammable)

Figure 4.14. Continued.

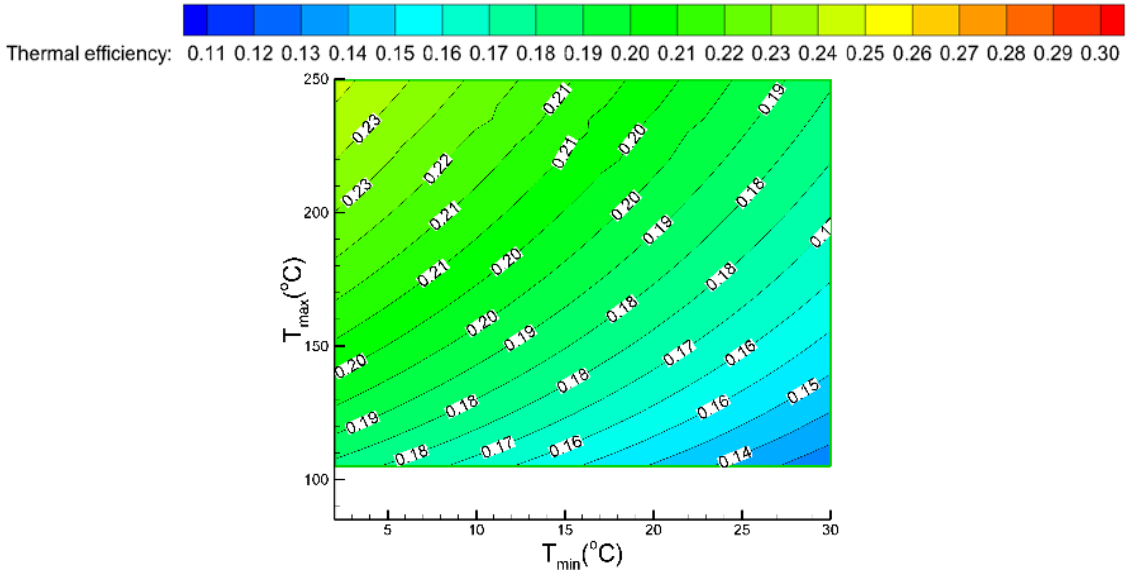

I) Iso-butane (flammable)

Figure 4.14. Continued.

Figure 4.14 shows that for all analyzed dry working fluids, thermal efficiency η_{th} of a regenerative ORC increases as the maximum temperature is increased at the constant minimum temperature. For example, for T_{min} =15°C and R113 (Figure 4.14A), increasing the maximum temperature from 180°C to 250°C results in an increase in thermal efficiency from 24% to 27%. In contrast, for the case of a simple ORC, depending on the operating conditions, thermal efficiency of the cycle operating with dry fluids may increase or decrease [109]. As discussed in Section 4.1.1, for the dry working fluids and certain cycle operating conditions, isobaric lines in T-s diagram converge with temperature, thus for a simple ORC thermal efficiency decreases as the maximum cycle temperature is increased.

Since the turbine inlet, turbine outlet, pump inlet, and pump outlet conditions are not affected by regeneration, adding regeneration to the ORC does not change the specific net work output.

4.2.2. Correlations for thermal efficiency of a regenerative ORC

As discussed in Section 2.3 of Chapter 2, a systematic, analytical method was developed in this work for the selection of the best working fluids. The detailed models of a regenerative ORC were developed using EBSILON Professional V11 (EPV-11) power systems modeling code [110]. The EPV-11 models were exercised over a range of operating conditions and multitude of working fluids to generate simulation results on cycle performance parameters, such as thermal efficiency and net work output. The statistical regression analysis was applied to the simulation results to develop analytical correlations for thermal efficiency and specific net work output as functions of the relevant cycle operating parameters, such as: T_{max}, T_{min} or T_{eva} assuming constant values of the regenerator effectiveness, turbine isentropic efficiency and critical temperature T_{cr}. The analysis was performed for the subcritical, superheated subcritical, and transcritical regenerative ORC configurations.

4.2.2.1. Subcritical ORC without the superheat

For a regenerative ORC without the superheat, a logarithmic relationship between η_{th} and T_{max}/T_{min} represented by Eqn. (4.28) was used in the regression analysis. For the ORC cycle without a superheat, maximum temperature T_{max} is equal to the evaporation temperature T_{eva} ($T_{max} = T_{eva}$).

$$\eta_{th} = c_1 * (\ln\left(\frac{T_{max}}{T_{min}}\right))^{c_2} \tag{4.28}$$

Coefficients c_1 and c_2 were determined by regressing performance data (EPV-11 simulation results) obtained for a regenerative ORC for 14 working fluids presented in Table 3.1, 31 evaporation temperatures (40 to 100°C), 5 values of regenerator effectiveness

(0.75 to 0.95), and 15 condensation temperatures (2 to 30°C), and 5 values of turbine isentropic efficiency (0.55 to 0.95), for the total of 162,750 cases. The statistical regression analysis gives a linear relationship for coefficients c_1 and c_2 in terms of ε_{reg} represented by Eqns. (4.29) and (4.30). Coefficients c_1 and c_2 are also presented in a graphical form in Figure 4.15A and Figure 4.15B.

$$c_1 = \eta_t(0.0716\varepsilon_{reg} + 0.5362) > 0 \quad (4.29)$$

$$c_2 = 0.0366\varepsilon_{reg} + 0.8041 > 0 \quad (4.30)$$

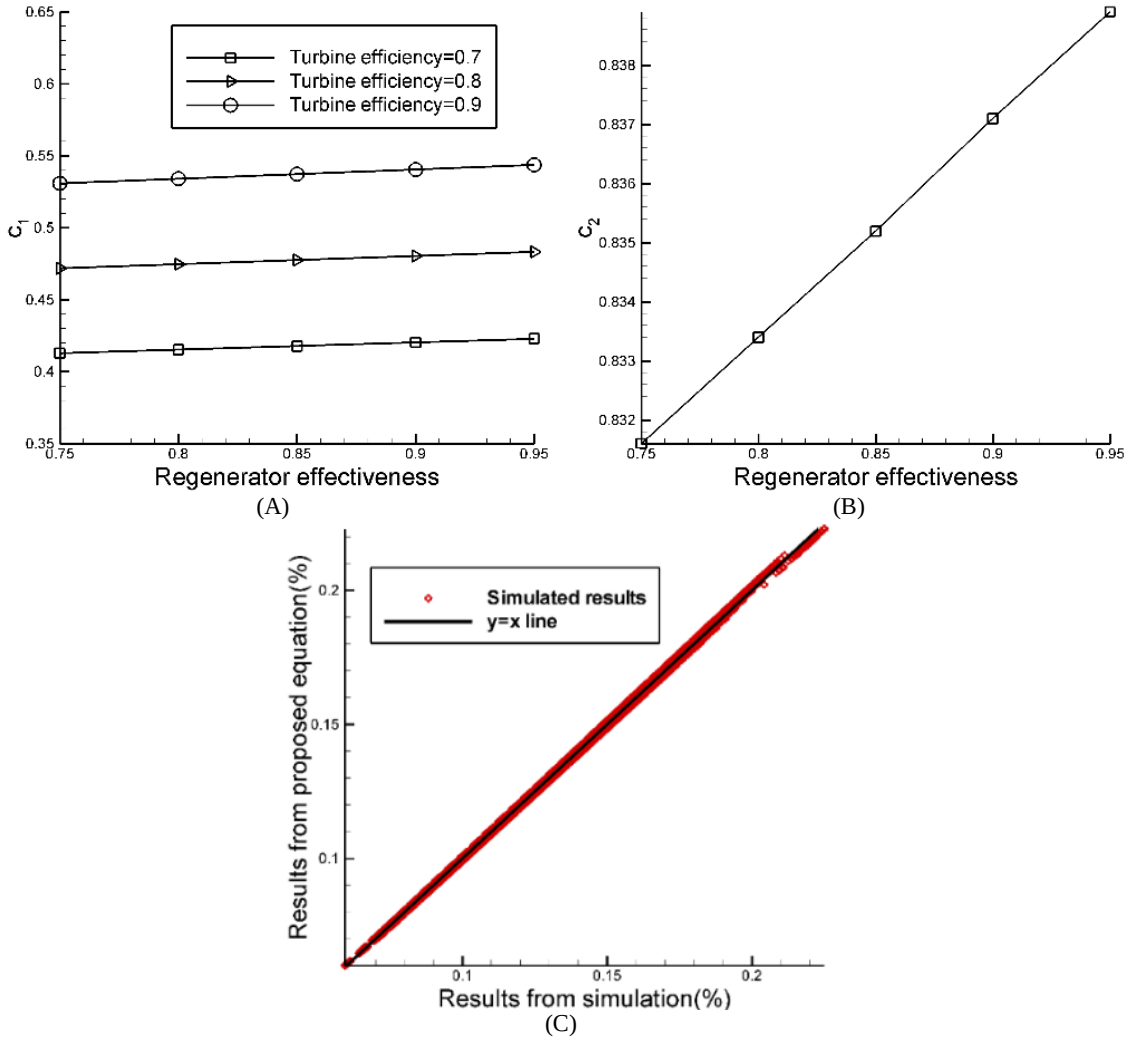

Figure 4.15. A) c_1 in Eqn. (4.28), B) c_2 in Eqn. (4.28), C) Comparison between Eqn. (4.28) and simulation results for a subcritical ORC without the superheat

Figure 4.15C shows an excellent agreement between the correlation (Eqn. (4.28)) and the EPV-11 simulation results. Since coefficients c_1 and c_2 are positive, thermal efficiency increases as the T_{max}/T_{min} ratio is increased, i.e., the maximum (evaporation) temperature is increased, and/or the minimum (heat rejection) temperature is decreased. Correlations for coefficients c_1 and c_2 and Figures 4.15A and 4.15B show that thermal efficiency is a linear function of the turbine isentropic efficiency and exponential function of the regenerator effectiveness ε_{reg}, with the turbine isentropic efficiency being a dominant factor.

The average relative error for all analyzed cases is 0.005024. The relative error was defined as:

$$Relative\ error = \frac{|correlation - EPV - 11\ simulation|}{EPV - 11\ simulation} \tag{4.31}$$

4.2.2.2. Subcritical ORC with the superheat

For a regenerative ORC with the superheat, both the evaporation T_{eva} and maximum T_{max} temperatures affect efficiency. The logarithmic relationship between η_{th} and T_{eva}/T_{min} and represented by Eqn. (4.32) was used in the regression analysis, where coefficients c_1 and c_2 are the functions of T_{max}.

$$\eta_{th} = c_1 * \ln\left(\frac{T_{eva}}{T_{min}}\right) + c_2 \tag{4.32}$$

To incorporate the effect of T_{max}, the number of analyzed cases was increased to 14 working fluids, 8 condensation temperatures (2 to 30°C), 11 evaporation temperatures (40 to 60°C), 5 values of regenerator effectiveness (0.75 to 0.95), 9 maximum temperatures (62 to 94°C), and 5 values of turbine isentropic efficiency (0.55 to 0.95), for the total of

277,200 cases. The regression analysis gives a linear relationship for coefficients c_1 and c_2 in terms of T_{max} and ε_{reg} of the following form:

$$c_1 = \eta_t\left(0.0029\varepsilon_{reg} - 0.0005\right)T_{max} - 0.9356\varepsilon_{reg} + 0.8856 > 0 \quad (4.33)$$

$$c_2 = \eta_t\left(0.0002\varepsilon_{reg} - 0.0001\right)T_{max} - 0.0557\varepsilon_{reg} + 0.0466 > 0 \quad (4.34)$$

The coefficients c_1 and c_2 are presented in a graphical form in Figure 4.16 for T_{max}=94°C.

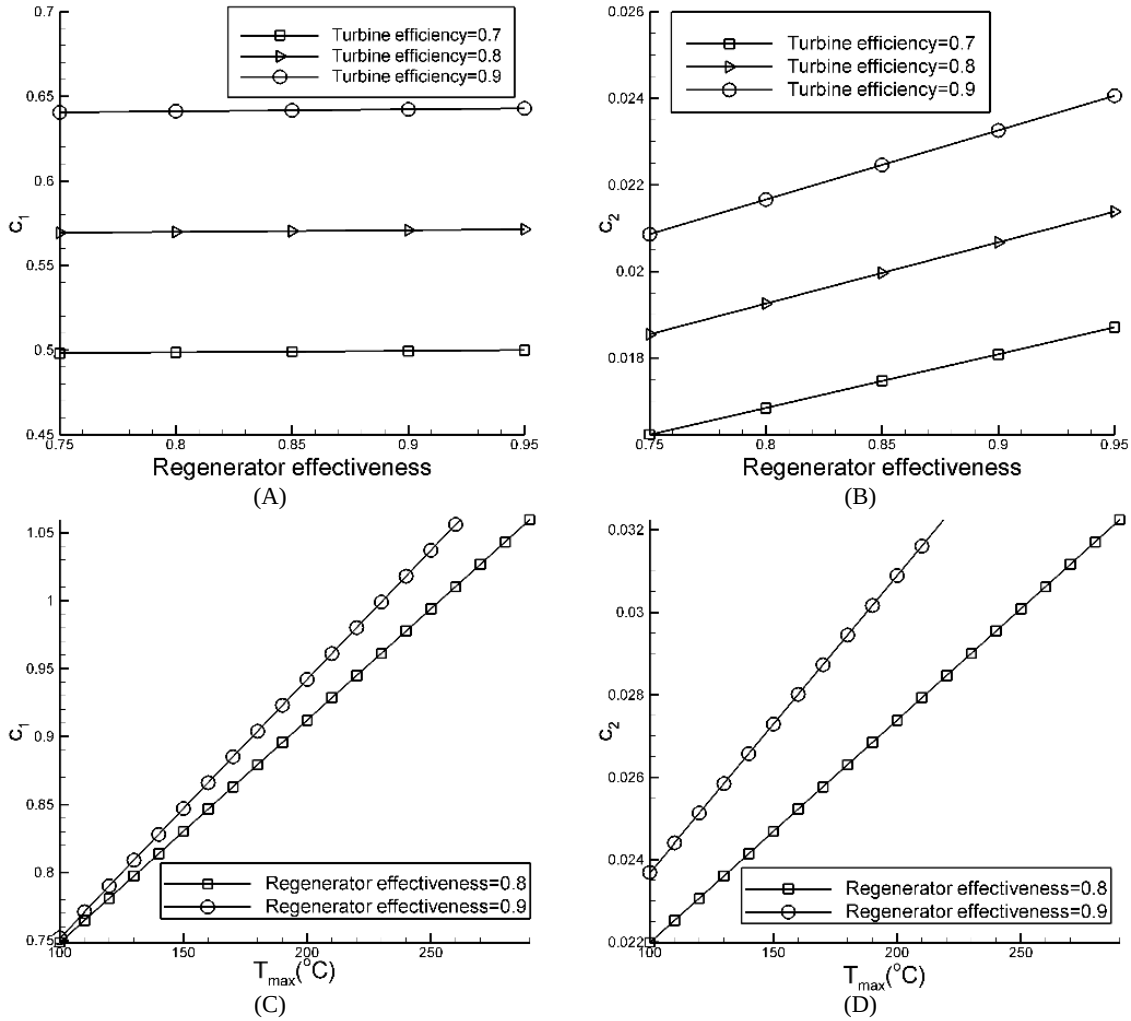

Figure 4.16. A) c_1-ε_{reg} in Eqn. (4.32), B) c_2-ε_{reg} in Eqn. (4.32), C) c_1-T_{max} in Eqn. (4.33), D) c_2-T_{max} in Eqn. (4.34), E) Comparison between Eqn. 4.32 and simulation results for a subcritical ORC with the superheat.

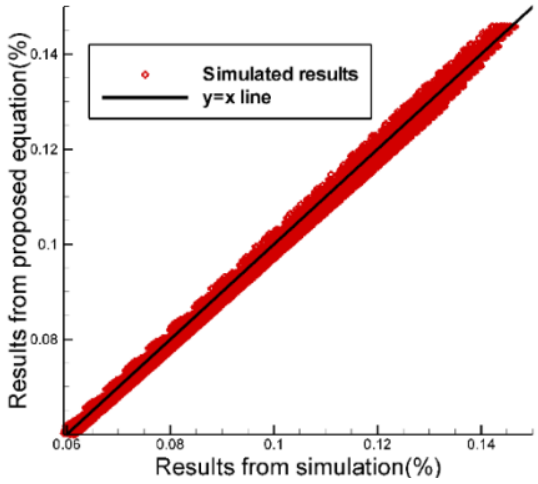

(E)

Figure 4.16. Continued.

Figure 4.16E shows an excellent agreement between the correlation given by Eqn. (4.32) and the EPV-11 simulation results. The average relative error for all analyzed cases is 0.015178.

Since coefficeints c_1 and c_2 are positive, increasing the T_{eva}/T_{min} gives higher efficiency. Correlations for c_1 and c_2 and Figure 4.16 also show that thermal efficiency is a linear function of the maximum temperature T_{max}, turbine isentropic efficiency η_t and an exponential function of the regenerator effectiveness ε_{reg}, with the maximum temperature and turbine isentropic efficiency being dominant factors.

4.2.2.3. Transcritical ORC

As mentioned in Section 4.1.1, for a constant minimum and maximum temperature and maximum pressure $P_{max} \geq P_{cr}$, thermal efficiency remains approximately constant. Thus, at constant T_{min} and T_{max}, increasing P_{max} in the supercritical region does not have a significant effect on thermal efficiency. Thus, for a transcritical regenerative ORC,

P_{max}=P_{cr} was assumed. Correlation between the thermal efficiency η_{th} and T_{max}/T_{min} given by Eqn. (4.35) was used in the regression analysis.

$$\eta_{th} = c_1 * \left(\ln\left(\frac{T_{max}}{T_{min}}\right)\right)^{c_2} \quad (4.35)$$

Coefficients c_1 and c_2 were determined by performing regression analysis of the cycle performance data (EPV-11 simulation results) obtained for 14 working fluids presented in Table 3.1, 41 values of T_r (1 to 1.2), 5 values of regenerator effectiveness (0.75 to 0.95), 15 condensation temperatures (2 to 30°C), and 5 values of turbine isentropic efficiency (0.55 to 0.95), for the total of 215,250 cases.

The statistical regression analysis gives the first and second order relationships for coefficients c_1 and c_2 in terms of the dimensionless maximum temperature T_r, and the first order (linear) relationship in terms of the regenerator effectiveness ε_{reg} of the following form:

$$c_1 = \eta_t(-1.211{T_r}^2 + (0.258\varepsilon_{reg} + 2.5521)T_r - 0.206\varepsilon_{reg} - 0.85735) > 0 \quad (4.36)$$

$$c_2 = (-1.597\varepsilon_{reg} + 2.6731)T_r + 1.6944\varepsilon_{reg} - 1.9168 > 0 \quad (4.37)$$

$$T_{\mathrm{r}} = \frac{T_{max}}{T_{cr}} \quad (4.38)$$

Coefficients c_1 and c_2 are also presented in a graphical form in Figure 4.17. Since both c_1 and c_2 are positive, increasing the T_{max}/T_{min} results in a higher thermal efficiency. Correlations for c_1 and c_2 (Eqns. (4.36) and (4.37)) and Figure 4.17 also show that thermal efficiency is a linear function of the turbine isentropic efficiency η_t, with the maximum temperature and turbine isentropic efficiency being the dominant factors.

Figure 4.17D shows an excellent agreement between the correlation given by Eqn. (4.35) and the EPV-11 simulation results. The average relative error for all analyzed cases is 0.01026.

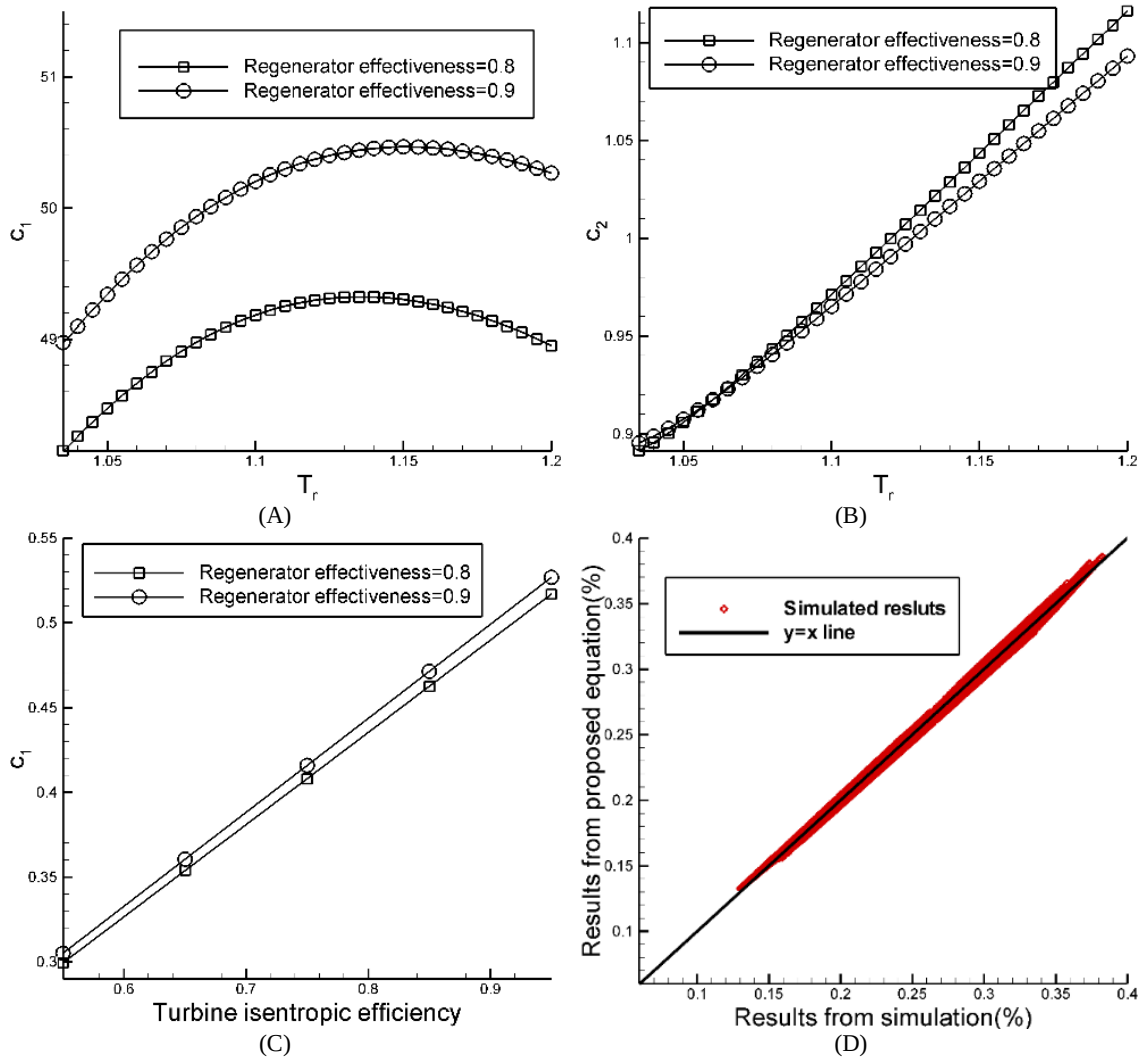

Figure 4.17. A) c_1-T_r in Eqn. (4.36), B) c_2-T_r in Eqn. (4.37), C) c_1-η_t in Eqn. (4.36), D) Comparison between Eqn. (4.35) and simulation results for a transcritical ORC.

Correlations developed for a simple and regenerative ORC may be used for a quick, systematic and precise determination of thermodynamic performance of the analyzed work cycles in terms of the cycle operating parameters for a working fluid(s) of interest, or for

the selection of the best working fluid, without the need for performing tedious parametric calculations and results analysis. Also, the developed correlations and thermodynamic expressions allow determination of the effect of the working fluid properties, such as specific heat, latent heat of evaporation, and critical temperature on cycle performance. Such analysis can also be used to investigate and predict cycle performance for mixtures of different working fluids without performing thermodynamic analysis of the working cycle(s).

4.2.3. Effect of working fluid properties on performance of a regenerative ORC

Correlations developed in this study (Chapter 4) can be used to investigate the effects of the working fluid properties on performance of a regenerative ORC. Eqns. (4.28) and 4.32 show that in a subcritical region, properties of the working fluid do not affect thermal efficiency. However, Eqn. (4.35) shows that in the supercritical region, thermal efficiency is affected by the critical temperature. It can be shown that the first derivative of Eqn. (4.35) in the supercritical region is positive (Eqn. (4.39)), meaning that at constant maximum and minimum temperatures, working fluids with higher critical temperature give higher thermal efficiency.

$$\frac{\partial \eta_{th}}{\partial T_{cr}} > 0 \qquad (4.39)$$

As discussed earlier, conditions at the turbine inlet, turbine outlet, pump inlet, and pump outlet are not affected by regeneration, thus adding regeneration to a simple ORC does not change the specific net work output. Since the first derivatives of w_{net} with respect to the specific heat c_p and critical temperature T_{cr} (expressed in dimensionless form as T_r)

are positive, Eqn. (4.40), working fluids with higher C_p or T_{cr} produce higher net work output.

$$\frac{\partial w_{net}}{\partial C_p} > 0, \frac{\partial w_{net}}{\partial T_{cr}} > 0 \tag{4.40}$$

The effect of the critical temperature T_{cr} on thermal efficiency (Eqn. (4.35)) and specific net work output (Eqn. (4.21)) is presented in Figure 4.18 for η_t=0.9, ε_{reg}=*0.9* and T_{max}=*250*°C.

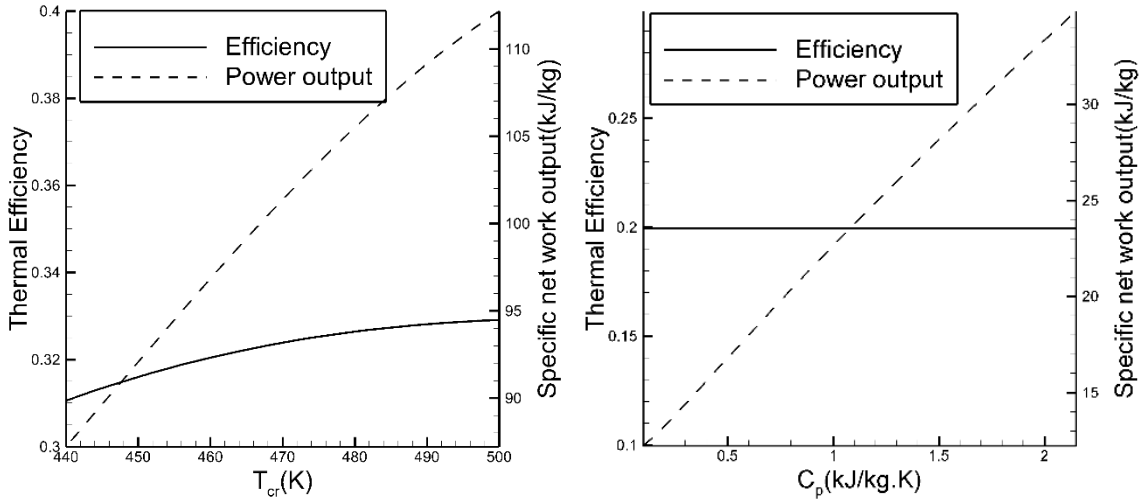

A) T_{cr} B) C_p

Figure 4.18. Effect of critical temperature and specific heat capacity on thermal efficiency and specific net work output of a transcritical regenerative ORC.

As the results show η_{th} and w_{net} increase as the critical temperature is increased. An increase in specific heat C_p, results in a higher specific net work output, which increases linearly with C_p. Thermal efficiency, however, remains unaffected.

4.3. A Simple Brayton Cycle

Based on the expressions for the specific net work output, specific heat input, thermal efficiency, and turbine and compressor discharge temperatures, developed in Section 2.3 in Chapter 2, for the perfect and semi-perfect gases, the following expressions

were developed for a simple Brayton cycle by employing the statistical regression analysis. A schematic representation of a simple Brayton cycle is presented in Figure 4.19.

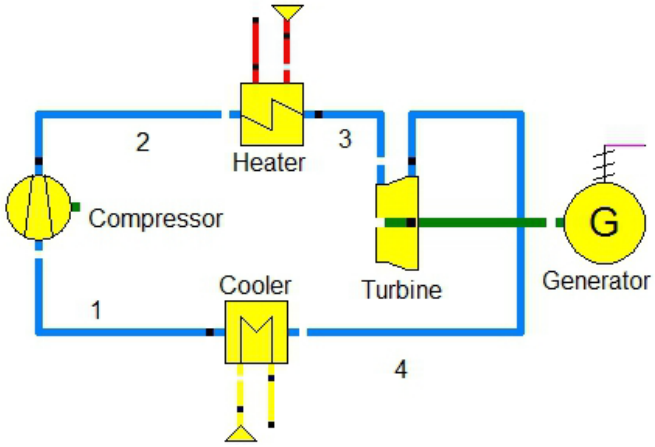

Figure 4.19. Schematic of a simple Brayton cycle.

4.3.1. Performance of a simple Brayton cycle

Performance of a simple Brayton cycle was calculated by employing the EPV-11 model of the cycle described in Section 2.3.3 of Chapter 2. To cover operating conditions applicable for a Brayton cycle integrated with a CSP plant, calculations were performed for 9 working fluids presented in Table 3.2, 15 maximum temperatures (300 to 1000°C), 4 values of the isentropic turbine efficiency (0.65 to 0.95), 3 values of the isentropic compressor efficiency (0.8 to 1) and 7 minimum temperatures (32 to 62 °C), for the total of 11,340 cases. A statistical regression analysis was used to develop expressions for the cycle performance parameters.

Based on the Eqn. (2.41) and the regression analysis, the expression for the specific net work output at the optimal pressure ratio, given by Eqn. (4.41), was developed:

$$\dot{w}_{net,max} = \frac{\dot{W}_{net,max}}{\dot{m}_f} = 0.9764 \frac{c_{p13}}{\eta_c} \left[(\eta_c \eta_T T_3)^{0.5} - T_1{}^{0.5} \right]^2 - 0.0975 \qquad (4.41)$$

For a semi-perfect gas (defined in Section 3.3 of Chapter 3), c_{p13} is the average specific heat capacity between the minimum and maximum temperatures T_1 and T_3. It should be noted that the leading coefficient in Eqn. (4.41) is 2.36% lower compared to the case where the perfect gas behavior (defined in Section 3.3 in Chapter 3) is assumed. In other words, real gasses produce lower net specific work output in comparison to the perfect gases.

A comparison between the expression for the net specific work given by Eqn. (4.41) and the results of EPV-11 performance simulations is presented in Figure 4.20A. As the figure shows, some of the simulation results, namely those obtained by using CO_2 as the working fluid, depart from the analytical correlation. This departure can be explained by the behavior of CO_2 in the Critical Zone (CZ), which was defined in this study as:

$$(1 - T_r)^2 + (1 - P_r)^2 < 0.1^2 \tag{4.42}$$

$$T_r = \frac{T_{min}}{T_{cr}}, P_r = \frac{P_{min}}{P_{cr}} \tag{4.43}$$

The Critical Zone for CO_2 in the T-s diagram is presented in Figure 4.20B.

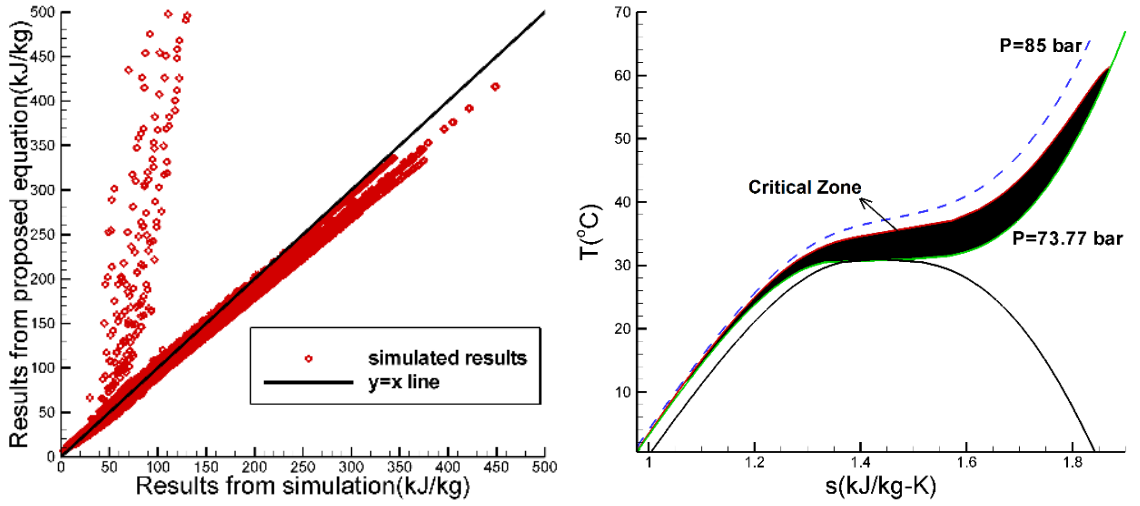

A) Specific net work output B) Critical zone in T-s diagram

Figure 4.20. A) Comparison between correlation (Eqn. (4.41)) and simulation results, B) Critical Zone for CO_2.

As presented in Figure 4.21A, excluding simulation results for the Critical Zone gives a good agreement between the Eqn. (4.41) and simulation results outside of the Critical Zone. The average relative error for 10,000 cases is 0.0215.

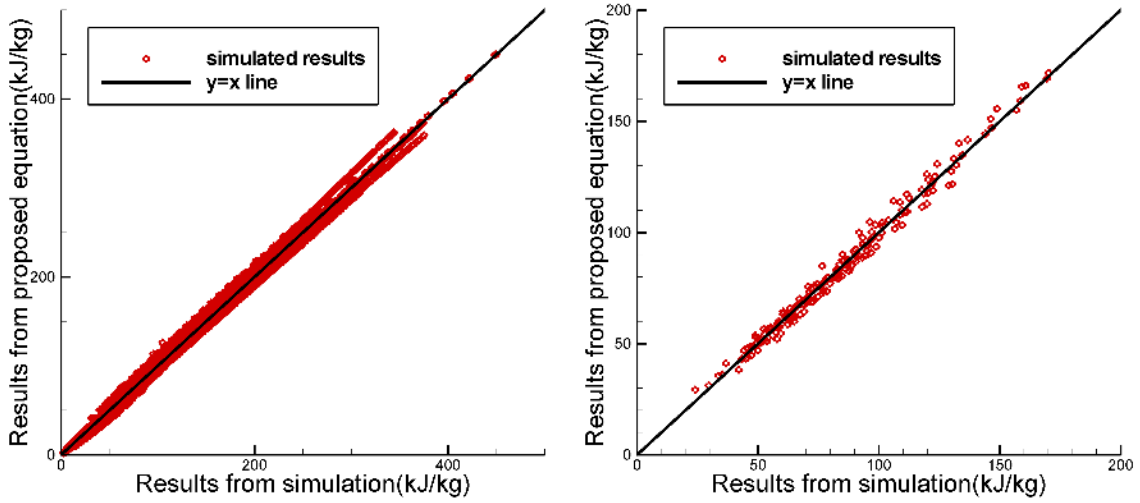

A) Outside the Critical Zone B) Inside the Critical Zone

Figure 4.21. Comparison between the statistical correlation and simulation results for the specific net work output.

Although, on average, the agreement between Eqn. (4.41) and simulation results is very good, the two groups of results, forming two lines, one above and the other one below the 45^o line (representing a perfect agreement) can be identified in Figure 4.21A. The data points above and below the 45^o line represent the results obtained for methane and Kr as the working fluids, respectively. Since for these two gases, the specific heat capacity is a strong function of temperature, compared to the other analyzed working fluids, the semi-perfect gas assumption does not work well for these two working fluids, thus resulting in a higher relative error between the results obtained from Eqn. (4.41) and the EPV-11 model results. The maximum relative error is around 5% for high values of the net specific work output.

As shown in Figure 4.20A, Eqn. (4.41) is not suitable for the Critical Zone. Thus, for CO_2, an expression given by Eqn. (4.44) was developed for the accurate prediction of the specific net work output inside its Critical Zone.

$$\dot{w}_{net,max} = \frac{\dot{W}_{net,max}}{\dot{m}_f} = 6.25251\left(\frac{c_p}{\eta_c}\left[(\eta_c \eta_T T_3)^{0.5} - T_1{}^{0.5}\right]^2\right)^{0.3978} \quad \text{(for } CO_2\text{)} \qquad (4.44)$$

where:

$$c_p = 0.05556 c_{p1} + 0.94444 c_{p3} \qquad \text{(for } CO_2\text{)} \qquad (4.45)$$

Near the critical point, the value of specific heat capacity tends to the infinity, leading to a very high theoretical specific net work output according to Eqn. (4.41). However, since the cycle performance simulation performed by the EPV-11 code gives finite values of the specific net work output and heat input, it can be concluded that the semi-perfect gas assumption is not valid near the critical point. Within the Critical Zone it is, therefore, reasonable to expect that c_{p3} (determined at the maximum cycle temperature)

will have a larger weight in comparison to c_{p1}. The linear model for the average specific heat c_p developed for the Critical Zone, given by Eqn. (4.45), shows that c_{p3} has a considerably higher weight compared to c_{p1}.

As shown in Figure 4.21B, inside the Critical Zone, there is an excellent agreement between the simulation results and expression given by Eqn. (4.44). The average of relative errors for 1,340 analyzed cases is 0.026.

Using the same approach for the specific heat input at the optimum pressure ratio leads to the following expressions. For the operating conditions outside the Critical Zone, Eqn. (4.46) should be used for the specific heat input:

$$\dot{q}_{in,max} = \frac{\dot{Q}_{in,max}}{\dot{m}_f} = 1.0237 * c_{p13}\left[(T_3 - T_1) - \left(\frac{T_3 T_1 \eta_T}{\eta_c}\right)^{0.5} + \frac{T_1}{\eta_c}\right] - 3.214 \qquad (4.46)$$

where c_{p13} is determined by assuming the semi-perfect gas behavior, i.e., the arithmetic average of specific heat capacities at the minimum and maximum cycle temperatures. The leading coefficient in Eqn. (4.46) is 2.37% higher compared to the case where the perfect gas behavior is assumed. Thus, in comparison with perfect gases, real gases require higher heat input to produce the same work output. Figure 4.22A shows that the correlation given by Eqn. (4.46) is in an excellent agreement with the simulation results. The average relative error for the analyzed 10,000 cases is 0.0114.

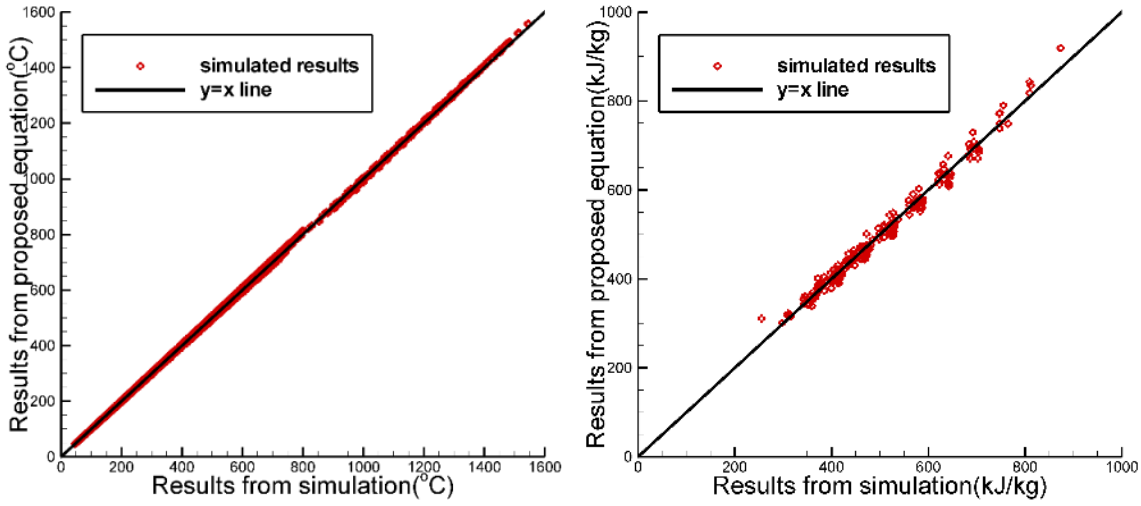

A) Specific heat input outside of the critical zone B) Specific heat input inside the critical zone

Figure 4.22. Comparison between correlation (Eqns. (4.46) and (4.47)) and the EPV-11 model results for the specific heat input.

Eqn. (4.47) was developed for calculating the specific heat input, when the compressor inlet is in the Critical Zone of CO_2:

$$\dot{q}_{in,max} = \frac{\dot{Q}_{in,max}}{\dot{m}_f} = 3.0601(c_p\left[(T_3 - T_1) - \left(\frac{T_3 T_1 \eta_T}{\eta_c}\right)^{0.5} + \frac{T_1}{\eta_c}\right])^{0.8514} \quad (4.47)$$

where:

$$c_p = 0.02439 c_{p1} + 0.9756 c_{p3} \quad (4.48)$$

The explanation concerning the linear model for the average c_p inside the Critical Zone given by Eqn. (4.48) is the same as for Eqn. (4.45).

As shown in Figure 4.22B, inside the Critical Zone, there is an excellent agreement between the simulation results and Eqn. (4.47). The average relative error for 1,340 analyzed cases is 0.0086.

For the operating conditions outside the Critical Zone, the expression for thermal efficiency of a simple Brayton cycle at the optimum pressure ratio can be obtained by dividing Eqn. (4.41) by Eqn. (4.46), resulting in the following expression:

$$\eta_{th} = \frac{\dot{W}_{net,max}}{\dot{Q}_{in,max}} = \frac{0.9764\frac{c_{p13}}{\eta_c}\left[(\eta_c\eta_T T_3)^{0.5} - {T_1}^{0.5}\right]^2 - 0.0975}{1.0237 * c_{p13}\left[(T_3 - T_1) - \left(\frac{T_3 T_1 \eta_T}{\eta_c}\right)^{0.5} + \frac{T_1}{\eta_c}\right] - 3.314} \tag{4.49}$$

where, according to the semi-perfect gas model, c_{p13} is the average of the specific heat capacity between the minimum and maximum cycle temperatures.

For the operating conditions inside the Critical Zone of CO_2, thermal efficiency of a simple Brayton cycle at the optimum pressure ratio can be obtained by dividing Eqn. (4.44) by Eqn. (4.47):

$$\eta_{th} = \frac{\dot{W}_{net,max}}{\dot{Q}_{in,max}} = \frac{6.25251\left(\frac{c_{p,w}}{\eta_c}\left[(\eta_c\eta_T T_3)^{0.5} - {T_1}^{0.5}\right]^2\right)^{0.3978}}{3.0601\left[c_{p,q}\left[(T_3 - T_1) - \left(\frac{T_3 T_1 \eta_T}{\eta_c}\right)^{0.5} + \frac{T_1}{\eta_c}\right]\right]^{0.8514}} \tag{4.50}$$

where specific heats $c_{p,w}$ and $c_{p,q}$ are obtained from Eqns. (4.45) and (4.48), respectively.

Thermal efficiency of a simple Brayton cycle at the optimal pressure ratio is a function of the maximum and minimum cycle temperatures, turbine and pump isentropic efficiencies, and, outside of the Critical Zone, it does not depend on the properties of the working fluid (Eqn. (4.49))[2]. However, inside the Critical Zone, thermal efficiency depends on the working fluid properties (Eqn. (4.50)).

A comparison between the expressions for thermal efficiency given by Eqns. (4.49) and (4.50) and the results of performance simulations performed by the EPV-11 code is presented in Figure 4.23. As it can be seen, Eqns. (4.49) and (4.50) are in excellent

[2] To be exact, outside of the Critical Zone, thermal efficiency is a very weak function of the working fluid properties.

agreement with the EPV-11 model results. The average relative error for 11,340 analyzed cases is 0.0201.

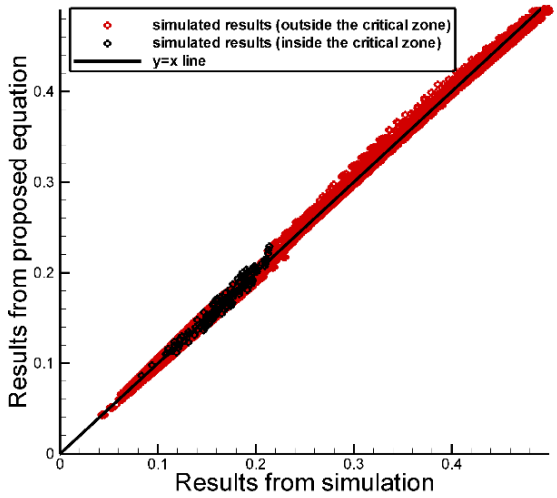

Figure 4.23. Comparison between Eqns. (4.49) and (4.50) and simulation results for thermal efficiency.

The error propagation analysis was used to estimate the uncertainty (relative error) in thermal efficiency of a simple Brayton cycle calculated from Eqn. (4.51). The uncertainty *E* in thermal efficiency can be determined from the following expression:

$$\frac{E_\eta}{\eta_{th}} = \sqrt{\left(\frac{E_w}{\dot{w}_{net,max}}\right)^2 + \left(\frac{E_q}{\dot{q}_{in,max}}\right)^2} \qquad (4.51)$$

where E_η is uncertainty (relative error) in thermal efficiency, while E_w and E_q are uncertainties (relative errors) in the specific net work output and specific heat input, respectively. The average relative error determined from Eqn. (4.51) is 0.0208 for the 11,340 analyzed cases and it is in good agreement with average relative error determined from Eqns. (4.49) and 4.50 (0.0201).

For a simple Brayton cycle, correlations (Eqns. (4.41), (4.44), (4.49), and (4.50)) may be used for a quick, systematic and precise determination of its thermodynamic

performance of in terms of the operating parameters for a working fluid(s) of interest, or for a selection of the best working fluid without the need for preforming numerous parametric calculations and tedious analysis of the results.

4.3.2. The effect of operating conditions on performance of a simple Brayton cycle

Thermal performance of a simple Brayton cycle was determined by using a detailed EPV-11 model of the cycle. Results of the calculations, performed at the optimum pressure ratio over a range of operating conditions for nine different working fluids given in Table 3.2, are presented in this section. The cycle parameters used in the calculations are summarized in Table 4.4. The temperature difference between the turbine inlet temperature (TIT) and the heat source temperature of 10°C was assumed in the calculations. The maximum pressure of 30 MPa was used to achieve supercritical condition for CO_2. A 5% pressure drop for the heater (primary heat exchanger) and 0.05 MPa for the cooler has been assumed [84].

Table 4.4. Cycle parameters for a simple Brayton cycle.

Parameter	Value
Minimum temperature, T_1 (°C)	32-62
Maximum temperature, T_4 (°C)	300-1000
Turbine isentropic efficiency, η_t	0.9
Compressor isentropic efficiency, η_c	0.85
Mass flow rate, $\dot{m}_f$ (kg/s)	37
Generator efficiency	0.975
Turbine mechanical efficiency (%)	0.99
Maximum pressure (MPa)	30

The main reasons for selecting a number of working fluids, including CO_2, for the analysis were to develop expressions for the cycle performance parameters valid over a wide range of thermo-physical properties, and to compare the commonly considered working fluids to the supercritical CO_2.

All monoatomic gases exhibit an identical behavior in a Brayton cycle because all have the same C_P on the molar basis (or equal C_P/R on mass basis). Likewise, all diatomic gases behave similarly. Although the critical point for the commonly considered working fluids is far from the operating conditions usually selected for the Brayton cycle, this is not the case for the supercritical CO_2. In fact, one of the fundamental reasons for higher efficiency of the supercritical CO_2 (sCO_2) Brayton cycle, compared to "conventional" Brayton cycle is the proximity of the Critical Point and the "liquid-like region", where thermo-physical properties (density, specific heat, etc.) of sCO_2 resemble properties of a fluid. As discussed in Chapter 3, the terms "liquid-like" and "gas-like" regions are used to explain different behavior of CO_2.

The effect of operating conditions and working fluid properties on thermal efficiency of a simple Brayton cycle is presented in Figure 4.24. Because of the upper temperature limit for some working fluids such as Kr and methane, the EPV-11 calculations for these working fluids were performed at a lower maximum cycle temperature.

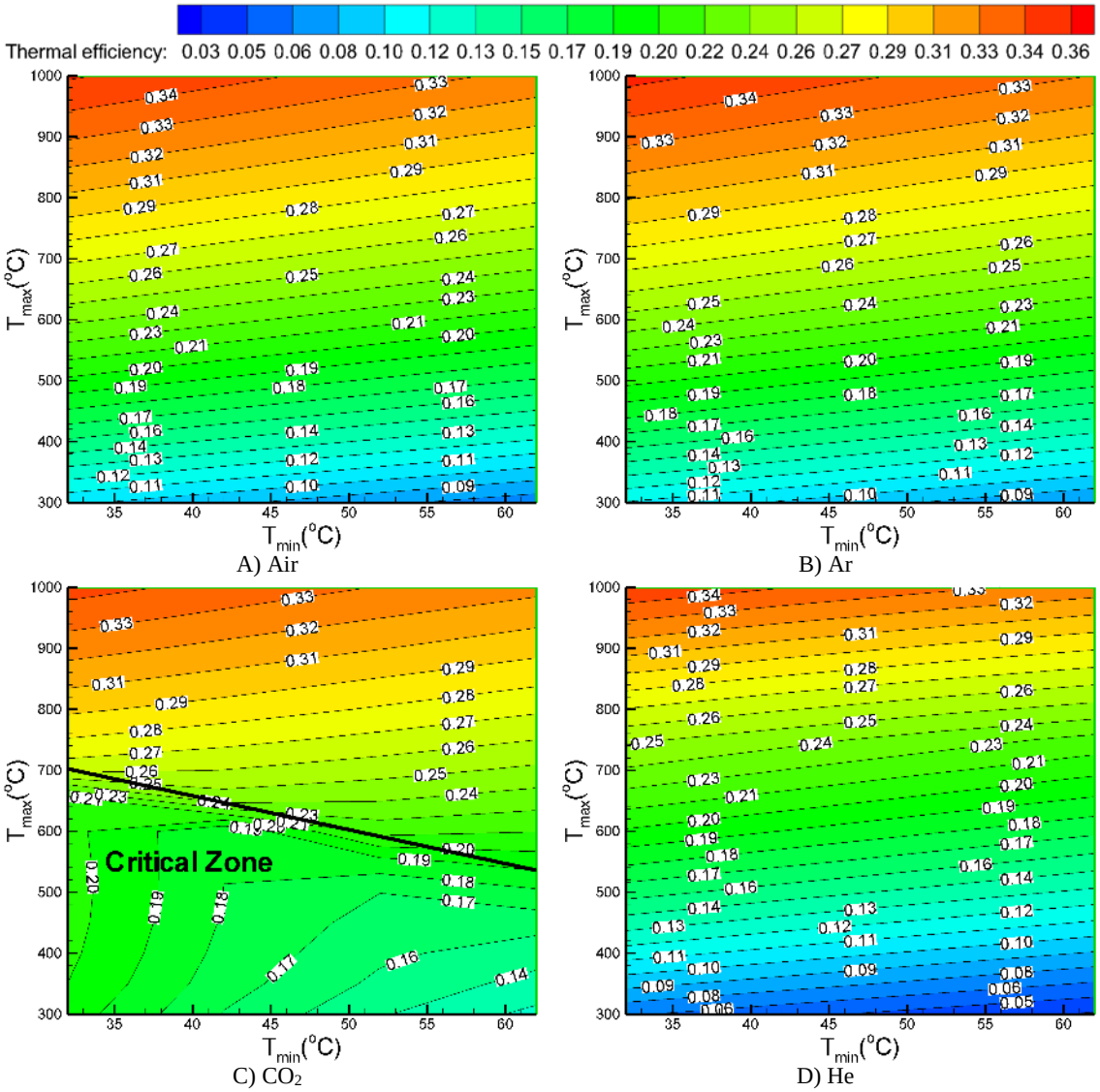

Figure 4.24. Thermal efficiency of a simple Brayton cycle for nine working fluids analyzed in this study for P_{max} = 30 MPa.

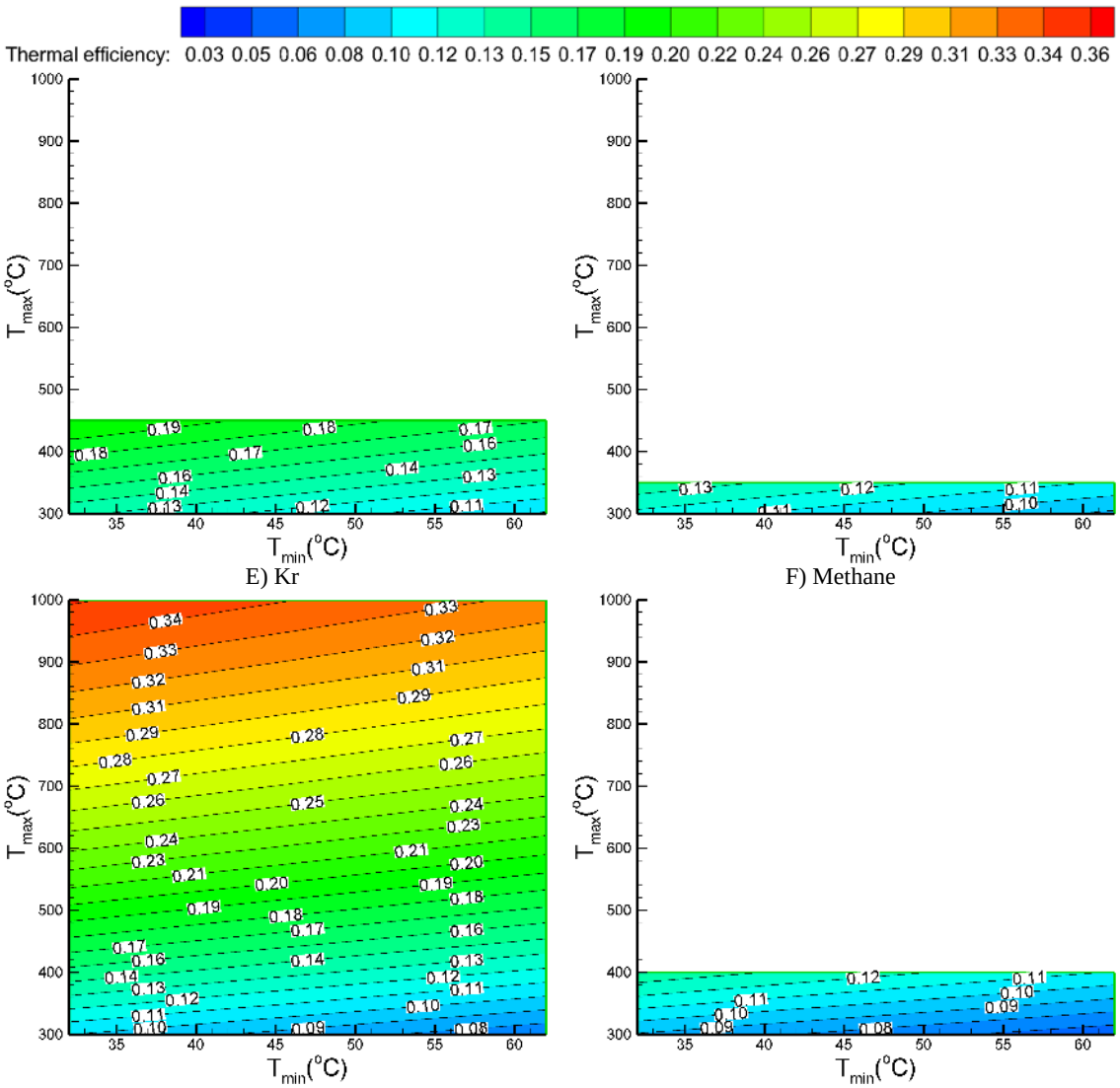

E) Kr F) Methane

G) N_2 H) Ne

Figure 4.24. Continued.

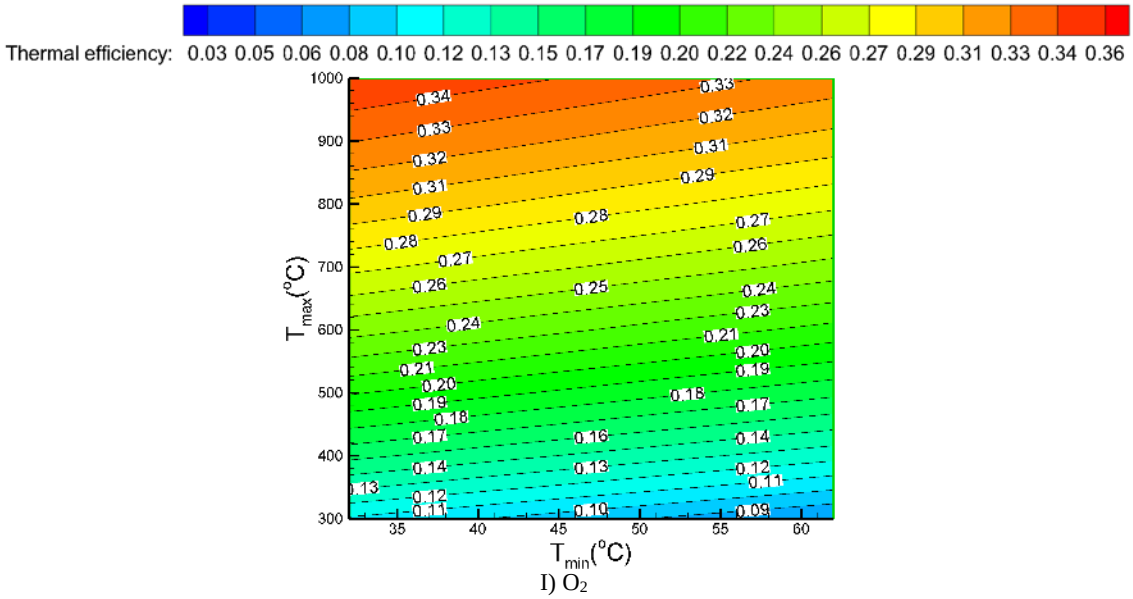

I) O_2

Figure 4.24. Continued.

By considering Eqn. (4.49), for the operating conditions outside the Critical Zone (as expected) thermal efficiency does not depend on the working fluid properties. Thus, for the same operating conditions, all working fluids give the same thermal efficiency. For example, for the minimum cycle temperature of 60°C and maximum cycle temperature of 800°C, as shown in Figure 4.24, all working fluids give the value of thermal efficiency of 28%. Over the analyzed range of operating conditions, the variation in thermal efficiency between the analyzed working fluids is less than 1%-point.

The expression for thermal efficiency given by Eqn. (4.50) shows that inside the Critical Zone thermal efficiency depends on the working fluid properties (i.e., on the ratio of specific heat capacities $c_{p,w}$ and $c_{p,q}$). In this case, different working fluids give different value of thermal efficiency. For example, for the minimum cycle temperature of 33°C and maximum cycle temperature of 400°C, as shown in Figure 4.24, thermal efficiency for CO_2 is 4%-points higher compared to the other working fluids.

For the sCO_2, the compressor inlet is typically located in the "liquid-like" region, i.e., in the region of high density to minimize the compression work. The turbine is, on the other hand, located in the "gas-like" region to maximize the expansion work. This behavior can be illustrated by calculating the compression work for the same pressure ratio in the "liquid-like" and "gas-like" regions, and comparing the results to the compression work for a liquid and a gas. Figure 4.25 shows the specific compressor work at $r_p=2.5$ for CO_2, Air, N_2, and water. As the results show, there is a dramatic decrease in the compressor work for CO_2 near its critical point.

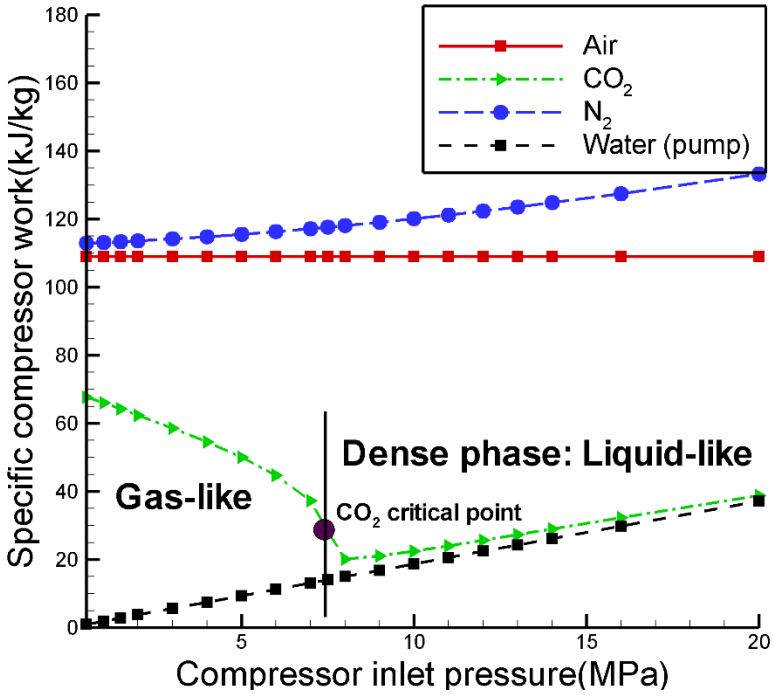

Figure 4.25. The specific compression work for CO_2, Air, N_2, and water.

The specific compressor work input for a CO_2 is shown in Figures 4.26A and 4.26B for the maximum cycle pressures of 5 MPa (transcritical operation), and 30 MPa (supercritical operation). As the results show, for the supercritical operation, the

compressor work is greatly reduced, resulting in a higher net specific work output, and higher thermal efficiency.

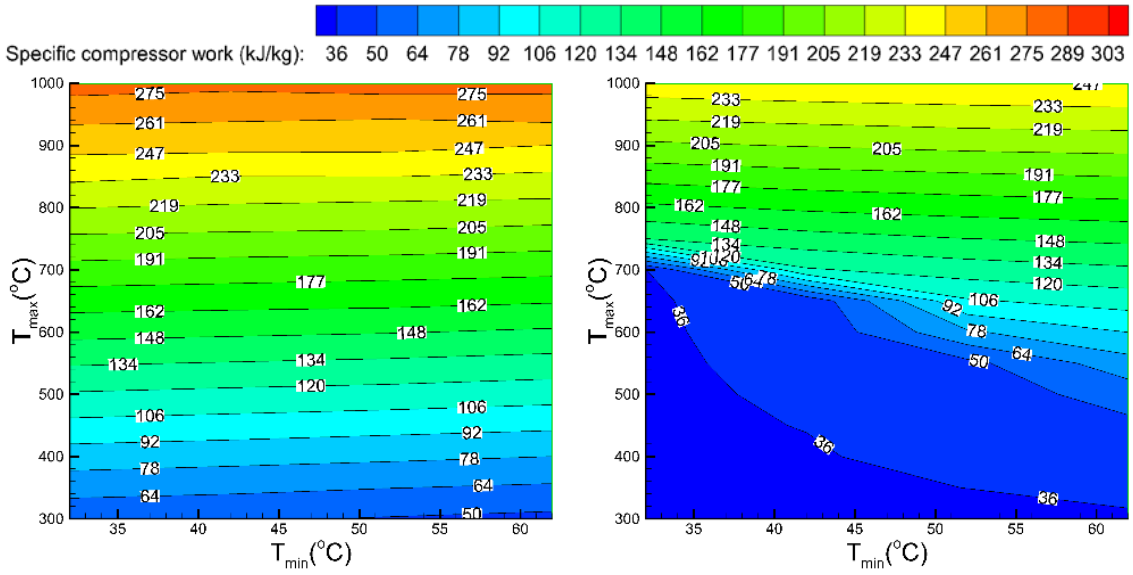

A) Pmax=5MPa B) Pmax=30MPa

Figure 4.26. Specific compressor work input (kJ/kg) for CO_2: (A) P_{max}=5 MPa, (B) P_{max}=30MPa.

For a simple Brayton cycle and all analyzed working fluids, thermal efficiency of 35% can be achieved with the maximum cycle temperature of 1,000^{o}C, minimum cycle temperature of 32^{o}C, and maximum pressure of 30 MPa, using the values of other cycle parameters given in Table 4.4.

The specific net work output determined for nine working fluids over the range of operating conditions is presented in Figure 4.27.

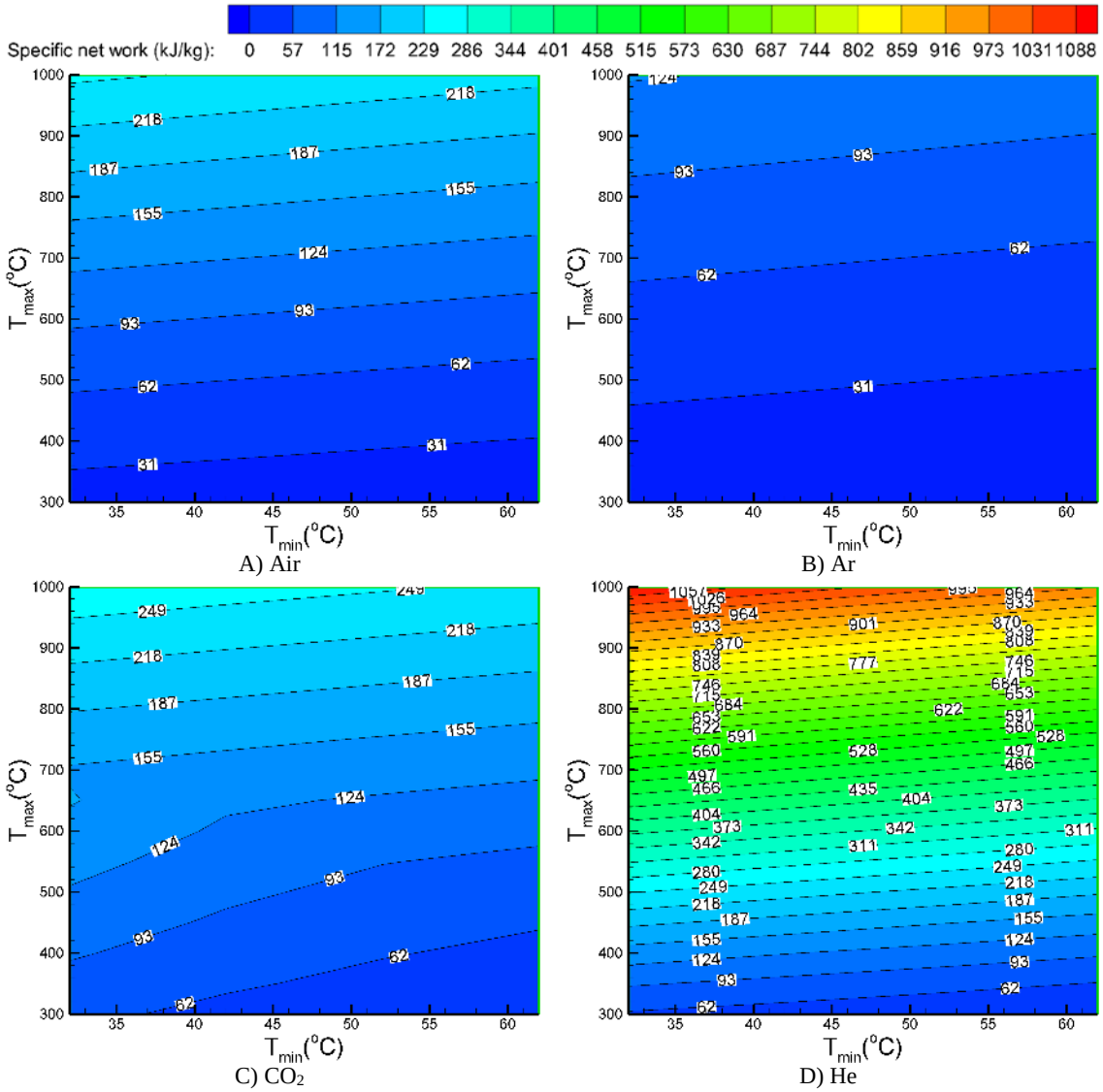

Figure 4.27. Specific net work output (kJ/kg) results for a simple Brayton cycle for nine working fluids analyzed in this study.

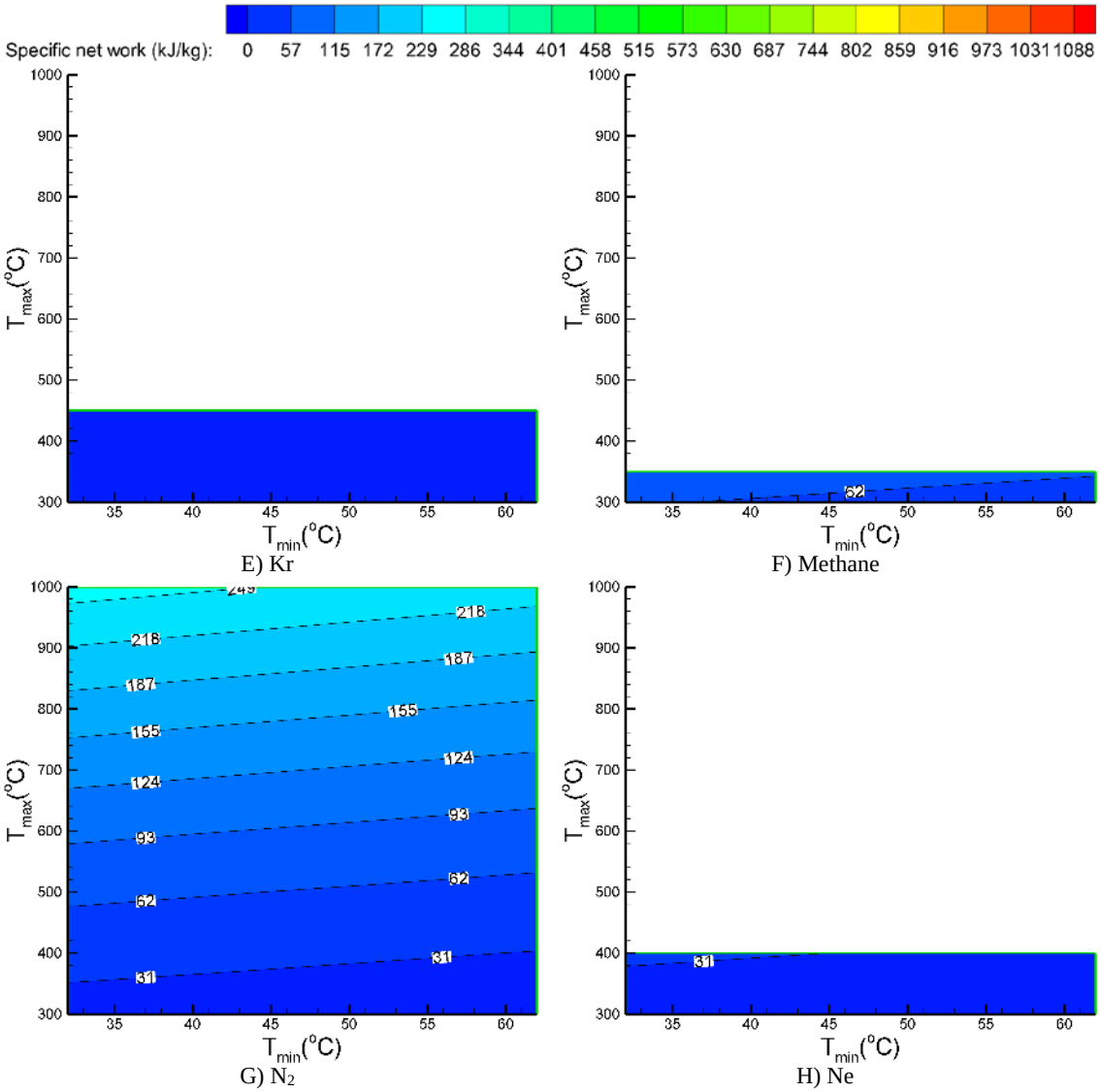

E) Kr F) Methane

G) N_2 H) Ne

Figure 4.27. Continued.

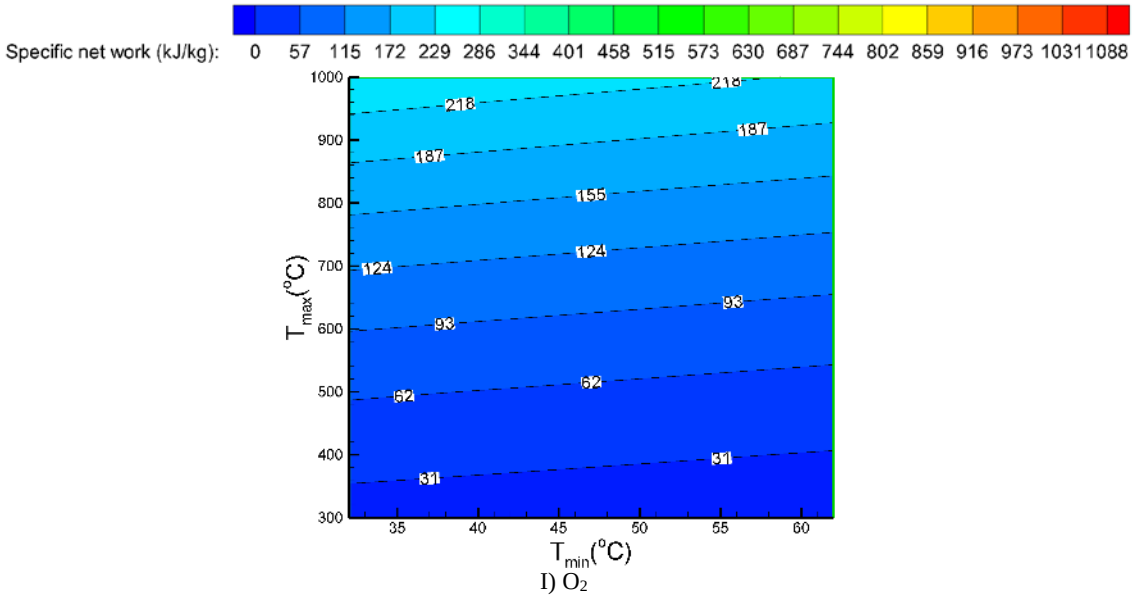

I) O_2

Figure 4.27. Continued.

In some applications where available space is one of the constraints, the cycle power output (i.e., equipment size and its footprint) might be more important than thermal efficiency [109, 111]. As the results presented in Figure 4.27 show, a simple Brayton cycle using Helium as a working fluid has the highest specific net work output, followed by CO_2 and N_2. For TIT below 450°C, Helium produces specific net work output higher than 218 kJ/kg, while for the same conditions CO_2 produces the net power output between 78 and 108 kJ/kg. However, for TIT of 1000°C, CO_2 produces the net power output between 242 and 265 kJ/kg. As it can be seen from Eqns. (4.41) and (4.44) and Figure 4.27, working fluids with higher c_p, such as Helium and CO_2, produce higher net work output.

4.3.3. Effect of the working fluid properties on thermal efficiency and specific net work output

Expressions for thermal efficiency and net specific work output developed in this study can be used to investigate effects of the working fluid properties on the performance

of a simple Brayton cycle. Eqns. (4.41), (4.44), (4.49), and (4.50) show that properties of the working fluid affect thermal efficiency and specific net work output. It can be shown that the first derivative of Eqns. (4.41) and (4.44) with respect to the specific heat capacity is positive (Eqn. (4.52)), meaning that at constant maximum and minimum cycle temperatures, inside or outside the critical zone, working fluids with higher specific heat capacity give higher specific net work output.

$$\frac{\partial \dot{w}_{net,max}}{\partial c_p} > 0 \tag{4.52}$$

It can also be shown that the first derivative of Eqns. (4.49) and (4.50) with respect to the specific heat capacity is negative (Eqn. (4.53)), meaning that at constant maximum and minimum cycle temperatures, inside or outside the critical zone, working fluids with higher specific heat capacity give lower thermal efficiency.

$$\frac{\partial \eta_{th}}{\partial c_p} < 0 \tag{4.53}$$

The effect of the specific heat capacity on thermal efficiency and specific net work output is presented in Figure 4.28 for η_t=0.9, η_c=0.85. As the results show, η_{th} and $w_{net,max}$ decrease and increase as the specific heat capacity is increased, respectively.

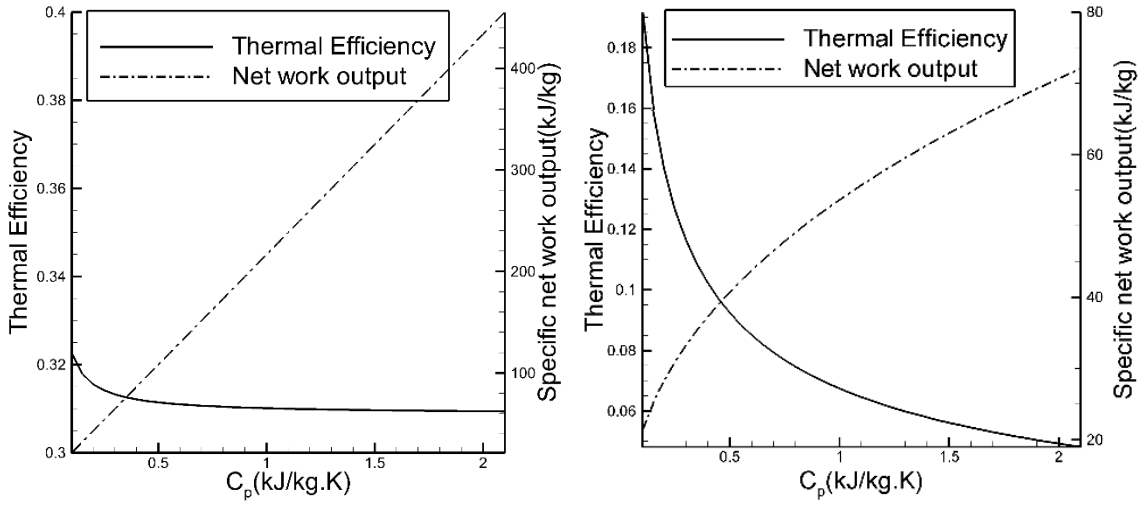

A) Outside the critical zone

B) Inside the critical zone

Figure 4.28. Effect of the specific heat capacity on thermal efficiency and specific net work output for a simple Brayton cycle inside and outside the Critical Zone.

4.3.4. Effect of the pressure drop

Figure 4.29 shows the effect of pressure drop on thermal efficiency and specific net work output of a simple Brayton cycle at T_{max}=600°C and T_{min}=32°C. As the results show, although, increasing the pressure drop lowers thermal efficiency of a simple Brayton cycle; it does not affect the selection (choice) of the best working fluid; the CO_2 and Helium are still the best working fluids giving the highest thermal efficiency and specific net work output.

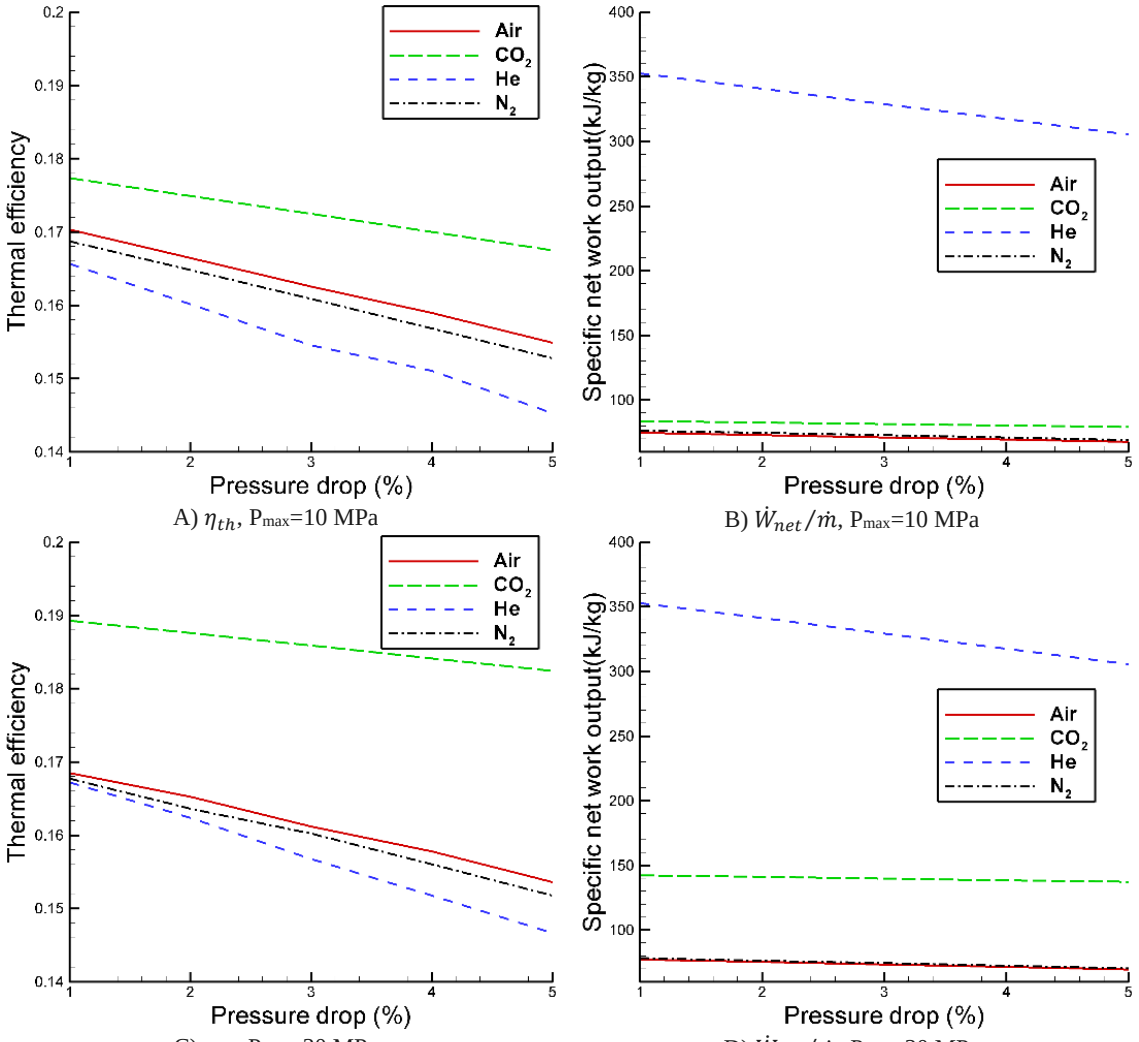

A) η_{th}, P_{max}=10 MPa B) $\dot{W}_{net}/\dot{m}$, P_{max}=10 MPa

C) η_{th}, P_{max}=30 MPa D) $\dot{W}_{net}/\dot{m}$, P_{max}=30 MPa

Figure 4.29. Effect of pressure drop on performance of a simple Brayton cycle.

As Figure 4.29 shows, pressure drop has the highest and lowest effect for CO_2 and Helium, respectively. Increasing the maximum cycle pressure P_{max} from 10 to 30 MPa, increases the pressure drop from 1% to 5%, and results in a 3.6% and 12.3% relative decrease in thermal efficiency for CO_2 and Helium, respectively. It has to be kept in mind that the pressure drop is also a function of the equipment size and design, and a straight comparison of the absolute values may not be representative. For example, since CO_2 is a

very dense working fluid compared to Helium, the equipment size (especially turbomachinery) for CO_2 is much smaller (about 10 times smaller).

4.4. Regenerative Brayton Cycle

Based on the expressions for the specific net work output, specific heat input, thermal efficiency, and turbine and compressor discharge temperatures developed in Chapter 2 for a regenerative Brayton cycle by assuming the perfect and semi-perfect gases (defined in Section 3.3 in Chapter 3), the following correlations were developed by employing the statistical regression analysis to correlate the EPV-11 simulation results. A schematic representation of a regenerative Brayton cycle is presented in Figure 4.30.

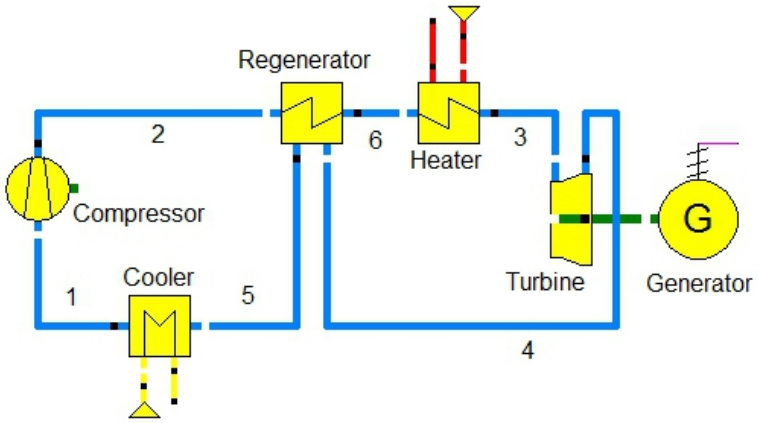

Figure 4.30. Schematic of the regenerative Brayton cycle.

4.4.1. Correlations for a regenerative Brayton cycle

To develop statistical correlations for a regenerative Brayton cycle, performance simulations were performed by using the EPV-11 model of the cycle for 9 working fluids given in Table 3.2, 15 maximum temperatures (300 to 1000°C), 3 values of the isentropic turbine efficiency (0.9 to 1), 3 values of the isentropic compressor efficiency (0.8 to 1), 7

minimum temperatures (32 to 62°C), and 5 values of the regenerator effectiveness (0.75 to 0.95), for the total of 42,525 case studies.

Using the same methodology as for a simple Brayton cycle leads to the following correlations for the regenerative Brayton cycle. Since the specific net work output of the Brayton cycle is not affected by regeneration, Eqns. (4.41) and (4.44) developed for a simple Brayton cycle can also be used for the regenerative Brayton cycle.

For the operating conditions outside the Critical Zone, Eqn. (4.54) was developed for the specific heat input at the optimum pressure ratio:

$$\dot{q}_{in,reg,max} = \frac{\dot{Q}_{in,reg,max}}{\dot{m}_f} = 0.9789 c_{p13}\left[T_3 - T_2 - \varepsilon_{reg}(T_4 - T_2)\right] + 5.3456 \qquad (4.54)$$

$$T_2 = 1.0572\left(\frac{(\eta_T \eta_c T_1 T_3)^{0.5} - T_1}{\eta_c} + T_1\right) - 25.912 \qquad (4.55)$$

$$T_4 = 0.9703\left[(1-\eta_T)T_3 + \frac{\eta_T T_3}{r_p^{\frac{k_3-1}{k_3}}}\right] + 20.101 \qquad (4.56)$$

Assuming the semi-perfect gas behavior (defined in Section 3.3 in Chapter 3), c_{p13} is determined as the arithmetic average of the specific heat capacities between the minimum and maximum cycle temperatures. The turbine and compressor discharge temperatures T_4 and T_2 can be obtained from Eqns. (4.55) and (4.56). The comparison of the correlation given by Eqn. (4.54) and the EPV-11 model (simulation) results presented in Figure 4.31A shows a very good agreement. The average relative error for the analyzed 31,900 cases is 0.011.

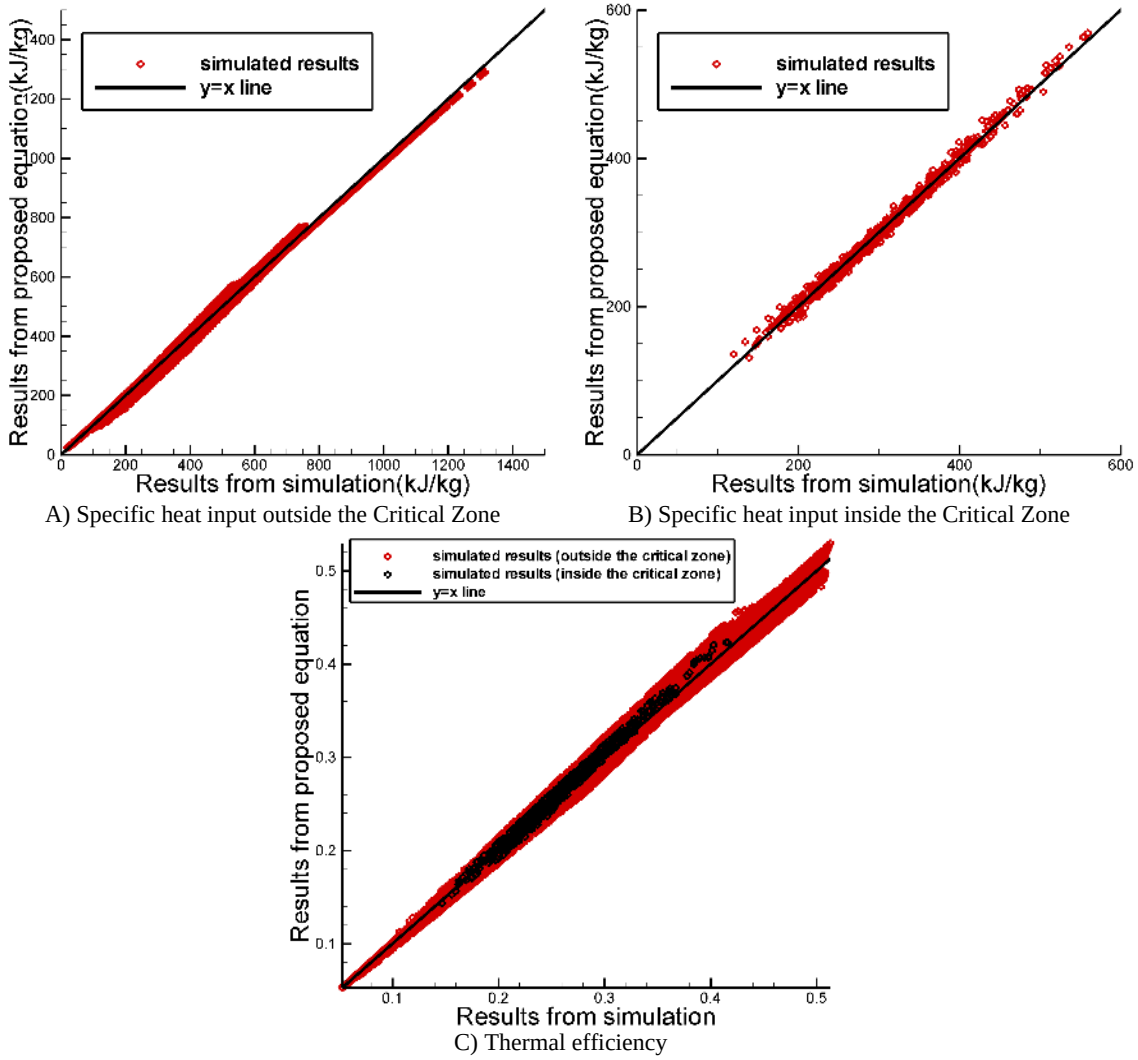

A) Specific heat input outside the Critical Zone

B) Specific heat input inside the Critical Zone

C) Thermal efficiency

Figure 4.31. Comparison between correlations and the EPV-11 model results for a regenerative Brayton cycle.

For the operating conditions inside the Critical Zone, the specific heat input can be determined from Eqn. (4.57).

$$\dot{q}_{in,reg,max} = \frac{\dot{Q}_{in,reg,max}}{\dot{m}_f} = 4.7802[c_p\left(T_3 - T_2 - \varepsilon_{reg}(T_4 - T_2)\right)]^{0.7453} \quad (4.57)$$

where:

$$c_p = 0.02459c_{p1} + 0.97541c_{p3} \quad (4.58)$$

Figure 4.31B shows that the analytical correlation is in a very good agreement with the EPV-11 model results. The average relative error for analyzed 2625 cases is 0.013.

For the operating conditions outside the Critical Zone, the expression for thermal efficiency of a regenerative Brayton cycle at the optimum pressure ratio can be obtained by dividing Eqn. (4.41) by Eqn. (4.54):

$$\eta_{th} = \frac{\dot{W}_{net,max}}{\dot{Q}_{in,reg,max}} = \frac{0.9764\frac{c_{p13}}{\eta_c}\left[(\eta_c\eta_T T_3)^{0.5} - {T_1}^{0.5}\right]^2 - 0.0975}{0.9789 c_{p13}\left[T_3 - T_2 - \varepsilon_{reg}(T_4 - T_2)\right] + 5.3456} \tag{4.59}$$

where, according to the semi-perfect gas model, c_{p13} is the average specific heat capacity between the minimum and maximum cycle temperatures.

For the operating conditions inside the Critical Zone, thermal efficiency of a regenerative Brayton cycle at the optimum pressure ratio can be obtained by dividing Eqn. (4.44) by Eqn. (4.57):

$$\eta_{th} = \frac{\dot{W}_{net,max}}{\dot{Q}_{in,reg,max}} = \frac{6.25251\left(\frac{c_{p,w}}{\eta_c}\left[(\eta_c\eta_T T_3)^{0.5} - {T_1}^{0.5}\right]^2\right)^{0.3978}}{4.7802\left[c_p\left(T_3 - T_2 - \varepsilon_{reg}(T_4 - T_2)\right)\right]^{0.7453}} \tag{4.60}$$

where specific heats $c_{p,w}$ and $c_{p,q}$ are obtained from Eqns. (4.45) and (4.58), respectively.

Figure 4.31C shows a good agreement between the analytical correlations given by Eqns. (4.59) and (4.60) and the results of performance simulations. The average relative error for 42,525 analyzed cases is 0.014. The maximum error is 0.048.

Although the average relative error inside and outside the Critical Zone is small, in the region near the Critical Zone the errors can be significantly higher. As shown in Figure 4.32, the relative error in thermal efficiency of a regenerative CO_2 Brayton cycle determined from the correlation (Eqn. (4.60)) is higher near the boundary of the Critical Zone compared to the average value.

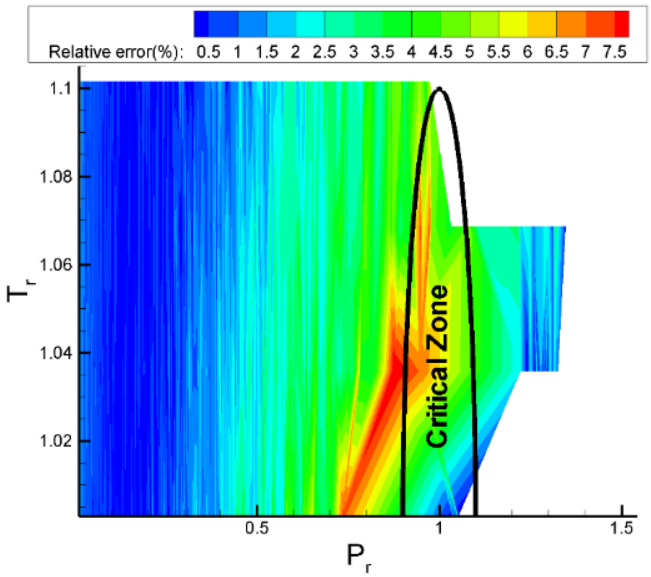

Figure 4.32. Relative error for thermal efficiency of a regenerative CO_2 Brayton cycle.

The effect of the specific heat capacity of a working fluid on the specific net work output and thermal efficiency of a regenerative Brayton cycle is the same as for a simple Brayton cycle, which was discussed in Section 4.3.3.

4.4.2. The effect of operating conditions on performance of a regenerative Brayton cycle

Thermal performance of a regenerative Brayton cycle was determined by using the EPV-11 model of the cycle. The results of the calculations performed over a range of operating conditions for nine different working fluids given in Table 3.2 are presented in this section. The cycle parameters used in the calculations are the same as for a simple Brayton cycle (Table 4.4), except the value of the regenerator effectiveness of 0.85 was used for a regenerative Brayton cycle. The maximum cycle pressure of 30 MPa was used to achieve supercritical operating conditions for the CO_2. The effect of the operating conditions (maximum and minimum cycle temperature) and thermo-physical properties of

the working fluids on thermal efficiency of a regenerative Brayton cycle operating at the maximum pressure of 30 MPa is presented in Figure 4.33.

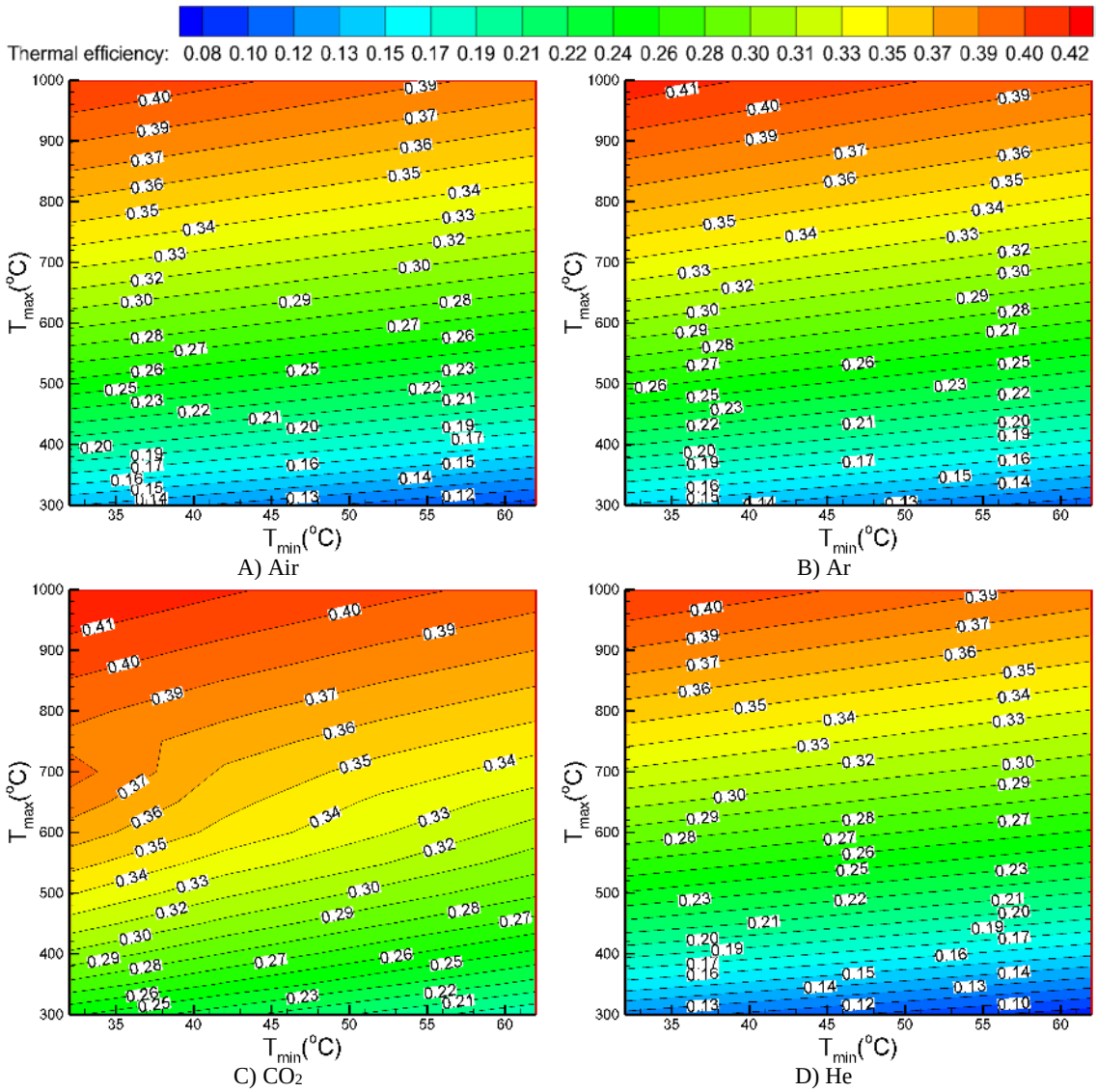

Figure 4.33. Thermal Efficiency Results of a regenerative Brayton cycle for Nine Working Fluids.

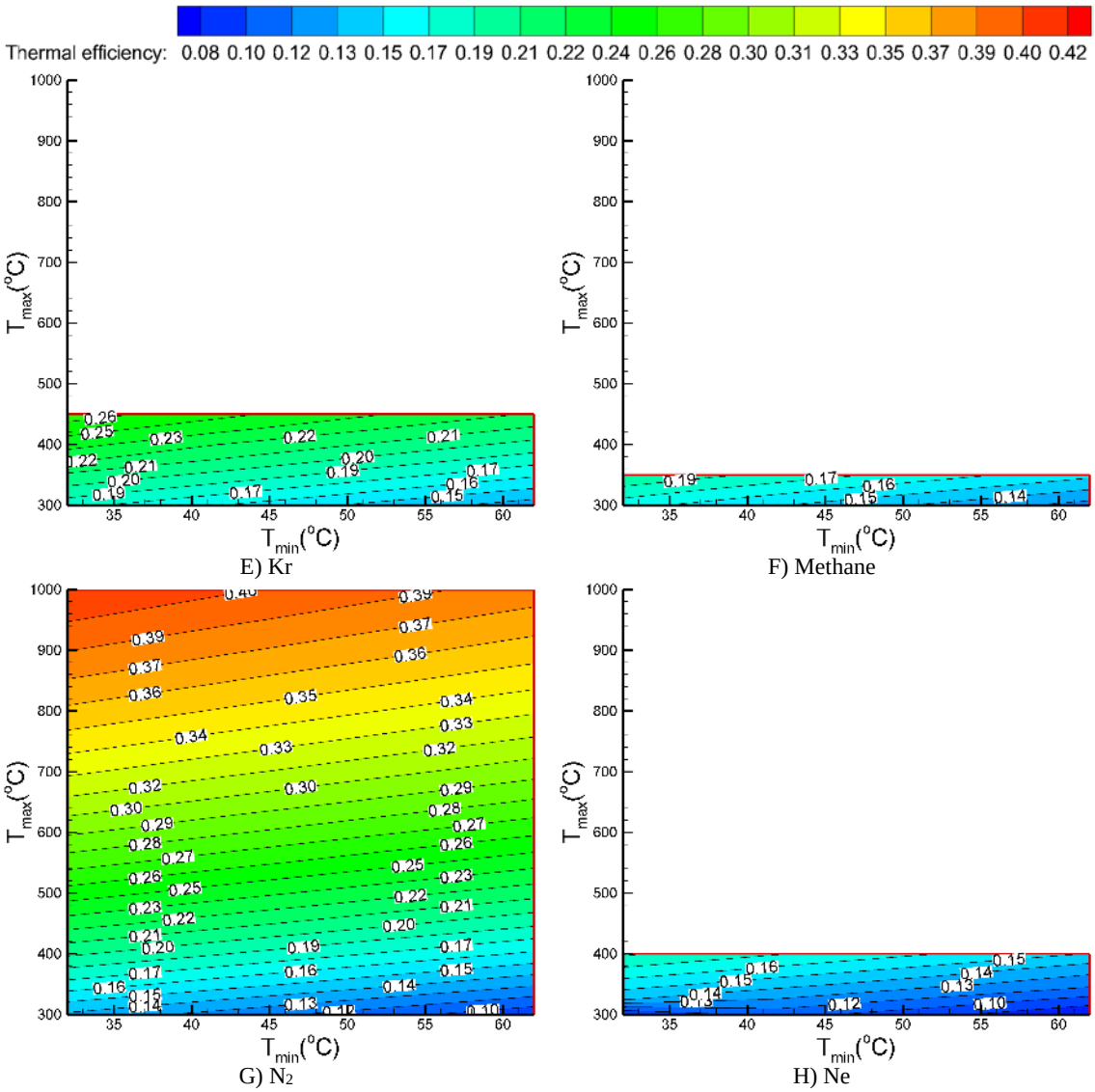

E) Kr F) Methane

G) N_2 H) Ne

Figure 4.33. Continued.

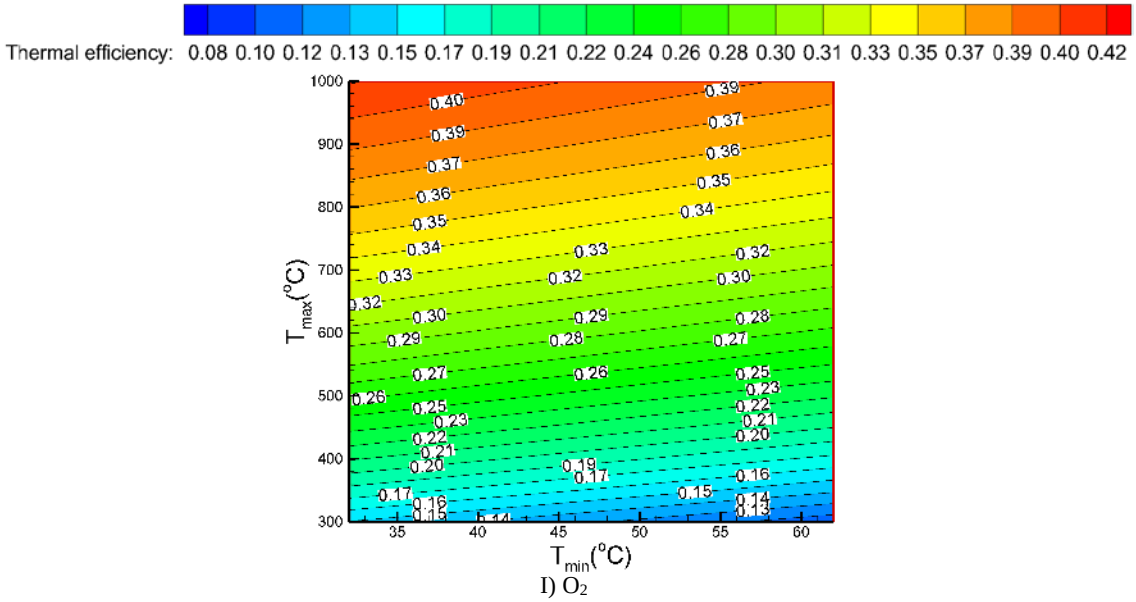

I) O_2

Figure 4.33. Continued.

As it can be seen in Figure 4.33 and according to Eqns. (4.59) and (4.60), thermal efficiency of a regenerative Brayton cycle depends on the working fluid properties. As the results presented in Figure 4.33 show, a regenerative CO_2 Brayton cycle has the highest thermal efficiency, followed by Ar and N_2. For the maximum and minimum temperature of 1000°C and 35°C, respectively, thermal efficiency of a regenerative CO_2 Brayton cycle is 41%, i.e., 7%-points higher compared to a simple CO_2 Brayton cycle (Figure 4.24). For the operating conditions inside the Critical Zone, thermal efficiency of a sCO_2 Brayton cycle is 9%-points higher compared to the other working fluids. For example, for the minimum cycle temperature of 38°C and the maximum cycle temperature of 450°C, thermal efficiency for the CO_2 and Ar is 32% and 23%, respectively.

The cycle exhaust (heat rejection) temperature (T_5) for nine working fluids is presented in Figure 4.34 over the range of operating conditions. As the results show, depending on the operating conditions, a regenerative CO_2 Brayton cycle has the highest

and lowest cycle exhaust temperature, followed by air and O_2. For example, for TIT of 1000°C, CO_2 produces the cycle exhaust temperature around 350°C. For the range of the analyzed operating conditions, the exhaust temperature of the regenerative CO_2 Brayton cycle is between 100 to 350°C which is within the ORC operating range. Thus the ORC can be selected as the bottoming cycle in the combined Brayton/ORC cycle configuration.

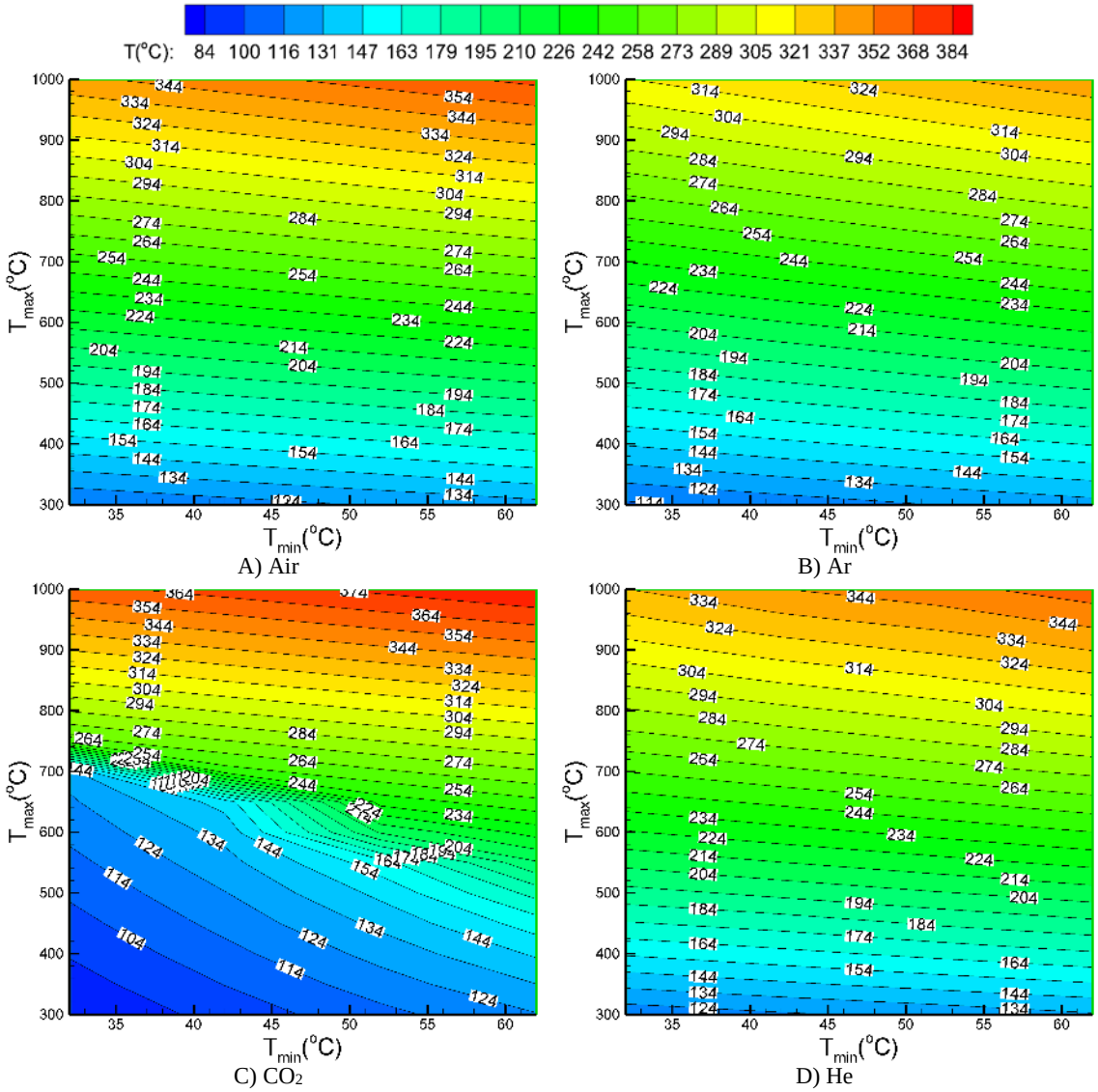

Figure 4.34. Cycle exhaust temperature for a regenerative Brayton cycle for nine working fluids.

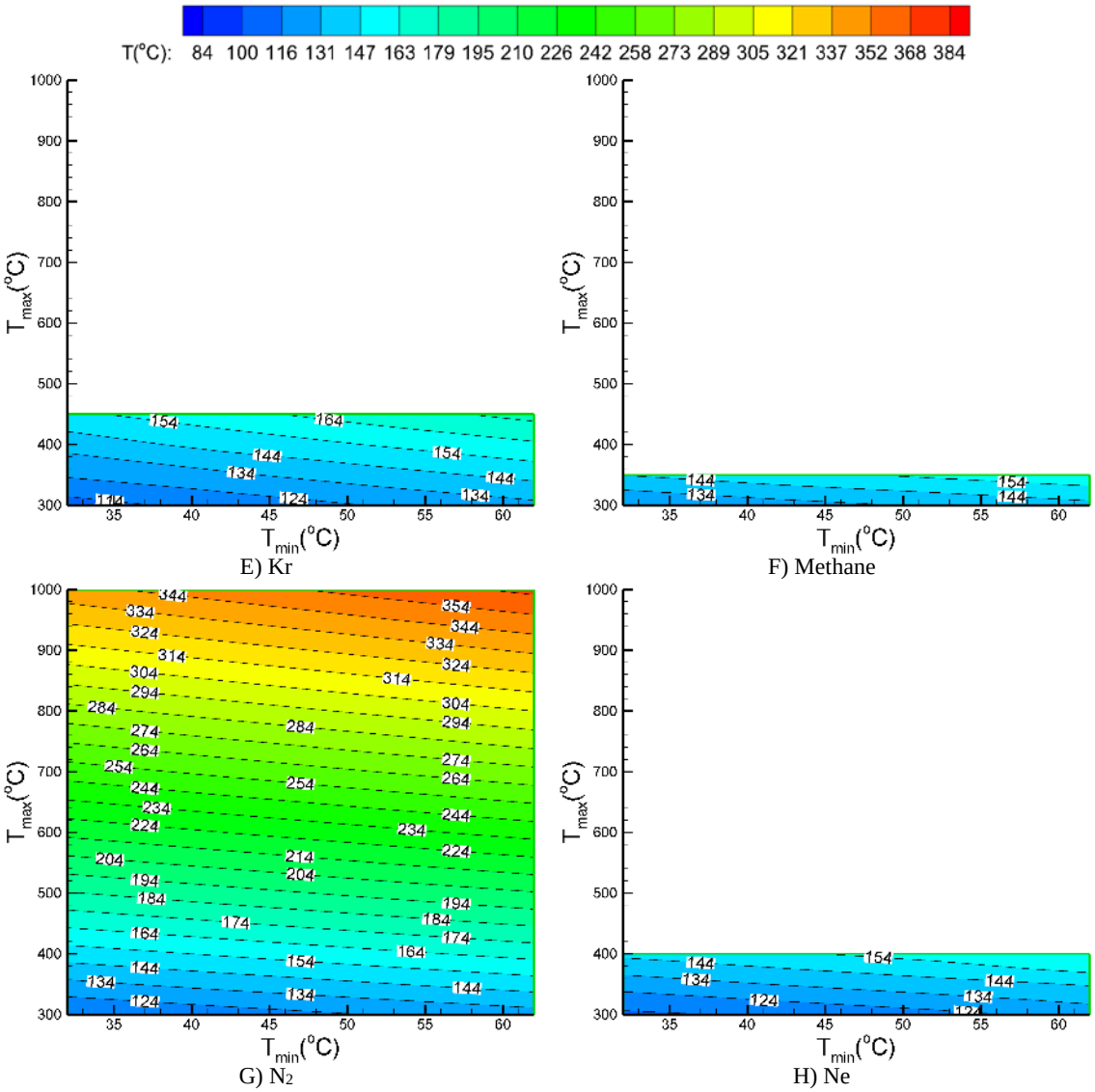

Figure 4.34. Continued.

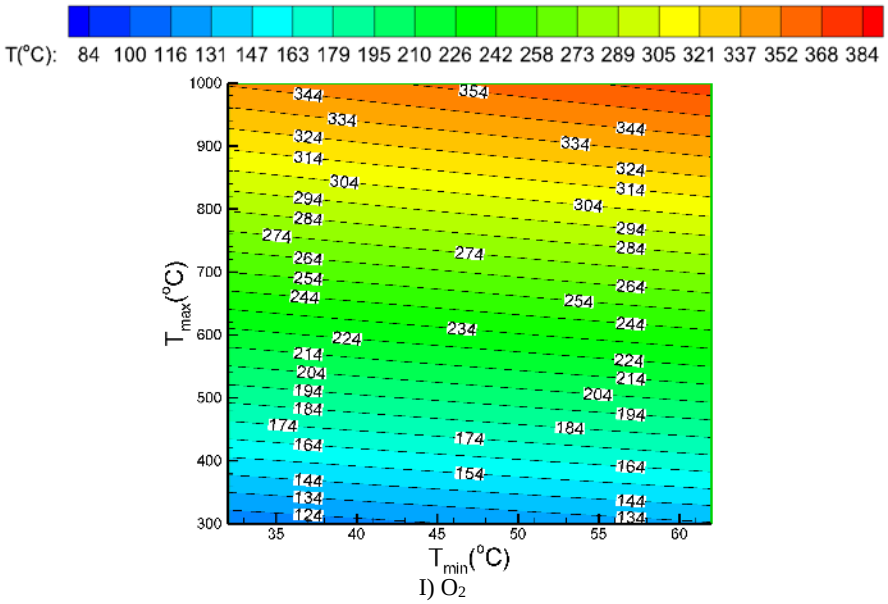

I) O_2

Figure 4.34. Continued.

4.4.3. Performance maps of a Brayton cycle

One of the main objectives of this thesis is selection of the preferred (best) working fluid(s) for the given set of cycle operating conditions. Performance maps for thermal efficiency of a simple and regenerative Brayton cycle were constructed to enable selection of the best working fluid(s) for the given set of cycle operating conditions (maximum pressure and temperature, and turbomachinery performance). The performance maps presented in Figure 4.35 show that for a simple or regenerative Brayton cycle operating at the optimum pressure ratio, depending on the operating conditions, either N_2 or CO_2 give the highest efficiency. In other words, there are two best working fluid zones: the N_2 zone and the CO_2 zone. Although Ar could also be a choice for the best working fluid, Ar is very expensive and it would significantly increase the power plant cost.

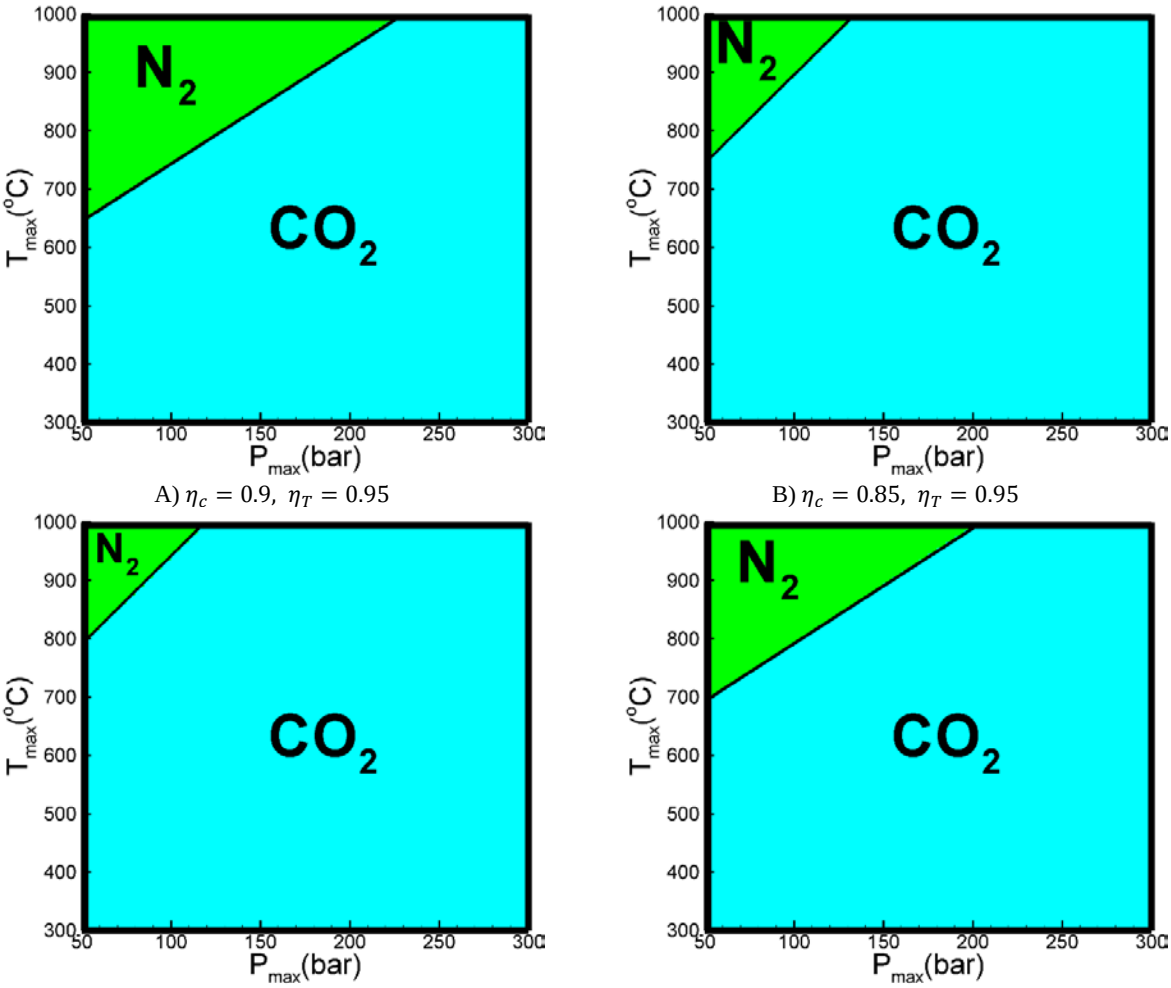

A) $\eta_c = 0.9,\ \eta_T = 0.95$ B) $\eta_c = 0.85,\ \eta_T = 0.95$

C) $\eta_c = 0.85,\ \eta_T = 0.9$ D) $\eta_c = 0.9,\ \eta_T = 0.9$

Figure 4.35. Performance Map for Thermal Efficiency of a simple and regenerative Brayton Cycle.

As shown in Figure 4.35, for high maximum cycle temperatures and low maximum cycle pressures, N_2 is the preferred working fluid giving the highest thermal efficiency. However, for higher maximum cycle pressures or lower maximum cycle temperatures, CO_2 is the best working fluid.

Performance of the turbomachinery, i.e., isentropic efficiencies of the compressor and turbine affect section of the best working fluid, with higher isentropic efficiencies increasing the size of the N_2 zone.

Using the statistical regression analysis, Eqn. (4.61) was developed for the boundary between the N_2 and CO_2 zones shown in Figure 4.35, where P_{max} is in bar, and isentropic efficiencies of the turbine and compressor are given as fractions:

$$T_{\mathrm{tmax}}(℃) = (-20\eta_c + 20)P_{\max} - 1109.8\eta_c\eta_T + 1498.3 \quad (4.61)$$

The performance map for the specific net work output of a simple and regenerative Brayton cycles is shown in Figure 4.36. Of all working fluids analyzed in this study, He produces the highest specific net work output over the entire range of the analyzed operating conditions. The performance map for the net specific work output is independent of the minimum cycle temperature and isentropic efficiencies of the compressor and turbine.

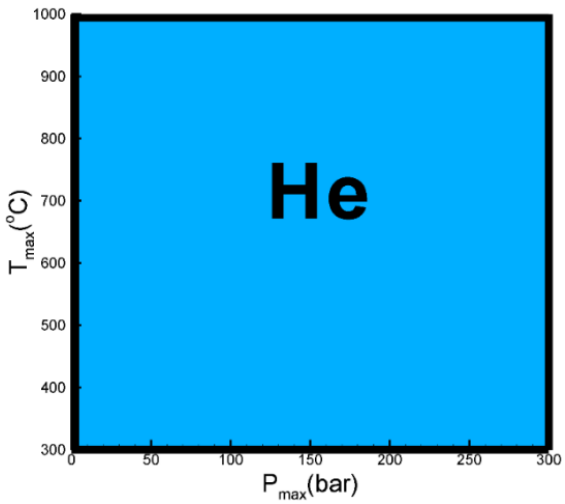

Figure 4.36. Performance map for the specific net work output.

Although the minimum cycle temperature affects thermal efficiency and net specific work output, selection of the working fluids is independent of the minimum cycle temperature. Thus, Figures 4.35 and 4.36 are valid for any minimum cycle temperature.

4.5. Regenerative Brayton Cycle with Recompression

The use of supercritical CO_2 as the working fluid has primarily been the focus of the research concerning the regenerative Brayton cycle with recompression (RBCR). Schematic representation of a regenerative Brayton cycle with recompression is presented in Figure 4.37.

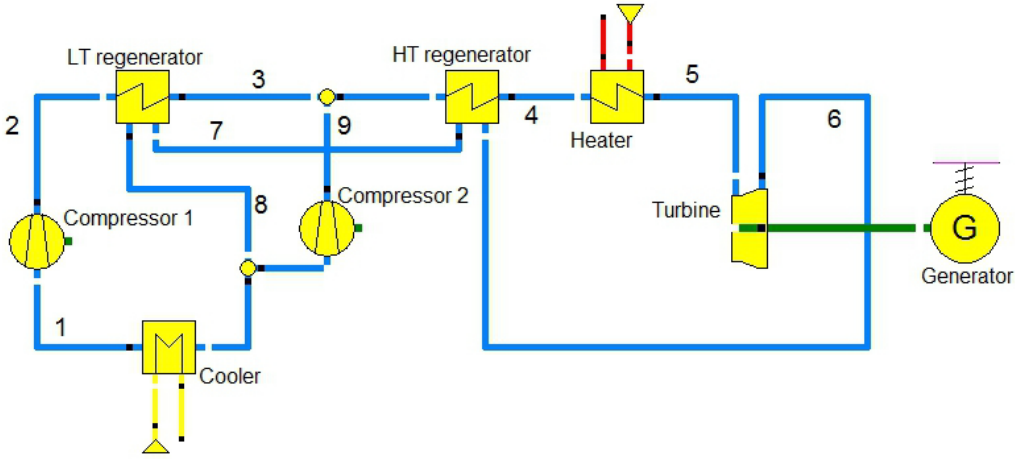

Figure 4.37. Schematic of the RBCR.

As discussed in Section 4.3.2, operation of the compressor in the "liquid-like" region reduces the compressor work and increases the thermal efficiency. The cycle performance results obtained for Air, Helium, Carbon Dioxide, and Nitrogen as working fluids are presented in this section. The cycle parameters used in the calculations are summarized in Table 4.5.

Table 4.5. RBCR parameters.

Power cycle parameter	**Value for CO_2**
Maximum temperature, T_4 (°C)	300 to 1000
Maximum pressure, P_2 (MPa)	10, 30
Turbine isentropic efficiency	0.90
compressor isentropic efficiency	0.89
HT Regenerator effectiveness	0.976
LT Regenerator effectiveness	0.88
$P_{loss,\ evaporator}$ (%)	5

The effect of the operating conditions on thermal efficiency of a regenerative Brayton cycle with recompression at P_{max}=30 MPa is presented in Figure 4.38 for four working fluids (air, CO_2, He, and N_2).

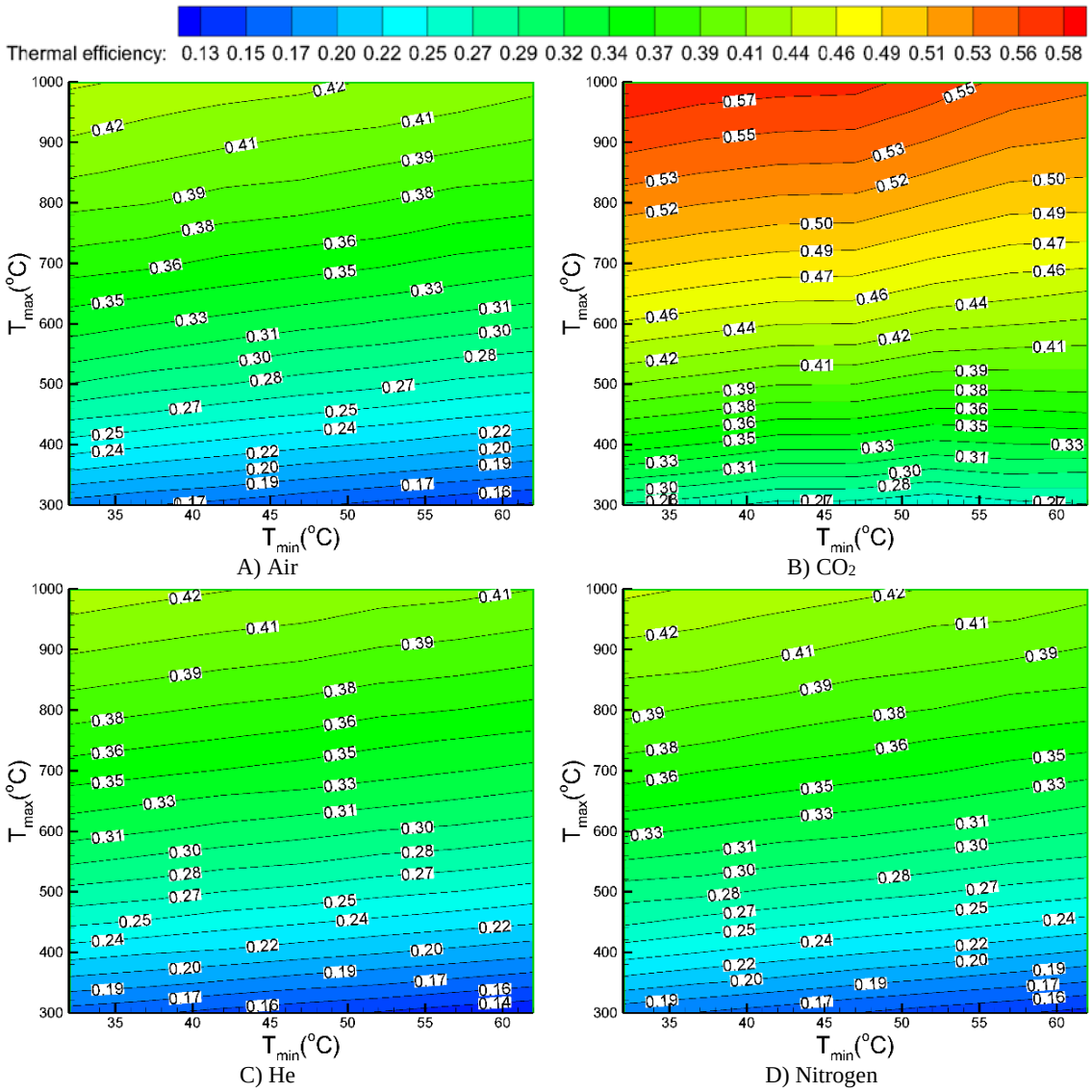

Figure 4.38. Thermal efficiency of a regenerative Brayton cycle with recompression for four analyzed working fluids for P_{max} = 30 MPa.

As the results show, a regenerative Brayton cycle with recompression using CO_2 as a working fluid has the highest thermal efficiency. Air, Helium, and N_2 have the same

thermal efficiency, significantly lower compared to the CO_2. Thermal efficiency of 57% can be obtained by using CO_2 at the maximum cycle temperature of 1000°C and maximum cycle pressure of 30 MPa.

The specific net work output determined for the four analyzed working fluids over the range of operating conditions is presented in Figure 4.39.

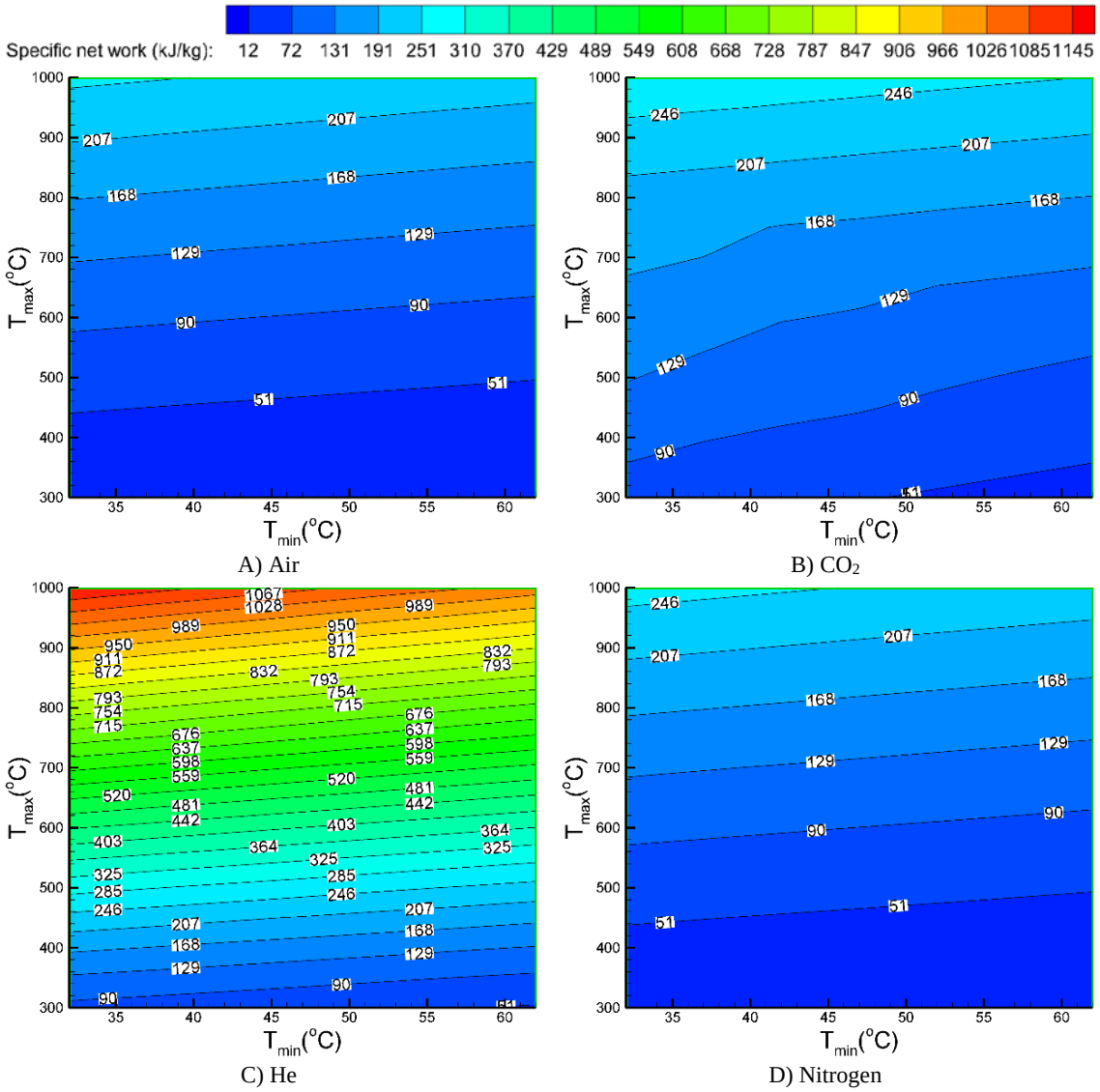

Figure 4.39. Specific net work output of a regenerative Brayton cycle with recompression for four analyzed working fluids for P_{max} = 30 MPa.

As the results show, the regenerative Brayton cycle with recompression using Helium as a working fluid has the highest specific net work output, followed by CO_2 and N_2. For TIT below 450°C, Helium produces specific net work output higher than 207 kJ/kg, while for TIT of 1000°C, CO_2 produces the net power output between 246 and 285 kJ/kg.

As discussed in Section 4.3.2, for the supercritical CO_2 Brayton cycles, the compressor inlet is located in the "liquid-like" region, i.e., in the region of high density to minimize the compression work. This fact is shown in Figure 4.40A and B for a CO_2 RBCR where the thermodynamic cycle is presented in the T-s diagrams for the maximum cycle pressures of 10 MPa (transcritical operation), and 30 MPa (supercritical operation). For the supercritical operation, the compressor work is greatly reduced, resulting in a higher net specific work output, and higher thermal efficiency.

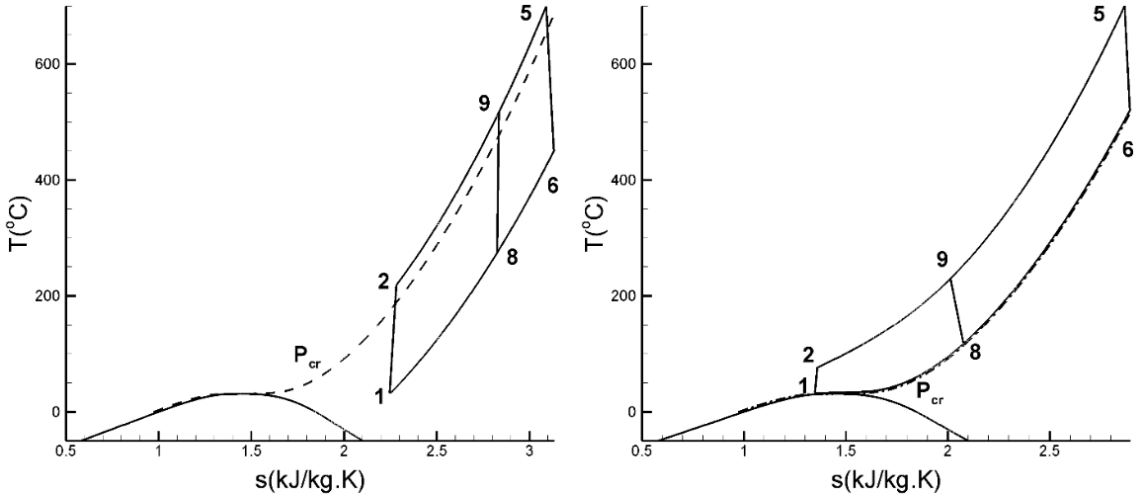

A) Pmax=10 MPa B) Pmax=30 MPa

Figure 4.40. T-s diagram of RBCR.

4.6. Combined Brayton/ORC Cycle

Thermal efficiency of a combined Brayton/ORC cycle was determined over a range of operating conditions and a number of working fluid combinations. The working fluids

used for the bottoming (ORC) cycle are listed in Table 3.1, while the working fluids used for the topping regenerative Brayton cycle are given in Table 3.2. A schematic representation of a combined Brayton/ORC cycle is presented in Figure 4.41. The cycle parameters used in the calculations are summarized in Table 4.6.

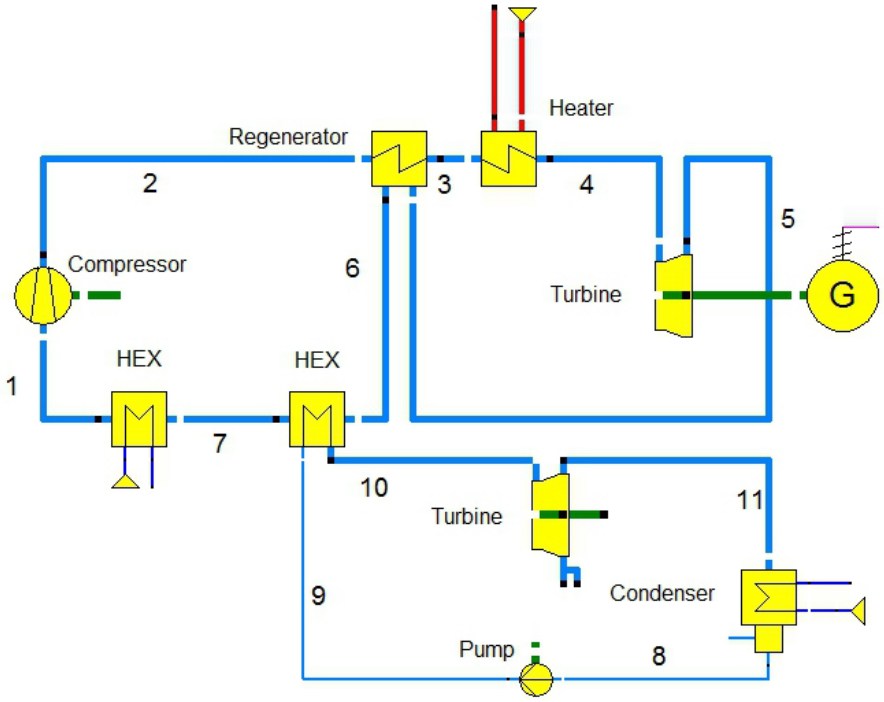

Figure 4.41. Schematic representation of a combined Brayton/ORC cycle.

Table 4.6. Cycle parameters for a combined Brayton/ORC cycle.

Parameter	Value
Brayton cycle turbine isentropic efficiency	0.90
ORC turbine isentropic efficiency	0.87
Compressor and pump isentropic efficiency	0.80
P_2(MPa)	5-30
T_1(°C), T_8(°C)	32-62
T_3(°C)	300 to 1000
Effectiveness	0.85
Upper temperature difference for HEX(°C)	10
P_{10}(MPa), $T_{10}>T_{cr}$	P_{cr}
P_{10}(MPa), $T_{10}<T_{cr}$	P_{sat}

The temperature difference between the topping cycle turbine inlet temperature (TC-TIT) and the heat source temperature of 10°C was used in the calculations. Also, the optimal pressure ratio of the topping cycle was determined, as described in [112]. At the optimal pressure ratio, the cycle net work output reaches its maximum value. Since the flow rate of the working fluid in the bottoming cycle is dependent on the mass flow rate of the working fluid in the topping cycle, a constant gross power output of 100 MW was assumed for the topping cycle.

Figure 4.42 shows the effect of the exhaust temperature of the topping cycle (TC-ET) on the *A* value given in Eqn. (2.52), where quantity *A* represents the improvement in thermal efficiency of the combined cycle with respect to the topping cycle. The five working fluids having the highest *A* value (efficiency improvement) are shown in Figure 4.42. As the results show, for the values of the topping cycle exhaust temperature up to 227°C, Iso-butane performs better than other analyzed working fluids. R11 is the preferred working fluid for TC-ET in the 227°C and 327°C range. For TC-ET higher than 327°C, Ethanol gives the highest *A* value (highest efficiency improvement).

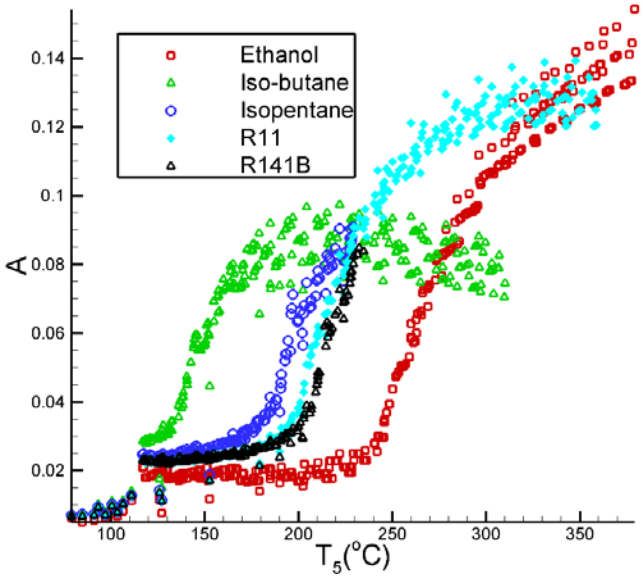

Figure 4.42**.** Effect of the topping cycle exhaust temperature on thermal efficiency improvement of a combined Brayton/ORC cycle relative to the topping regenerative Brayton cycle.

A performance map for thermal efficiency of a combined Brayton/ORC cycle was developed to enable selection of the best working fluids for the topping and bottoming cycles, Figure 4.43.

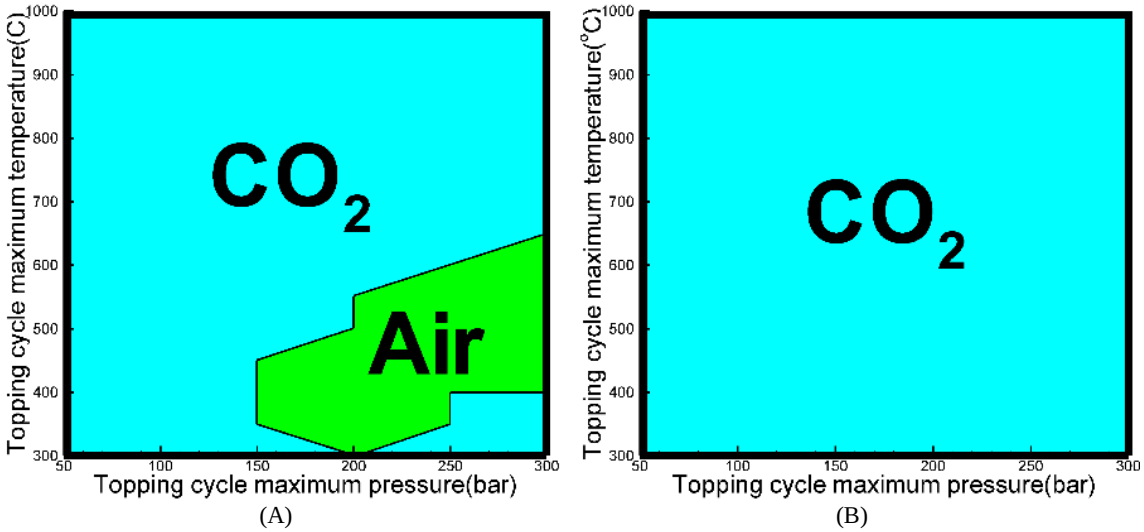

Figure 4.43**.** Performance map for thermal efficiency of a combined Brayton/ORC cycle. (A) Topping cycle for T_{min}<42°C, (B) Topping cycle for T_{min}>42°C, (C) Bottoming cycle.

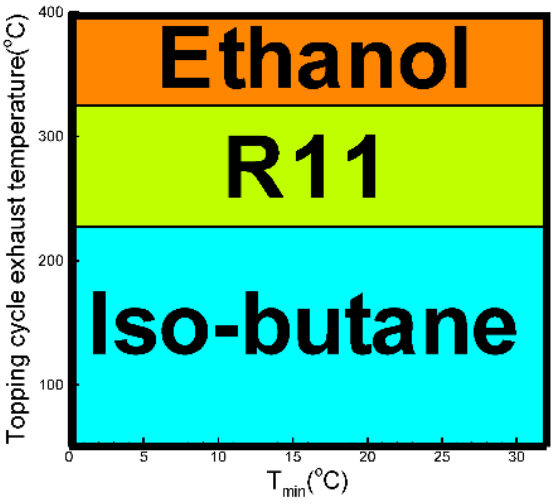

(C)

Figure 4.43. Continued.

Performance maps for the topping cycle are presented in Figure 4.43A and B. As shown in Figure 4.43A, for the minimum temperature of the combined Brayton/ORC cycle lower than 42°C, depending on the maximum temperature and pressure, CO_2 or air are the preferred working fluids. As shown in Figure 4.43B, for the minimum temperature higher than 42°C, CO_2 is the preferred working fluid over the entire range of analyzed operating conditions. Performance map for the bottoming ORC is presented in Figure 4.43C. Depending on the TC-ET, Iso-butane, R11, or Ethanol are the preferred working fluids.

Thermal efficiency of a combined Brayton/ORC cycle is shown in Figure 4.44A for P_{max} = 30 MPa. At the maximum topping cycle temperature of 1000°C, and the minimum topping cycle temperature of 32°C, the combined Brayton/ORC cycle has a thermal efficiency of 55%. The *A* value given in Eqn. (2.52), i.e., the improvement in thermal efficiency of the combined Brayton/ORC cycle with respect to the regenerative Brayton cycle is shown in Figure 4.44B. Since the cycle exhaust temperature of a

regenerative Brayton cycle is quite high, the rejected heat used by a bottoming ORC increases thermal efficiency of the combined cycle by up to 15%-points (i.e., *A*=0.15). Also, as shown in Figure 4.44B, the efficiency improvement increases as the maximum temperature of the topping cycle is increased. This is because higher maximum temperature results in a higher exhaust temperature (T_6), thus the topping cycle is providing more heat at a higher temperature to the bottoming ORC cycle, which increases work output and efficiency of the bottoming cycle.

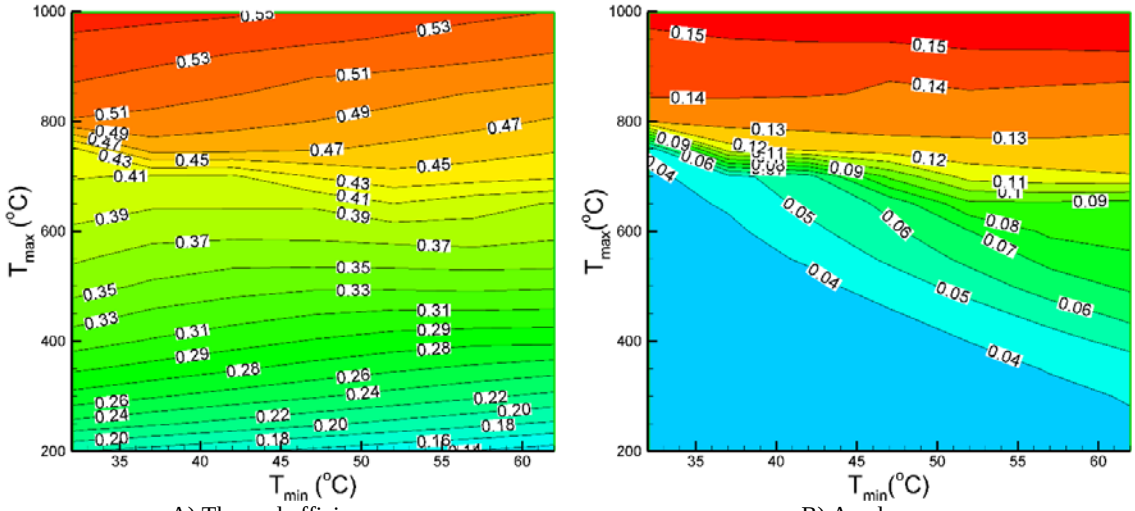

A) Thermal efficiency B) A value

Figure 4.44**.** Thermal efficiency and the *A* value for a combined Brayton/ORC cycle.

Figures 4.45A and 4.45B show the net power output in MW generated by the combined Brayton/ORC cycle and the bottoming ORC, respectively. By the using the waste heat from the topping cycle operating at T_{max} of 1000°C and P_{max} of 30 MPa, the power output of the bottoming ORC exceeds 25% of the total net power output (13 MW). Also, as shown in Figure 4.45B, for the maximum topping cycle temperatures lower than 700°C, the minimum temperature of the topping cycle has a significant effect on the power generated by the bottoming ORC. On the other hand, for the maximum topping cycle

temperatures higher than 700°C, the minimum topping cycle temperature does not have a significant effect on the power output of the bottoming ORC. This fact can be explained by the variation of the topping cycle exhaust temperature with the minimum topping cycle temperature. As it can be seen in Figure 4.34C, for T_{max}< 700°C, T_{min} has a significant effect on the topping cycle exhaust temperature. However, for T_{max}>700°C the topping cycle exhaust temperature is virtually independent of T_{min}.

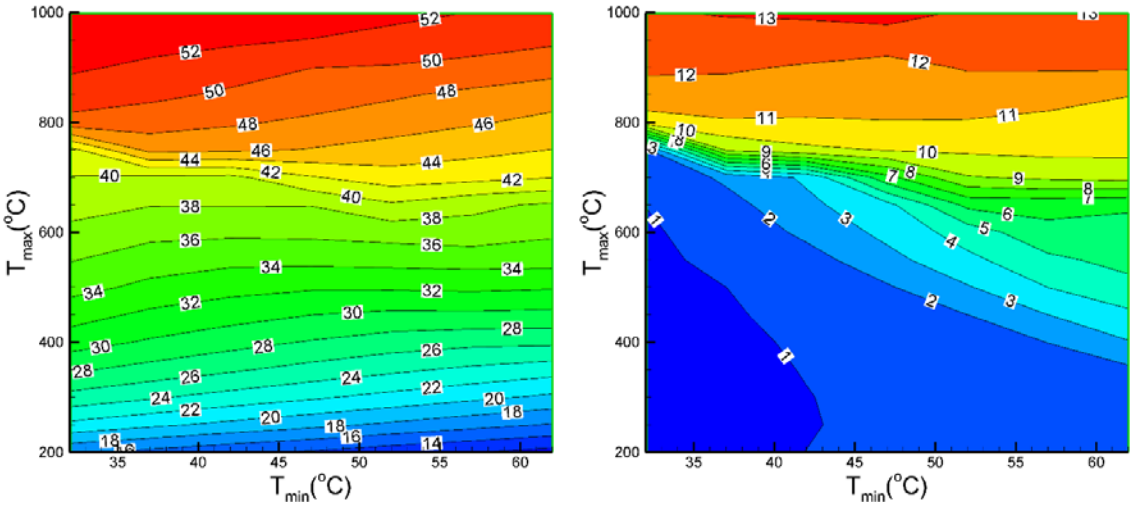

A) Combined Brayton/ORC cycle B) Bottoming ORC

Figure 4.45**.** Net power output in MW of a combined Brayton/ORC cycle and a bottoming ORC.

4.7. Regenerative Steam Rankine Cycle with the Reheat

The cycle parameters used for modeling of a regenerative steam Rankine cycle with the reheat (RSRC) are presented in Table 4.7. A schematic representation of the cycle is presented in Figure 4.46.

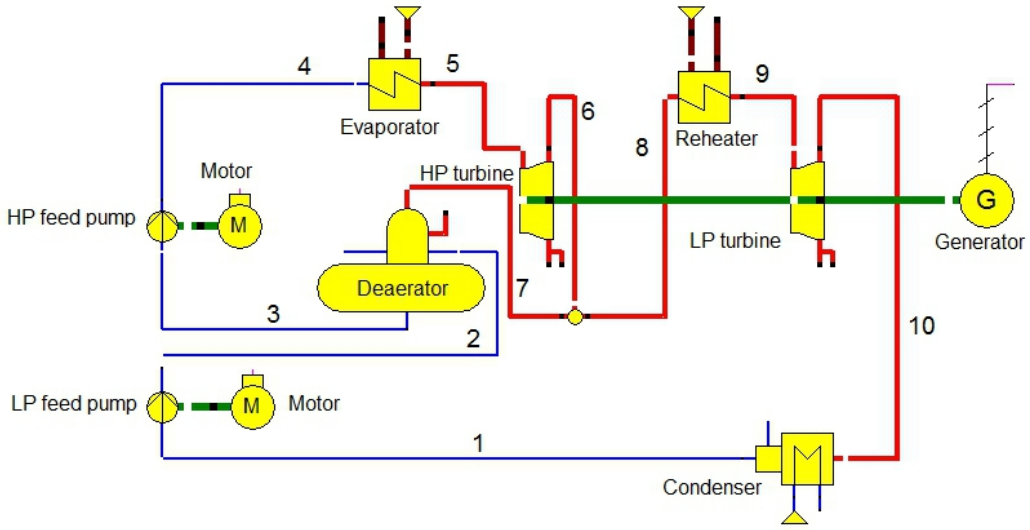

Figure 4.46. Schematic of a RSRC.

The analysis was performed over a range of live (main) steam pressures and temperatures. For each temperature and pressure combination, the deaerator pressure was varied to optimize the ratio of the main steam and IP turbine inlet steam flows ($\dot{m}_8/\dot{m}_5$ flow ratio) and achieve the highest thermal efficiency. The maximum live (main) steam temperature was varied from 400 to 650°C, while the maximum steam pressure was varied in the 10 to 30 MPa range. The critical temperature and pressure of the steam are 374.15°C and 22.1 MPa respectively, thus, the analysis covered the subcritical and transcritical operating conditions. In the power industry, the transcritical steam Rankine cycle is referred to as the supercritical Rankine cycle.

Table 4.7. Regenerative steam Rankine cycle with the reheat parameters.

Power cycle parameter	Value
Maximum temperature, T_9, T_5 (°C)	400 to 650
Maximum pressure, P_4 (MPa)	10 to 30
HP and LP feed pump isentropic efficiency	0.85
HP turbine isentropic efficiency	0.9
LP turbine isentropic efficiency	0.9

For the optimal value of the $\dot{m}_8/\dot{m}_5$ mass flow rate ratio, thermal efficiency reaches the maximum value. Figure 4.47 shows the optimum mass flow rate ratio over the range of cycle operating conditions.

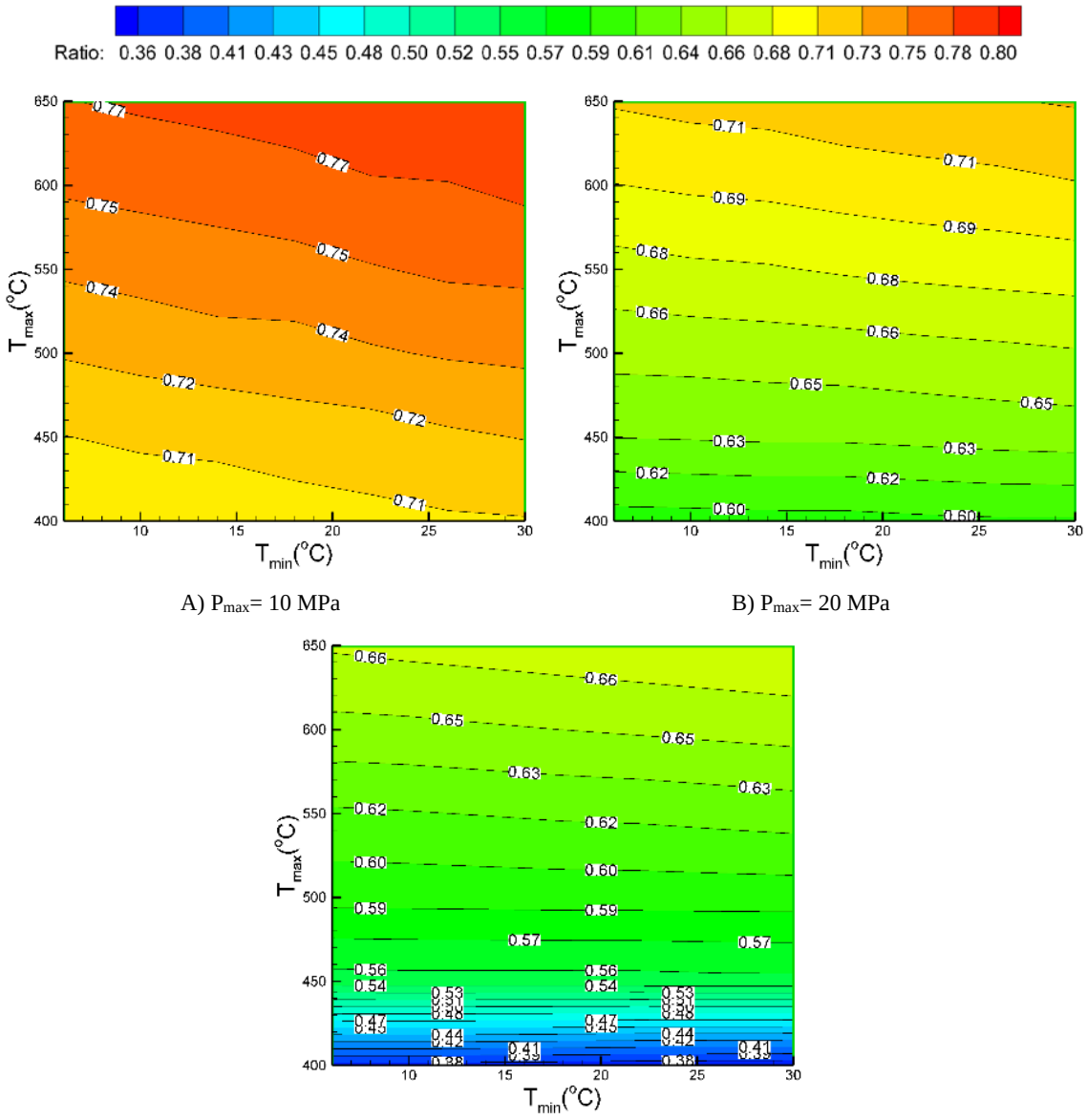

A) P_{max}= 10 MPa

B) P_{max}= 20 MPa

C) P_{max}= 30 MPa

Figure 4.47. Optimal mass flow rate ratio $\dot{m}_8/\dot{m}_5$ of a RSRC for a range of maximum steam temperature.

As it can be seen in Figure 4.47, for lower maximum steam pressure (10MPa), the optimal mass flow rate ratio varies from 0.7 to 0.77. However, for the higher maximum steam pressure (30MPa), the variation in optimum mass flow rate ratio is considerably larger, from 0.35 to 0.66.

As shown in Figure 4.47, higher maximum steam pressure results in a lower $\dot{m}_8/\dot{m}_5$ mass flow rate ratio. This can be explained with the aid of mass and energy balance equations for the deaerator.

$$\dot{m}_3 = \dot{m}_2 + \dot{m}_7 \tag{4.62}$$

$$\dot{m}_3 h_3 = \dot{m}_2 h_2 + \dot{m}_7 h_7 \tag{4.63}$$

$$\frac{\dot{m}_8}{\dot{m}_5} = \frac{\dot{m}_2}{\dot{m}_3} = \frac{h_7 - h_3}{h_7 - h_2} \tag{4.64}$$

For a constant maximum steam temperature (T_5), higher maximum steam pressure (P_5) results in a higher pressure, temperature, and enthalpy at the HP turbine exhaust (SP6). Higher enthalpy at SP6 results in a higher enthalpy at SPs 7, 3, and 2 and lower $\dot{m}_8/\dot{m}_5$ flow ratio.

The effect of the cycle operating conditions on thermal efficiency of a RSRC is presented in Figure 4.48. The results show that higher maximum steam pressure results in a higher thermal efficiency. At T_{max}=650°C and T_{min} =30°C, RSRC has thermal efficiency of 45, 47, and 48% for P_{max} =10, 20 and 30 MPa, respectively. Thermal efficiency higher than 48% can be achieved for maximum steam temperatures higher than 600°C, however, at present time, the materials for operation at steam temperature higher than 600°C and high pressure are commercially not available.

Also, by increasing the minimum temperature of the cycle from 6 to 30°C, thermal efficiency decreases 3%-points. Since heat engines reject the heat into the ambient water and air, which vary in temperature daily and seasonally, the minimum cycle temperature is a parameter typically outside of our control.

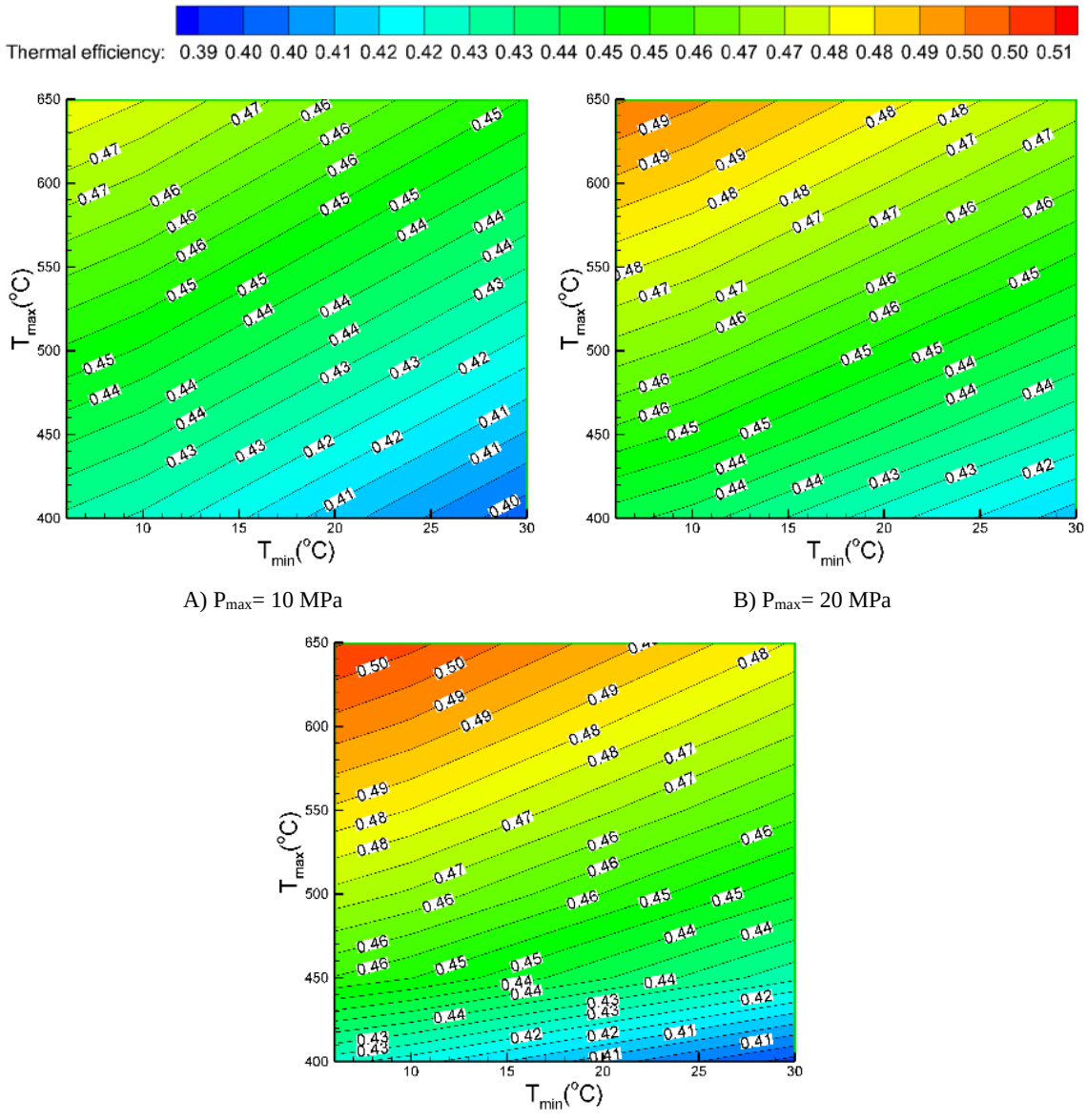

A) P_{max}= 10 MPa

B) P_{max}= 20 MPa

C) P_{max}= 30 MPa

Figure 4.48. Thermal efficiency of a RSRC over the range of operating conditions.

Figure 4.49 shows the exhaust temperature of a RSRC. As it can be seen, the cycle exhaust temperature is equal to the minimum cycle temperature for the most of the operating conditions. However, for P_{max}=10 MPa and high maximum and minimum temperatures, the exhaust temperature is higher than the minimum temperature of the RSRC. This fact can be explained by using a T-s diagram of water. The T-s diagram of a RSRC is shown in Figures 4.50A and B for T_{max}=650°C and P_{max}=10 MPa, and T_{min} =10 and 30°C. As Figure 4.50B shows, for T_{min}=30°C the cycle exhaust temperature (T_{10}) is higher than the minimum RSRC temperature since the steam turbine exhaust is located in the superheat steam region. For T_{min}=10°C the steam turbine exhaust is in the wet region (Figure 4.50A), thus the cycle exhaust and minimum (heat rejection) temperatures are the same.

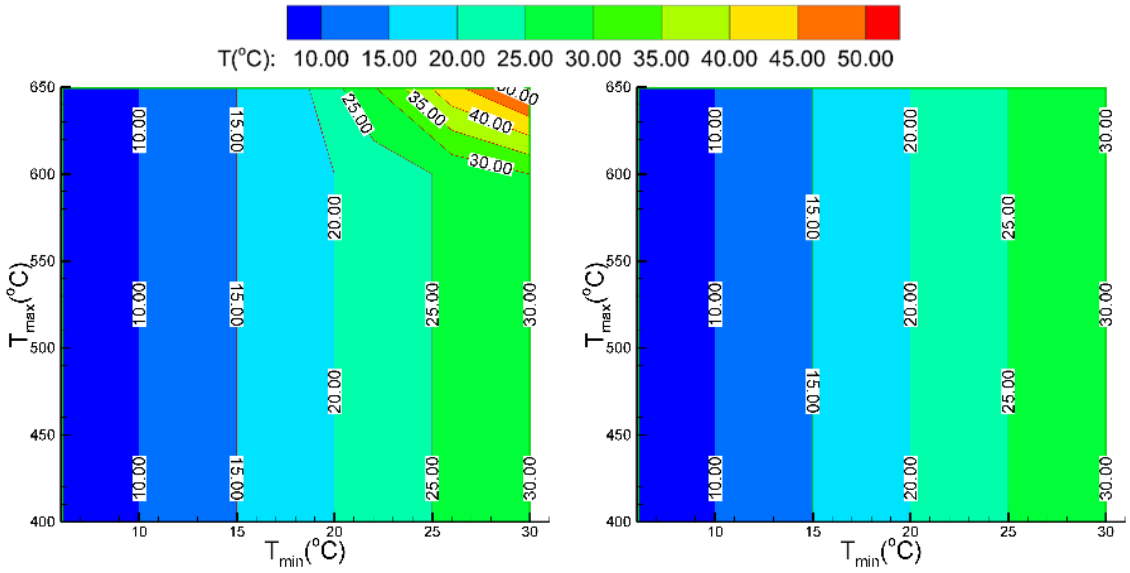

A) P_{max}= 10 MPa B) P_{max}= 20 MPa

C) P_{max}= 30 MPa

Figure 4.49. Cycle exhaust temperature of a RSRC for different operating conditions.

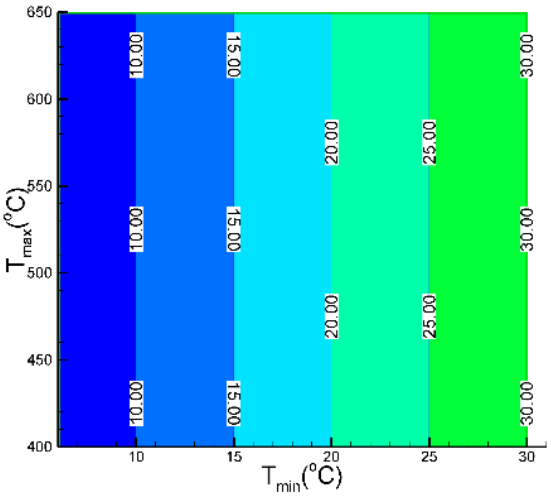

C) P_{max}= 30 MPa

Figure 4.49. Continued.

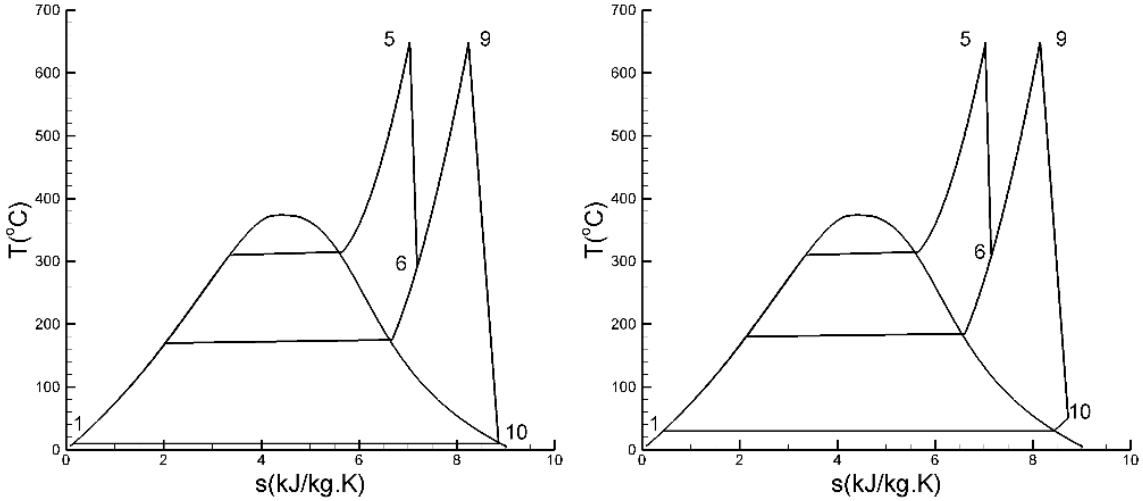

A) T_{min}=10°C B) T_{min}=30°C

Figure 4.50. T-s diagram of Water.

The heat rejected by a RSRC cycle to the ambient includes mostly the latent heat of condensation of steam, which is, due to its low temperature (slightly higher than the ambient temperature) and low exergy not a very useful heat source for a bottoming cycle.

More importantly, using a bottoming cycle working with the same minimum cycle temperature as the topping cycle is thermodynamically not viable.

4.8. Combined Rankine/ORC Cycle

In a combined Rankine/ORC cycle, RSRC was selected as a topping cycle and a simple ORC as a bottoming cycle. A schematic representation of a combined steam Rankine/ORC cycle analyzed in this study is presented in Figure 4.51.

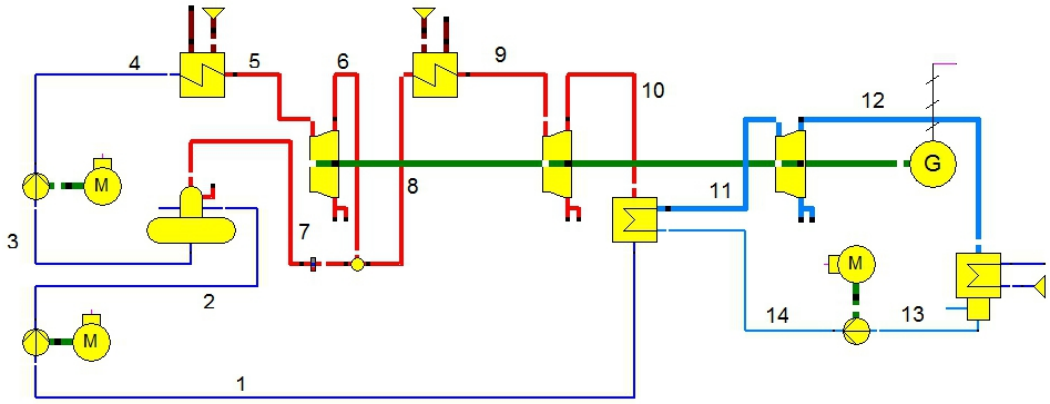

Figure 4.51. Schematic of a combined Rankine/ORC cycle.

The cycle parameters used in the calculations are summarized in Table 4.8. Since the flow rates of the two cycles vary with respect to each other, the gross power output of the topping cycle is assumed to be 100MW. A 3°C temperature difference between the exhaust steam from the topping cycle (State Point 10 in Figure 4.51) and the maximum temperature of the bottoming ORC (State Point 11 in Figure 4.51) was assumed. Based on the previous studies [113-116], 14 working fluids listed in Table 4.9 have been selected for a combined steam Rankine/ORC cycle. All working fluids are non-flammable. The parametric calculations were performed by varying the maximum temperature of the

topping cycle in the 400 to 650°C range; and the maximum pressure in the 10 to 30 MPa range.

Table 4.8. Combined Rankine/ORC parameters.

Power cycle parameter	Value
Maximum temperature, T_9, T_5 (°C)	400 to 650
Rankine cycle maximum pressure, P_4 (MPa)	10 to 30
Rankine HP turbine isentropic efficiency	0.9
Rankine LP turbine isentropic efficiency	0.9
ORC turbine isentropic efficiency	0.9
All Pumps isentropic efficiency	0.85
P_{14}(MPa), if $T_{11}>T_{Critical}$	$P_{Critical}$
P_{14}(MPa), if $T_{11}<T_{Critical}$	$P_{Saturation}$

Table 4.9. Working fluids used in a bottoming cycle.

Working fluids used in ORC	
R11	Ammonia
RC318	R236fa
R227ea	R141b
R12	R236ea
R134a	R114
R123	R113
R22	R245fa

For some of the selected working fluids, there is the optimum condenser back-pressure for the topping steam Rankine cycle, at which the efficiency of the combined Rankine/ORC cycle reaches its maximum value. Figure 4.52 shows the effect of the saturation temperature, corresponding to the condenser back-pressure, on thermal efficiency of a combined steam Rankine/ORC cycle. The results were obtained for the following operating conditions: P_{max}=10 MPa and T_{max}=400°C for the topping cycle, and minimum temperature of 10°C for the bottoming ORC. As the results show, for some working fluids such as Ammonia and R11, there is the optimum minimum cycle temperature (condenser back-pressure).

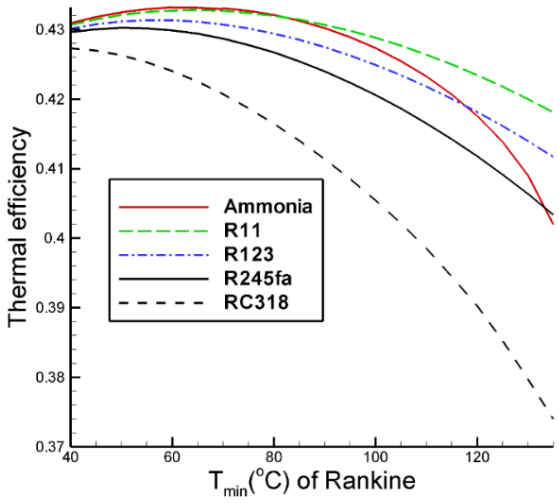

Figure 4.52. Effect of condenser back pressure on thermal efficiency of a combined Rankine/ORC cycle.

As discussed in the previous section, if the minimum temperature of the topping steam Rankine cycle is equal to the minimum temperature of the combined cycle (minimum temperature of the ORC), the steam turbine exhaust is in the wet steam region, the steam temperature corresponds to the saturation pressure set by the ambient temperature, and the steam enthalpy is lower than the saturation enthalpy. By increasing the condenser back-pressure, the enthalpy of the exhaust steam increases, increasing the amount of heat available to the bottoming ORC, thus increasing its work output. However, as the condenser back-pressure is increased, the enthalpy drop through the steam turbine decreases, resulting in a lower net work output of the topping steam Rankine cycle. Thus, there is optimal condenser back-pressure at which work output of the combined steam Rankine/ORC cycle is the highest. For RC318, the optimal condenser back-pressure is outside the range of the operating conditions analyzed in this study. Thus, for this working

fluid, thermal efficiency of a combined Rankine/ORC cycle decreases monotonically as the condenser back-pressure increased.

The rest of the results concerning performance of a combined steam Rankine/ORC cycle presented in this section were obtained by assuming the optimal condenser back-pressure.

Thermal efficiency of a combined steam Rankine/ORC cycle for the six working fluids analyzed in this work is presented in Figure 4.53. As it can be seen in Figure 4.53, Ammonia followed by R11 and R141b is the preferred choice for a working fluid in the bottoming ORC. However, Ammonia and R11 are toxic and phased out, respectively. Thus, R141b is the best choice for a bottoming ORC in a combined steam Rankine/ORC cycle. As shown in Figure 4.53A, for the maximum cycle temperature higher than 600°C, there is virtually no difference in performance of different working fluids.

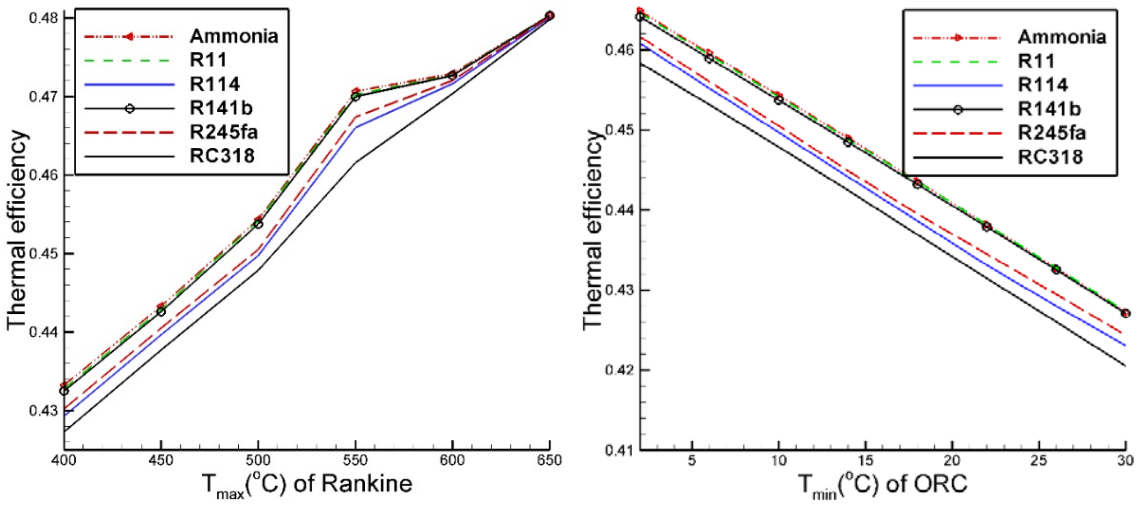

A) P_{max}=10 MPa, T_{min} of ORC= 10°C

A) P_{max}=10 MPa, T_{max} of ORC= 500°C

Figure 4.53. Thermal efficiency of a combined steam Rankine/ORC cycle for the six analyzed working fluids.

Thermal efficiency of a combined steam Rankine/ORC cycle is presented in Figure 4.54. The contour graphs are plotted in terms of the minimum and maximum cycle temperature, T_{min} and T_{max} for P_{max} = 10, 20, and 30 MPa.

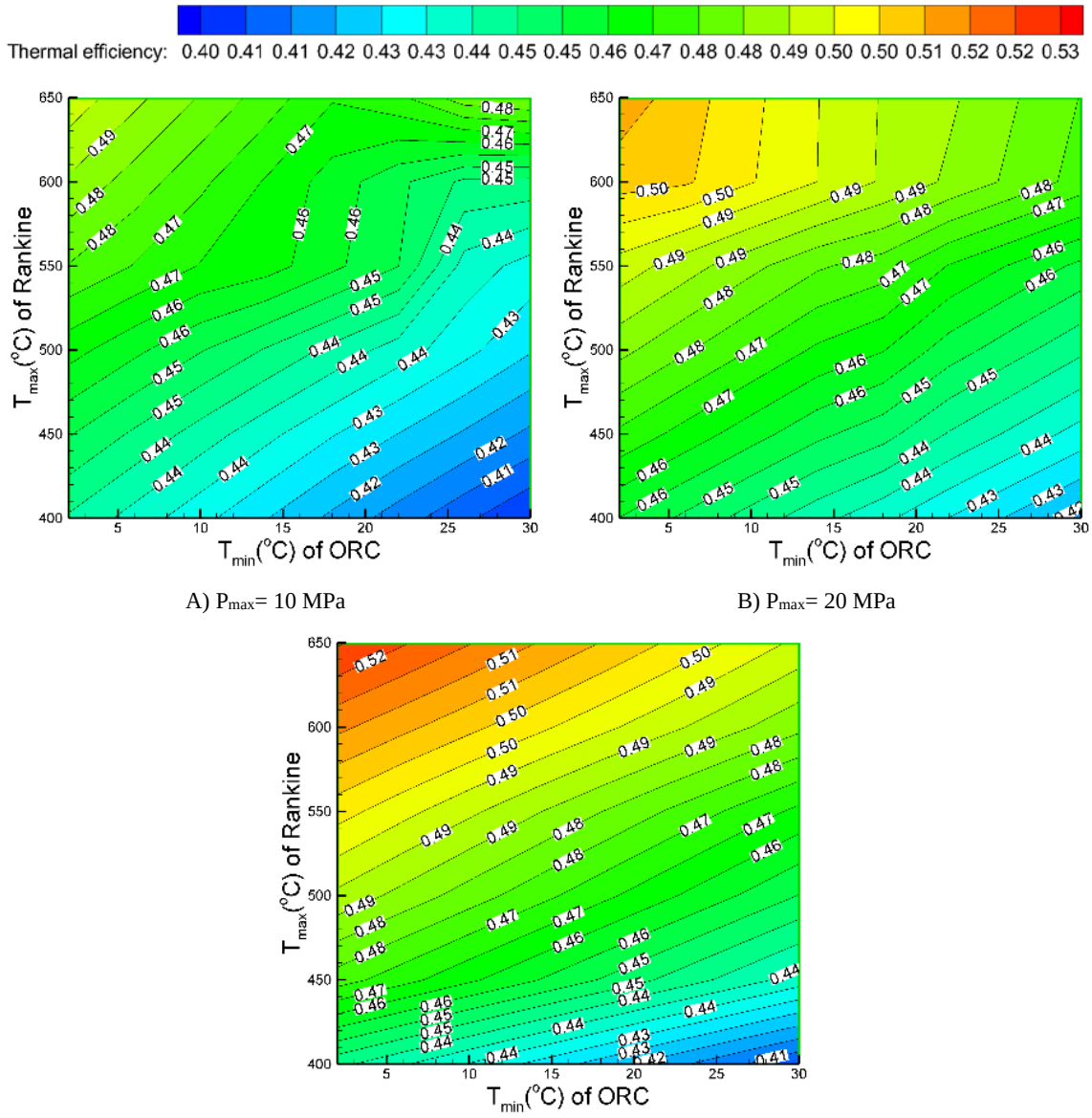

A) P_{max}= 10 MPa

B) P_{max}= 20 MPa

C) P_{max}= 30 MPa

Figure 4.54. Thermal efficiency of combined steam Rankine/ORC cycle for three maximum pressures.

As shown in Figure 4.54, an increase in the maximum pressure of the topping steam Rankine cycle results in a higher thermal efficiency of the combined steam Rankine/ORC cycle. Also, a decrease in the minimum temperature of the bottoming ORC results in a lower thermal efficiency. For example, at T_{max}=650°C and P_{max} = 30 MPa, the combined steam Rankine/ORC cycle has the thermal efficiency of 52 and 49% at T_{min} =2 and 30°C, respectively. Thermal efficiency higher than 49% can be achieved with maximum steam temperatures higher than 600°C, however, presently; the materials required for such high temperature and pressure operation are commercially not available. Also, similar to a regenerative Rankine cycle with the reheat (RSRC) analyzed in the previous section, an increase in the minimum cycle temperature from 6 to 30°C reduces thermal efficiency by 3%-points.

The difference in thermal efficiency between the combined steam Rankine/ORC cycle and RSRC is shown in Figure 4.55. As Figure 4.55 shows, adding an ORC to the steam Rankine cycle can increase the overall efficiency between 1 to 2%-points. Thus, the benefit of adding a bottoming ORC to a steam Rankine cycle is relatively small.

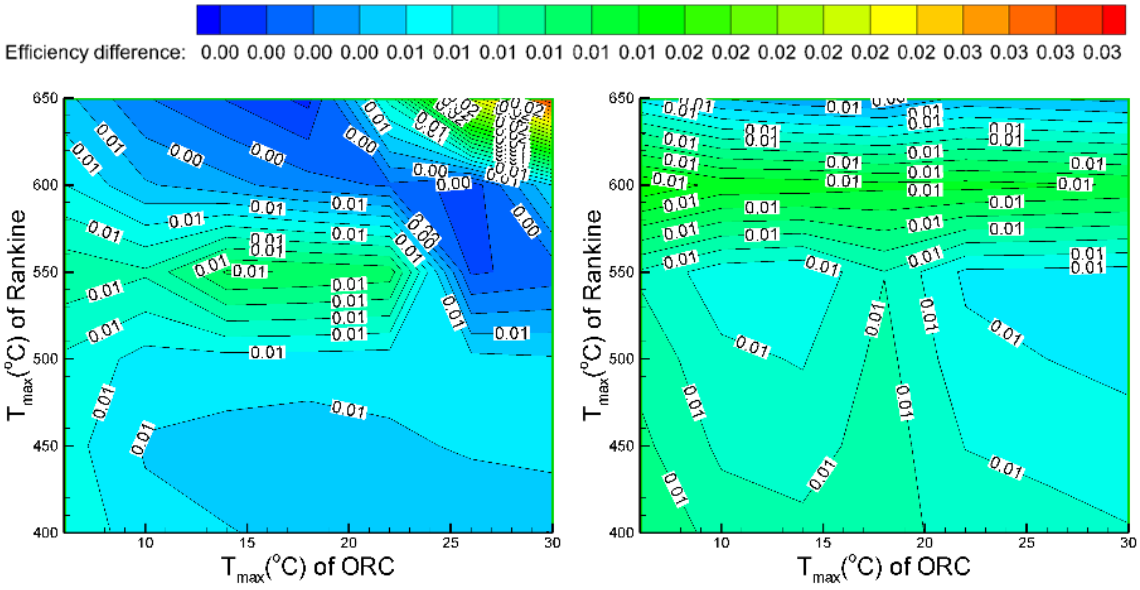

A) P_{max}= 10 MPa

B) P_{max}= 20 MPa

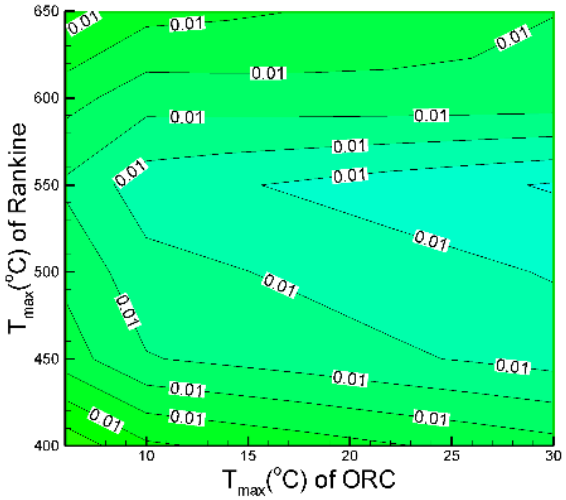

C) P_{max}= 30 MPa

Figure 4.55. Thermal efficiency difference between the combined Rankine/ORC and RSRC.

As shown in Section 4.6., adding an ORC to the Brayton cycle can increase thermal efficiency of the system around 15%-points, while adding an ORC to the steam Rankine cycle can increase the thermal efficiency by less than 2%. This fact can be explained by the T-s diagram of these combined cycles. Figure 4.56 shows a T-s diagram of the

combined Brayton/ORC and the combined steam Rankine/ORC cycles. As Figure 4.56 shows, due to the low exhaust temperature of the topping steam Rankine cycle, compared to the topping Brayton cycle, the amount of heat available to the bottoming cycle is significantly lower. Thus, the ratio of the process area corresponding to the bottoming cycle to the process area of the topping cycle is much lower for the combined steam Rankine/ORC cycle, compared to the combined Brayton/ORC cycle.

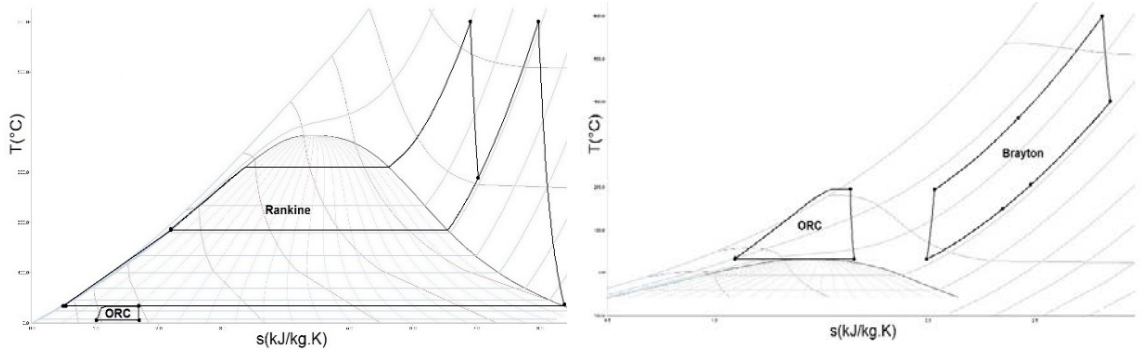

A) Combined Rankine/ORC cycle B) Combined Brayton/ORC cycle

Figure 4.56. T-s diagram of combined Rankine/ORC and combined Brayton/ORC cycle.

4.9. Sensitivity Analysis of Developed Correlations

Consider a function *Y* with *N* independent input variables.

$$Y = f(x_1, x_2, .., x_N) \tag{4.65}$$

By using Taylor series expansion, function *Y* can be written as:

$$f(x + \Delta x) = f(x) + \frac{\partial f}{\partial x}\Delta x \tag{4.66}$$

$$f(x - \Delta x) = f(x) - \frac{\partial f}{\partial x}\Delta x \tag{4.67}$$

$$\Delta f = \frac{f(x+\Delta x) - f(x-\Delta x)}{2} = \frac{\partial f(x)}{\partial x}\Delta x \tag{4.68}$$

where Δf is the error and $\Delta f / f$ is the relative error of the function *Y* indicating the uncertainty of the system. The relation between the uncertainty of the output function and uncertainty in the input variable can be expressed by:

$$\frac{\Delta f}{f} = CN_x \frac{\Delta x}{x} \tag{4.69}$$

$$CN_x = \frac{x}{f}\frac{\partial f(x)}{\partial x} \tag{4.70}$$

where CN_x is the sensitivity coefficient. Higher value of the sensitivity coefficient means that the input variable has a higher effect on the output function.

The total uncertainty of the system can be expressed by:

$$\frac{\Delta f}{f} = \sqrt{\sum_{i=1}^{N}\left(\frac{\Delta f(x_i)}{f(x_i)}\right)^2} \tag{4.71}$$

Sensitivity coefficients of the input variables in statistical correlations, developed in previous sections, for thermal efficiency of the analyzed power cycles are summarized in Table 4.10. Eqn. (4.70) is applied on the proposed correlations (Eqns. (4.6), (4.10), (4.16), (4.28), (4.32), (4.35), (4.49), (4.50), (4.59), (4.60)) developed in previous sections to obtain sensitivity coefficients in Table 4.10.

Table 4.10. Sensitivity coefficients of input parameters for the analyzed power cycles.

Cycle	η_t	η_c	ε_{reg}	T_{min}	T_{max}	T_{eva}	T_{cr}	C_p	C_{ps}	h_{fg}
Simple ORC-subcritical without superheat	1.00	0.00	0.00	-5.65	5.56	0.00	0.00	-0.12	0.00	0.12
Simple ORC-subcritical with superheat	1.00	0.00	0.00	-22.77	17.12	0.01	0.00	0.00	0.00	0.0002
Simple ORC-supercritical	1.00	0.00	0.00	-3.25	0.38	0.00	3.63	0.00	0.00	0.000
Regenerative ORC-subcritical without superheat	1.00	0.00	0.04	-5.83	5.83	0.00	0.00	0.00	0.00	0.000
Regenerative ORC-subcritical with superheat	1.00	0.00	0.21	-8.41	8.41	0.99	0.00	0.00	0.00	0.00
Regenerative ORC-supercritical	1.00	0.00	0.47	-15.34	18.40	0.00	-3.05	0.00	0.00	0.00
Simple Brayton-outside Critical Zone	4.32	2.83	0.00	-1.75	1.74	0.00	0.00	-0.01	0.00	0.00
Simple Brayton-inside Critical Zone	0.61	0.42	0.00	-0.13	0.004	0.00	0.00	-0.06	0.00	0.00
Regenerative Brayton-outside Critical Zone	4.11	3.00	0.11	-4.63	4.55	0.00	0.00	-0.005	0.00	0.00
Regenerative Brayton-inside Critical zone	0.51	0.42	0.45	-7.46	8.54	0.00	0.00	-0.05	0.00	0.00

As it can be seen in Table 4.10, for all analyzed power cycles, the maximum and minimum cycle temperatures have the largest effect on the thermal efficiency of the power cycle. Conversely, the latent heat of evaporation has the smallest effect on the thermal efficiency of the analyzed power cycles.

When using statistical correlations for thermal efficiency and other cycle performance parameters, developed in this work, the uncertainty of the final result can be affected by the following three uncertainties associated with the input parameters: the EPV-11 modeling code error, the error in thermo-physical properties of the working fluids calculated by the REFPROP code, and the error of the developed statistical correlations. The error in calculation of thermo-physical properties of the working fluids is less than 0.002 in the RFPROP code [81]. Also, the EPV-11 modeling code error is 0.001 [1]. Thus, the errors associated with the EPV-11 and REFPROP codes are approximately zero and can be neglected. Thus, the total uncertainty is predominately due to the errors associated with statistical correlations developed in this work.

The values obtained from the correlations (Eqns. (4.6), (4.10), (4.16), (4.28), (4.32), (4.35), (4.49), (4.50), (4.59), (4.60)) and the EPV-11 model are being referred to as $Pred(i)$ and $Real(i)$, respectively. The relative error of the correlation for a specific case is:

$$Relative\ error = RE = \frac{|Pred(i) - Real(i)|}{|Real(i)|} \tag{4.69}$$

The mean relative error (*MRE*) for the total number of *TN* cases is:

$$MRE = \frac{1}{TN}\sum_{i=1}^{TN}\frac{|Pred(i) - Real(i)|}{|Real(i)|} \tag{4.70}$$

where *i* is the case number. The standard deviation of the relative error (*SDRE*) can be defined by:

$$SDRE = \sqrt{\frac{\sum_{i=1}^{TN}(RE - MRE)^2}{TN-1}} \tag{4.71}$$

With a confidence interval (*CI*) of:

$$CI = MRE \pm t * \frac{SDRE}{\sqrt{TN}} \tag{4.72}$$

$$CI_{min} = MRE - t * \frac{SDRE}{\sqrt{TN}} \tag{4.73}$$

$$CI_{max} = MRE + t * \frac{SDRE}{\sqrt{TN}} \tag{4.74}$$

where quantity t is the Student t, equal to 2.576 for the confidence level of 99%. The relative standard deviation of the relative error (*SDRE*) is the ratio of *SDRE* over *MRE*.

The uncertainties of the proposed correlations for the analyzed power cycles are summarized in Table 4.11.

Table 4.11. Total uncertainty of proposed correlations for power cycles analyzed in this study.

Cycle	Number of Case studies(TN)	*MRE*	*SDRE*	CI_{min}	CI_{max}	*RSDERE*
Simple ORC-subcritical without superheat	10695	0.010	0.003	0.010	0.010	0.300
Simple ORC-subcritical with superheat	18216	0.039	0.005	0.039	0.040	0.128
Simple ORC-supercritical	14145	0.05	0.018	0.049	0.050	0.360
Regenerative ORC-subcritical without superheat	30225	0.005	0.001	0.005	0.005	0.200
Regenerative ORC-subcritical with superheat	51480	0.014	0.002	0.014	0.014	0.142
Regenerative ORC-supercritical	39975	0.010	0.003	0.010	0.010	0.300
Simple Brayton-outside Critical Zone	11368	0.035	0.010	0.035	0.035	0.285
Simple Brayton-inside Critical Zone	575	0.031	0.009	0.030	0.032	0.290
Regenerative Brayton-outside Critical Zone	55973	0.041	0.016	0.041	0.041	0.390
Regenerative Brayton-inside Critical Zone	921	0.043	0.013	0.042	0.044	0.302

Table 4-11 shows that correlation for a simple supercritical ORC has the highest mean relative error of around 5%. Conversely, the correlations developed for the regenerative ORCs are the most accurate.

CHAPTER 5: MODEL VALIDATION

5.1. Overview

In Chapter 5 thermodynamic models of the analyzed power cycles are validated by comparing the results obtained in this work to the experimental and numerical data from the open literature.

5.2. Validation of the Results for a Regenerative Steam Rankine Cycle with the Reheat

The values of thermal efficiency obtained by using the EPV-11 model of a single reheat regenerative steam Rankine cycle are compared to the results reported by [84]. Cycle parameters used in the calculations are summarized in Table 5.1. The maximum cycle pressure and temperature were varied between 10 and 30 MPa and from 500 to 1100°C, respectively.

Table 5.1. Cycle parameters for regenerative steam Rankine Cycle with reheat.

Cycle parameter	Value
Pump efficiency (HP)	0.85
Pump efficiency (LP)	0.85
Turbine efficiency (HP)	0.88
Turbine efficiency (LP)	0.917
P, loss, receiver (%)	5
P, loss, HEX (%)	5
Condenser back pressure at saturation point	0.00476

The effect of turbine inlet temperature on thermal efficiency is shown in Figure 5.1. As the figure shows, the results obtained from the EPV-11 cycle models are in an excellent agreement with the results from [84]; with the average relative error of 0.8%. As expected, the results show that higher maximum pressure results in a higher thermal efficiency; increasing the maximum pressure form 10 to 30MPa results in a 2.8%-point increase in thermal efficiency.

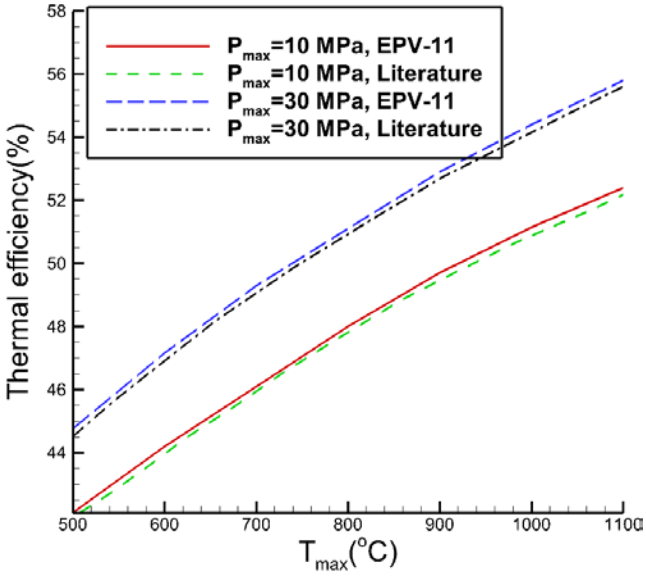

Figure 5.1. Effect of turbine inlet temperature on thermal efficiency of a regenerative steam Rankine Cycle with reheat.

5.3. Validation of the Results for a Regenerative ORC

5.3.1. Subcritical ORC without the superheat

Values of thermal efficiency obtained by using the EPV-11 model of the regenerative ORC and a correlation developed in Section 4.2.2 in Chapter 4, represented by Eqn. (4.28), were compared to the results reported by Wang et al. [105]. The cycle parameters used in the calculations are summarized in Table 5.2. The temperature difference between the TIT and the heat source temperature of 10°C was used in the calculations.

Table 5.2. Cycle parameters for regenerative ORC.

Parameter	Value
Maximum pressure, P_4 (MPa)	Saturation pressure at minimum temperature
Turbine isentropic efficiency, η_t	0.8
Pump isentropic efficiency	0.9
Regenerator effectiveness	0.55
Minimum pressure (MPa)	Saturation pressure at minimum temperature

Wang et al. [105] analyzed simple and regenerative ORC having the net power output of 10 kW by using a custom-written Matlab code. Physical properties of the working fluids were provided by the REFPROP code developed by NIST. The results obtained by Wang et al. [105] and in this study for seven working fluids are compared in Table 5.3.

Table 5.3. Comparison of results for a subcritical regenerative ORC without superheat.

Fluid	P_{max} (MPa)	T_{max} (K)	T_{min} (K)	P_{min} (MPa)	Mass flow rate (kg/s)	Thermal Efficiency from [105] (%)	Thermal Efficiency from EPV-11 Model	Thermal Efficiency from Eqn. (4.28)	Relative Error Between [105] and EPV-11 Model (%)	Relative Error Between [105] and Eqn. (4.28) (%)
R245fa	1.4923	380.90	304.44	0.1874	0.498	9.51	9.44	9.45	0.73	0.68
R245ca	1.4923	395.05	315.56	0.1882	0.481	9.61	9.62	9.55	0.10	0.62
R236ea	1.7231	377.51	300.00	0.2196	0.597	9.55	9.52	9.64	0.31	1.01
R114	1.8154	385.81	300.00	0.2275	0.672	10.22	10.22	10.29	0.00	0.68
R113	1.7692	444.74	346.67	0.2223	0.619	10.35	10.34	10.32	0.09	0.27
Butane	2.0000	387.51	300.00	0.2580	0.233	10.46	10.43	10.5	0.28	0.38
R123	1.5385	406.00	320.00	0.1926	0.545	10.00	9.98	9.94	0.20	0.60

As shown in Table 5.3, thermal efficiency values obtained by the EPV-11 model and the correlation for a subcritical ORC without a superheat, represented by Eqn. (4.28), are in an excellent agreement with the results from Wang et al. [105]. The relative error between the results obtained from Eqn. (4.28) and by Wang et al. [105] is in the 0.27 and 1.01% range. The relative error between the results obtained by the EPV-11 model and Wang et al. [105] is in the 0.00 to 0.73% range.

5.3.2. Subcritical ORC with the superheat

Values of thermal efficiency obtained by using the EPV-11 model of a regenerative ORC, and the correlation developed in Section 4.2.2 in Chapter 4, represented by Eqn. (4.32), were compared to the results reported by Peris et al. [117]. Peris designed, built, and tested a regenerative ORC operating in a superheated subcritical region using R245fa. The reported experimental uncertainty in thermal efficiency for the net power output in the

6.85 to 16.93kW range is ±4.55%. The comparison of thermal efficiency values reported by Peris at al., Ref. [117] and calculated in this study by using the EPV-11 model of the cycle and Eqn. (4.32) is presented in Table 5.4 over a range of cycle operating conditions.

Table 5.4. Comparison of results for a subcritical regenerative ORC with superheat.

	P_{max} (MPa)	T_{max} (K)	P_{min} (MPa)	Mass flow rate(kg/s)	Thermal Efficiency from [117](%)	Thermal Efficiency from EPV-11 model	Thermal Efficiency from Eqn. (4.32)	Relative error Between [117] and EPV-11 model(%)	Relative error Between [117] and Eqn. (4.32) (%)
1	1.41	395.42	0.25	0.39	7.16	7.30	7.33	2.02	2.44
2	1.63	402.99	0.26	0.47	8.38	8.69	8.61	3.74	2.79
3	1.76	406.54	0.26	0.52	9.00	9.37	9.30	4.09	3.31
4	1.90	410.03	0.27	0.58	9.94	10.34	10.25	3.99	3.08
5	1.94	411.03	0.26	0.59	10.00	10.49	10.42	4.90	4.21
6	1.96	411.26	0.25	0.60	10.49	10.97	10.77	4.59	2.71
7	2.01	412.55	0.23	0.62	10.83	11.20	11.25	3.47	3.91
8	2.03	413.12	0.23	0.64	10.90	11.35	11.30	4.12	3.66

Considering experimental uncertainty of ±4.55%, results obtained from the EPV-11 model and Eqn. (4.32) are in a very good agreement with the results from Peris at al. [117]. The relative error between the results obtained from Eqn. (4.32) and Ref. [117] is in the 2.44% to 4.21% range, while the relative error between the results from EPV-11 model and Ref. [117] is in the 2.02% to 4.90% range.

5.4. Validation of the Results for a Simple Brayton Cycle

Values of thermal efficiency obtained by using the EPV-11 model of a simple Brayton cycle were compared to the results reported by Ho et al. [89]. Cycle parameters used in the calculations are summarized in Table 5.5. The temperature difference between the TIT and the heat source temperature of 25°C,assumed in Ref. [89], was used in the calculations.

Table 5.5. Cycle parameters for a simple Brayton cycle.

Parameter	Value
Maximum temperature(°C)	700
Maximum pressure, (MPa)	20
Turbine isentropic efficiency, η_t	0.9
Compressor isentropic efficiency	0.9
Minimum pressure (MPa)	6.4

A simple CO_2 Brayton cycle having the net power output of 100 MW was analyzed in Ref. [89]. Table 5.6 compares the results for CO_2 as the working fluid obtained by using the EPV-11 model of a simple Brayton cycle to the results reported in Ref. [89].

Table 5.6. Comparison of results for simple Brayton cycle.

Thermal Efficiency from [89](%)	Thermal Efficiency from EPV-11 Model	Relative Error Between [89] and EPV-11 Model (%)
16	15.8	0.6

As shown in Table 5.6, thermal efficiency value obtained by the EPV-11 model is in an excellent agreement with the results from [89]. The relative error between the results is 0.6%.

5.5. Validation of the Results for a Regenerative Brayton Cycle

Thermal performance of a regenerative supercritical CO_2 Brayton cycle determined by using the EPV-11 model of the cycle is validated in this section. Table 5.7 presents the cycle parameters used in the calculations. A pressure drop of 3.5% of the inlet pressure was set for the heat addition and rejection processes. The net power output was kept constant at 100MW.

Table 5.7. Cycle parameters for a regenerative supercritical Brayton cycle.

Parameter	Value
Minimum pressure (MPa)	8.5
Turbine isentropic efficiency, η_t	0.55
Pump isentropic efficiency, η_c	0.8
Minimum temperature (°C)	34.85

The results were validated against the study [64] where a regenerative Brayton cycle was modeled by using a Matlab code, while thermo-physical properties of the working fluid were determined by the REFPROP code [64]. Figure 5.2 shows the effect of the turbine inlet temperature on thermal efficiency at the optimum pressure ratio. As it can be seen in Figure 5.2, the results obtained from the EPV-11 model are in an excellent agreement with the results from [64]; the relative error is 0.95%.

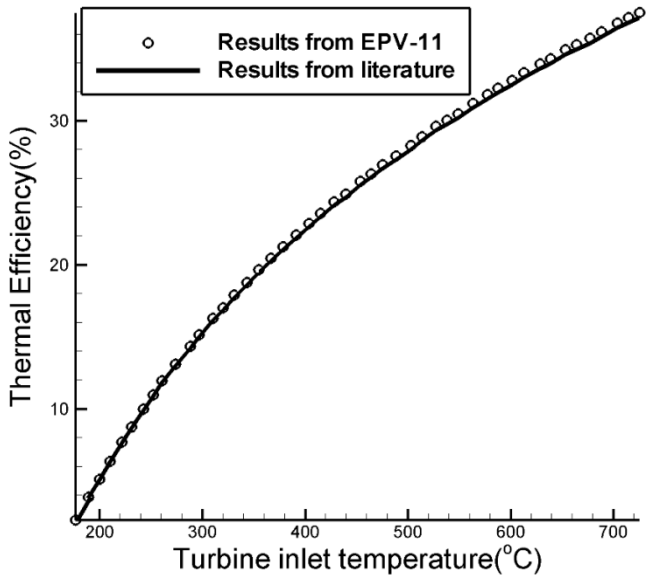

Figure 5.2. The effect of turbine inlet temperature on thermal efficiency of a regenerative Brayton cycle.

5.6. Validation of the results for a regenerative Brayton cycle with intercooling

A regenerative CO_2 Brayton cycle with one intercooling section (intercooler), shown in Figure 5.3, is analyzed in this section. For the highest thermal efficiency of the

cycle, the compression ratios of the LP and HP compressors have to be the same [84]. Thus, the pressure at State Point 3 is:

$$P_3 = \frac{P_{loss,HEX} + \sqrt{4P_1P_2 - (P_{loss,HEX})^2}}{2P_1} \quad (5.1)$$

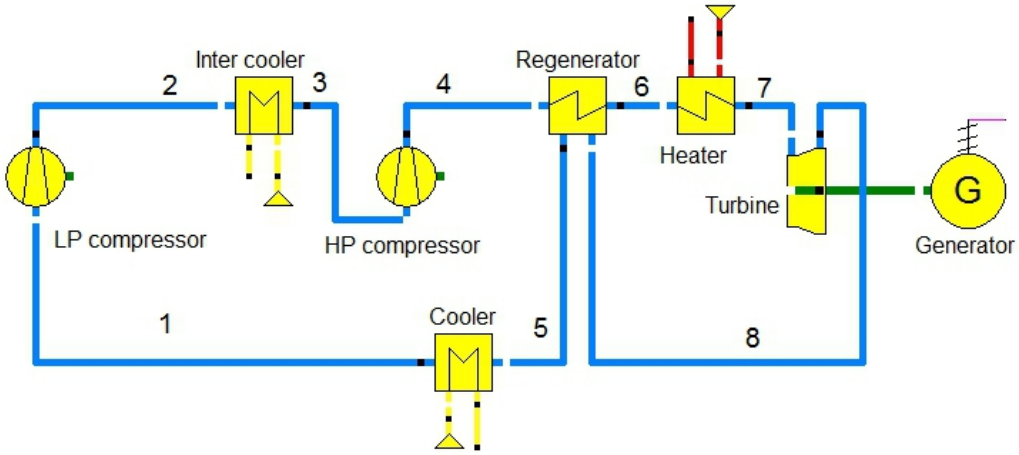

Figure 5.3. Schematic of a regenerative CO_2 Brayton cycle with intercooling.

Table 5.8 presents the cycle parameters used in the calculations. It should be noted that maximum temperature of 1100°C is not feasible with the current available materials and data from Table 5.8 is just used for validation. The results obtained from the EPV-11 model of the cycle developed in this study are compared to the results form Ref. [84].

Table 5.8. Cycle parameters for a regenerative supercritical CO_2 Brayton cycle with intercooling.

Cycle parameter	Value
Minimum Temperature(°C)	32
Maximum pressure (MPa)	10-30
Maximum Temperature(°C)	500-1100
Compressor efficiency	0.8
Turbine Efficiency	0.9
Regeneration effectiveness	0.85
P, loss, receiver (%)	5
P, loss, HEX (MPa)	0.05
Pinch point difference for ambient heat exchangers (°C)	10

Figure 5.4A shows the effect of the maximum cycle temperature on thermal efficiency of the analyzed power cycle. As the figure shows , the results obtained from the EPV-11 model are in an excellent agreement with the results from [84].

Also, as Figure 5.4A shows, for the maximum cycle temperature equal to 500°C and the maximum cycle pressure higher than 20 MPa, thermal efficiency is considerably higher compared to the case where maximum cycle pressure is lower than 20 MPa. This can be explained by the "liquid-like" behavior of CO_2 at the compressor inlet. For the maximum cycle temperature of 500°C and maximum cycle pressure higher than 20MPa, the compressor inlet is located in the "liquid-like" zone where density is high, resulting in a low compressor work and high thermal efficiency. As the maximum cycle pressure is increased, CO_2 density increases resulting in a further reduction in the compressor work, and an increase in cycle efficiency. More details can be found in Chapter 4.

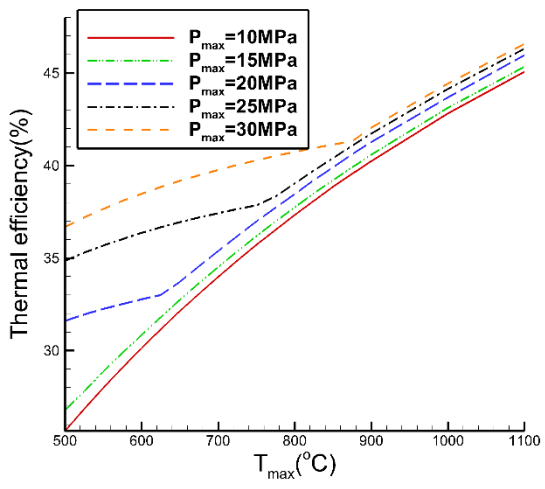

A) Thermal efficiency at different maximum pressures.

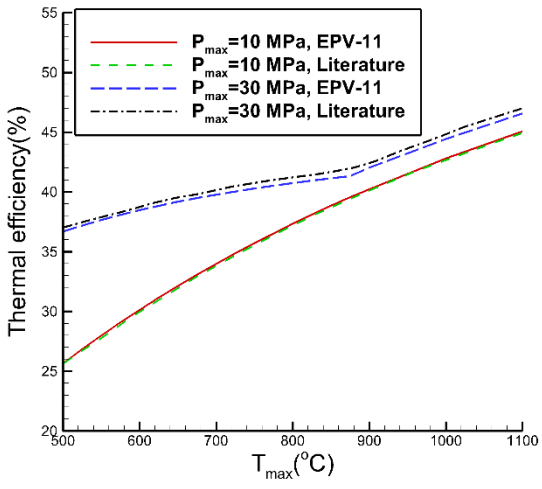

B) Compression of results from EPV-11 and results from Literature.

Figure 5.4. The effect of maximum temperature on thermal efficiency of a regenerative Brayton cycle with intercooling.

CHAPTER 6: POWER CYCLE SELECTION FOR THE CSP-T PLANTS

6.1. Overview

One of the main objectives of this study is selection of the preferred (best) power cycle(s) for the given set of cycle operating conditions. The effect of operating conditions on performance of the power cycles analyzed in this work is presented in this chapter. The best power cycle(s) having the highest thermal efficiency or highest net power output for a specified (selected) set of operating conditions have been identified. The results from Chapter 4 were used to select the best working fluid resulting in the highest thermal efficiency or highest specific net work output.

6.2. Cycle configurations and operating parameters

The results of thermal performance analysis of the following power cycles are presented and compared in this chapter: regenerative steam Rankine cycle with the reheat, regenerative Brayton cycle, recompression Brayton cycle, combined Brayton/ORC cycle, and combined Rankine/ORC cycle. A review of the cycle operating parameters used in the calculations is presented first.

The analysis of the cycle performance was performed by assuming the temperature difference between the turbine inlet temperature (TIT) and the heat source temperature of 10°C; the minimum cycle temperature was varied between 32 and 62°C. The selection of working fluid(s) and correlations for thermal efficiency of different power cycles were presented in Chapter 4. The friction and heat losses in the connecting pipes were neglected, and turbomachinery (turbine, feed pumps, and compressors) was assumed to be adiabatic. However, the friction and pressure drop in the heat exchangers were considered in

performance calculations. Other cycle parameters, used in the analysis, are summarized in Tables 6.1 to 6.6.

6.2.1. Simple ORC

A schematic representation of the analyzed simple ORC is presented in Figure 4.1. The cycle parameters used in the calculations are summarized in Table 6.1. The maximum cycle temperature was varied between 50 to 350°C. For the values of maximum cycle temperature lower than the critical temperature of the working fluid, the maximum cycle pressure was set to be equal to the saturation pressure corresponding to the maximum temperature. For a transcritical ORC, the maximum cycle pressure was set to be equal to the critical pressure of the working fluid.

Since the performance of an ORC depends on the physical properties of the working fluid, a careful selection of the appropriate working fluid is essential for the best performance. As presented in Chapter 4, working fluids such as R141b and Butane give the highest thermal efficiency and the highest specific net work output, respectively. Therefore, performance results obtained for R141b and Butane are presented in this chapter. Thermo-physical properties of R141b and Butane are listed in Table 3.1.

Table 6.1. Simple ORC parameters.

Power cycle parameter	**Value**
Maximum temperature, T_2 (°C)	50 to 350
Maximum pressure, P_1 (MPa)	Saturation or critical
$P_{loss,\ evaporator}$ (%)	5
Pump isentropic efficiency	0.80
Turbine isentropic efficiency	0.87

6.2.2. Regenerative Brayton cycle (RBC)

A schematic representation of the analyzed regenerative Brayton cycle is presented in Figure 4.29. The cycle parameters used in the calculations are summarized in Table 6.2. The performance results presented here are given for the optimal pressure ratio, which gives the highest specific net work output. The maximum cycle temperature and pressure were varied between 200 to 1000°C and 10 to 30MPa, respectively. Based on the results presented in Chapter 4, the performance results obtained for CO_2 and He, giving the highest efficiency and highest net specific power output, are presented here. Thermo-physical properties of CO_2 and He are listed in Table 3.2. Since the critical point of CO_2 is within the investigated temperature and pressure ranges, the analysis includes the results for the supercritical CO_2 (sCO_2) Brayton cycle.

Table 6.2. RBC parameters.

Power cycle parameter	**Value for CO_2**	**Value for He**
Maximum temperature, T_4 (°C)	200 to 1000	200 to 1000
Maximum pressure, P_2 (MPa)	10, 30	10, 30
Turbine isentropic efficiency	0.90	0.93
compressor isentropic efficiency	0.80	0.859
Regenerator effectiveness	0.956	0.85
$P_{loss,\ evaporator}$ (%)	5	5

6.2.3. Regenerative Brayton cycle with recompression (RBCR)

A schematic representation of the analyzed regenerative Brayton cycle with recompression is presented in Figure 4.36. The cycle parameters used in the calculations are summarized in Table 6.3. The maximum cycle temperature and pressure, and working fluids are the same as used for the regenerative Brayton cycle.

Table 6.3. RBCR parameters.

Power cycle parameter	Value for CO_2	Value for He
Maximum temperature, T_4 (°C)	200 to 1000	200 to 1000
Maximum pressure, P_2 (MPa)	10, 30	10, 30
Turbine isentropic efficiency	0.90	0.93
compressor isentropic efficiency	0.89	0.89
HT Regenerator effectiveness	0.976	0.87
LT Regenerator effectiveness	0.88	0.85
$P_{loss,\ evaporator}$ (%)	5	5

6.2.4. Combined Brayton/ORC cycle

A schematic representation of the analyzed regenerative Brayton cycle with recompression is presented in Figure 4.40. The cycle parameters used in the calculations are summarized in Table 6.4. As described in Section 4.6 of Chapter 4, the performance results presented here are for the optimal pressure ratio of the topping cycle, corresponding to the maximum cycle net work output, and for a constant gross power output of 100MW for the topping cycle. The maximum cycle temperature and pressure were varied between 200 to 1000°C and 10 and 30 MPa, respectively.

Table 6.4. Combined Brayton/ORC cycle parameters.

Power cycle parameter	Value
Maximum temperature, T_4 (°C)	200 to 1000
Rankine cycle maximum pressure, P_4 (MPa)	10, 30
Turbine isentropic efficiency	0.90
Regenerator effectiveness	0.85
Compressor isentropic efficiency	0.80
ORC turbine isentropic efficiency	0.87
Feed pump isentropic efficiency	0.80
$P_{loss,\ evaporator}$ (%)	5
P_{11}(MPa), if $T_{11}>T_{Critical}$	$P_{Critical}$
P_{11}(MPa), if $T_{11}<T_{Critical}$	$P_{Saturation}$

Based on the results presented in Chapter 4, the performance results for the combined cycle using air or CO_2 as working fluids in the topping cycle, and Iso-butane, R11, and Ethanol as the working fluids in the bottoming (ORC) are presented here.

6.2.5. Regenerative steam Rankine Cycle with the reheat (RSRC)

A schematic representation of the analyzed regenerative steam Rankine cycle with the reheat is presented in Figure 4.45. The cycle parameters used in the modeling and for performance calculations are summarized in Table 6.5. As discussed in Section 4.7 of Chapter 4, for each main steam temperature and pressure combination, the performance analysis was performed over a range of feedwater pressures to determine the optimal $\dot{m}_5/\dot{m}_8$ flow split giving the highest thermal efficiency. The maximum steam temperature and pressure were varied from 200 to 650°C and 10 and 30 MPa, respectively. The critical temperature and pressure of the steam are 374.15°C and 22.1 MPa respectively, thus, the analysis covers the subcritical and transcritical (supercritical) operating conditions.

Table 6.5. Regenerative steam Rankine cycle with reheat parameters.

Power cycle parameter	**Value**
Maximum temperature, T_9, T_5 (°C)	200 to 650
Maximum pressure, P_4 (MPa)	10, 30
$P_{loss,\ feedwater\ heater}$ (%)	5
$P_{loss,\ evaporator}$ (%)	5
HP and LP feed pump isentropic efficiency	0.85
HP turbine isentropic efficiency	0.88
LP turbine isentropic efficiency	0.917

6.2.6. Combined Rankine/ORC cycle

A schematic representation of the analyzed combined Rankine/ORC cycle is presented in Figure 4.50, where an RSRC was selected as a topping cycle, while a simple ORC was used as a bottoming cycle. The cycle parameters used in the calculations are

summarized in Table 6.6. As discussed in Section 4.8 of Chapter 4, since the flow rates of these two cycles vary with respect to each other, the gross power output of 100MW was assumed for the topping cycle. Also, the difference between the topping cycle exhaust temperature and the maximum temperature of the bottoming ORC of 3°C was used in the calculations.

Based on the results presented in Chapter 4, the performance results for Iso-butane as a working fluid in the bottoming cycle are presented here. The thermo-physical properties of Iso-butane are listed in Table 3.1. The maximum temperature and pressure of the topping cycle were varied between 200 to 650°C, and 10 and 30 MPa, respectively.

Table 6.6. Combined Rankine/ORC cycle parameters.

Power cycle parameter	**Value**
Maximum temperature, T_9, T_5 (°C)	200 to 650
Rankine cycle maximum pressure, P_4 (MPa)	10, 30
Rankine HP turbine isentropic efficiency	0.88
Rankine LP turbine isentropic efficiency	0.917
ORC turbine isentropic efficiency	0.87
All Pumps isentropic efficiency	0.85
$P_{loss,\ evaporator}$ (%)	5
P_{14}(MPa), if $T_{11}>T_{Critical}$	$P_{Critical}$
P_{14}(MPa), if $T_{11}<T_{Critical}$	$P_{Saturation}$

6.3. Results and Discussion

As discussed in Section 2.1 of Chapter 2, thermal performance of the analyzed power cycles was determined by using detailed EPV-11 models of each cycle. The results of the parametric calculations, performed over a range of operating conditions, are presented in this section.

6.3.1. Thermal efficiency

The effect of the maximum and minimum cycle temperatures on thermal efficiency of the six analyzed power cycles is presented in Figure 6.1 and 6.3 for P_{max}=10 and 30 MPa. Because of the upper temperature limit (see Sections 4.1 and 4.7 in Chapter 4) for some power cycles such as RSRC and ORC, calculations were performed for lower maximum cycle temperature.

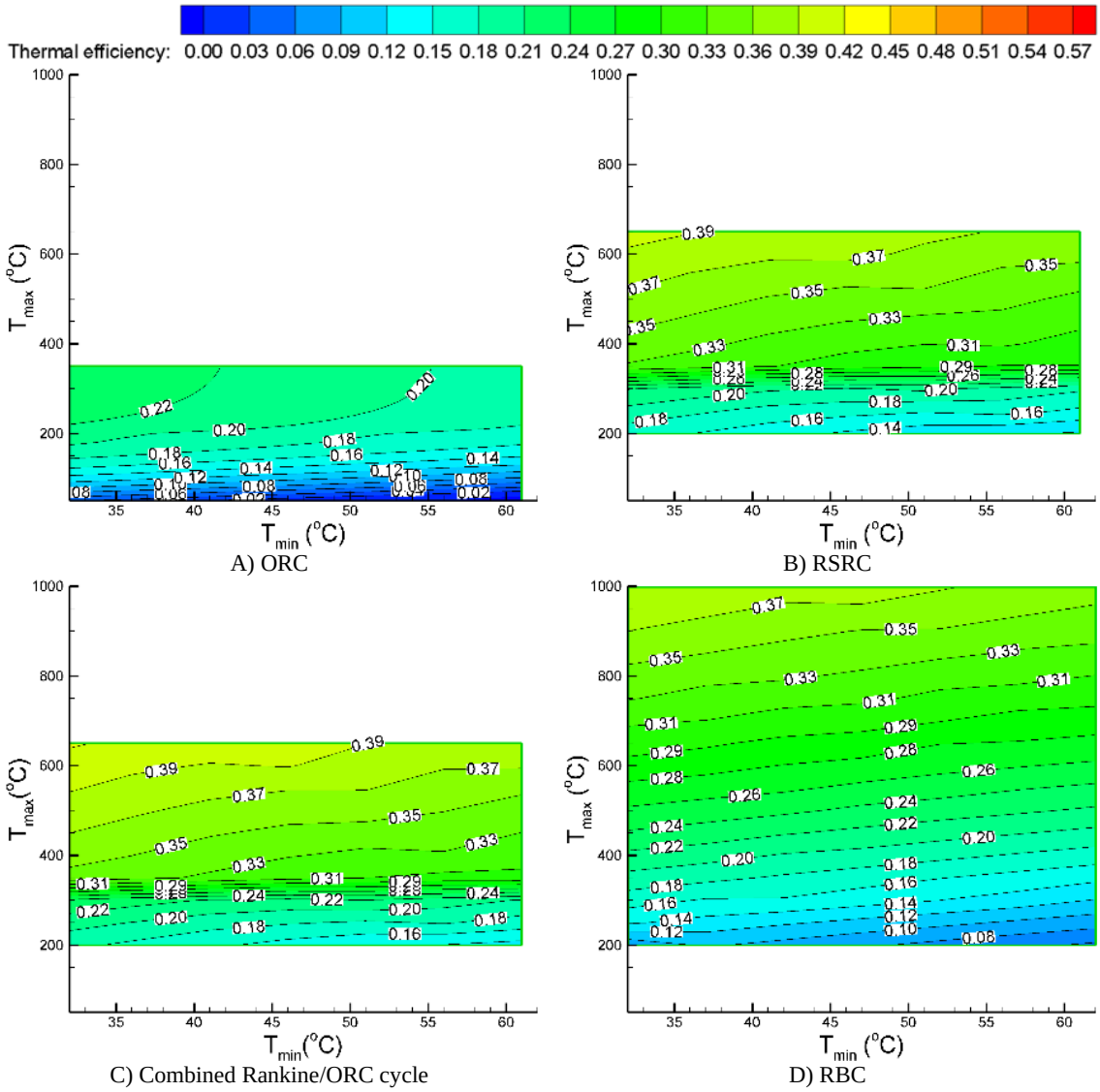

Figure 6.1. Thermal efficiency of the analyzed power cycles P_{max} = 10 MPa.

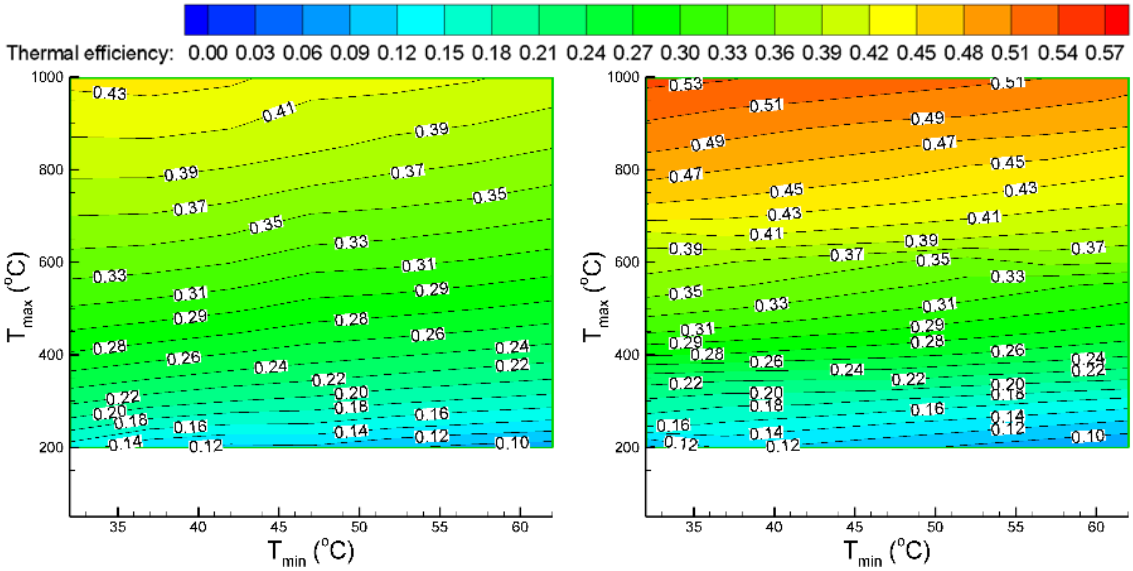

E) RBCR F) Combined Brayton/ORC cycle

Figure 6.1. Continued.

As the results presented in Figure 6.1 show, for the maximum cycle temperature lower than 300°C, the ORC has the highest thermal efficiency. Also, thermal efficiency of a subcritical ORC (T_{max}<200°C) is more sensitive to the maximum cycle temperature compared to a transcritical ORC (T_{max}>200°C). For the maximum temperature and pressure, and the minimum temperature ranges selected in this study, the highest thermal efficiency of the ORC is 23%.

Other power cycles can be employed for the medium maximum cycle temperature operation. Although, a combined Rankine/ORC cycle has the highest thermal efficiency for the maximum cycle temperature in the 300 to 650°C range, the difference with respect to a RSRC is less than 2%-points. As discussed in Section 4.7 of Chapter 4, due to a very low cycle exhaust temperature of the steam Rankine cycle, there is very little performance benefit of employing a bottoming cycle. Also, the capital investment for a combined cycle is higher, compared to a simple cycle. Thus, considering the performance and cost, it can

be concluded that for the medium temperature range, a single RSRC is the best choice. However, for the maximum cycle temperature of 600°C and the minimum temperature of 32°C, a combined Rankine/ORC cycle has thermal efficiency of 40%; 2%-points higher compared to a single RSRC cycle.

To make an objective and impartial selection of the best power cycle, a techno-economic analysis is needed to determine cost metrics, such as the investment cost and levelized cost of electricity (LCOE) which, everything else being equal, could be used to select the best power cycle. Techno-economic analysis and its results are presented in Chapter 7.

For the maximum cycle temperature higher than 650°C, a regenerative Brayton cycle without or with recompression (RBC), or a combined Brayton/ORC cycle can be used. Since the cycle exhaust temperature of a RBC is much higher compared to the steam Rankine cycle, the rejected heat can be efficiently recovered by an ORC, resulting in an increase in thermal efficiency of the combined cycle by up to 14%-points, compared to a simple Brayton cycle. Figure 6.2 shows that for the maximum and minimum cycle temperatures of 1000°C and 32°C, respectively, the combined Brayton/ORC cycle has the highest thermal efficiency (53%), compared to the other analyzed power cycles.

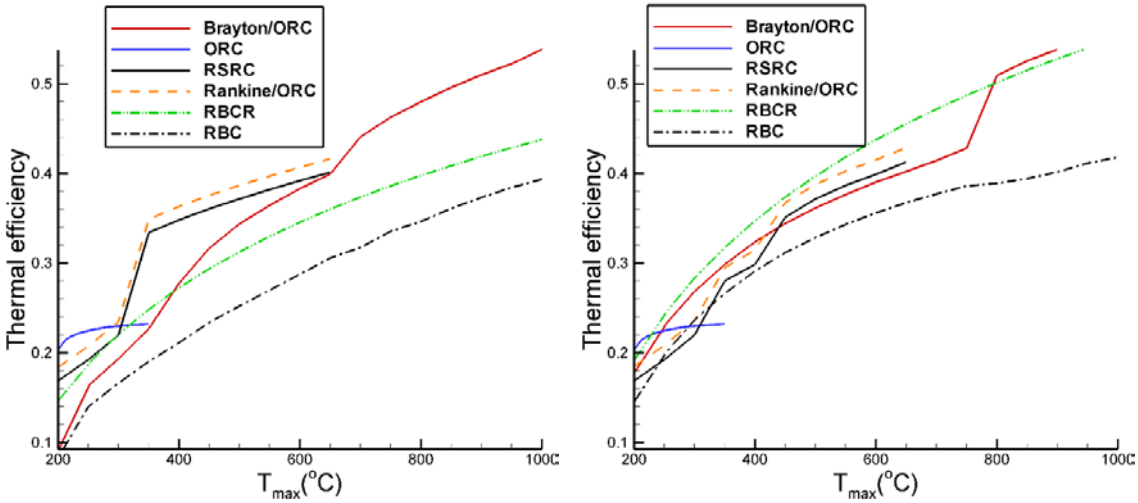

A) P_{max}=10 MPa B) P_{max}=30 MPa

Figure 6.2. Thermal efficiency of the analyzed power cycles at T_{min}=32°C.

Figure 6.2A shows thermal efficiency of the six analyzed power cycles for T_{min}=32°C and P_{max}=10 MPa. As the results show, efficiency of an ORC is the highest for the maximum cycle temperature up to 300°C. For the mid-temperature range, from 300 to 650°C, a combined Rankine/ORC has the highest efficiency (marginally higher than a RSRC). For the high-temperature range, i.e., the maximum cycle temperature higher than 650°C, efficiency of a combined Brayton /ORC cycle is the highest.

As it can be seen in Figure 6.2, there is a step change in thermal efficiency of a combined Brayton/ORC cycle for T_{max}=750°C and P_{max}= 30MPa. This step change is due to the change of the working fluid in a bottoming ORC; at T_{max}=750°C, R11 was changed to Ethanol to improve thermal efficiency. Also, the change of the working fluid from Iso-butane to R11 at T_{max}=650°C and P_{max}=10 MPa results in a slight step change in thermal efficiency of a combined Brayton/ORC cycle. More details can be found in Section 4.6 of Chapter 4.

The results for thermal efficiency corresponding to the maximum cycle pressure of 30MPa are shown in Figure 6.3.

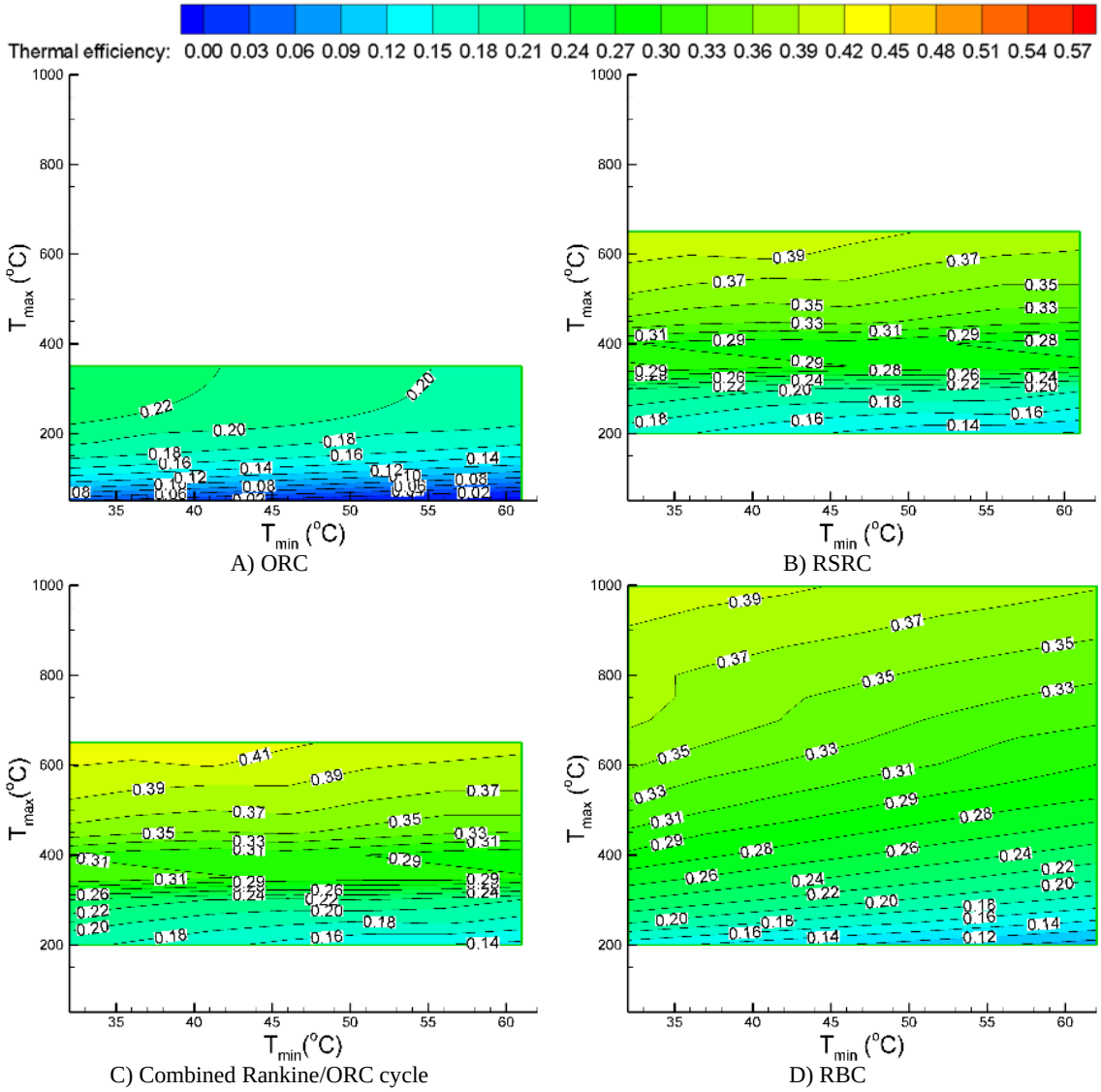

Figure 6.3. Thermal efficiency of the six analyzed power cycles for P_{max} = 30 MPa.

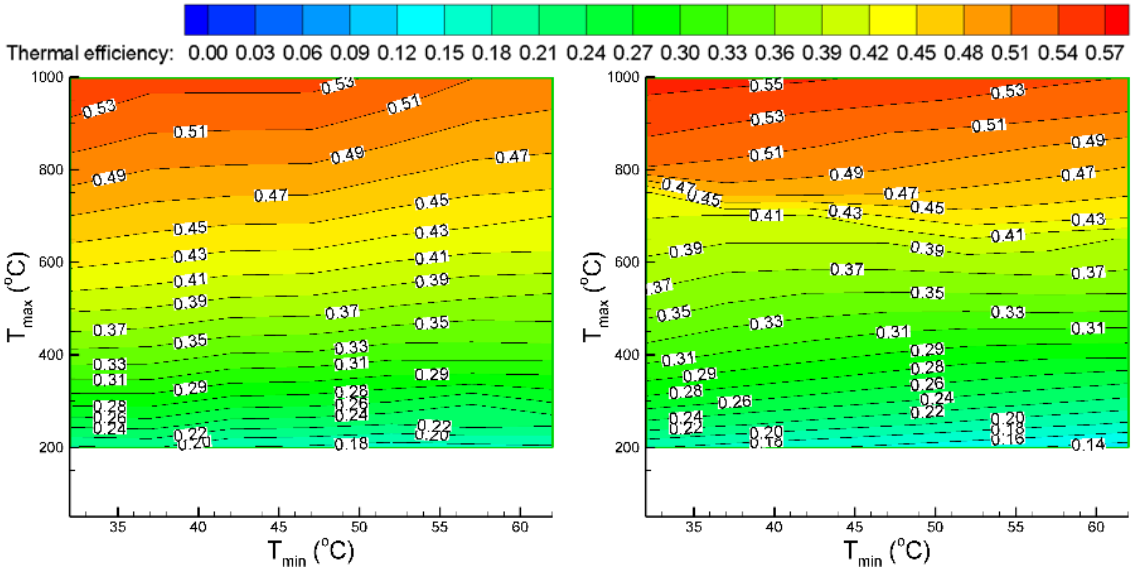

E) RBCR F) Combined Brayton/ORC cycle

Figure 6.3. Continued.

As the figure shows, thermal efficiency of a CO_2 RBCR is higher compared to the other analyzed cycles. Also, it is considerably higher compared to the same cycle operating at P_{max} = 10 MPa. For the maximum cycle pressure of 30 MPa, the compressor inlet is in a "liquid like" region near the critical point of CO_2 and the compressor work is greatly reduced as discussed in Section 4.3.2 of Chapter 4, resulting in higher thermal efficiency.

For the low maximum temperature applications, an ORC is the best option; while for the medium and high-temperature applications, a combined Brayton/ORC cycle, followed by a RBCR has the highest efficiency. For T_{max}=1000°C, P_{max}=30 MPa, and T_{min}= 32°C, a combined Brayton/ORC cycle has the highest thermal efficiency (56%); 3%-points higher compared to the maximum cycle pressure of 10MPa.

Thermal efficiency of the six analyzed power cycles for T_{min}=32°C and P_{max}=30 MPa is shown in Figure 6.2B. As the results show, efficiency of an ORC is the highest for the maximum cycle temperature up to 200°C. For the mid-temperature range from 200 to

800°C, the RBCR has the highest efficiency. For the high-temperature range, i.e., the maximum cycle temperature higher than 800°C, efficiency of a combined Brayton /ORC cycle is the highest.

6.3.2. Specific net work output

The results concerning the specific net power output of the six analyzed power cycles for the range of the cycle minimum and maximum temperatures, and the maximum cycle pressure P_{max} = 10 and 30 MPa are presented in Figures 6.4 and 6.5, respectively. As Figure 6.4 shows, for the low and medium maximum cycle temperatures, RSRC gives the highest specific net work output, followed by a combined Brayton/ORC cycle using Helium as the working fluid in the topping cycle and R11 in the bottoming ORC. For the maximum cycle temperature higher than 650°C, a combined Brayton/ORC cycle using Helium as the working fluid in the topping cycle and Ethanol in the bottoming ORC is giving the highest specific net work output.

For the medium temperature range, i.e., TIT (T_{max}) below 600°C, an RSRC produces the specific net work output higher than 1472 kJ/kg, while for the same conditions the combined Brayton/ORC cycle using Helium as the working fluid in the topping cycle produces the net power output between 384 and 416 kJ/kg. However, in the high temperature range, i.e., TIT of 1000°C, a combined Brayton/ORC cycle using Helium as the working fluid in the topping cycle and Ethanol in the bottoming ORC produces the net power output between 1024 and 1152 kJ/kg; 320 kJ/kg higher compared to a regenerative CO_2 Brayton cycle with recompression (RBCR).

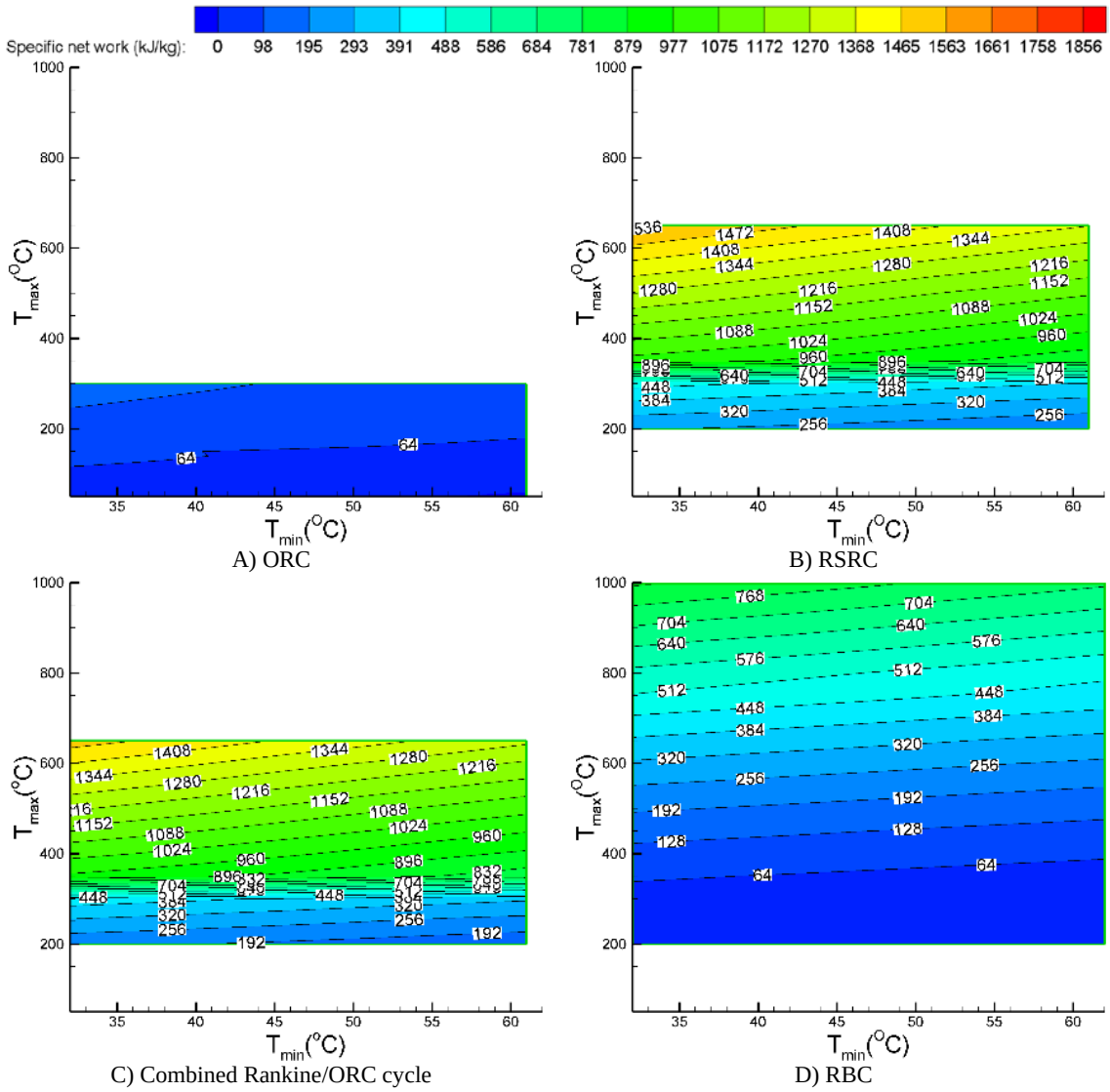

Figure 6.4. Specific net work output of the six analyzed power cycles for P_{max} = 10 MPa.

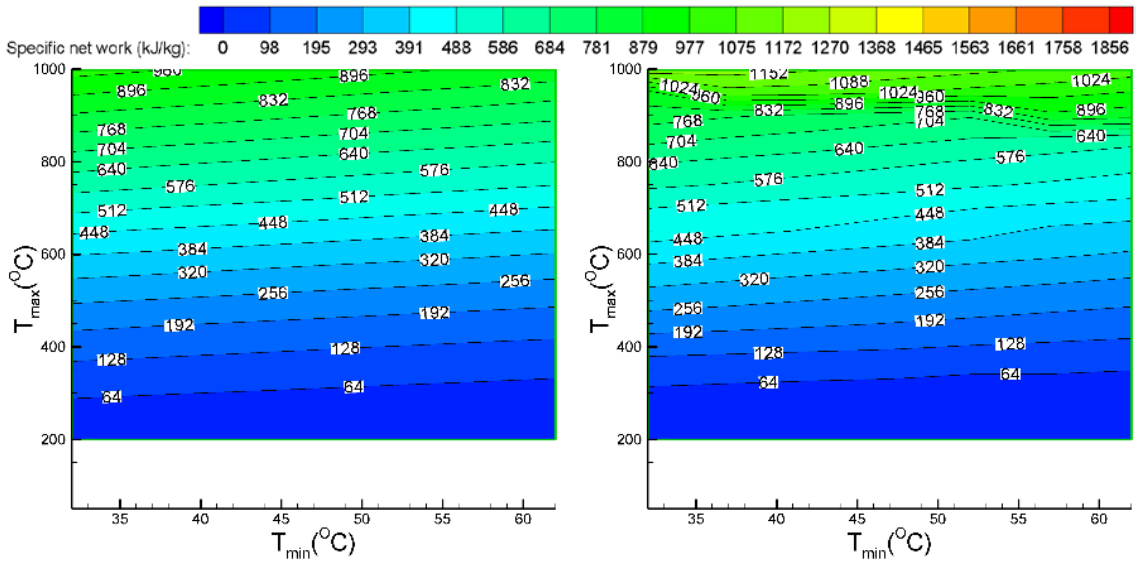

E) RBCR F) Combined Brayton/ORC cycle

Figure 6.4. Continued.

The effect of the operating conditions on the specific net work output of the six analyzed power cycles for P_{max}=30 MPa is presented in Figure 6.5. As the results show, RSRC is the best cycle for the low and medium temperature applications, while for the maximum temperature higher than 650°C a combined Brayton/ORC cycle using Helium as the working fluid in the topping cycle and Ethanol in the bottoming ORC is the best power cycle giving the highest specific net work output.

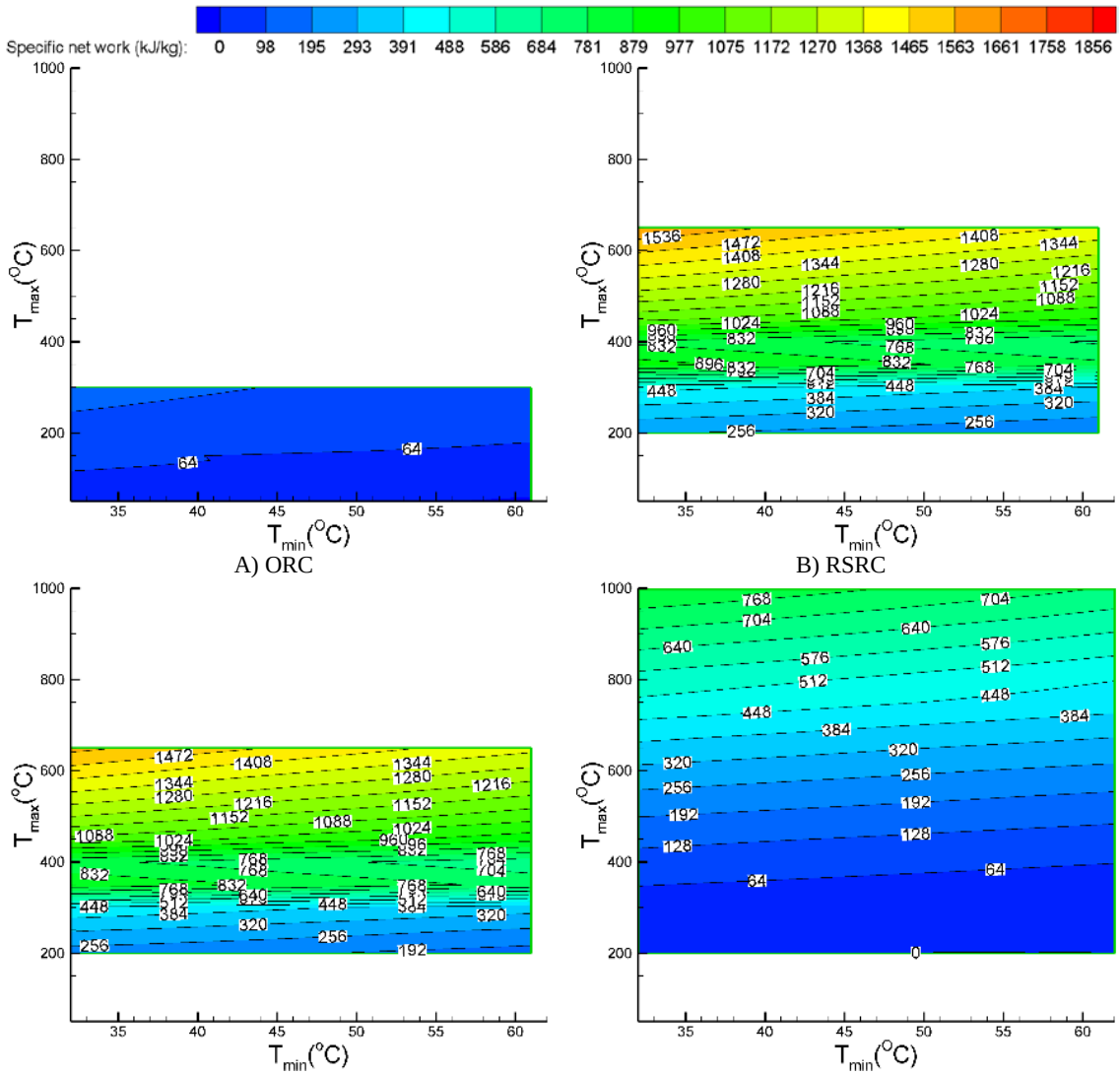

Figure 6.5. Specific net work output of the six analyzed power cycles for P_{max} = 30 MPa.

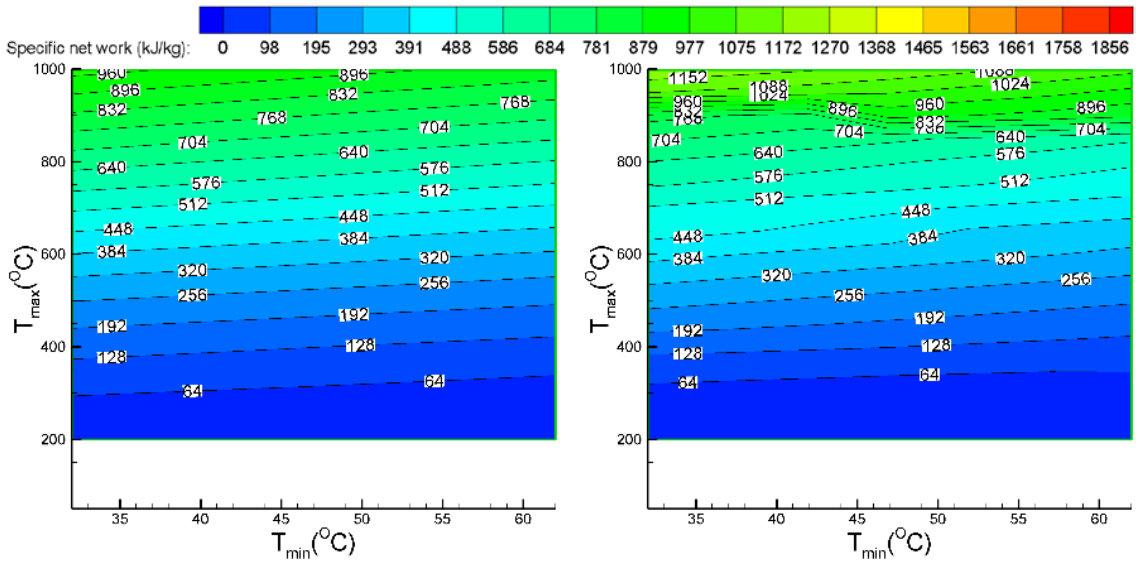

E) RBCR F) Combined Brayton/ORC cycle

Figure 6.5. Continued.

As mentioned before, selection of the preferred (best) power cycle(s) for the given set of cycle operating conditions is one of the main objectives of this study. The performance maps for thermal efficiency and specific net work output were constructed to enable selection of the best power cycle for the given set of cycle operating conditions (maximum pressure and temperature).

The performance map for thermal efficiency presented in Figure 6.6A shows that for the high maximum cycle temperature applications, a combined Brayton/ORC cycle is the best choice. For the medium maximum cycle temperature applications, depending on the maximum cycle pressure, either a combined Rankine/ORC cycle or a RBCR give the highest thermal efficiency.

The performance map for the net work output presented in Figure 6.6B shows that for the maximum temperature higher than 650°C, a combined Brayton/ORC cycle using Helium and Ethanol as the working fluids in the topping and bottoming cycles, respectively, is the

best option for producing the highest power output. For the low and medium maximum temperature applications, a RSRC gives the highest net power output.

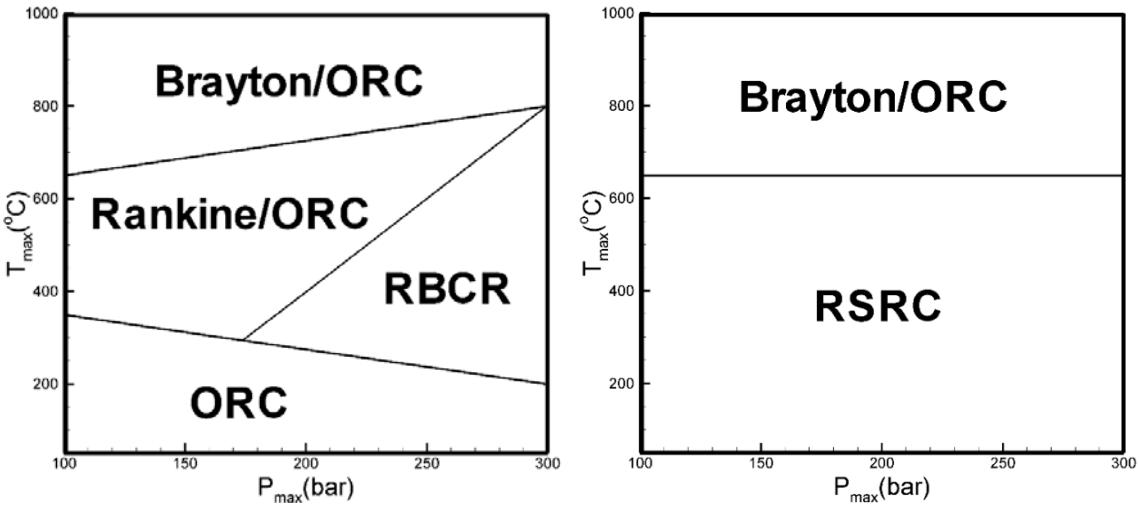

A) Thermal efficiency B) Specific net work output

Figure 6.6. Performance map of thermal efficiency and specific net work output.

6.4. Conclusions

A comparative analysis of the six thermodynamic power cycles: Regenerative steam Rankine with the reheat, regenerative Brayton with and without a recompression, combined Brayton/ORC, and combined Rankine/ORC is presented in this chapter. The best power cycles giving the highest thermal efficiency or highest net power output for the low-, medium, and high maximum cycle temperature ranges were identified. The results from Chapter 4 were used to select the best working fluid giving the highest thermal efficiency or specific net work output. The EPV-11 models were employed to calculate cycle performance.

For the maximum cycle temperatures lower than 300°C, the ORC has the highest thermal efficiency. For the medium maximum cycle temperatures, the combined

Rankine/ORC and RBCR are the best choices. For the maximum cycle temperature higher than 800°C, the combined Brayton/ORC cycle gives the highest thermal efficiency.

The results also show that for the low and medium maximum cycle temperatures, the RSRC gives the highest specific net work output, followed by the combined Brayton/ORC cycle using Helium as the working fluid in the topping cycle and Ethanol in the bottoming ORC. For the maximum temperature of higher than 650°C, the combined Brayton/ORC cycle using Helium as the working fluid in the topping cycle and Ethanol in the bottoming ORC gives the highest specific net work output.

CHAPTER 7: TECHNO-ECONOMIC ANALYSIS OF A CSP-T PLANT

7.1. Overview

The results of the techno-economic analysis performed for a simple ORC, a regenerative Brayton cycle, a regenerative Brayton cycle with recompression, and a combined Brayton/ORC cycle are presented in this chapter.

As discussed in Section 6.3 of Chapter 6, information on the power cycle cost metrics, such as the total investment cost (C_{TCI}) and the levelized cost of electricity (LCOE) is needed in addition to the performance data to make an impartial and objective selection of the best power cycle for the given plant and power block operating parameters.

7.2. Cost Estimation for a Power Block

It should be noted that the techno-economic analysis presented in this section includes the cost of the power block only, i.e., the cost analysis of the solar field, tower/receiver, and TES is not a part of this section. The analysis of the overall cost of a CSP-T including solar field, tower/receiver, and TES is presented in Section 7.3.

7.2.1. Cost Estimation for an ORC

The results concerning thermal efficiency, specific net work output, total capital investment, and LCOE for an ORC are analyzed in this section for the three working fluids (R11, R141b, and Butane) with the objective to select the best working fluid for the given operating parameters. In this analysis, the working fluid giving the lowest LCOE is considered as the best working fluid.

As discussed in Chapter 4, working fluids R11 or R141b give the highest thermal efficiency, while Butane produces the highest specific net work output. Therefore, these three fluids were selected for the techno-economic analysis of the ORC cycle.

The cycle operating parameters used in the calculations are summarized in Table 7.1. As described in Chapter 6, the maximum cycle temperature was varied between 50 to 350°C. For the maximum cycle temperate lower or higher than the critical temperature of the working fluid, the maximum cycle pressure was set to the saturation pressure or the critical pressure of the working fluid, respectively. The cycle gross power output of 10 MW was used to determine the flow rate of the working fluid.

Table 7.1. Simple ORC parameters.

Power cycle parameter	**Value**
Maximum temperature (°C)	50 to 350
Maximum pressure (MPa)	Saturation or critical
Minimum temperature (°C)	6-60
$P_{loss,\ evaporator}$ (%)	5
Pump isentropic efficiency	0.80
Turbine isentropic efficiency	0.87

Thermal efficiency and specific net work output of a simple ORC using R11, R141b, or Butane as the working fluid is shown in Figure 7.1. The contour graphs are plotted in terms of the maximum and minimum cycle temperature.

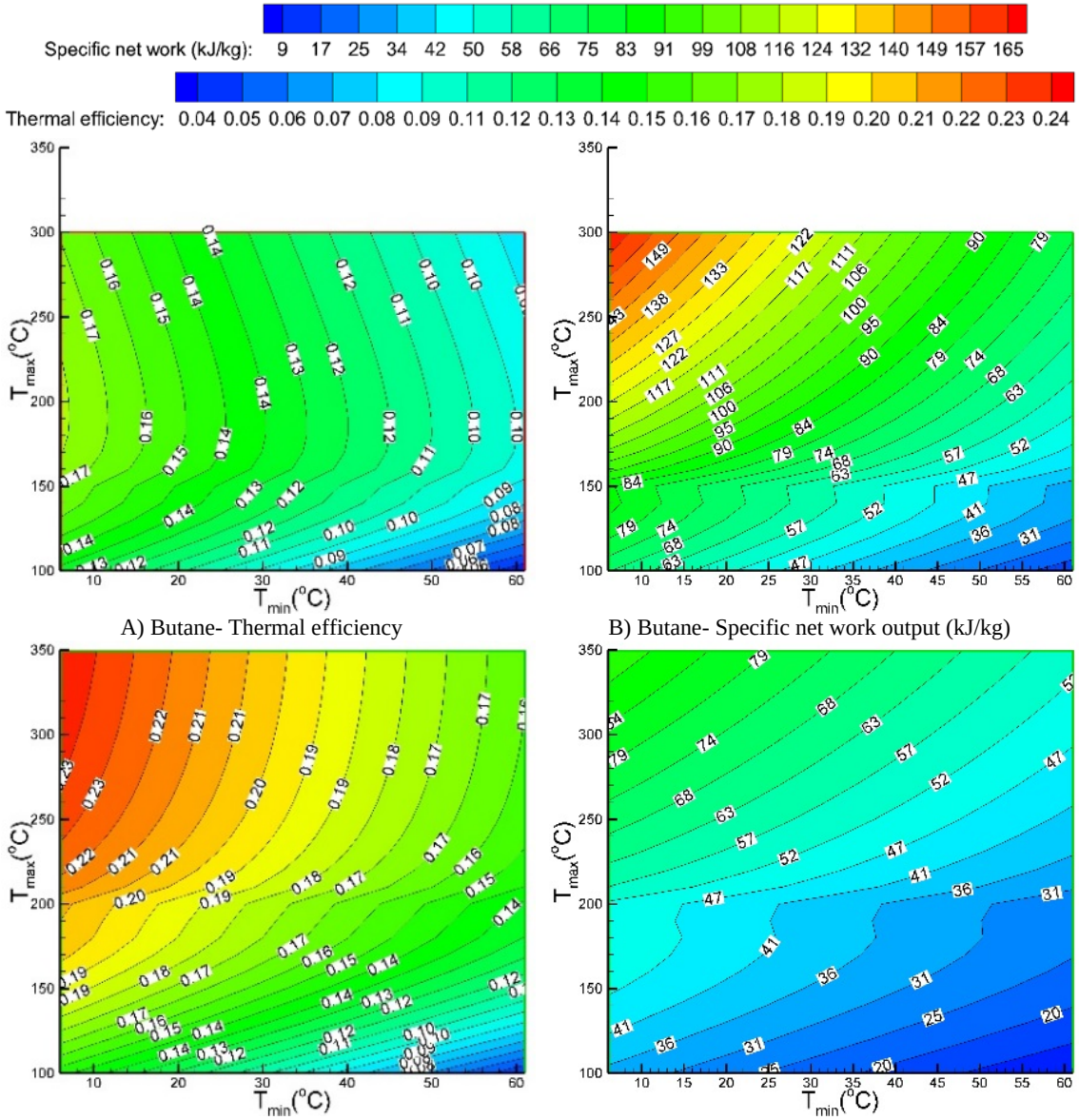

A) Butane- Thermal efficiency

B) Butane- Specific net work output (kJ/kg)

C) R11- Thermal efficiency

D) R11- Specific net work output (kJ/kg)

Figure 7.1. Thermal efficiency and specific net work output of a simple ORC.

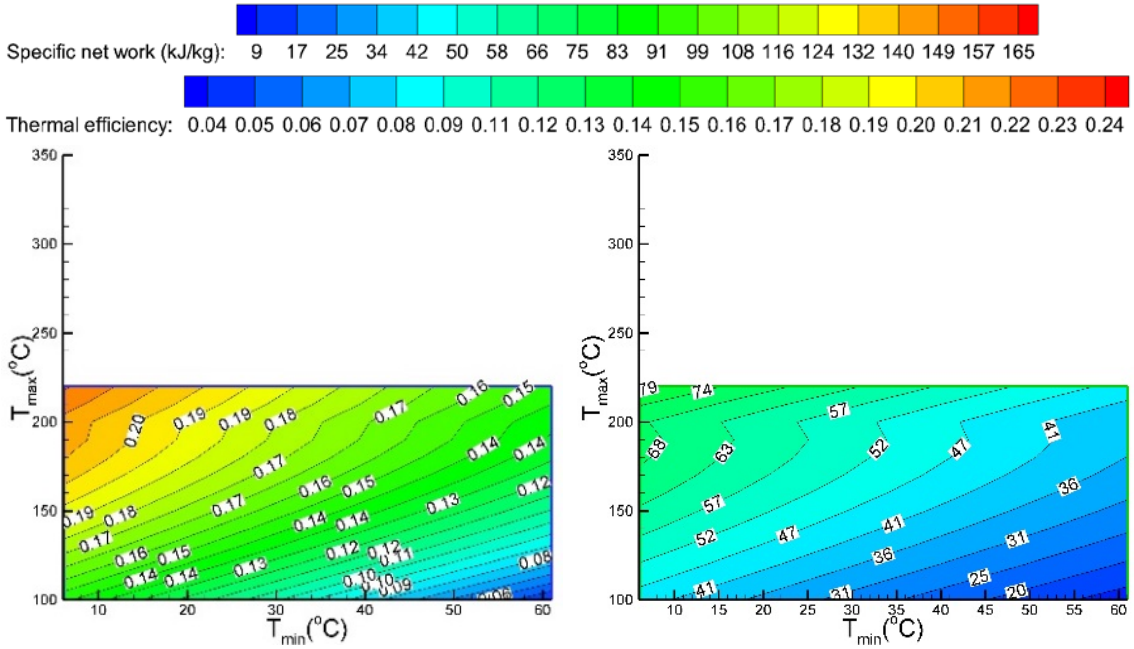

E) R141b- Thermal efficiency F) R141b- Specific net work output (kJ/kg)

Figure 7.1. Continued.

The presented results show that R141b and Butane give the highest and lowest thermal efficiency, respectively. For example, for T_{min}=6°C and T_{max}=225°C, a simple ORC using R141b and Butane has thermal efficiency of 22% and 17%, respectively. Thus, the choice of a working fluid has a large effect on thermal efficiency of a simple ORC.

As the results presented in Figure 7.1 show, Butane gives the highest specific net work output over the range of operating conditions analyzed in this study. For example, for T_{min}=6°C and T_{max}=300°C, a simple ORC using R11 and Butane as working fluids gives the specific net work output of 90 kJ/kg and 160 kJ/kg, respectively. Figure 7.1 and the results presented in Chapter 4 show that working fluids with higher specific heat capacity produce higher net work output. Because of the transition from the subcritical to

supercritical region, the net work output contours for Butane, R11, and R141b change shape as T_{max} exceeds 152, 198, and 204°C, respectively.

Figure 7.2 shows the total capital investment (C_{TCI}) and levelized cost of electricity (LCOE) for a simple ORC using Butane, R11, and R141b as working fluids and operating over the same range of parameters as shown in Figure 7.1. As the results show, a simple ORC using R11 has the lowest C_{TCI} and lowest LCOE. For example, for T_{min}=6°C and T_{max}=225°C, a simple ORC using R141b has the power block total capital investment C_{TCI} of 2335 \$/kW$_{net}$ and LCOE of 56\$/MWh. It should be noted that the techno-economic analysis presented in this section includes the cost of the power block only, i.e., the cost analysis of the solar field, tower/receiver, and TES is not a part of this section.

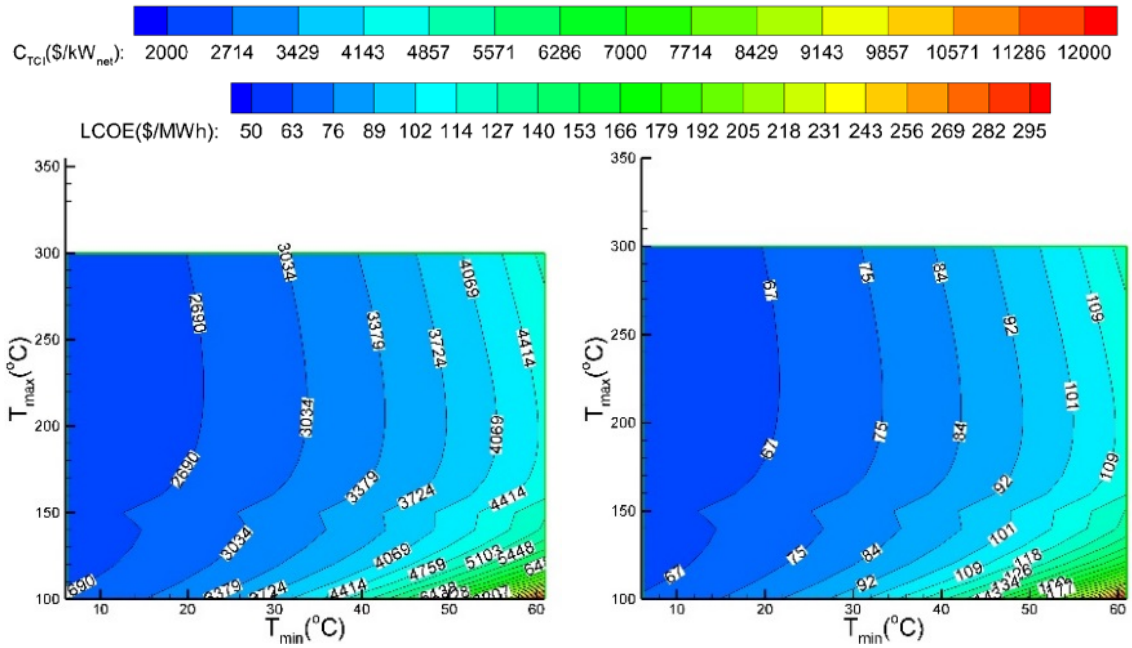

A) C_{TCI} of Butane B) LCOE of Butane

Figure 7.2. Power block total capital investment (\$/kW$_{net}$) and LCOE (\$/MWh) for a simple ORC and three working fluids.

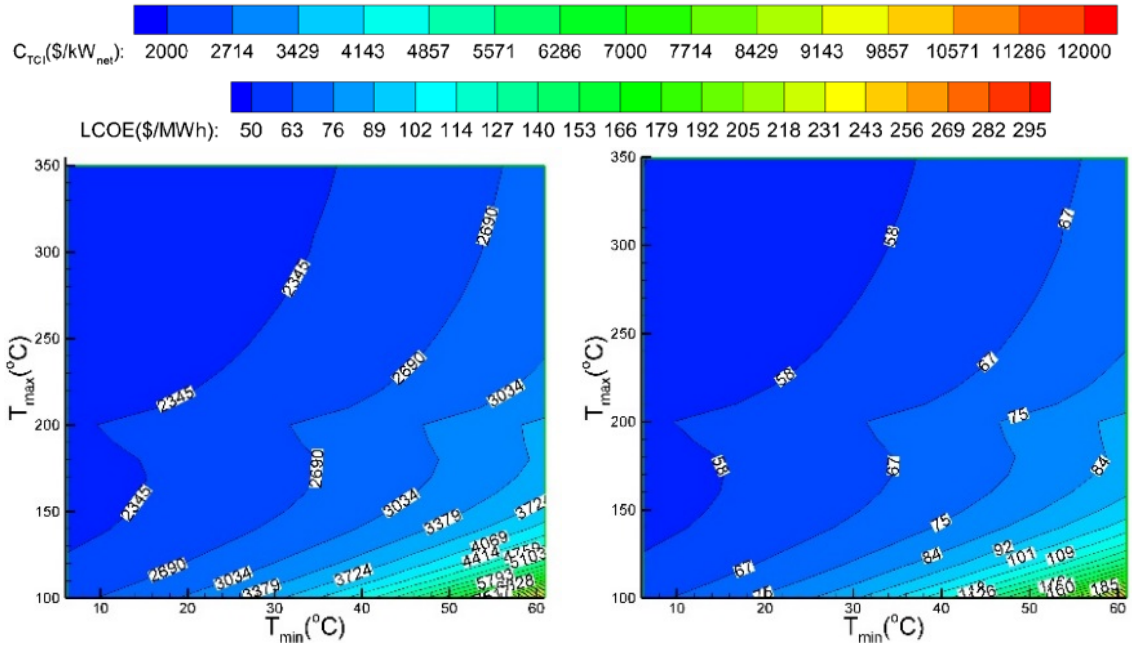

C) C_{TCI} of R11 D) LCOE of R11

E) C_{TCI} of R141b F) LCOE of R141b

Figure 7.2. Continued.

As the results presented in Figures 7.1 and 7.2 show, higher thermal efficiency results in a lower capital investment and lower LCOE. Thus, it follows that for the selection of a working fluid for an ORC, thermal efficiency is more important than the specific net work output. Similar to the efficiency and specific net work output, the C_{TCI} and LCOE contours for Butane, R11, and R141b presented in Figure 7.2 change shape as T_{max} exceeds

152, 198, and 204°C, respectively, because of the transition from the subcritical to the supercritical region.

The relative costs of the ORC components in the power block using R11 and Butane are given in Figure 7.3. The relative cost is the ratio of the component cost and the total capital cost of the power block. As it can be seen in Figure 7.3, the turbine (expander) and the fans for the air-cooled condenser (ACC fans) contribute to the largest portions of the power block cost. Since the power output of the ORC is assumed to be constant, higher minimum cycle temperature results in a lower cycle efficiency and, thus increases the amount of rejected heat and the cooling requirements. Therefore, higher mass and volumetric flow rates of the cooling air through the Cooling Tower are needed, requiring larger and more expensive ACC fans. (As Eqns. (2.53) and (2.54) show, there is a logarithmic relationship between the ACC cost and the cooling air flow.)

In addition, the cost of R11 is much higher compared to the cost of Butane.

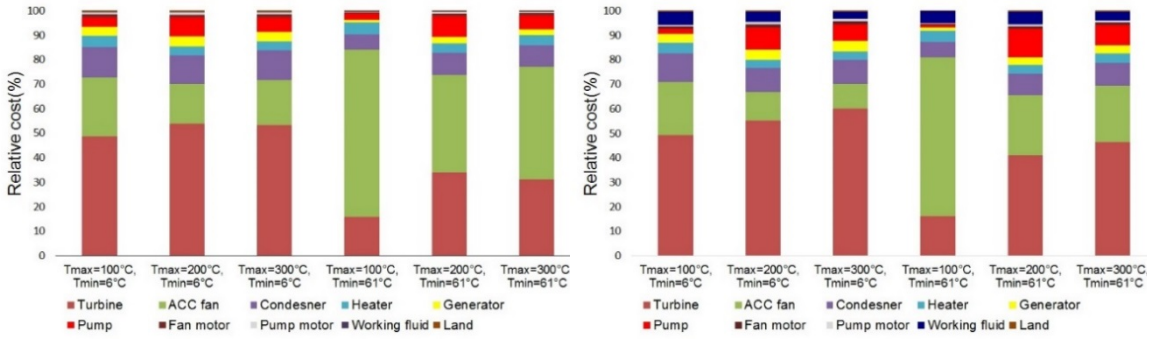

A) Butane B) R11

Figure 7.3. The relative cost of the ORC power block components.

7.2.2. Cost Estimation for a Regenerative Brayton cycle

The results concerning thermal efficiency, specific net work output, C_{TCI} and LCOE for Air, CO_2, and Helium are analyzed in this section to select the best working fluid for a regenerative Brayton cycle (RBC). The working fluid giving the lowest LCOE for the prescribed (selected) cycle operating parameters is considered as the best working fluid.

As discussed in Chapter 4, working fluids Air and CO_2 give the highest thermal efficiency, while He gives the highest specific net work output. Thus, these working fluids were selected for the techno-economic analysis of a regenerative Brayton cycle. The cycle operating parameters are summarized in Table 7.2. Due to the limitations for material selection for the RBC components, the maximum cycle temperature was varied between 350 to 900°C (The temperature limits for material selection were not considered in thermal performance analysis, thus, in Chapters 4 and 6 the analysis was performed over a wider maximum cycle temperature range, i.e., from 200 to 1000°C). The optimum pressure ratio (P_{max}/P_{min}) was considered to achieve the highest specific net work output. Since the critical point of CO_2 is within the investigated temperature and pressure ranges, the analysis includes the results for the sCO_2 Brayton cycle. The cycle gross power of 110 MW was assumed to determine the flow rate of the working fluid.

Table 7.2. RBC parameters.

Power cycle parameter	**Value for CO_2**	**Value for He**
Maximum temperature (°C)	350 to 900	350 to 900
Maximum pressure (MPa)	10, 30	10, 30
Minimum temperature (°C)	32-62	32-62
Turbine isentropic efficiency	0.90	0.93
compressor isentropic efficiency	0.80	0.859
Regenerator effectiveness	0.956	0.85
$P_{loss,\ evaporator}$ (%)	5	5

Thermal efficiency and specific net work output of the RBC using Air, CO_2, and Helium as the working fluid is shown in Figure 7.4. The contour graphs are plotted in terms of the maximum and minimum cycle temperature for P_{max}=30 MPa.

The results show that CO_2 and Helium give the highest and lowest thermal efficiencies, respectively. For example, for T_{min}=32°C and T_{max}=900°C, an RBC using CO_2 and Helium has thermal efficiency of 36 and 31%, respectively. Thus, the choice of the working fluid has a considerable effect thermal efficiency of an RBC.

As the results presented in Figure 7.4 show, for the range of operating conditions analyzed in this study, Helium gives the highest specific net work output, followed by CO_2 and Air. For example, for the turbine inlet temperature (TIT) below 450°C, Helium produces the specific net work output higher than 128 kJ/kg, while for the same conditions CO_2 produces the net power output between 67 and 88 kJ/kg. For TIT of 900°C He gives the net power output between 856 and 776 kJ/kg, while CO_2 produces the net power output between 155 and 189 kJ/kg.

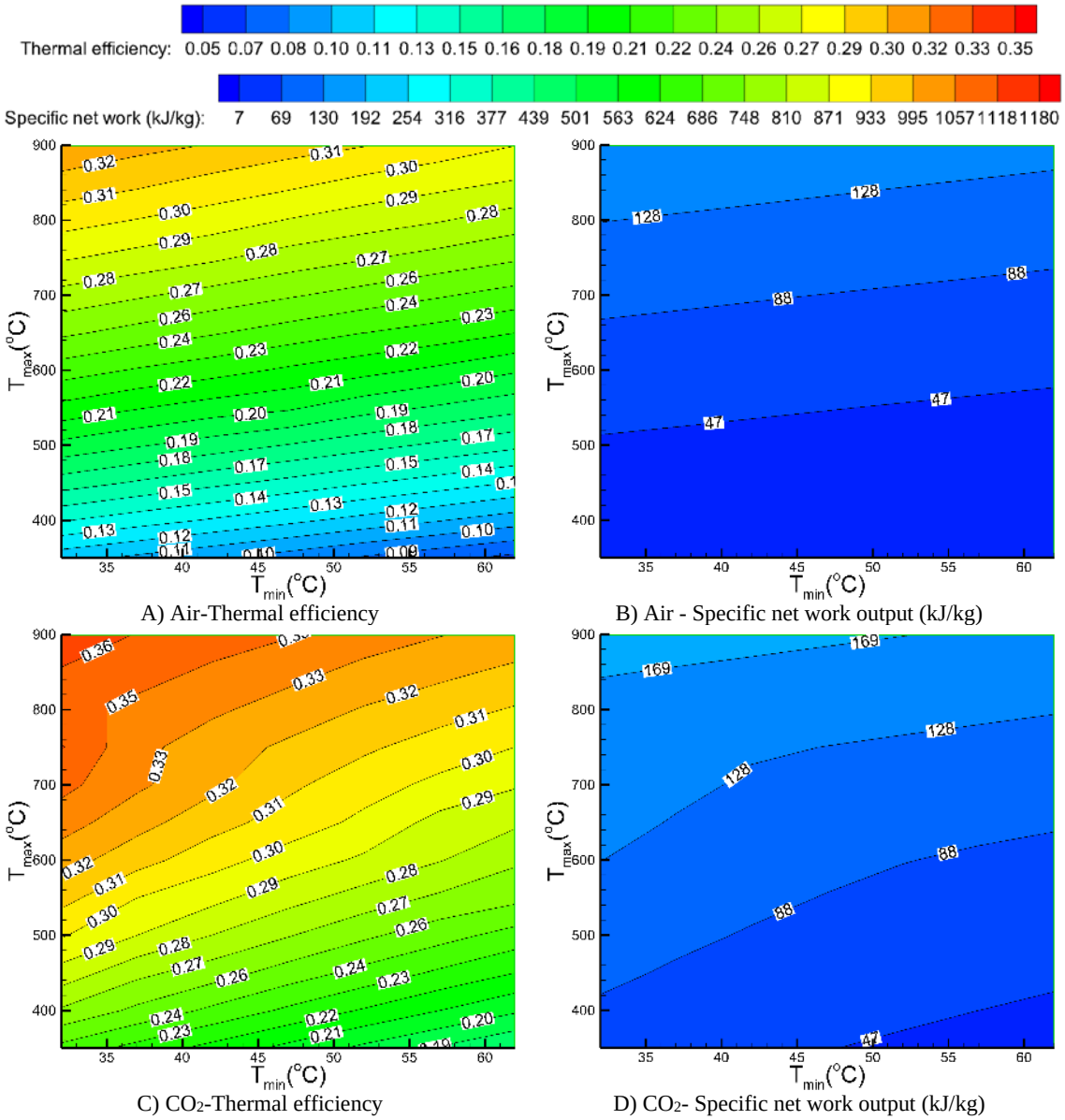

Figure 7.4. Thermal efficiency and specific net work output of RBC for three working fluids.

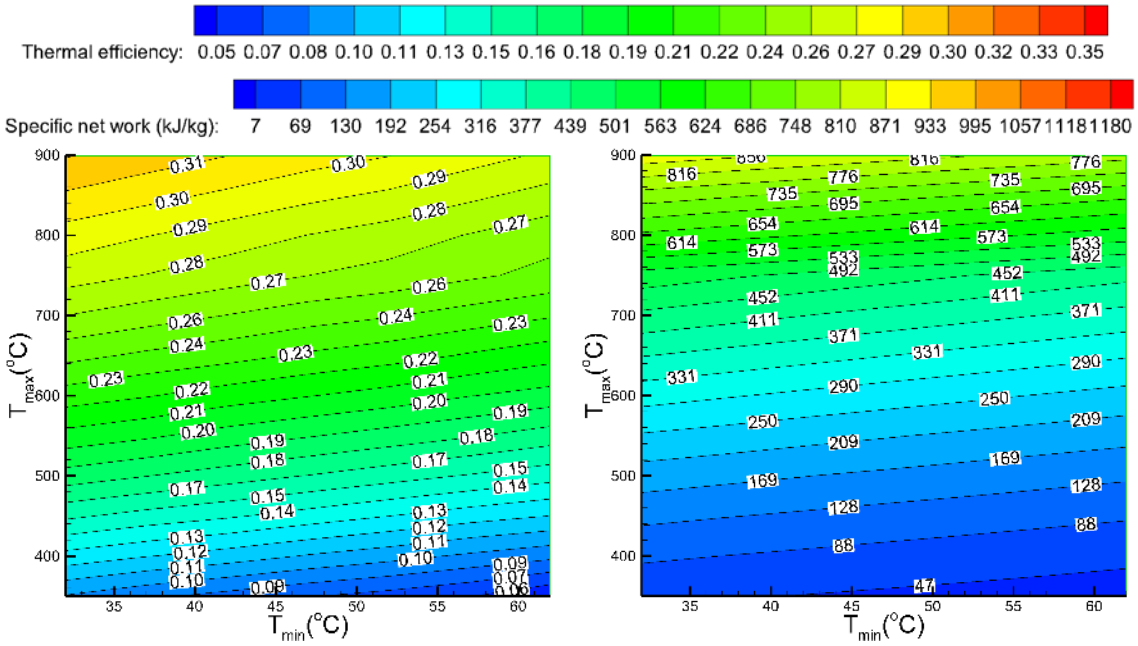

E) He-Thermal efficiency F) He - Specific net work output (kJ/kg)

Figure 7.4. Continued.

The total capital investment C_{TCI} and LCOE for the RBC using Air, CO_2, or He as the working fluid, and operating over the same range of parameters as shown in Figure 7.4, are presented in Figure 7.5. As the results show, the RBC using CO_2 as the working fluid has the lowest capital investment cost and the lowest LCOE. For example, for T_{min}=32°C and T_{max}=900°C, the RBC using CO_2 as the working fluid has the total capital investment cost of 1157 \$/kW_{net} and LCOE of 28.8 \$/MWh. It should be noted that the techno-economic analysis presented in this section includes the cost of the power block only, i.e., the cost analysis of the solar field, tower/receiver, and TES is not a part of this section.

As the results presented in Figures 7.4 and 7.5 show, higher thermal efficiency results in a lower capital investment and lower LCOE. Thus, similar to the ORC, for the selection of a working fluid for a regenerative Brayton cycle (RBC), thermal efficiency is more important parameter than the specific net work output.

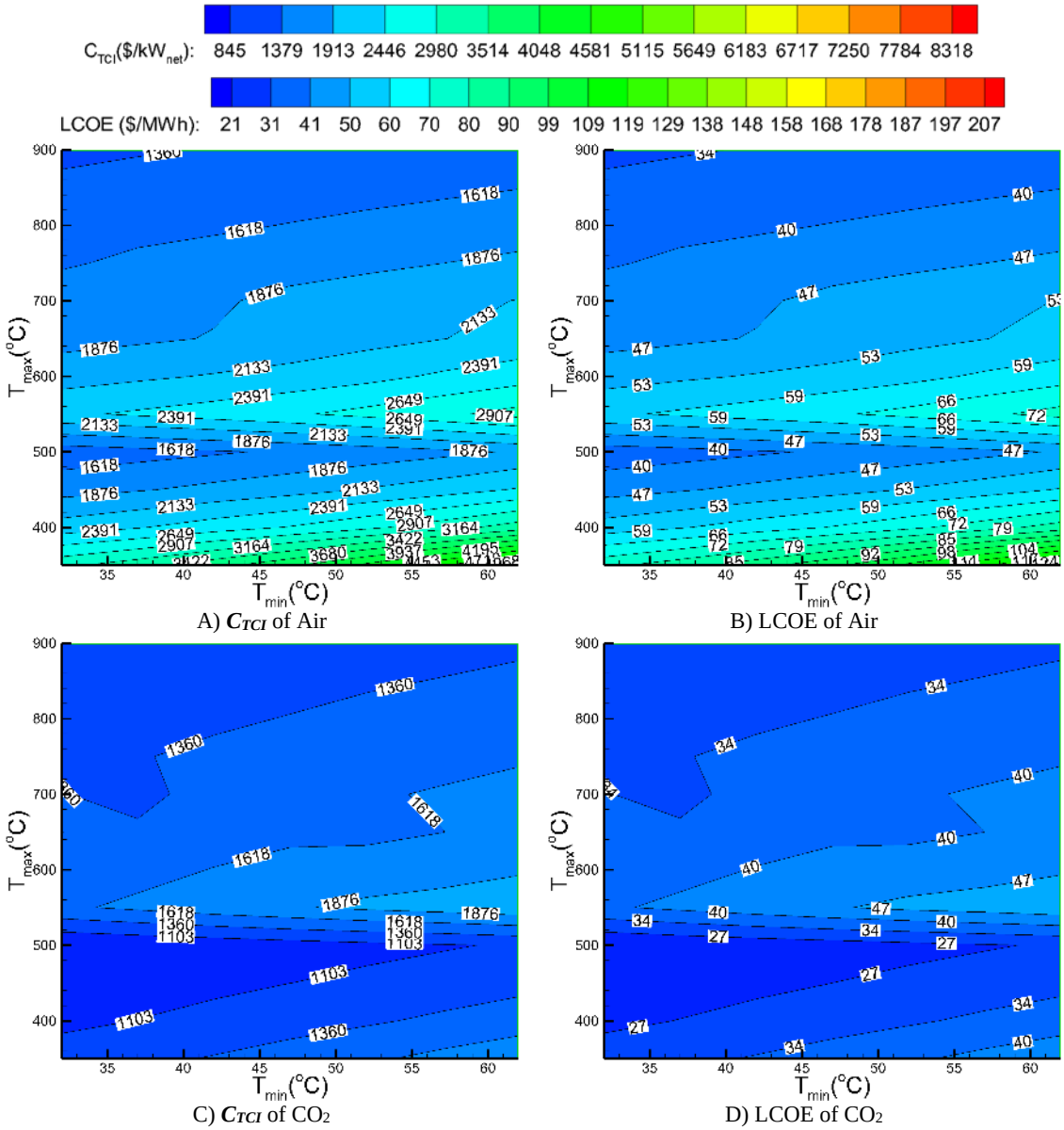

Figure 7.5. Power block total capital investment ($/kW$_{net}$) and LCOE ($/MWh) for an RBC and three working fluids.

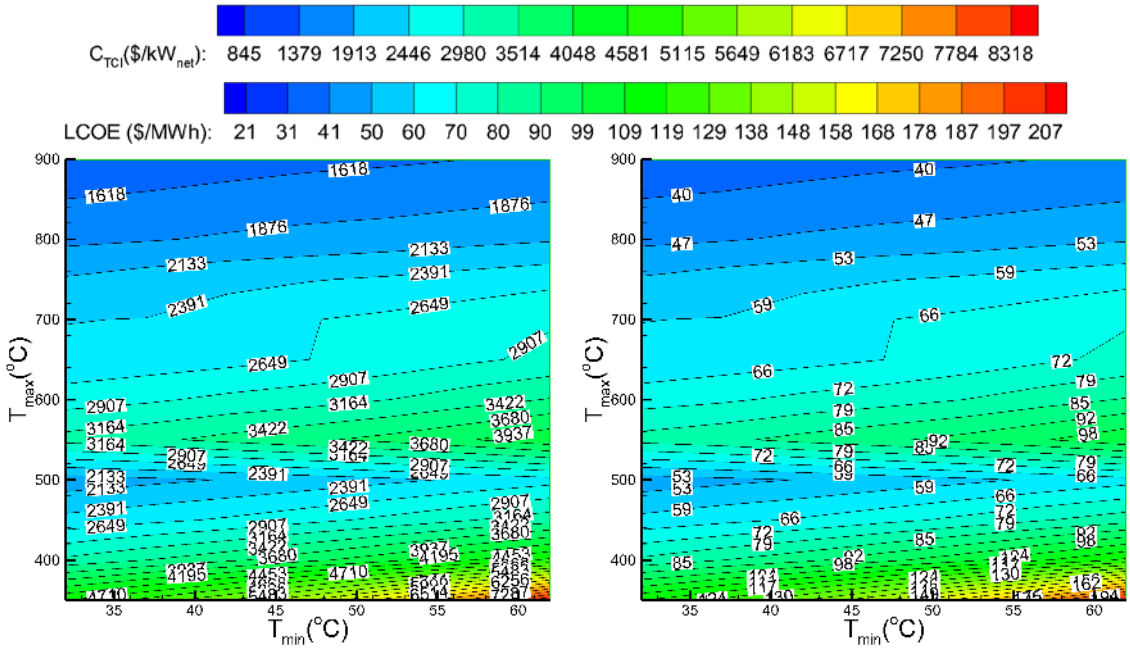

E) C_{TCI} of Helium F) LCOE of Helium

Figure 7.5. Continued.

The total capital investment for an RBC is shown in Figure 7.6 as a function of the maximum cycle temperature for the three working fluids (air, CO_2, and He) and two maximum cycle pressures (P_{max} = 10 and 30 MPa). As the results show, for T_{max}= 500°C there is a significant increase in the total capital investment and LCOE. This is because for T_{max}>500°C a more expensive stainless steel must be used instead of a carbon steel for all RBC system components. Also, depending on the maximum cycle pressure, there is also a cost increase for the maximum cycle temperature of 650°C (for P_{max}= 30MPa) and 750°C (for P_{max}=10 MPa). This is because for these maximum temperatures the expensive Nickel alloys must be used instead of the stainless steel for the turbine and the heater (primary heat exchanger). Since the operating temperature of other components is much lower compared to the maximum cycle temperature, there is no need to change the material of construction for the cycle components such as the cooler or the compressor.

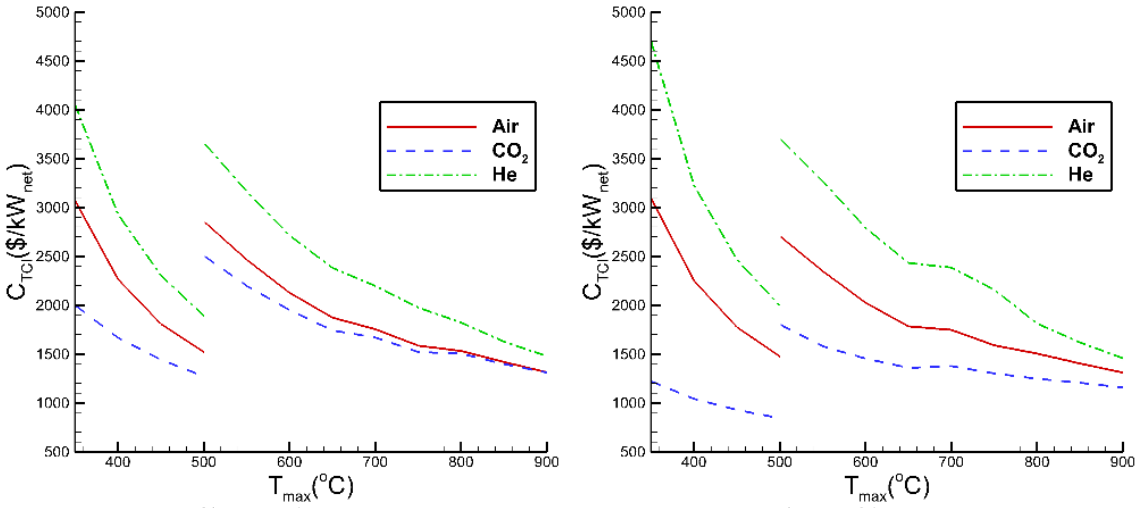

A) P_{max}=10 MPa B) P_{max}=30 MPa

Figure 7.6. Power block total capital investment ($/kW$_{net}$) for the RBC for maximum cycle pressures of 10 and 30 MPa.

The relative costs of the RBC power block components for Air, CO_2, and Helium as the working fluids for P_{max}=30 MPa are presented in Figure 7.7. The relative cost is the ratio of the component cost and the total capital cost of the power block. Similar to the simple ORC, the turbine, ACC, and the compressor contribute to the largest portions of the power block cost. However, for CO_2, where the compressor inlet is in the "liquid-like" region, the compressor work is small compared to the other working fluids, thus the relative cost of the CO_2 compressor is lower compared to the other working fluids.

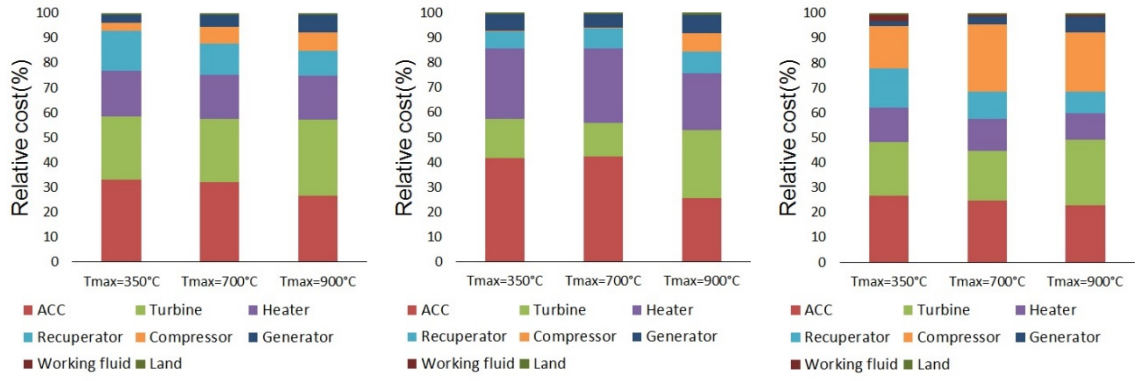

A) Air B) CO_2 C) Helium

Figure 7.7. The relative cost of the RBC power block components for P_{max} = 30 MPa.

7.2.3. Cost Estimation for a Regenerative Brayton cycle with recompression (RBCR)

The results concerning thermal efficiency, size of the heat exchangers, total capital investment C_{TCI} and LCOE for the CO_2 regenerative Brayton cycle with recompression (RBCR) are analyzed in this section.

The cycle operating parameters are summarized in Table 7.3. The maximum temperature and pressure used in the analysis are the same as for the RBC. CO_2 was selected as the working fluid for the RBCR. The cycle gross power output of 110 MW was used to determine the flow rate of the working fluid. Due to the limitation for material selection for the RBCR components, the maximum cycle temperature was varied between 350 to 900°C (The temperature limits for material selection were not considered in thermal performance analysis, thus, in Chapters 4 and 6 the analysis was performed over a wider maximum cycle temperature range, i.e., from 200 to 1000°C).

Table 7.3. RBCR parameters.

Power cycle parameter	**Value for CO_2**
Maximum temperature (°C)	350 to 900
Maximum pressure (MPa)	10, 30
Minimum temperature (°C)	32-62
Turbine isentropic efficiency	0.90
compressor isentropic efficiency	0.89
HT Regenerator effectiveness	0.976
LT Regenerator effectiveness	0.88
$P_{loss,\ evaporator}$ (%)	5

Figure 7.8 shows the effect of the maximum cycle temperature and pressure on thermal efficiency of the RBCR and RBC for T_{min}=32°C. As the results show, the RBCR has higher thermal efficiency compared to the RBC. For example, for T_{max}=900°C and P_{max}=10 MPa, thermal efficiency of the RBCR and RBC is 39.5% and 34.5%, respectively.

Also, an increase in the maximum cycle pressure results in a higher difference in thermal efficiency of the RBCR and RBC.

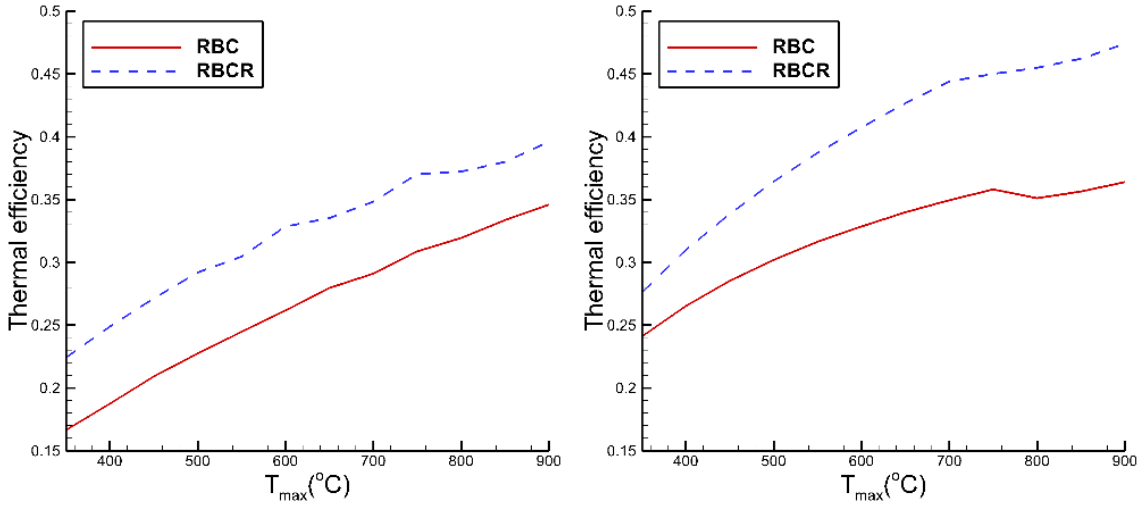

A) P_{max}=10 MPa B) P_{max}=30 MPa

Figure 7.8. Thermal efficiency of the RBC and RBCR.

Figure 7.9 shows the effect of the maximum cycle temperature and pressure on the heat exchanger size (overall *UA*) required for the RBCR and RBC at T_{min}=32°C.

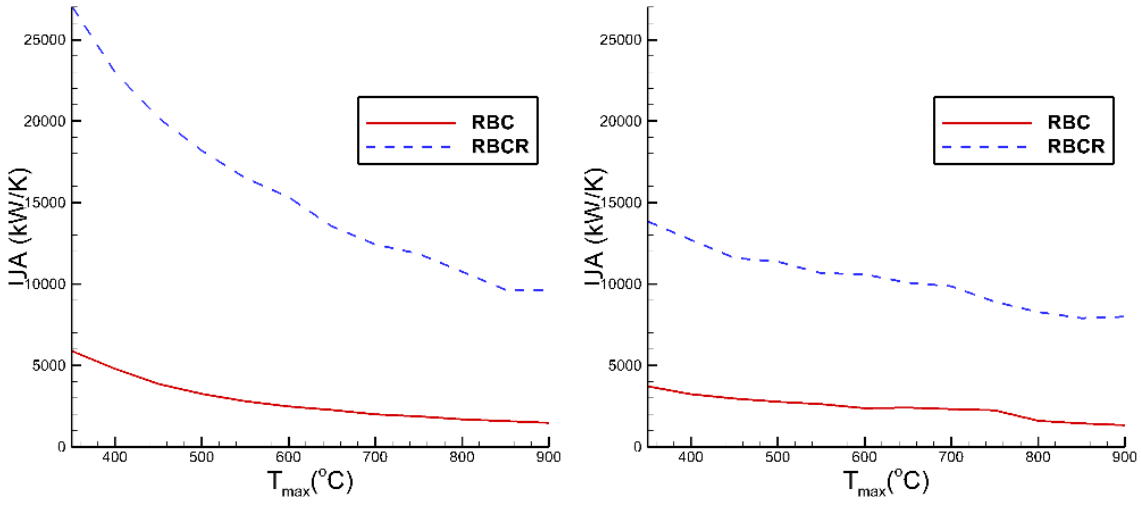

A) P_{max}=10 MPa B) P_{max}=30 MPa

Figure 7.9. Overall UA (kW/K) for the RBCR and RBC.

As the results show, the *UA* required for the RBCR is higher compared to the RBC because two heat exchangers are needed for the RBCR, compared to one for the RBC. Thus, the total capital investment for the heat exchanger is higher for the RBCR compared to the RBC.

The total capital investment and LCOE for the RBCR and RBC are compared in Figure 7.10, where the results are presented as functions of the maximum cycle temperature for two maximum cycle pressures (P_{max} = 10 and 30 MPa) and T_{min}=32°C.

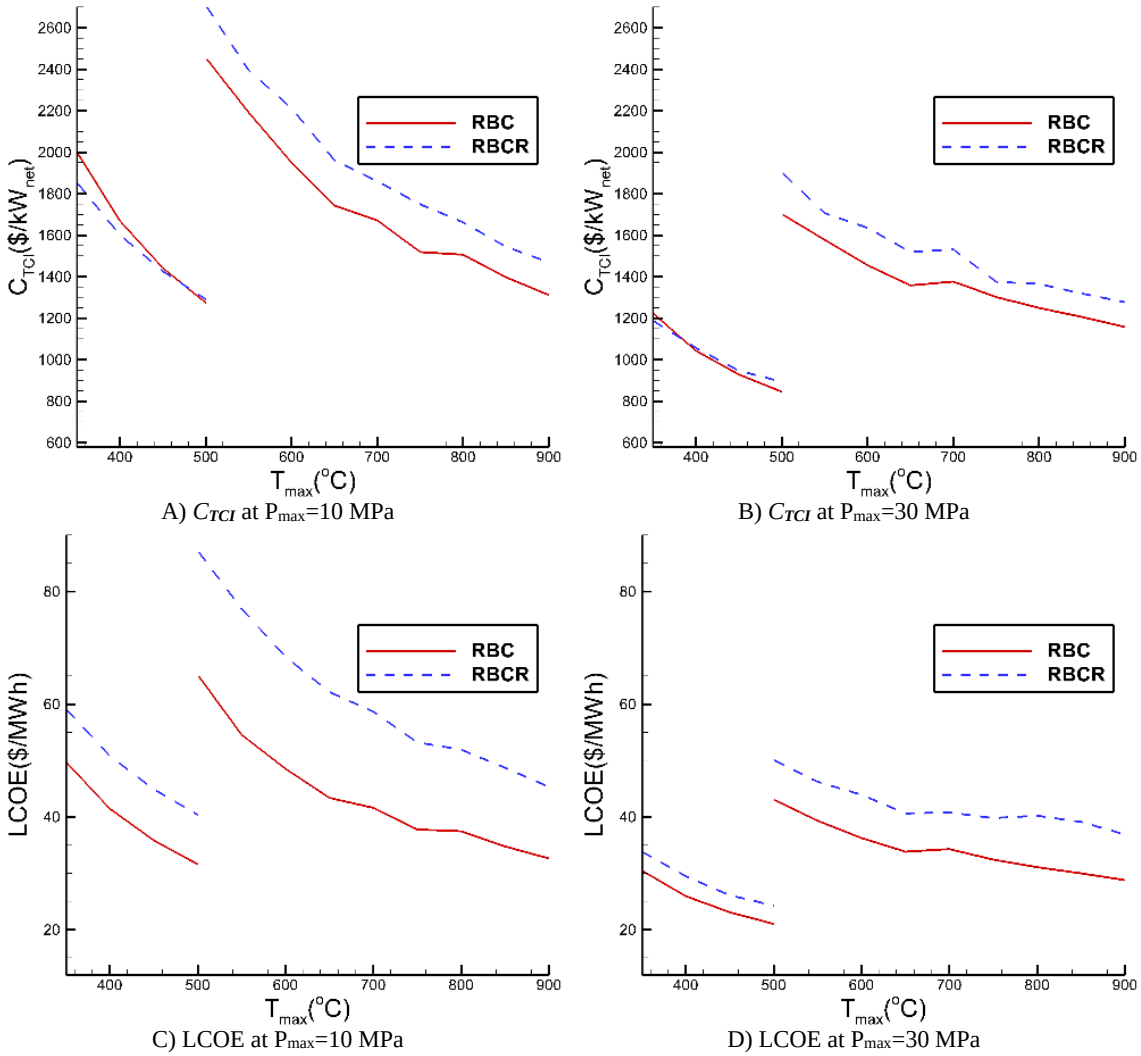

A) C_{TCI} at P_{max}=10 MPa

B) C_{TCI} at P_{max}=30 MPa

C) LCOE at P_{max}=10 MPa

D) LCOE at P_{max}=30 MPa

Figure 7.10. Power block total capital investment ($/kW$_{net}$) and LCOE ($/MWh) for the RBC and RBCR for P_{max} = 10 and 30 MPa.

As the results show, RBCR has higher capital investment and higher LCOE compared to the RBC. For example, for T_{max}=550°C and P_{max} = 10 MPa, LCOE of the RBCR is 77 $/MWh, while at the same operating conditions LCOE of the RBC is lower, 55 $/MWh. An increase in the maximum pressure lowers the total capital investment and LCOE. It should be noted that the techno-economic analysis presented in this section includes the cost of the power block only, i.e., the cost analysis of the solar field, tower/receiver, and TES is not a part of this section.

7.2.4. Cost Estimation for a Combined Brayton/ORC cycle

The results concerning thermal efficiency, total capital investment, and LCOE of a combined Brayton/ORC cycle are analyzed in this section.

The cycle parameters are summarized in Table 7.4. The thermal performance results presented in this section correspond to the optimal pressure ratio of the topping cycle. As described in Chapters 4 and 6, at the optimal pressure ratio the cycle net work output reaches its maximum value. Due to the limitation for material selection for the components of RBC, the maximum cycle temperature was varied between 350 to 900°C. The temperature limits for material selection were not considered in thermal performance analysis, thus, in Chapters 4 and 6 the analysis was performed over a wider maximum cycle temperature range, i.e., from 200 to 1000°C). The maximum cycle pressure was varied between and 10 and 30 MPa. Since the flow rate of the working fluid in the bottoming cycle is dependent on the mass flow rate of the working fluid in the topping cycle, and also to compare power cycles, a constant gross power output of 110MW of the topping cycle was assumed (The heat input of 100MW_{th} was assumed for a combined Brayton/ORC cycle in Chapters 4 and 6).

Based on the analysis of performance results presented in Chapter 4, the performance results for the combined cycle using Air or CO_2 as working fluids in the topping cycle are presented here. Iso-butane, R11, and Ethanol are selected as the working fluids for the bottoming ORC.

Table 7.4. Combined Brayton/ORC cycle parameters.

Power cycle parameter	**Value**
Maximum temperature (°C)	350 to 900
Rankine cycle maximum pressure (MPa)	10, 30
Minimum temperature (°C)	32-62
Turbine isentropic efficiency	0.90
Regenerator effectiveness	0.85
Compressor isentropic efficiency	0.80
ORC turbine isentropic efficiency	0.87
Feed pump isentropic efficiency	0.80
$P_{loss,\ evaporator}$ (%)	5
P_{11}(MPa), if $T_{11}>T_{Critical}$	$P_{Critical}$
P_{11}(MPa), if $T_{11}<T_{Critical}$	$P_{Saturation}$

Thermal efficiency of the combined Brayton/ORC cycle is shown in Figure 7.11. The contour graphs are plotted in terms of the maximum and minimum cycle temperature for P_{max}=10 and 30 MPa of the topping cycle.

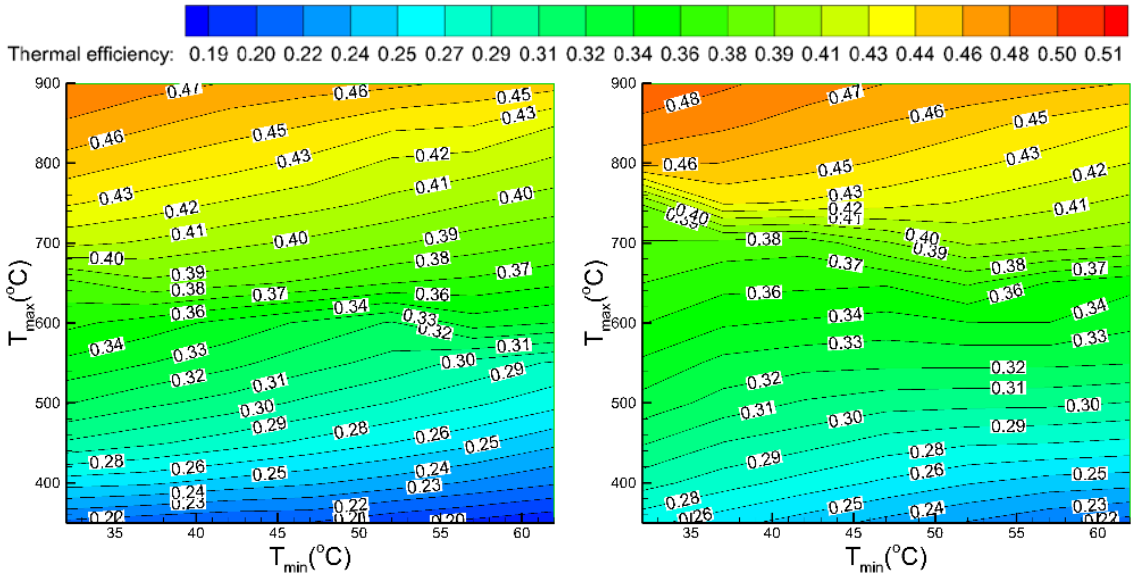

A) P_{max}=10 MPa B) P_{max}=30 MPa

Figure 7.11. Thermal efficiency of a combined Brayton/ORC cycle.

As it can be seen in Figure 7.11, increasing the maximum pressure of the topping cycle from 10 to 30 MPa results in an approximately 1%-point increase in thermal efficiency. For example, for T_{max}=900°C and T_{min}=32°C, thermal efficiency of a combined Brayton/ORC cycle for P_{max}=10 and 30MPa is 48% and 48.9%, respectively. Also, for T_{max}=900°C, increasing the minimum cycle temperature from 32 to 62°C results in a 3%-points decrease in thermal efficiency.

Figure 7.12 compares thermal efficiency of the various configurations of the Brayton cycle determined for T_{min}=32°C: a CO_2 regenerative Brayton cycle (RBC), a CO_2 regenerative Brayton cycle with recompression (RBCR), and a combined Brayton/ORC cycle. This figure is a simplified version of Figure 6.2, which compares efficiencies of all power cycles analyzed in this study.

As the results show, for P_{max}=10 MPa, a combined Brayton/ORC cycle has the highest thermal efficiency, compared to the other analyzed Brayton cycle configurations.

However, for P_{max}=30 MPa and the maximum cycle temperature lower than 800°C, RBCR has the highest thermal efficiency.

A step change in thermal efficiency of a combined Brayton/ORC cycle shown in Figure 7.12 is due to the change of the working fluid. For T_{max} > 750°C, Ethanol was used as a working fluid instead of R11. More details can be found in Section 6.3 of Chapter 6.

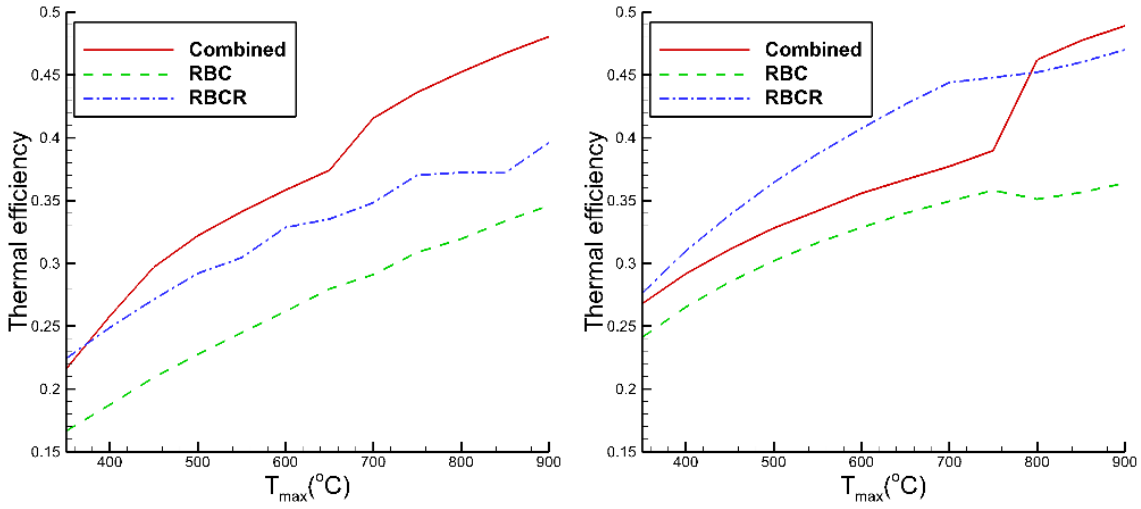

A) P_{max}=10 MPa B) P_{max}=30 MPa

Figure 7.12. Thermal efficiency of a RBC, RBCR, and combined Brayton/ORC cycle.

The total capital investment C_{TCI} and LCOE of the combined Brayton/ORC cycle are shown in Figure 7.13 for the maximum cycle pressures of 10 and 30 MPa. As the results presented in Figures 7.11 and 7.13 show, the maximum cycle pressure does not have a significant effect on thermal efficiency of the combined Brayton/ORC cycle. However, higher P_{max} results in a lower total capital investment and LCOE. For example, for a combined Brayton/ORC for P_{max}=10 MPa, T_{max}=900°C and T_{min}=32°C, the total power block capital investment C_{TCI} = 1110 \$/kW_{net} and LCOE = 27.6\$/MWh, while for the higher maximum cycle pressure P_{max} of 30 MPa C_{TCI} = 1100 \$/kW_{net} and LCOE =

25.8$/MWh. As discussed in Section 7.2.2, an increase in the total capital investment occurs for T_{max}> 500°C because of the material change. It should be noted that the techno-economic analysis presented in this section includes the cost of the power block only, i.e., the cost analysis of the solar field, tower/receiver, and TES is not a part of this section.

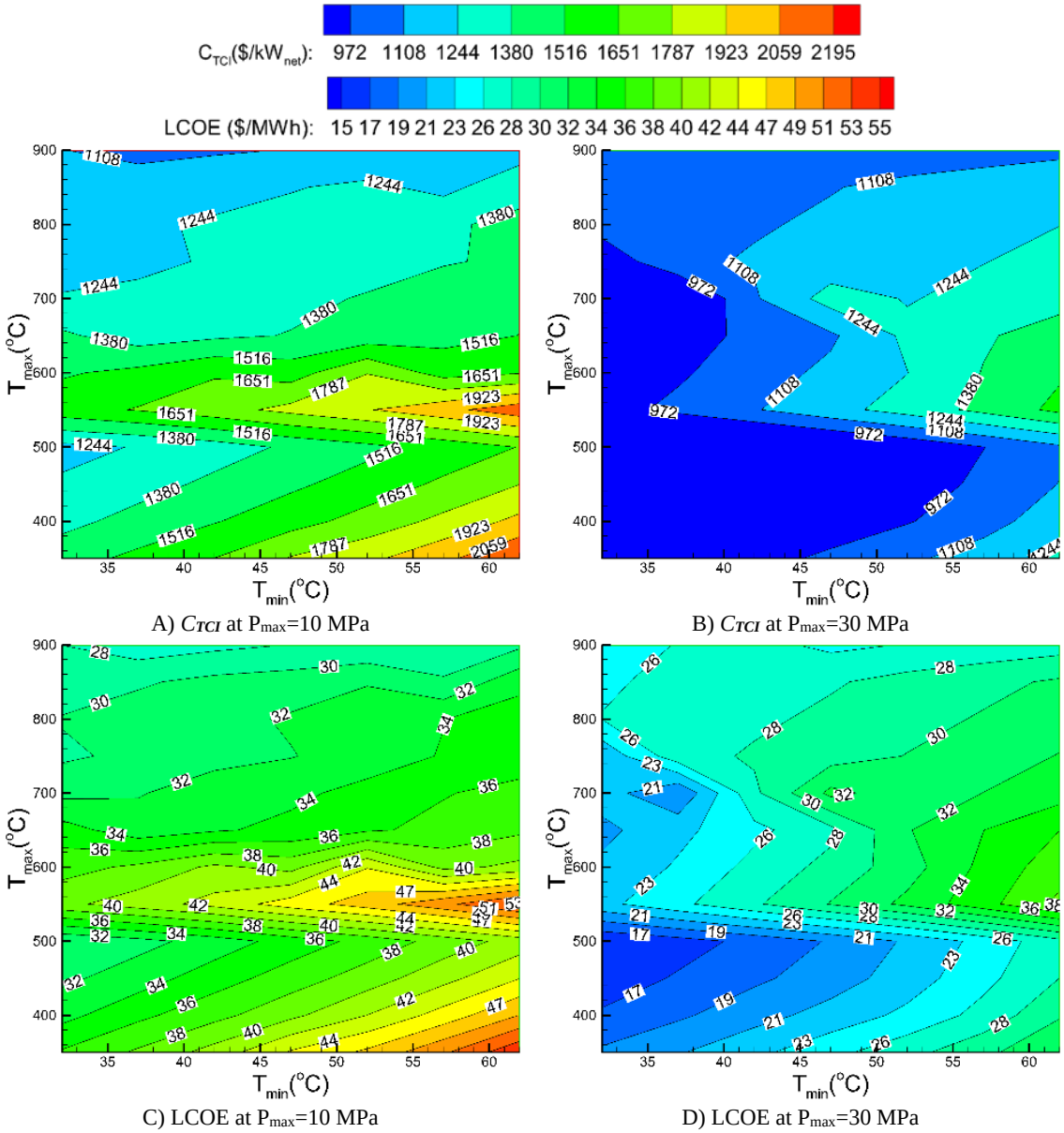

A) C_{TCI} at P_{max}=10 MPa

B) C_{TCI} at P_{max}=30 MPa

C) LCOE at P_{max}=10 MPa

D) LCOE at P_{max}=30 MPa

Figure 7.13. Power block total capital investment ($/kW$_{net}$) and LCOE ($/MWh) for a combined Brayton/ORC cycle.

The total power block capital investment and LCOE of the RBC and combined Brayton/ORC cycle for T_{min}=32°C are compared in Figure 7.14, where the results are presented as functions of the maximum cycle temperature for the maximum cycle pressures of 10 and 30 MPa.

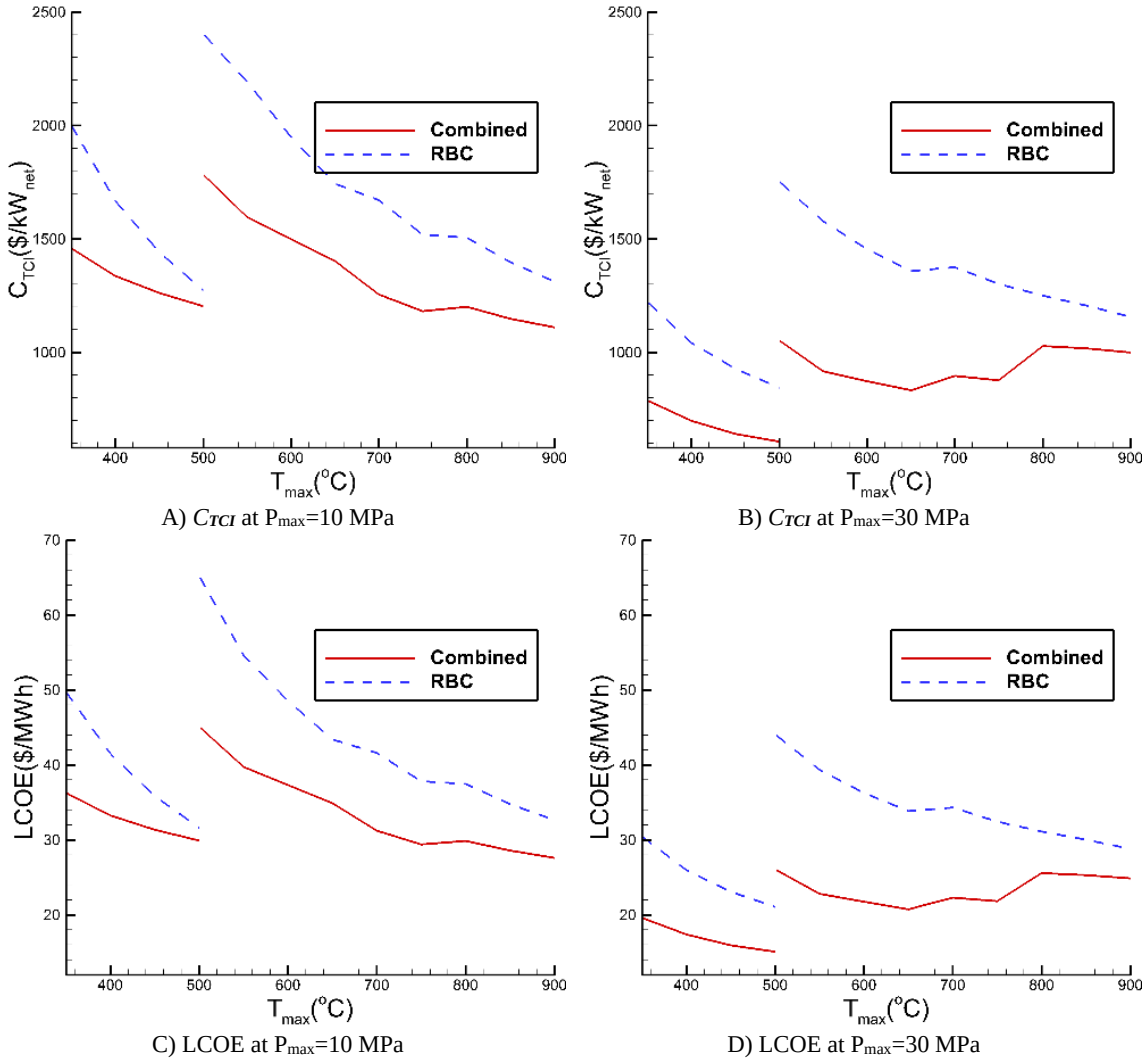

A) C_{TCI} at P_{max}=10 MPa

B) C_{TCI} at P_{max}=30 MPa

C) LCOE at P_{max}=10 MPa

D) LCOE at P_{max}=30 MPa

Figure 7.14. Power block total capital investment ($/kW$_{net}$) and LCOE ($/MWh) for the RBC and combined Brayton/ORC cycle.

As the results show, the total capital investment and LCOE for a combined Brayton/ORC cycle are lower compared to the regenerative Brayton cycle (RBC). As presented in Section 7.2.3, RBCR has a higher total capital investment and LCOE

compared to the RBC. For example, for T_{max}=550°C and P_{max}=30 MPa, LCOE of the combined Brayton/ORC cycle, is 13$/MWh lower compared to the RBC. As explained in Section 7.2.2, for T_{max}> 500°C there is an increase in the total capital investment because of the material change.

7.3. Cost Estimation for a CSP-T Plant

For the given power output of a CSP-T plant, thermal efficiency of a power block (power cycle) affects the required heat input. Since the heat input to the power block is provided by the solar field, tower/receiver, and TES, its thermal efficiency has a direct effect on the size of the solar field, the height of the tower/receiver, the size of the thermal energy storage system (TES), and the cost of these components.

The results concerning LCOE of a CSP-T plant, including the solar field, tower/receiver, and TES integrated with the power block employing the RBC and combined Brayton/ORC cycles are presented in this section.

7.3.1. CSP-T integrated with a RBC

The LCOE of a CSP-T plant integrated with the RBC is shown in Figure 7.15 as a function of the maximum cycle temperature. The results were obtained for the three working fluids (Air, CO_2, and He), for, P_{max} of 10 and 30 MPa, and T_{min}=32°C. As the results presented in Figure 7.15 show, a CSP-T plant integrated with the regenerative Brayton cycle (RBC) using CO_2 as the working fluid, has the lowest LCOE. For example, for P_{max}=10 MPa and T_{max}=650°C, the plant LCOE is 160 $/MWh.

Figures 7.4, 7.5, and 7.15 show that for the selection of the working fluid, thermal efficiency is more important than the specific net work output. Also, an increase in the

maximum cycle pressure increases the difference in LCOE for different working fluids. As discussed before, for T_{max} > 500°C the total capital investment and LCOE increase because of the material change.

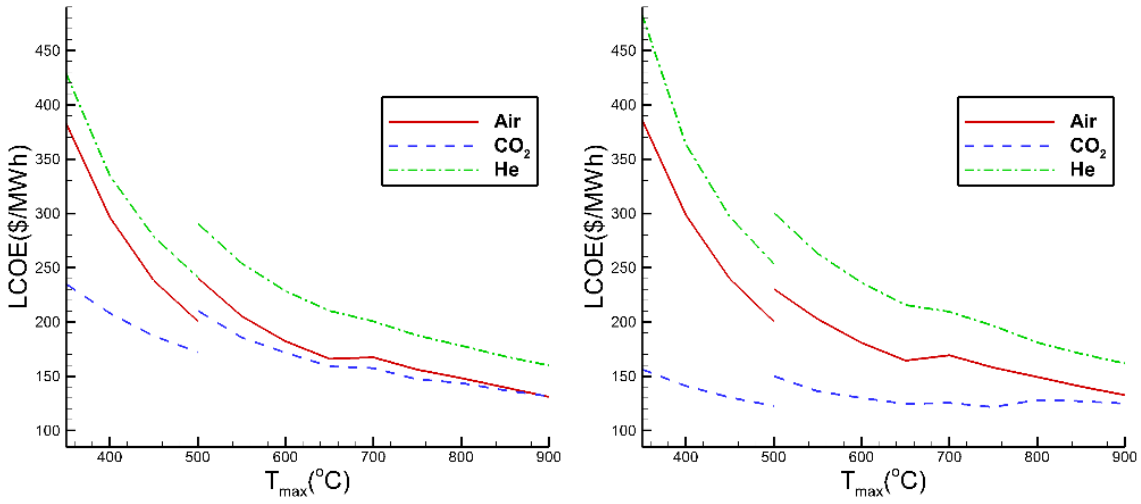

A) P_{max}=10 MPa B) P_{max}=30 MPa

Figure 7.15. LCOE ($/MWh) of CSP-T plant integrated with a RBC.

7.3.2. CSP-T integrated with a combined Brayton/ORC cycle

Figure 7.16 compares LCOE for a CSP-T plant integrated with the RBC and the combined Brayton/ORC cycle. As the results show, the LCOE for a CSP-T plant integrated with the combined Brayton/ORC (100$/MWh) is significantly lower compared to the RBC (135$/MWh): 35$/MWh for T_{max}=900°C, P_{max}=30 MPa, and T_{min}=32°C. As discussed before, for T_{max} > 500°C LCOE increases because of the material change.

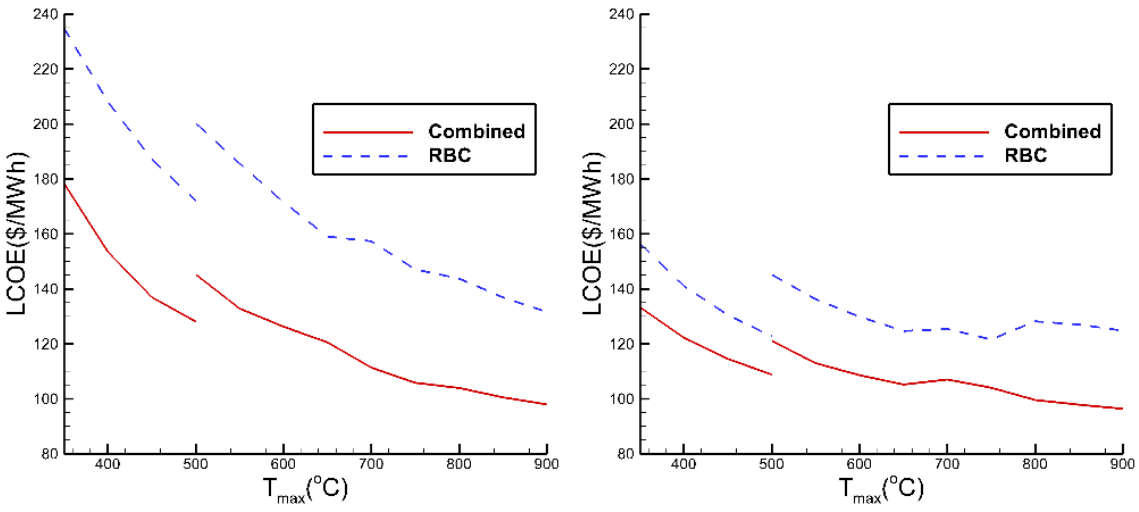

A) P_{max}=10 MPa B) P_{max}=30 MPa

Figure 7.16. LCOE ($/MWh) for a CSP-T plant integrated with the RBC and combined Brayton/ORC cycle.

As discussed earlier, thermal efficiency of the power cycle affects the size and cost of the power block, solar field, tower/receiver, and TES. For the cost analysis it is, therefore, useful to determine the ratio of LCOE for the power block and the overall CSP-T plant. A parameter R_{LCOE}, representing this ratio is used in this work. R_{LCOE} is defined as:

$$R_{LCOE} = \frac{LCOE_{Power\ block}}{LCOE_{CSP-T\ plant}} * 100 \qquad (7.1)$$

The results of the cost analysis are presented in Figure 7.17, where the ratio R_{LCOE}, LCOE for the power block, LCOE for the overall CSP-T plant, and the area of the solar field are presented as functions of the maximum cycle temperature and thermal efficiency for P_{max}=30 MPa and T_{min}=32°C. As Figure 7.17A shows, for the assumptions used in the analysis, the cost of the power block is between 14 to 28% of the overall cost of the CSP-T plant, and increases as the maximum cycle temperature is increased. Also, the size of the solar field decreases as T_{max} is increased. The step change in the solar field area shown in Figure 7.17A is due to the change of the working fluid from R11 to Ethanol in bottoming

ORC and the associated change in thermal efficiency of the power block (see section 7.2.4). More details can be found in Section 6.3 of Chapter 6 and Section 7.2.4.

The effect of the power block efficiency on the total capital investment for the solar field, tower/receiver, and TES and the size of the solar field are presented in Figure 7.17B. Both quantities decrease as thermal efficiency of the power block is increased, due to the lower thermal input to the power block. Since the cost of the solar field, tower/receiver, and TES is included in the total capital investment shown in Figure 7.17B, an increase in the power block efficiency decreases the total cost of these components at a higher rate compared to the solar field area. The effect of the power block efficiency on the total capital investment for the power block and the overall CSP-T plant is shown in Figure 7.17C. As the results show, although an increase in thermal efficiency of the power block generally increases the cost of the power block, it decreases the cost of the overall CSP-T plant because, the total cost of the solar field, tower/receiver, and TES is a dominant factor affecting the total CSP-T plant cost.

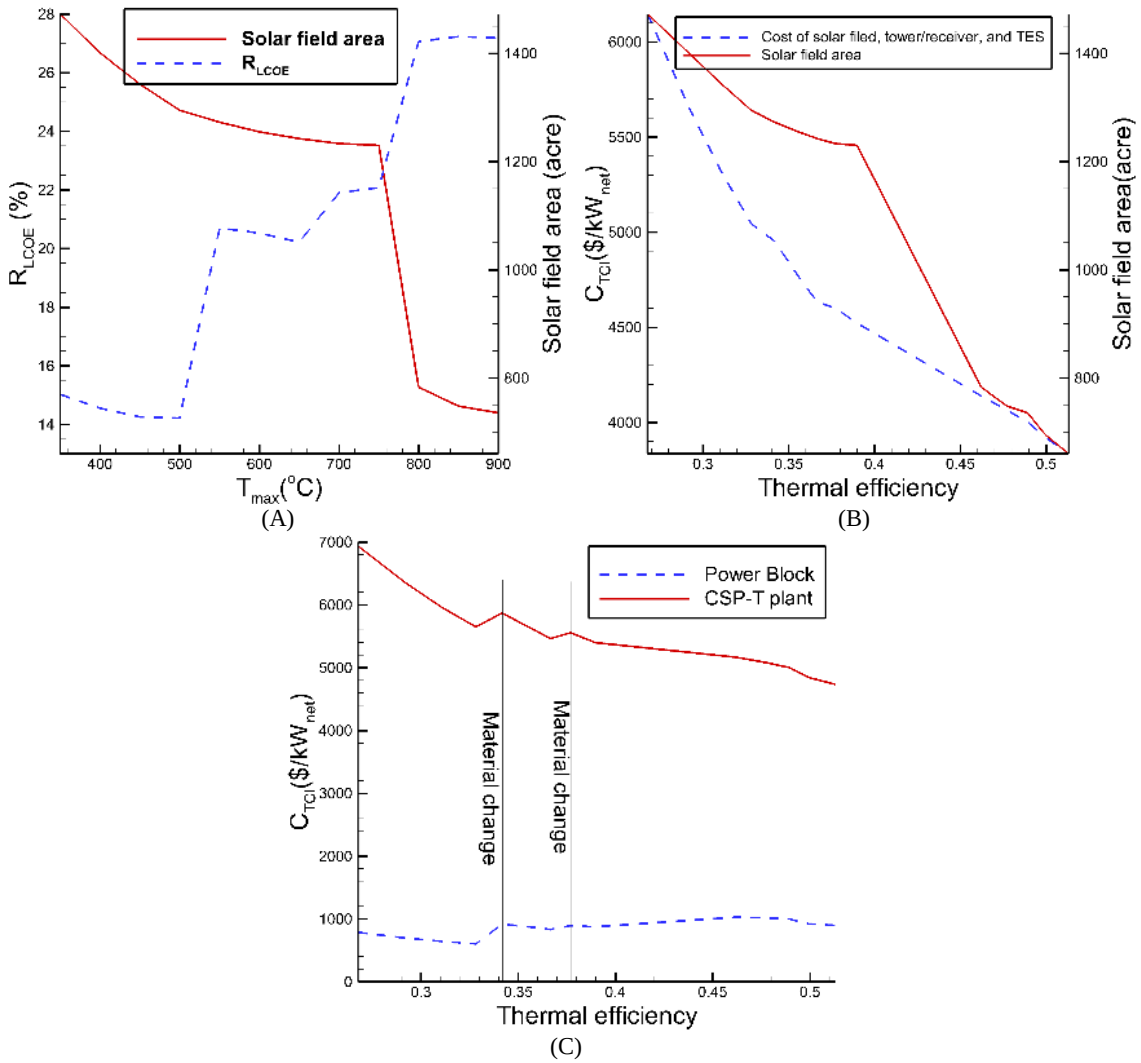

Figure 7.17. A) The effect of the maximum cycle temperature on R_{LCOE} *(%)* and area of the solar field (acre), B) The effect of thermal efficiency of the power block on the area of the solar field and the total capital investment for the solar field, tower/receiver, and TES, C) The effect of thermal efficiency of the power block on the total capital investment for the power block and the CSP-T plant.

Figure 7.18A shows the effect of a solar multiple (SM) (defined in Section 2.4.2 of Chapter 2) on the LCOE and capacity factor (CF) for a CSP-T plant integrated with a combined Brayton/ORC cycle for T_{max}=800°C, P_{max}=30 MPa, and T_{min}= 32°C, and a constant DNI (defined in Section 2.4.2 of Chapter 2). For example, there is a large decrease

in LCOE (75 $/MWh) for SM=1 and 2, which means that adding a TES to the CSP-T plant results in a significant reduction in the plant LCOE. Also, as the results show, there is no benefit of having a solar multiple higher than 4. Although the plant capacity factor (CF) increases with SM, the LCOE for a plant has the minimum value for SM = 4. The effect of the SM on the CSP-T plant capacity factor (CF) is given by Eqn. (7.2). Based on the previous studies [92], there is a quadratic relationship between the capacity factor and solar multiple.

$$CF = \frac{(2.5717*DNI+694)*(-0.0371*SM^2+0.4171*SM-0.0744)}{8760} \quad (7.2)$$

By considering daily variations in DNI, the optimum in solar multiple shifts to a higher value [92].

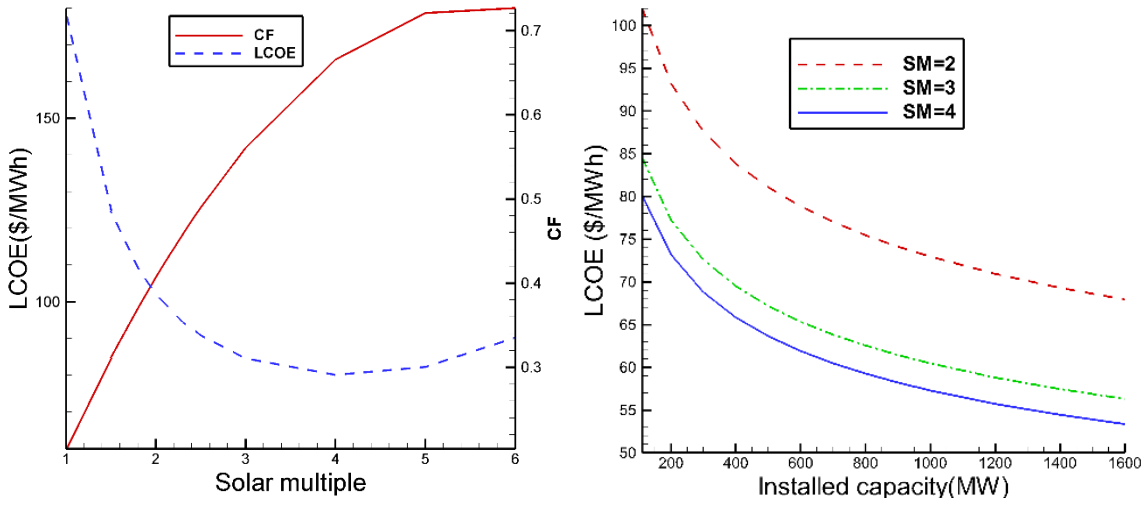

A) Solar multiple B) Installed capacity

Figure 7.18. Effect of the solar multiple and installed capacity on LCOE and capacity factor for a CSP-T plant.

Learning curves are used in economic analysis to show the rate of improvement or the cost reduction of a technology over time [118]. The empirical data show that improvement correlates to the installed capacity. Thus, as the installed capacity of the CSP-

T plants increases, the cost decreases due to the “learning by doing” effect, i.e., as more capacity is installed and a technology improves, manufacturing and construction costs decrease. Figure 7.18B shows the learning curves (LCOE vs. installed capacity) for a CSP-T plant integrated with the combined Brayton/ORC cycle for several values of the solar multiple.

According to the learning curve, the cost of a CSP-T plant may be calculated as:

$$C_t = C_0 \times \left(\frac{P_t}{P_0}\right)^{\frac{\text{Log PR}}{\text{Log 2}}} \quad (7.3)$$

where C_t is the cost at time t, C_0 is the cost at the starting year, P_t is installed capacity at time t, P_0 is installed capacity at the starting year, and PR=0.9 (90%) is the progress ratio. A progress ratio of 90% means that the LCOE is reduced by 10% each time the installed capacity doubles. The results presented in Figure 7.18B show that LCOE decreases as the installed capacity is increased. The large difference in LCOE from SM=2 and 3 can be explained by the slope of LCOE curve in Figure 7.18A. As this figure shows, the slope of the LCOE curve decreases as SM exceeds the value of 4.

7.4. Validation of Techno-Economic Results for a Simple ORC and RBC

Values of the total capital investment determined in this work were compared to the results reported by Le et al. [119] and Ho et al. [89] for a simple ORC and RBC, respectively. The cycle parameters used in the analysis are summarized in Tables 7.5 and 7.6. For the simple ORC and RBC, working fluids R25fa and CO_2 were used, respectively.

Table 7.5. Cycle parameters for simple ORC from Ref. [119].

Parameter	Value
T_{max}(°C)	119.8
Mass flow rate(kg/s)	48.08
Net power(kW)	1602
Maximum pressure (MPa)	1.92
Minimum pressure (MPa)	0.178

Table 7.6. Cycle parameters for RBC from Ref. [89].

Parameter	Value
T_{max}(°C)	700
Net power output (MW)	100
Maximum pressure (MPa)	20
Minimum pressure (MPa)	8
Minimum temperature(°C)	55

The results from this study and Refs [89, 119] are shown Tables 7.7 and 7.8. As shown in Tables 7.7 and 7.8, the total capital investment values obtained in this study are in an excellent agreement with the results from [119] and [89]. The relative error between the results obtained in this study and [119] for a simple ORC is 0.034%, while the relative error between the results for the RBC obtained in this work and [89] is 0.25%.

Table 7.7. Comparison of results for the simple ORC.

Cost	Result for R245fa from Ref. [119]	Result for R245fa from EPV-11	Relative error (%)
C_{BM}^{pump} *(k$)*	70.3	70.5	0.3
$C_{BM}^{Turbine}$ *(M$)*	378.4	378.5	0.02
C_{BM}^{eva} *(k$)*	2.16	2.161	0.05
C_{BM}^{cond} *(k$)*	431.0	431.2	0.05
C_{BM}^{motor} *(k$)*	73.9	74.1	0.3
$C_{BM}^{genrator}$ *(k$)*	94.7	94.9	0.21
C_{BM}^{wf} *(k$)*	766.5	767	0.06
C_{BM}^{spares} *(k$)*	144.2	148.05	2.66
C_{site} *(k$)*	206.0	206.26	0.129
C_{serve} *(k$)*	206.0	206.26	0.129
C_{alloc} *(k$)*	169.3	169.3	0
C_{cont} *(k$)*	846.0	847.29	0.152
$C_{startup}$ *(k$)*	554.6	555.44	0.152
C_{TCI} *(M$)*	6.101	6.1099	0.146
C_{TCI}/Net power ($/kWnet)	**4012**	**3998**	**0.34**

Table 7.8. Comparison of results for RBC.

Cost	Result for CO_2 from Ref. [1]	Result for CO_2 from EPV-11	Relative error (%)
C_{BM}^{comp} *($/kWe)*	230	232	0.87
$C_{BM}^{turbine}$ *($/kWe)*	128	125.7	1.79
C_{BM}^{heater} *($/kWe)*	212	209	1.415
C_{BM}^{ACC} *($/kWe)*	85	89	4.7
$C_{BM}^{recuperator}$ *($/kWe)*	243	240	1.234
Total($/kWe)	**898**	**895.7**	**0.25**

7.5. Techno-Economic Results for a Steam Rankine Cycle

Steam Rankine cycle is a very well-known power cycle. The economic analysis of a steam Rankine cycle was performed by the Department of Energy (DOE) and National Energy Technology Laboratory (NTEL) [120]. The results show that for a gross power output of 110 MW, the cost of a power block operating at the subcritical steam conditions is 1440$/kW$_{gross}$. For a steam Rankine cycle operating at the supercritical steam conditions, the power block cost is higher, 1496 $/kW$_{gross}$ due to the higher cost of materials used for high-pressure parts of the plant. The cost of each component is summarized in Table 7.9. More details can be found in Refs. [120, 121].

Table 7.9. Estimated cost for a steam Rankine cycle.

Components	**Subcritical**	**Supercritical**
Turbomachinery and generator($/kW)	275	286
Heat exchangers and pumps($/kW)	255	267
steam generator ($/kW)	130	147
Dry cooling systems($/kW)	330	330
Piping, insulation, valves, and fitting ($/kW)	100	116
Working fluid treatment system ($/kW)	30	30
Electrical system, control system, buildings, fire protection system, Mechanical system ($/kW)	320	320
Sum ($/kW)	**1440**	**1496**

CHAPTER 8: HEAT REJECTION BY DRY COOLING

8.1. Overview

This chapter is concerned with the direct dry cooling system described in Section 1.5.3 of Chapter 1. Since it is expected that the majority of the CSP-T plants will be built in deserts and other arid areas, the heat rejection will be accomplished by employing a direct or indirect dry cooling tower (CT) system. To alleviate the negative effects of dry cooling, a Cold Energy Thermal Storage System (CE-TES) is proposed. The System is described in Section 8.3. The different configurations of the heat rejection system (wet, dry, direct, and indirect) were described in Section 1.5.3 of Chapter 1.

The effect of a CE-TES system used in conjunction with the dry cooling and closed-loop hybrid cooling on net power output of several power cycles was analyzed. A regenerative steam Rankine cycle with a reheat (RSRC), a simple organic Rankine cycle (ORC) using R11, a CO_2 regenerative Brayton cycle (RBC), and a combined CO_2 Brayton/R11 ORC cycle were selected for the analysis. The results are presented in the sections below.

8.2. Thermodynamic Power Cycle Modeling

One of the main parameters governing performance of an air-cooled condenser (ACC) is the difference between the condensing temperature (T_{cond}) and the inlet air temperature ($T_{a,inlet}$), defined as the initial temperature difference (ITD), or as the approach.

$$ITD = T_{cond} - T_{a,inlet} \tag{8.1}$$

For a given ACC geometry, the heat load Q (W/s) is related to the *ITD* by

$$\frac{Q}{ITD} = Constant \tag{8.2}$$

For a given heat load, the “size” (i.e., the dimensionless mass transfer size, similar to the NTU) of an ACC is inversely related to the *ITD* as

$$ACC \text{ "Size" } \propto 1/ITD^{\beta} \quad (8.3)$$

where β is a constant. Thus, a low ITD relates to a large ACC “size”.

The Ivanpah CSP plant, located in southern California, was selected as a Reference plant for the analysis. Annual variation in the ambient temperature (T_{amb}) at the Ivanpah location for 2015 is shown in Figure 8.1 [94]. The minimum and maximum daily temperatures in 2015 were -7 and 45°C, respectively [94]. The annual mean temperature of 19.75°C was chosen as the design [94] temperature or the reference point for the heat rejection analysis.

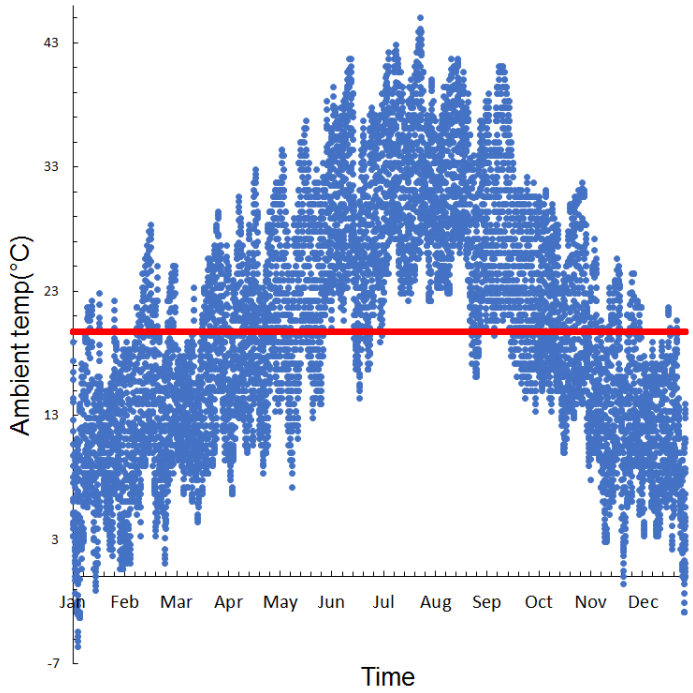

Figure 8.1. Annual variation of ambient temperature at Ivanpah CSP.

The effect of the ambient temperature on thermal efficiency of a regenerative steam Rankine cycle with the reheat (RSRC), simple organic Rankine cycle (ORC) using R11,

CO_2 regenerative Brayton cycle (RBC), and a combined CO_2 Brayton/R11 ORC cycle is shown in Figure 8.2A. As the results show, an increase in the ambient temperature has a negative effect on thermal efficiency. Since an ORC is working with a lower maximum temperature and lower maximum-to-minimum temperature difference compared to other cycles, it is more sensitive to changes in the ambient temperature compared to other power cycles. Relative changes in thermal efficiency are calculated by using Eqn. (8.4).

$$d\eta_{th}(\%) = \frac{\eta_{th} - \eta_{th,ref}}{\eta_{th,ref}} * 100 \quad (8.4)$$

The quantity $\eta_{th,ref}$ is thermal efficiency of the power cycle at the reference point, where the minimum temperature was selected to be equal to the annual average of the ambient temperature at the Ivanpah location (19.75°C).

The results of the performance analysis performed for the selected power cycles presented in Figure 8.2B show that variation in the ambient temperature corresponding to the Ivanpah location would change thermal efficiency of an ORC by up to ±21.5% or ±4%-points. Of the analyzed power cycles, the least sensitive cycle is the RBC; the ambient temperature variation corresponding to the Ivanpah location would change its thermal efficiency by up to ±7% or 2%-points.

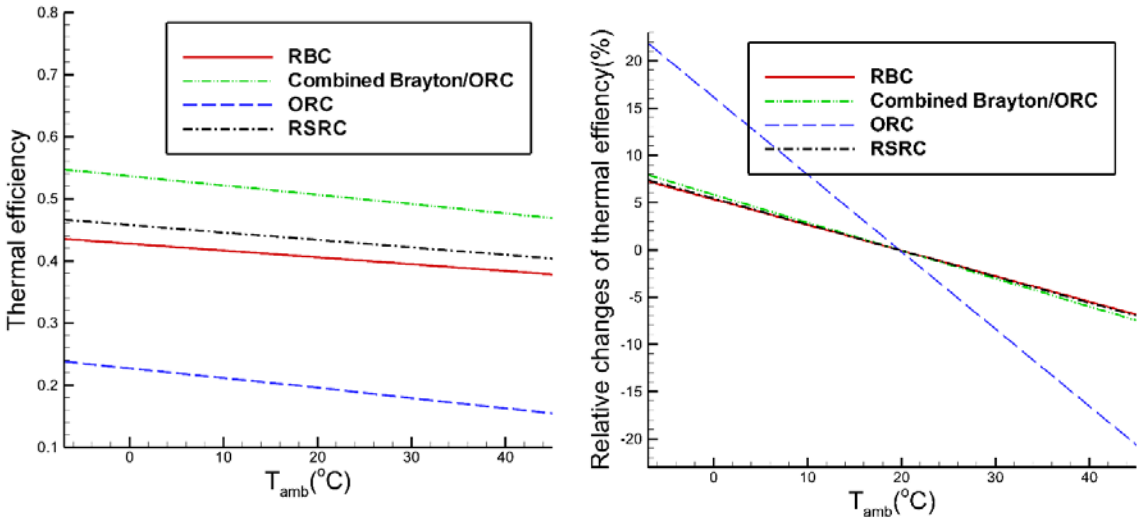

A) η_{th} B) $d\eta_{th}$

Figure 8.2. Effect of the ambient temperature on thermal efficiency of the analyzed power cycles.

8.2. Dry-Cooled Power Cycles Coupled with a CE-TES

8.2.1 Dry-cooled regenerative steam Rankine cycle with the reheat

A schematic representation of a dry-cooled RSRC coupled with the cold thermal energy (heat) storage system (CE-TES) is presented in Figure 8.3. In a dry cooling system, the power cycle is cooled by air instead of water (more details can be found in Section 1.5.3 of Chapter 1). The cycle operating parameters are summarized in Table 8.1. The gross power output of the cycle of 100 MW corresponding to the maximum steam temperature of 550°C and heat rejection at the reference temperature of 19.75°C was used in the analysis.

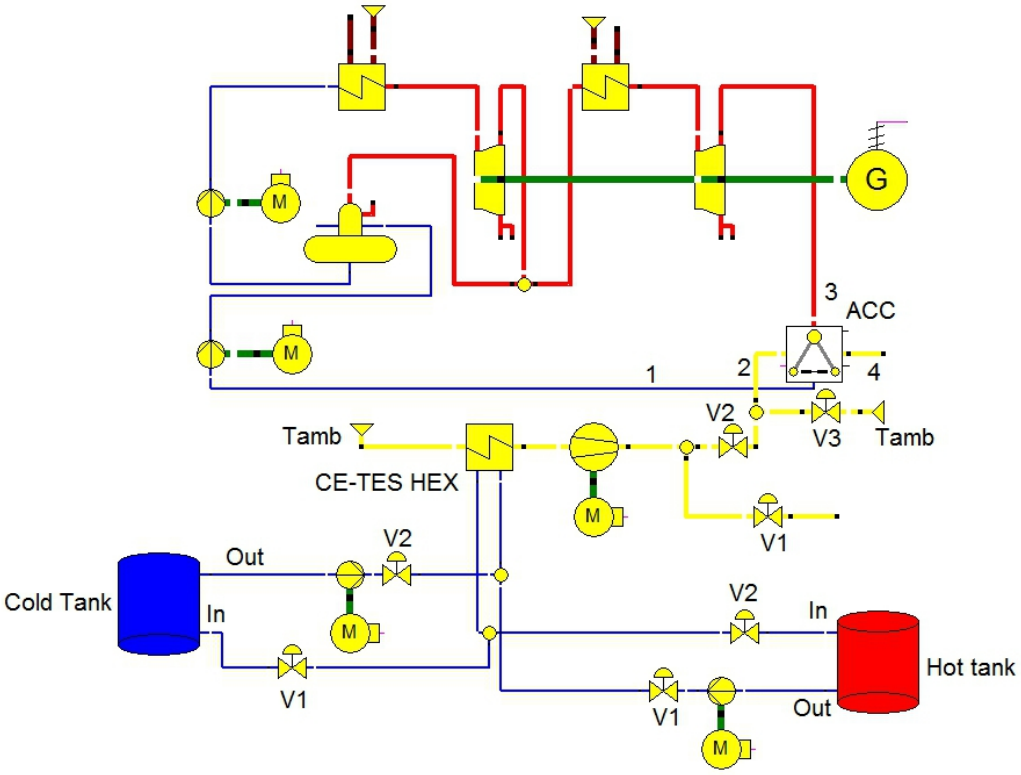

Figure 8.3. Schematic of a dry-cooled RSRC coupled with a CE-TES.

Table 8.1. Operating Parameters of a Dry-Cooled RSRC.

Power cycle parameter	Value
T_{max}(°C)	550
ITD (°C)	17
$T_{min}(T_1)$ (°C)	T_{amb}+ITD
P_{max}(MPa)	20
Pump isentropic efficiency	0.85
Turbine isentropic efficiency, HP	0.88
Turbine isentropic efficiency, LP	0.917
Steam Mass flow rate(kg/s)	80.02
Gross Power, Net power(MW_e)	100, 97.3
Fan efficiency	0.55 to 0.85
Air side pressure drop in heat exchanger and air-cooled condenser (mbar)	0.75 (0.301 In H_2O)

8.2.2 Dry-cooled simple ORC

A schematic representation of a dry-cooled ORC coupled with a CE-TES is illustrated in Figure 8.4. Due to the technical issues related to the EPV-11 graphical user interface (GUI), the symbol used for the ACC in a simple ORC is different from the symbol used for the same component (ACC) in a RSRC. The cycle operating parameters are summarized in Table 8.2. The gross power output of the ORC of 10 MW corresponding to the maximum cycle temperature of 300°C, heat rejection at the reference temperature of 19.75°C, and R11 as the working fluid was used in the analysis.

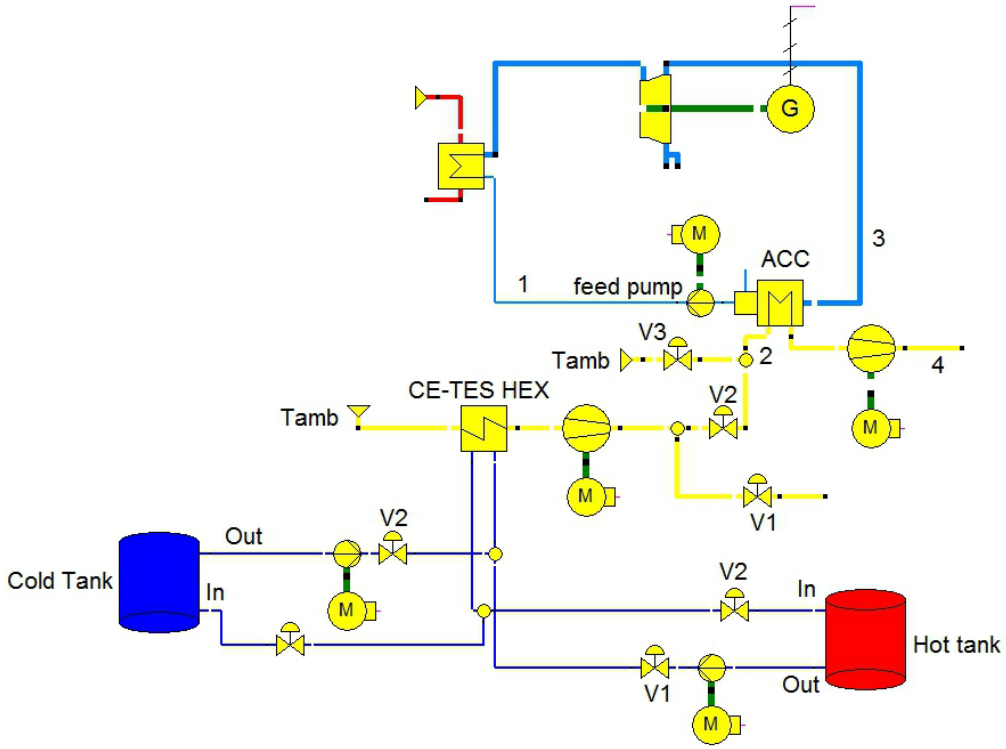

Figure 8.4. Schematic of a dry-cooled simple ORC coupled with a CE-TES.

Table 8.2. Operating Parameters of a Dry-Cooled Simple ORC.

Power cycle parameter	Value
T_{max}(°C)	300
ITD (°C)	8
$T_{min}(T_1)$ (°C)	T_{amb}+ITD
P_{max}(MPa)	P_{sat}
Pump isentropic efficiency	0.80
Turbine isentropic efficiency	0.87
Steam Mass flow rate(kg/s)	117.6
Gross Power, Net power(MW_e)	10, 9.01
Fan efficiency	0.55 to 0.85
Air side pressure drop in heat exchanger and air-cooled condenser (mbar)	0.75 (0.301 In H_2O)

8.2.3 Dry-cooled CO_2 regenerative Brayton cycle

A schematic representation of a dry-cooled CO_2 RBC coupled with a CE-TES is presented in Figure 8.5. Due to the technical issues related to the EPV-11 GUI, the symbol used for ACC in the RBC is different from the symbol used in the RSRC. The cycle operating parameters are summarized in Table 8.3. The gross power output of the cycle of 100 MW corresponding to the maximum cycle temperature of 900°C, heat rejection at the reference temperature of 19.75°C, and CO_2 as the working fluid was used in the analysis.

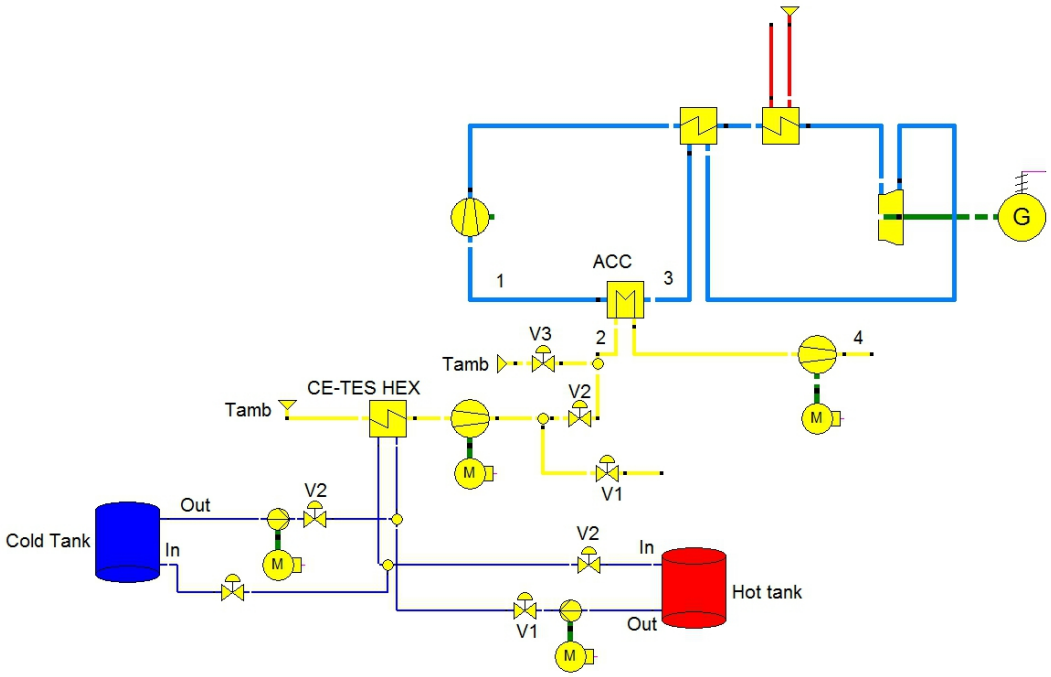

Figure 8.5. Schematic of a dry-cooled RBC coupled with a CE-TES.

Table 8.3. Operating Parameters of a Dry-Cooled RBC.

Power cycle parameter	Value
T_{max}(°C)	900
ITD (°C)	17
$T_{min}(T_1)$ (°C)	T_{amb}+ITD
P_{max}(MPa)	20
Pump isentropic efficiency	0.80
Turbine isentropic efficiency	0.9
Steam Mass flow rate(kg/s)	326
Gross Power, Net power(MW_e)	100, 52.5
Fan efficiency	0.55 to 0.85
Air side pressure drop in heat exchanger and aircooled condenser (mbar)	0.75 (0.301 In H_2O)

8.2.4 Dry-cooled CO_2 regenerative Brayton/ORC cycle

A schematic representation of a dry-cooled combined Brayton/ORC cycle coupled with a CE-TES is shown in Figure 8.6. Due to the technical issues related to the EPV-11 GUI, the symbol for ACC in the combined Brayton/ORC cycle is different from the symbol used in the RSRC.

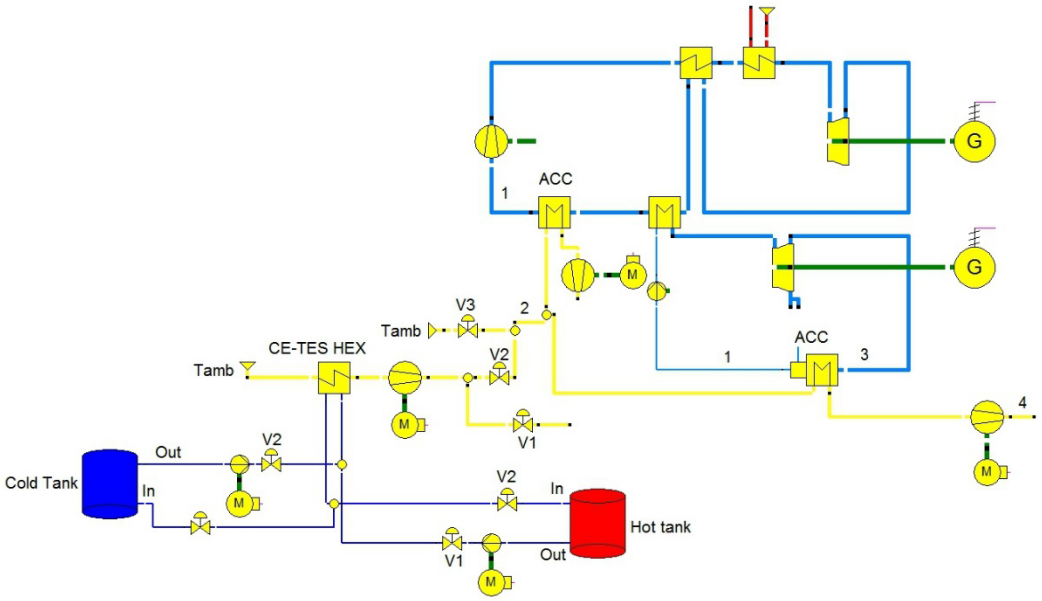

Figure 8.6. Schematic of a dry-cooled combined Brayton/ORC coupled with a CE-TES.

The operating parameters for the topping and bottoming cycles are summarized in Tables 8.3 and 8.4, respectively. The analysis was performed for the optimal pressure ratio of the topping cycle. The gross power output of the cycle of 100 MW corresponding to the maximum cycle temperature of 900°C, heat rejection at the reference temperature of 19.75°C, and CO_2 and R11 as the working fluids for the topping and bottoming cycles was used in the analysis.

Table 8.4. Bottoming cycle properties of a combined Brayton/ORC cycle.

Power cycle parameter	**Value**
T_{max}(°C)	268
ITD (°C)	8
$T_{min}(T_1)$ (°C)	T_{amb}+ITD
P_{max}(MPa)	P_{sat}
Pump isentropic efficiency	0.80
Turbine isentropic efficiency	0.87
Steam Mass flow rate(kg/s)	220
Gross Power, Net power(MW_e)	15.473,14.2
Fan efficiency	0.55 to 0.85
Air side pressure drop in heat exchanger and air-cooled condenser (mbar)	0.75 (0.301 In H_2O)

The control valves V1, V2 and V3 in Figures 8.3 and 8.6 should be open or closed during the system charging and discharging (see Section 8.3). Table 8.5 shows the operation status of control valves V1, V2, and V3 during the system charging and discharging, and during the normal (regular) operation when CE-TEs is not used.

Table 8.5. Operation of different control valves for different power cycles.

Control valve	Operation status
V1= Closed, V2=Open, V3=Closed	Discharging
V1= Open, V2=Closed, V3=Closed	Charging
V1= Closed, V2=Closed, V3=Open	Normal operation (Without using CE-TES)

8.3. CE-TES Coupled with Dry Cooling

As shown in Figures 8.7 and 8.8, the CE-TES system includes the Warm and Cold Tanks. During the night, when the ambient air temperature is much lower compared to the day-time temperature (especially in deserts and arid regions), the heat storage fluid from the Warm Tank is pumped through the air-to-water heat exchanger (HEX), cooled by the cold ambient air, and stored in the Cold Tank as shown in Figure 8.7. This operating mode is referred to as charging. During the CE-TES charging, the heat is rejected from the power cycle by the ACC. The water-glycol mixture is proposed as the heat storage fluid due to its low cost, high specific heat capacity, and low corrosiveness. Performance of the heat storage system may be improved by using encapsulated phase change materials (PCHs) immersed in the Cold Tank.

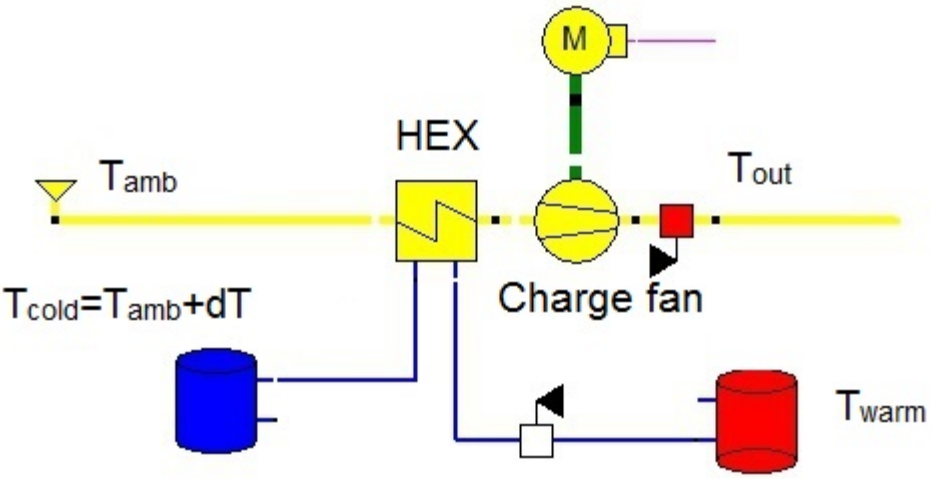

Figure 8.7. CE-TES charging Process.

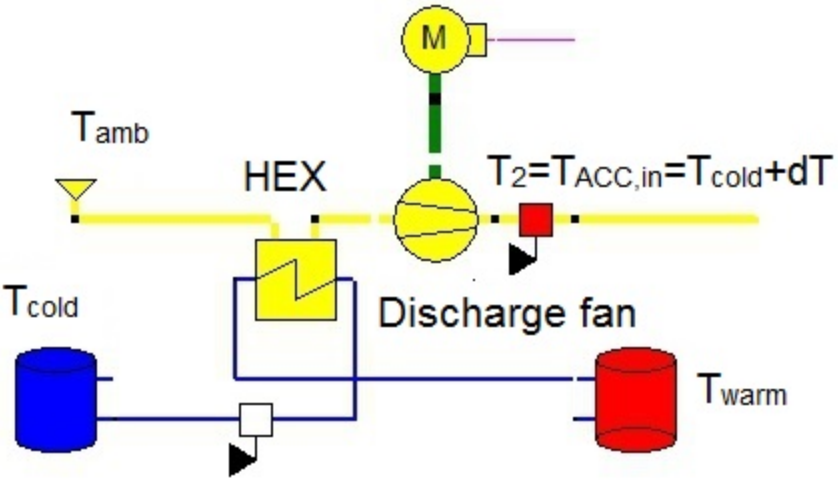

Figure 8.8. CE-TES discharging process.

During the hottest period of the day, the hot ambient air is cooled in the air-to-water HEX prior to entering the air-cooled condenser (ACC) by the cold heat storage fluid pumped from the Cold Tank. The warm heat storage fluid leaving the HEX is stored in the Warm Tank, as shown in Figure 8.8. This operating mode is referred to as discharging.

The charging and discharging modes of operation, superimposed on a daily variation of the ambient temperature, are presented in Figure 8.9. To illustrate the operating principle of the CE-TES and evaluate its performance, the analysis of the CE-TES performance was performed for the hottest day of the year (July 11th for the Ivanpah location).

As presented in Figure 8.9, on July 11th the sunrise and sunset times are 5:36 AM and 20:01 PM, respectively. During the night when the ambient air temperature is much lower compared to the day-time temperature, the Cold Tank is charged with the heat storage fluid cooled by the ambient air in the air-to-water HEX. As shown in Figure 8.9, charging starts at midnight (12:00 AM) and ends at sunrise.

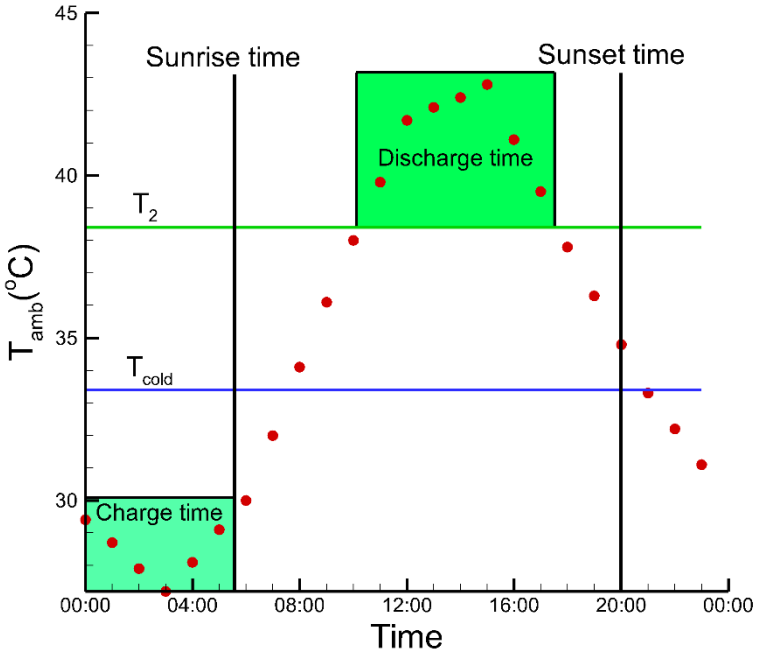

Figure 8.9. Variation of the ambient temperature, CE-TES charging, and discharging on July 11th.

The temperature of the heat storage fluid in the Cold Tank, i.e., the Cold Tank temperature (T_{cold}) after the system charging is calculated by using Eqn. (8.5), where *n* is duration of the charging time interval in hours. For the charging time interval of 6 hours shown in Figure 8.9 and the approach[3] [122] (temperature difference between the ambient air entering the air-to-water HEX and the cold heat storage fluid leaving it and entering the Cold Tank) of 5ºC, the Cold Tank temperature is equal to 33.4°C.

$$T_{cold} = \frac{\sum_{i=1}^{n} T_{amb}(i)}{n} + dT = \frac{29.4+28.7+27.9+27.2+28.1+29.1}{6} + 5 = 28.5 + 5 = \ 33.\ 4℃ \quad (8.5)$$

During the hottest period of the day, the hot ambient air is cooled in the air-to-water HEX prior to entering the ACC by the cold fluid leaving the Cold Tank at temperature T_{cold}. The warm heat storage fluid leaving the HEX is stored in the Warm Tank. Figure 8.8 show schematic of the discharging process.

Accounting for the approach dT, the temperature of the air leaving the air-to-water HEX, i.e., the ACC inlet temperature $T_{ACC,in}$ can be determined from the following expression:

$$T_{ACC,in} = T_{cold} + \ dT \quad (8.6)$$

For the Cold Tank temperature of 33.4ºC calculated by Eqn. (8.5) and the approach of 5ºC, $T_{ACC,in}$ is equal to 38.4ºC. This is the minimal air temperature at the ACC inlet than could be achieved on July 11th for the 6-hour charging interval shown Figure 8.9 and the approach of 5ºC.

[3] In general, the approach is defined as the temperature difference between the leaving process fluid and the entering service fluid.

The air temperature $T_{ACC,in}$ determines the beginning of the system discharging time interval and its duration, because for the CE-TES to be effective, the ambient temperature T_{amb} has to be higher than $T_{ACC,in}$. The discharging time interval for July 11th is presented in Figure 8.9.

By combining Eqns. (8.5) and (8.6), the minimal difference between the ACC inlet temperature and the average ambient temperature during the CE-TES charging can be defined as:

$$\Delta T = 2 * dT \tag{8.7}$$

ΔT is an important parameter since, during the CE-TES discharging, it determines the minimum temperature of the cooling air at the ACC inlet, and thus the turbine back-pressure and its power output, and thermal efficiency of the power block. A lower value of ΔT increases the power output due to the lower turbine back-pressure, and generation due to the lower value of $T_{ACC,in}$ and longer discharging time interval. However, the HEX size and its cost increase exponentially with ΔT [122].

To determine the mass flow rate of the heat storage fluid (water-glycol mixture), the HEX energy balance needs to be performed. The energy balance for the HEX is:

$$\dot{m}_{air} C_{p,air} (T_{amb-} T_2) = \dot{m}_{water} C_{p,water} (T_{warm-} T_{cold}) \tag{8.8}$$

The HEX effectiveness of 0.85 was assumed. According to the HEX theory [83], the heat exchanger effectiveness is defined as

$$\varepsilon = \frac{\dot{m}_{air} C_{p,air} (T_{amb-} T_2)}{\dot{m}_{water} C_{p,water} (T_{amb-} T_{cold})} = 0.85 \tag{8.9}$$

Since ε and T_2 are known, the flow rate of the heat storage fluid ($\dot{m}_{water}$) can be obtained.

The analysis of the power cycles described in Section 8.2 was performed to determine the increase in the daily and annual electricity (energy) generation that would be achieved by using the CE-TES system at the Ivanpah location.

The daily and annual increases in energy generation dE_{day} and dE_{year} were calculated by using Eqns. (8.10) to (8.13):

$$dE_{day}(kWh) = Total\ energy\ generation\ with\ TES\ for\ a\ day - Total\ energy\ generation\ without\ TES\ for\ a\ day \quad (8.10)$$

$$dE_{day}(\%) = \frac{Total\ energy\ generation\ with\ TES\ for\ a\ day - Total\ energy\ generation\ without\ TES\ for\ a\ day}{Total\ energy\ generation\ without\ TES\ for\ a\ day} 100 \quad (8.11)$$

$$dE_{year}(kWh) = Total\ energy\ generation\ with\ TES\ for\ a\ year - Total\ energy\ generation\ without\ TES\ for\ a\ year \quad (8.12)$$

$$dE_{year}(\%) = \frac{Total\ energy\ generation\ with\ TES\ for\ a\ year - Total\ energy\ generation\ without\ TES\ for\ a\ year}{Total\ energy\ generation\ without\ TES\ for\ a\ year} \times 100 \quad (8.13)$$

It was assumed that a CSP plant is operating from the sunrise to the sunset. The net power output of the analyzed power cycles is presented in Figure 8.10 as a function of time (0 to 24 hours) for July 11th for the case without the CE-TES (the Base Case) and the case with the CE-TES in operation (as described previously). As the results show, without the CE-TES (Base Case), the CSP power output changes throughout the day as the ambient temperature varies; it decreases as the ambient temperature increases, reaches the minimum value during the hottest time of the day, and increases as the ambient temperature decreases toward the end of the day – forming a typical "U-shape". With the CE-TES system, the cycle power output is constant during the discharging time interval since the ambient air is cooled by the heat storage fluid from the Cold Tank to a constant temperature $T_{ACC,in}$. Since during the discharging time interval the power output is higher compared to the Base Case,

daily energy generation is also higher. The results on net power output presented in Figure 8.10 account for the CE-TES fan and pump power requirements.

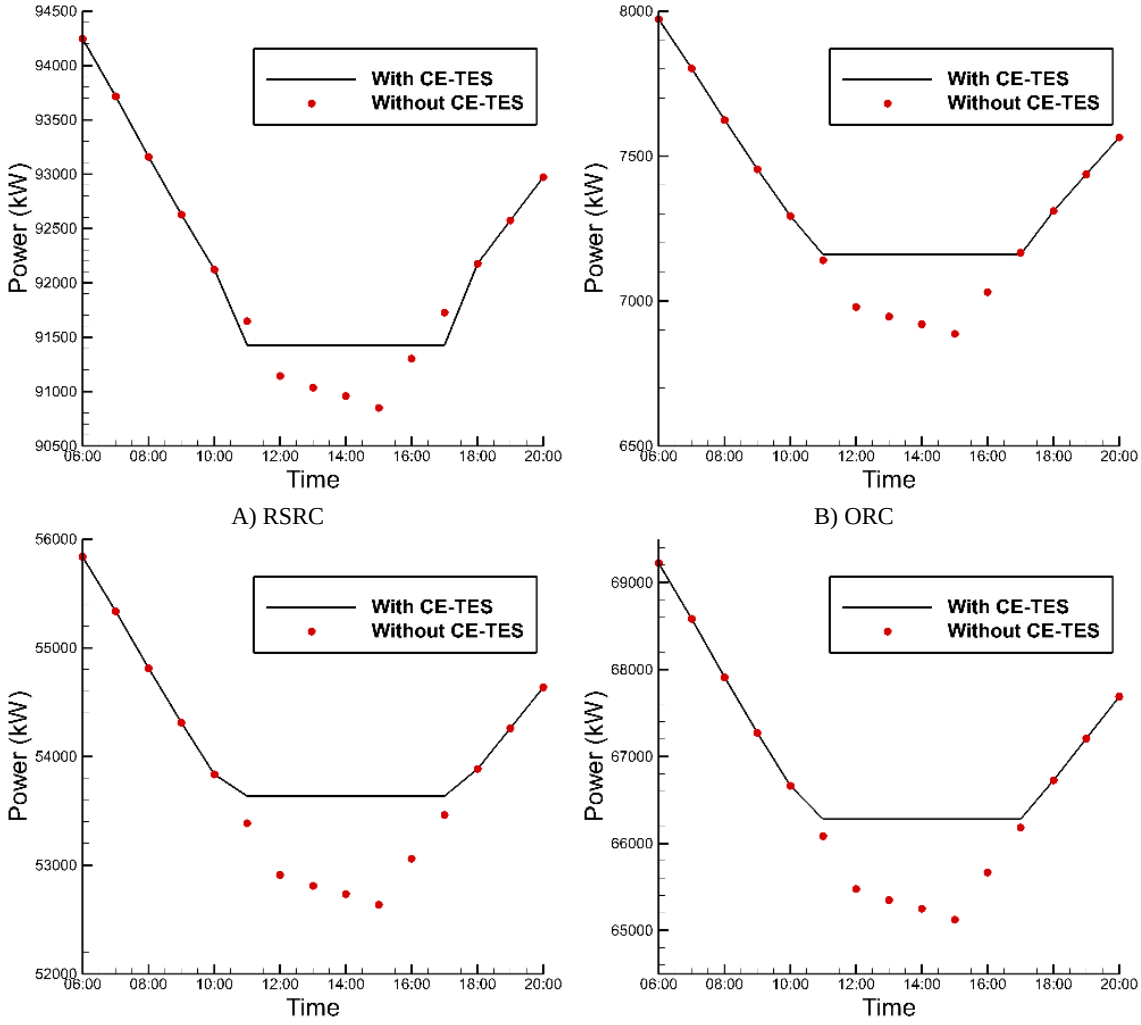

Figure 8.10. Net power output of the analyzed power cycles with and without the CE-TES on July 11th.

The daily energy generation increase for the analyzed power cycles is summarized in Table 8.6 for July 11th. As the results show, the increase in the daily energy generation is the highest for the ORC and the lowest for the RSRC. The fan power requirements for the CE-TES are the lowest for the RBC, compared to other analyzed power cycles. As it

can be seen in Table 8.6, about 75% of the required CE-TES power is used by the discharge fan (see Figure 8.8) during the discharging process, while the rest is used during the charging process.

Table 8.6. Daily energy generation increase for analyzed power cycled on July 11th.

Cycle	dE_{day} (kWh)	dE_{day} (%)	Total energy required for CE-TES fan (kWh)	Energy required for discharge fan (kWh)	Energy required for charge fan (kWh)
RSRC	1858	0.14	2944	2178	765
ORC	1053	0.96	600	450	150
RBC	4453	0.55	178	135	43
Combined Brayton/ORC	4822	0.48	1778	1333	444

Since the ACC inlet temperature and flow rate, and effectiveness of the air-to-water heat exchanger (HEX) are known, the mass flow rate of the heat storage fluid (water-glycol mixture), m_{water}, can be obtained from Eqn. (8.8).

For the analyzed case, the Hot Tank temperature and the total amount of the heat storage fluid required for the CE-TES, calculated by using Eqns. (8.14) and (8.15) are:

$$T_{hot} = \frac{\sum_{i=1}^{n} \dot{m}_i T_{hot}(i)}{\sum_{i=1}^{n} \dot{m}_i} = 40.69℃ \quad (8.14)$$

$$\dot{m}_{total} = \sum_{i=1}^{n} \dot{m}_i = 4446 \ \frac{kg}{s} \rightarrow m_{total} = \dot{m}_{total} * 3600 = 16{,}005{,}600 \ kg \quad (8.15)$$

where *n* is duration of the discharging time interval in hours.

The analysis procedure applied for July 11th may be repeated for other days in a year to determine the annual energy generation increase. The size of the storage tanks needed for the CE-TES system will be governed by the highest daily storage requirement in a year.

8.4. Closed-Loop Hybrid Cooling

As presented in the previous section, the CE-TES system integrated with a direct dry cooling method results in a better power block performance during the hottest time of the day, thus increasing the daily (and annual) electricity generation. However, as the results presented above show, the proposed CE-TES system configuration is only moderately effective in increasing the generation. This is because the heat is being exchanged twice between the heat storage fluid and the ambient air.

During charging, the heat is transferred from the warmer heat storage fluid to the colder ambient air via the air-to-water heat exchanger (HEX). Due to the finite value of the approach dT, the Cold Tank temperature is higher compared to the temperature of the ambient cooling air. During discharging, the hot ambient air is cooled by the cold heat storage fluid from the Cold Tank prior to entering the ACC. Due to the finite value of the approach, temperature of the cooling air entering the ACC is higher compared to the Cold Tank temperature. Since the heat is transferred twice, the minimal overall temperature difference ΔT between the cooled cooling ambient air at the ACC inlet during the day and the cold ambient air during the night is equal to 2dT. Assuming the approach of $5^{o}C$, the overall temperature difference is $10^{o}C$, i.e., $T_{ACC,in}$ is considerably higher compared to the ambient air temperature at the night time. The high ΔT has a significant negative effect on performance of the CE-TES system and, thus on the power block performance.

A closed-loop hybrid method is proposed to alleviate the negative effect of a high temperature difference ΔT associated with the dry cooling method. As presented in Figures 8.11 and 8.12, during the CE-TES discharging, the cold heat storage fluid from the Cold

Tank is circulated through to the ACC tube bundles without exchanging heat with the ACC cooling air. The CE-TES charging process is the same as for the dry cooling system.

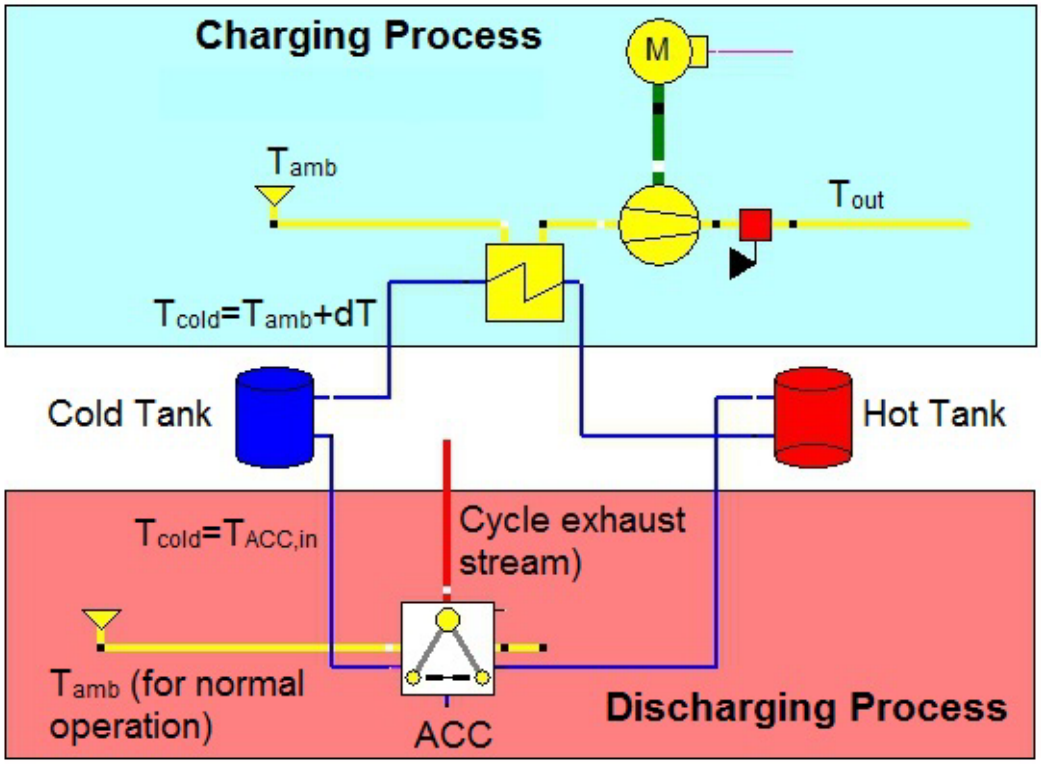

Figure 8.11. Charging and discharging processes for the closed-loop hybrid cooling system.

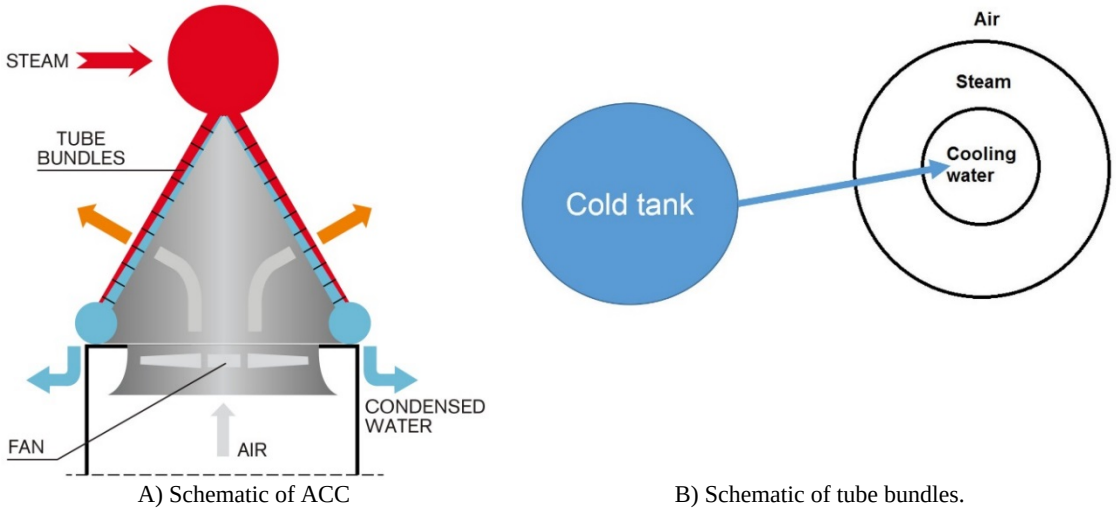

A) Schematic of ACC B) Schematic of tube bundles.

Figure 8.12. Schematic of the air-cooled condenser and a modified ACC tube.

The design of the standard ACC tube bundles will need to be modified to include the concentric inner tube for the cold heat storage fluid. With the modified design, the steam will be cooled and condensed by the cold heat storage fluid flowing through the inside tube during the discharging time and by the ambient air flowing on the outside of the ACC tube during the normal operating time, as shown schematically in Figure 8.12B. After passing through the ACC tube bundle, the warm heat storage fluid will be stored in the Warm Tank completing the hybrid cooling loop.

Since the heat transfer coefficient during the phase change (condensation, in this case) is very high, the temperature difference between the heat storage fluid and condensing steam is very small. Thus, neglecting the heat conduction through the inner tube wall, it can be assumed that the overall temperature difference ΔT for the closed-loop hybrid cooling system is approximately equal to the approach associated with the air-to-water heat exchanger (HEX) during the system charging, i.e.

$$\Delta T_{hybrid} = dT \tag{8.16}$$

To illustrate the operating principle of the closed-loop hybrid CE-TES, evaluate its performance, and compare it to the dry cooling system described in Section 8.4, the analysis was performed for the hottest day of the year (July 11th for the Ivanpah location). Also, the amount of the heat storage fluid and the size of the storage tanks were assumed to be the same as for the dry cooling system. Therefore, duration of the discharge cycle is shorter compared to the dry cooling system. Since the heat storage fluid is used for direct cooling, the discharge fan for the cooling air and the air-to-water heat exchanger (HEX) are not used during the discharge cycle. The only power required during the discharge cycle

is the power for the circulating pumps, which is much smaller compared to the fan power. Also, since in the closed-loop hybrid cooling system the heat between the ambient air and cooling fluid is transferred only once, the overall temperature difference ΔT is equal to one half of the overall temperature difference for the dry cooling system. Therefore, as the results presented in Figure 8.13 and Table 8.7 show, the closed-loop hybrid cooling system is significantly more efficient, compared to the dry cooling system and the increase in generation is considerably higher despite shorter discharge time.

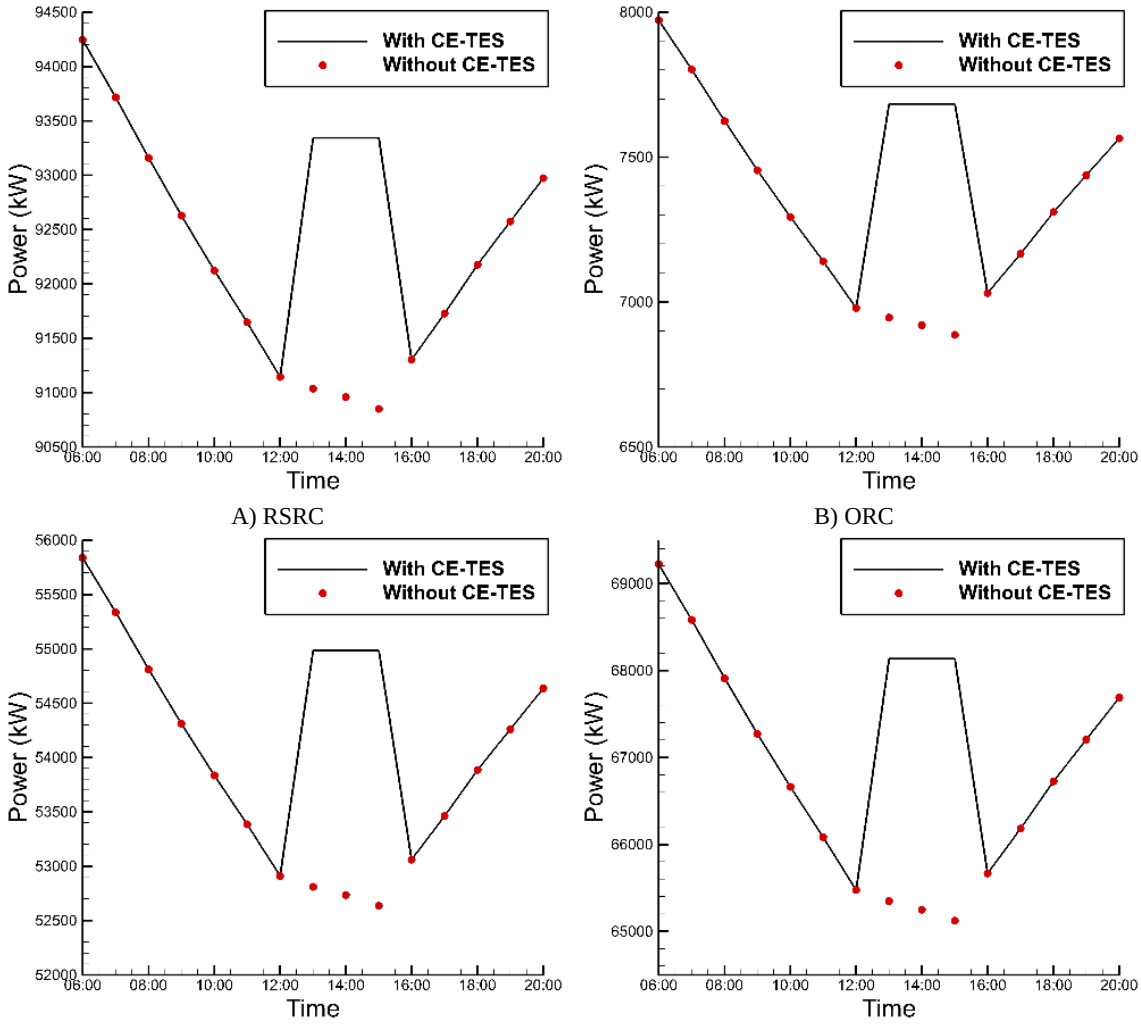

Figure 8.13. Net power output of the analyzed power cycles with and without the closed-loop hybrid cooling system on July 11th.

As the results presented in Figure 8.13 show, the net power output of the analyzed power cycles varies during the day as temperature of the ambient air changes. As described before, for the Base Case, the net power output decreases as the ambient temperature increases, reaches the minimum during the hottest period of the day, and increases toward the end of the day as the ambient air temperature decreases. With the closed-loop hybrid cooling system in operation, i.e., during the discharging period, the cold heat storage fluid from the Cold Tank is circulated through the ACC tube bundles, as presented in Figure 8.12B, assisting in steam condensation, and lowering condensation temperature compared to the dry cooling system. The lower condensation temperature results in a lower turbine back-pressure, and thus in higher power output and higher generation.

As mentioned before, since the amount (volume) of the heat storage fluid used for the closed-loop hybrid and dry cooling was assumed to be the same to allow for a direct comparison of the two systems, duration of the discharge period for the hybrid system is shorter compared to the dry cooling system and, as shown in Figure 8.9, it is centered around the hottest time of the day (from 10:00 AM to 17:00 PM on July 11th). However, if the amount (volume) of the heat storage fluid in the CE-TES were increased, duration of the discharge period would increase, resulting in a larger increase in energy generation. The optimal volume of the heat storage fluid in the CE-TES system could be determined by performing economic analysis to determine the site-specific cost-benefit tradeoffs.

The daily increase in energy generation for the analyzed power cycles coupled with the dry and closed-loop hybrid cooling systems is compared in Table 8.7 for July 11th. As the results show, the daily increase in energy generation for a power block cooled by the closed-loop hybrid system is significantly higher compared to the dry cooling system, and

is the highest for the ORC system for the reasons discussed in Section 8.3. Increasing the volume of the heat storage fluid would further increase the difference between the two cooling systems.

Table 8.7. Comparison of the increase in daily energy generation between the dry and closed-loop hybrid cooling systems.

Cycle	$dE_{day,dry}$ (kWh)	$dE_{day,dry}$ (%)	$dE_{day,hybrid}$ (kWh)	$dE_{day,hybrid}$ (%)	Relative increase from dry to hybrid cooling (%)
RSRC	1858	0.14	7065	0.51	380
ORC	1053	0.96	2298	2.1	218
RBC	4453	0.55	6779	0.84	152
Combined Brayton/ORC	4822	0.48	8862	0.89	183

As discussed in Section 8.3, the analysis procedure used for July 11th to illustrate the CE-TES concept and quantify its benefits may be repeated for other days in a year to determine the annual increase in energy generation. The size of the cold and warm storage tanks will be determined by the highest daily storage requirement.

8.5. Results and Discussion

8.5.1 Charging time and duration – Charging scenarios

As presented in Figure 8.9, the ambient air temperature varies during the day and, for the Ivanpah location, it is generally the lowest between the midnight and sunrise (3 AM on July 11th). The duration and the onset of the charging period affect the Cold Tank temperature at the end of the charging period. The analysis was performed for July 11th where the onset and duration of the charging period (charging time, CT) was varied to determine the effect on system performance. The following charging scenarios were investigated:

1. Scenario 1: Charging from 12:00 AM (midnight) until sunrise (5:36 AM)

2. Scenario 2: Charging from 01:00 AM until sunrise (5:36 AM)

3. Scenario 3: Charging from 02:00 AM until sunrise (5:36 AM)

4. Scenario 4: Charging begins 1hr before the time of the minimum ambient temperature and ends 1hr after the time of the minimum ambient temperature.

Expressing the time of the day as a function of the ambient temperature, the charging time may be defined as:

$$t\left(T_{amb,min}\right) - 1hr < CT(hr) < t\left(T_{amb,\min}\right) + 1hr \quad (8.16)$$

5. Scenario 5: Charging time is set for 1 hour at the time of the minimum ambient temperature.

The analysis was performed for the approach dT of 5^{o}C and the CE-TES coupled with the dry-cooled RSRC power block. The results are presented in Table 8.8, as a specific increase in energy generation (i.e., the increase in energy generation per unit volume of the heat storage fluid in the system) as functions of the Charging Scenarios 1 to 5 described above. The specific increase in energy generation is a good indicator of system economics: the higher the increase in energy generation per unit volume of the heat storage fluid in the system, the better the economics. The results show that Charging Scenario 4 (charging begins one hour before the minimum ambient air temperature and ends one hour after) is the best choice for the Ivanpah location, resulting in the highest specific increase in daily energy generation. Charging Scenario 5 is the second best.

The subsequent analyses were performed by using the best charging scenario (Charging Scenario 4) both for the dry and closed-loop hybrid cooling systems.

Table 8.8. Increase in daily energy generation per volume of heat storage fluid used in the system for different charging scenarios.

Charging Scenario	***dE $_{daily}$/Amount of heat storage fluid (kWh/m^3)***
00:00<ct<Sunrise	0.115
01:00<ct<Sunrise	0.128
02:00<ct<Sunrise	0.135
$t(T_{min})$-1< ct<$t(T_{min})$+1	0.156
At $t(T_{min})$	0.150

8.5.2 Approach dT

As discussed before, the value of the approach, *dT*, has a significant effect on performance of the CE-TES system. Figure 8.14 shows the effect of *dT* on a number of transfer units (NTU) of the air-to-water heat exchanger (HEX) used in a CE-TES coupled with the RSRC, and the increase in the daily energy generation dE_{day} (%) for July 11th. As the results show, a decrease in the *dT* results in an exponential increase in the daily energy generation (due to the lower $T_{ACC,in}$), but also in an exponential increase in the heat exchanger size (NTU). Thus, there is a tradeoff between the size and cost of the heat exchanger and the increase in energy generation.

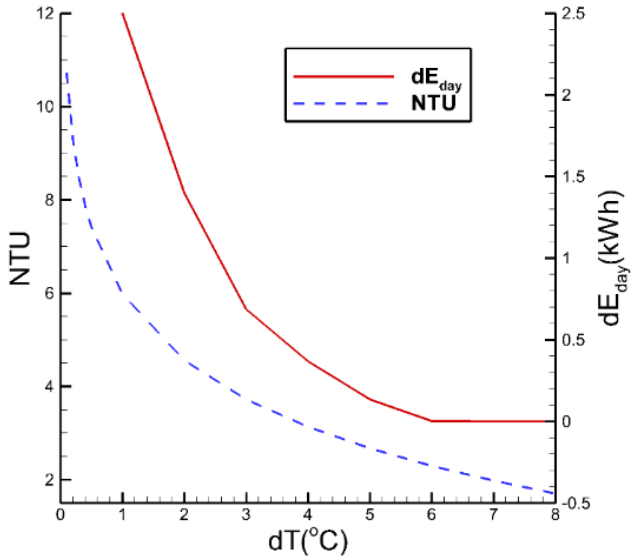

Figure 8.14. Effect of dT on NTU and dE_{day} (%).

8.5.3 Performance of the dry cooling and closed-loop hybrid cooling systems

The results concerning the annual generation increase determined for the four analyzed power cycles coupled with the dry cooling and closed-loop hybrid cooling systems are presented and compared for the range of design parameters (approach, fan efficiency, and maximal variation in daily temperature). For the efficient operation of the CE-TES system, the following three conditions have to be satisfied:

A) $T_{max,day}$-$T_{min,day}$ > *2*dT* for dry cooling and *1*dT* for closed-loop hybrid cooling

B) $T_{cold}+dT < T_{max,day}$

C) $W_{net,\ with\ CE\text{-}TES} > W_{net,\ without\ CE\text{-}TES}$, i.e., the increase in gross power generated by CE-TES should be higher than the power required for the CE-TES fans.

The amount (volume) of the heat storage fluid (water-glycol mixture) required for the operation of the CE-TES system coupled with the four analyzed power cycles (power blocks) is presented in Figure 8.15 as a function of the heat exchanger effectiveness for the values of the approach in the 3 to 6^{o}C range. As the results show, a CE-TES coupled with the RBC cycle requires the lowest volume of the heat storage fluid. The required volume of the heat storage fluid is the highest for the combined Brayton/ORC. For the heat exchanger effectiveness of 0.8 (80%), the volume of the heat storage fluid required for a 100 MW_{gross} RBC and combined Brayton/ORC cycle is 4,000 and 41,000 m^3 and, respectively. Also, lower values of the approach dT require larger volume of the heat storage fluid because of the longer duration of the system discharge.

For the higher values of the approach *dT*, the three conditions presented above are satisfied over shorter periods of time, compared to the lower values of the approach.

Therefore, the CE-TES system can be used over a shorter period of time, i.e., duration of the system discharge is shorter, requiring smaller volume of the heat storage fluid.

For all four analyzed power cycles, the heat exchanger effectiveness and the amount of the heat storage fluid are inversely related. As stated before, the amount (volume) of the heat storage fluid used for the closed-loop hybrid and the dry cooling was assumed to be the same to allow for a direct comparison of these two systems.

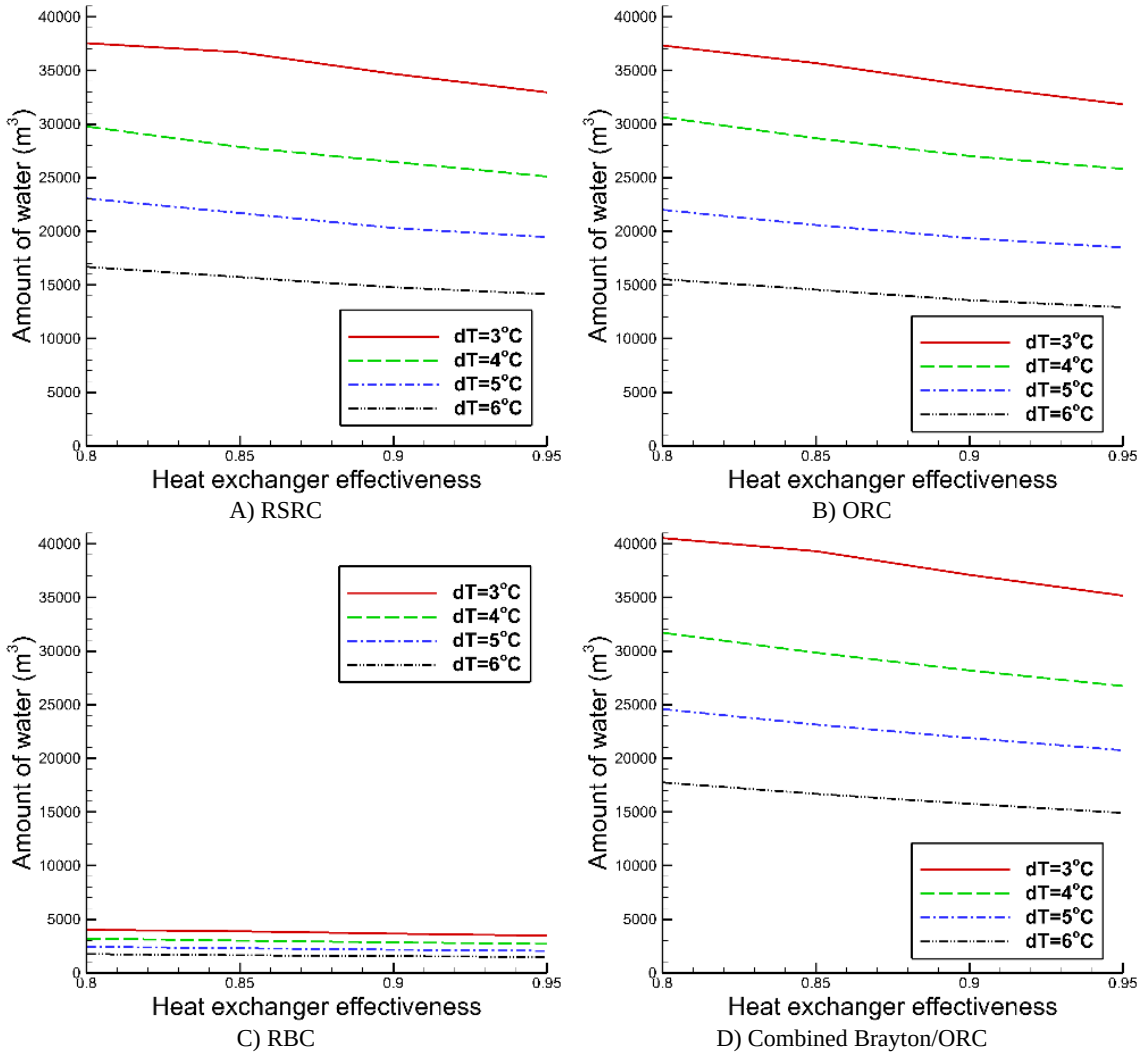

Figure 8.15. Volume of the energy storage fluid required for the CE-TES system as a function of the approach for the four analyzed dry-cooled power cycles.

8.5.3.1. Dry cooling system

The absolute (MWh) and relative (%) annual increase in energy generation that could be achieved by using a CE-TES coupled with the dry cooling method are shown in Figures 8.16 and 8.17. The effect of the heat exchanger effectiveness on the annual increase in energy generation increase is small and can be neglected.

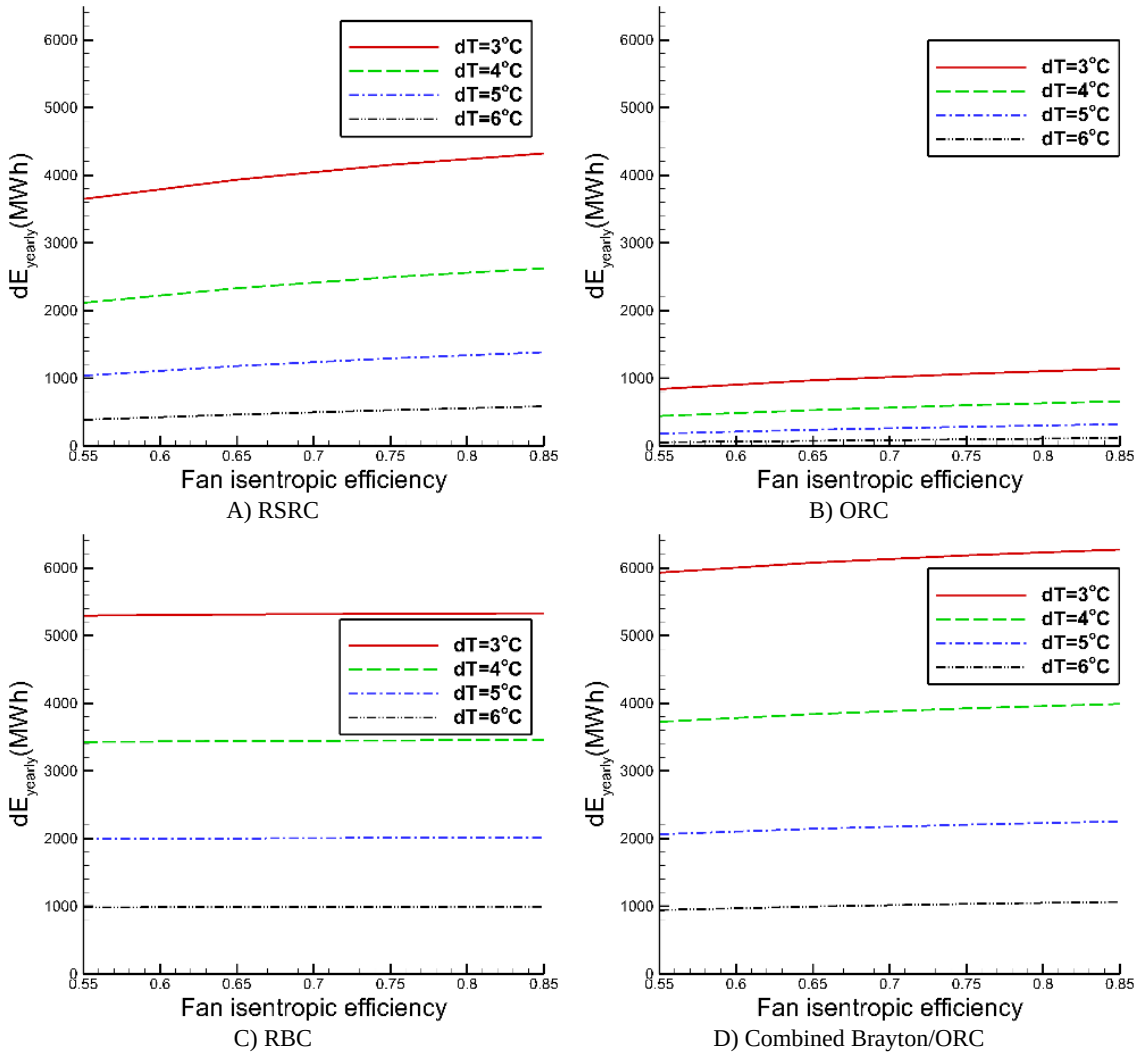

Figure 8.16. Absolute annual increase in energy generation (MWh) by using a CE-TES coupled with the dry cooling method for the four analyzed power cycles.

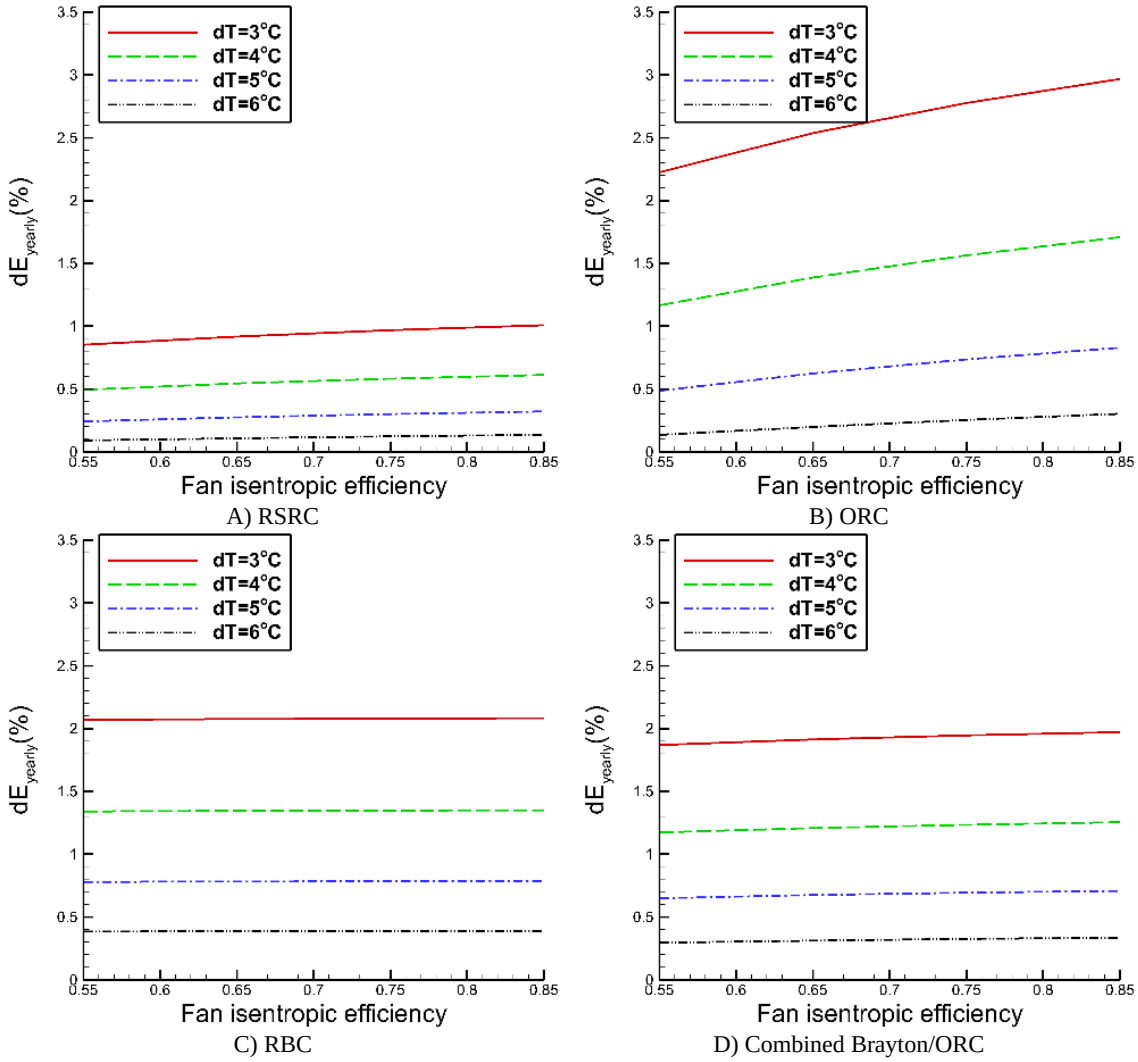

Figure 8.17. Relative increase in annual energy generation (%) by using a CE-TES coupled with the dry cooling method for the four analyzed power cycles.

As the results show, an increase in the fan isentropic efficiency results in a higher increase in the annual energy generation because of the lower fan power requirements. The effect of the fan efficiency on the annual energy increase is larger for lower values of the approach. For *dT=3°C* and fan isentropic efficiency of 0.55, the increase in the annual energy generation for the RSRC, ORC, RBC, and combined Brayton/ORC cycle is 0.85, 2.25, 2.05, and 1.87%, respectively. The corresponding total annual energy generation for

the RSRC, ORC, RBC, and combined Brayton/ORC cycle is 427,845, 37,781, 255,859, and 317,468 MWh, respectively.

The annual increase in energy generation for the four analyzed power cycles achieved by using a CE-TES coupled with the dry cooling method is compared in Figure 8.18. As the results presented in Figures 8.16, 8.17, and 8.18 show, the positive effect of CE-TES is the highest for an ORC, and ranges from 2.2 to 3 %. Also, the effect of fan efficiency on the annual generation increase is the highest for the ORC. The effect of a CE-TES on the annual increase in energy generation is the lowest for the RSRC; less than 1%, and is virtually independent of the fan efficiency.

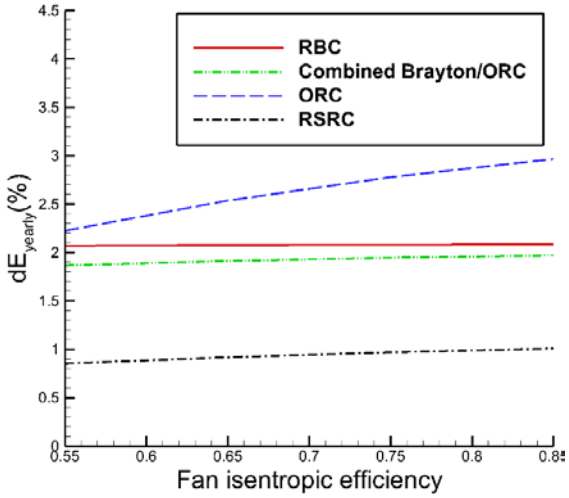

Figure 8.18. A comparison of the annual increase in energy generation for the four analyzed power cycles using CE-TES coupled with dry cooling.

Variation of the maximal daily difference in the ambient temperature ($\Delta T_{max} = T_{max} - T_{min}$) for the Ivanpah location and its effect on the daily increase in energy generation for a dry-cooled RSRC with the CE-TES are shown in Figure 8.19. The performance results were obtained for $dT=3°C$, fan isentropic efficiency of 0.55, and heat exchanger

effectiveness of 0.9. As the results show, for the Ivanpah location ΔT_{max} is between 11 to 18°C for most days in a year. Also, a higher ΔT_{max} results in a higher increase in the daily energy generation. Thus, it follows that a CE-TES system will be more effective in deserts and other arid areas where temperature difference between the day and night is larger and more frequent.

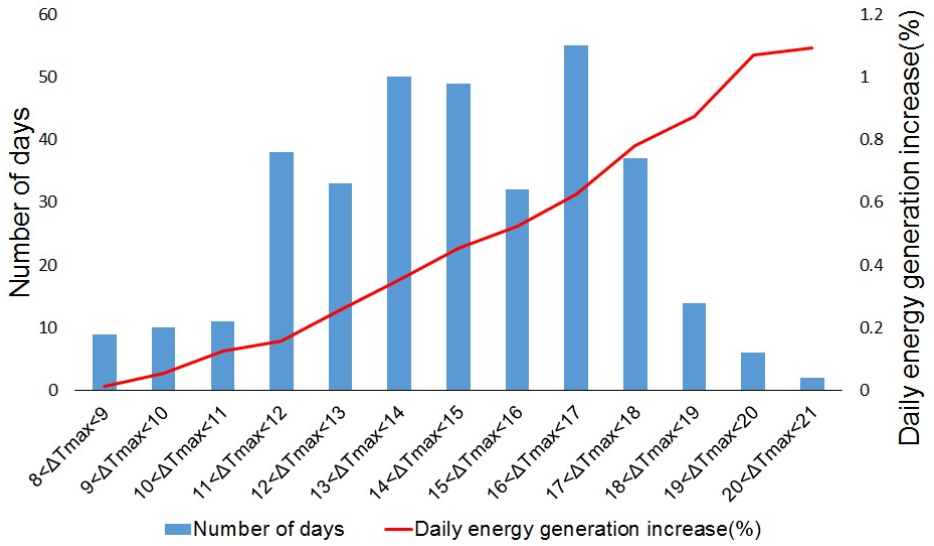

Figure 8.19. Effect of Maximal Daily Temperature Difference (ΔT_{max}) on Daily Increase in Energy Generation for a Dry-cooled RSRC with a CE-TES.

8.5.3.2. Closed-Loop hybrid cooling system

Since a heat exchanger is used only during the charging cycle of a CE-TES system coupled with the closed-loop hybrid cooled power block, the effect of the heat exchanger effectiveness and fan isentropic efficiency on the annual increase in energy generation is small and can be neglected.

The annual increase in energy generation achieved by using a CE-TES coupled with a closed loop hybrid cooling is presented in Figure 8.20 for the four analyzed power cycles.

As the results show, similar to the dry cooling, a CE-TES coupled with a closed-loop hybrid cooling has the highest effect on the ORC, where (depending on the approach) the improvement in annual energy generation ranges from 2.3 to 7.1. For the RSRC, the improvement is smaller, 0.9 to 2%. Also, the value of the approach *dT* has a dramatic effect on the annual increase in energy generation, which increases as dT is reduced. A CE-TES system coupled with a closed-loop hybrid cooling results in the annual increase in energy generation of 8,500, 2,700, 8,100, and 10,400 MWh for the RSRC, ORC, RBC, and combined Brayton/ORC cycle, respectively for *dT=3°C*.

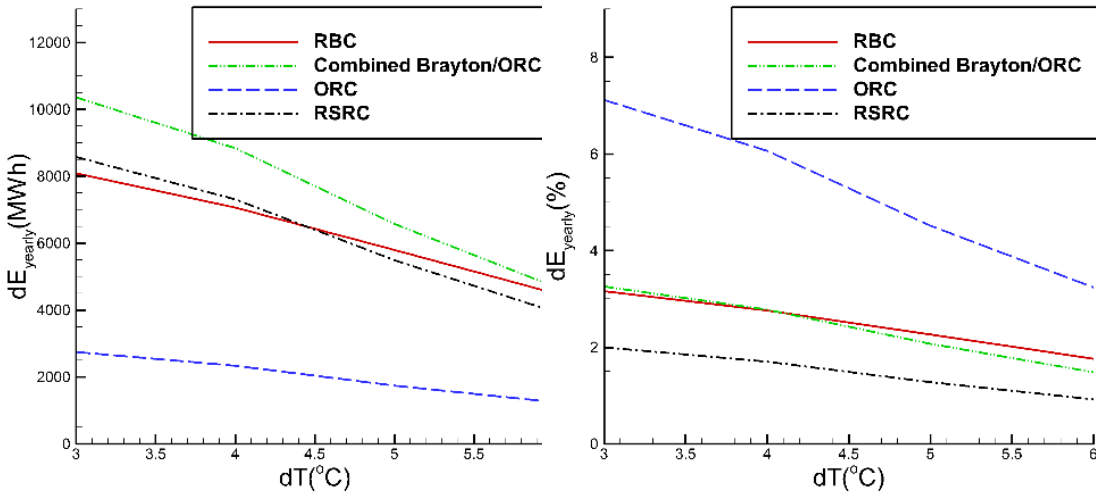

A) dE_{yearly} (MWh) B) dE_{yearly} (%)

Figure 8.20. Annual increase in energy generation by using CE-TES with a closed-loop hybrid cooling for the four analyzed power cycles.

A comparison between the dry and closed-loop hybrid cooling systems for the four analyzed power cycles is presented in Figure 8.21. The cooling system (dry cooling or closed-loop hybrid) has the largest effect on performance of the ORC and RSRC. For the ORC, *dT=3°C*, and fan isentropic efficiency of 0.55, the annual increase in energy

generation achievable by employing a CE-TES coupled with the dry cooling and closed-loop hybrid cooling on the relative scale is 2.2 and 7%, respectively. On the absolute scale, the use of the closed-loop hybrid cooling instead of the dry cooling results in the annual increase in energy generation up to 4,700 (1%-point), 1,900 (4.9%-point), 2,800 (1.2%-point), and 4,200 (1.4%-point) MWh for the RSRC, ORC, RBC, and combined Brayton/ORC, respectively.

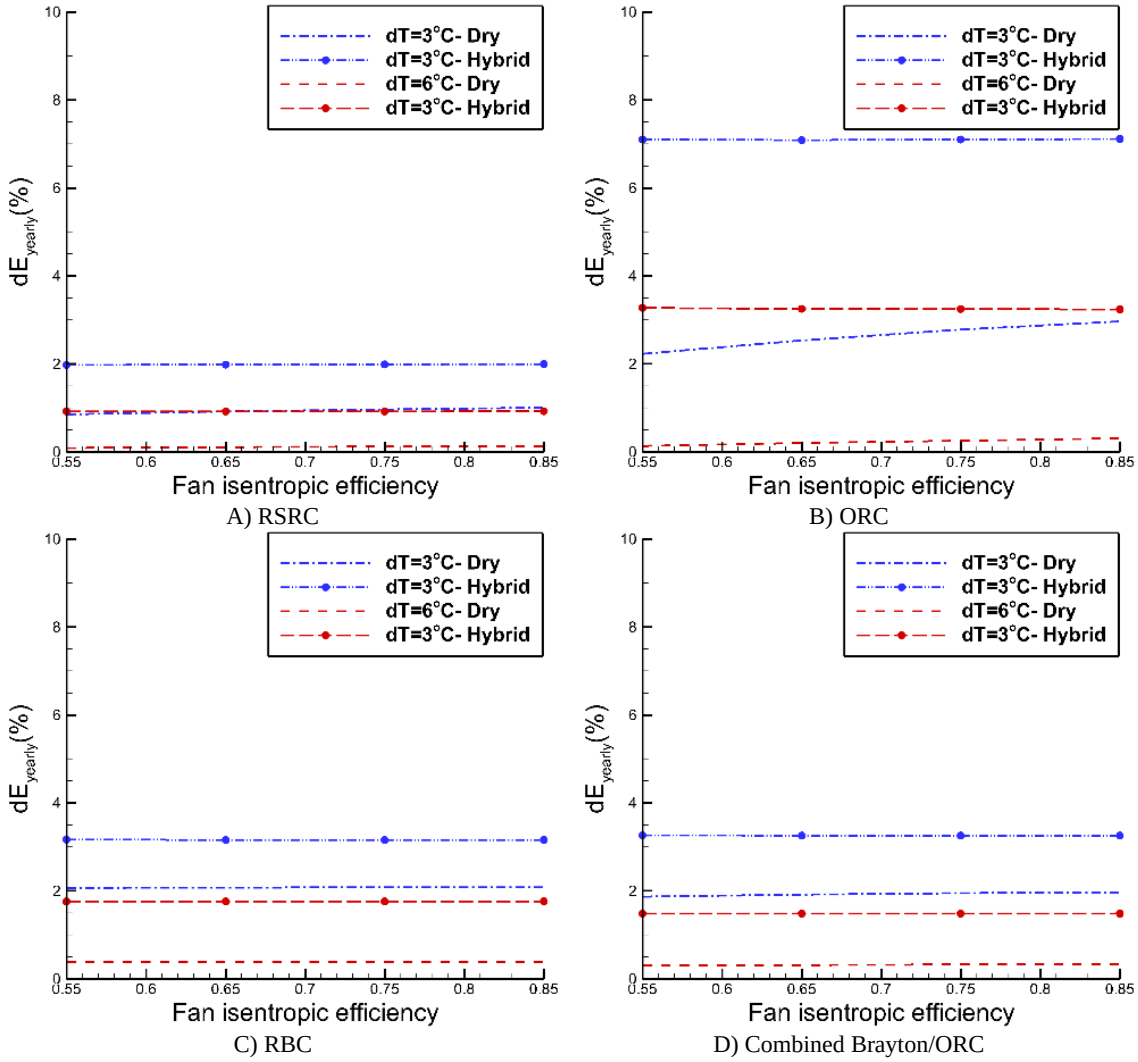

Figure 8.21. The comparison between the dry and hybrid cooling systems for different power cycles.

8.6. Conclusions

An improvement to the direct dry cooling, involving the cold energy storage system (CE-TES), has been proposed to improve the cooling efficiency and performance of the dry-cooled power plants. Two configurations of the CE-TES are proposed: the dry cooling, and the closed-loop hybrid cooling systems. The closed-loop hybrid system is more efficient in improving the power output and generation of the power block, compared to the dry cooling system; however, further development of the proposed concept is needed to verify the assumptions used in the analysis.

For the analyzed CSP plant location (Ivanpah site), employing a CE-TES with the dry cooling system could increase energy generation of the RSRC and simple ORC power block by 1 to 3%, respectively. The large overall temperature difference[4] is, however, the main drawback of the CE-TES. This is because the heat is exchanged between the air and the energy storage fluid twice, first during the system charging and, second during the system discharging, resulting in the overall temperature difference being twice the value of the HEX approach.

In a closed-loop hybrid cooling system, heat is exchanged only once, during the CE-TES charging. During the system discharging, the cold heat storage fluid is used in conjunction with the cooling air for the direct cooling, i.e., condensation of steam in the ACC. Thus, the overall temperature difference is equal to the HEX approach, resulting in a lower steam condensation temperature, lower turbine back-pressure, higher power output, and higher generation (up to 2.2% for the RSRC, and up to 7% of the ORC).

[4] Temperature difference between the cooling air at the ACC inlet during the system discharging and the ambient air during the system charging.

CHAPTER 9: SUMMARY AND CONCLUSIONS

9.1. Introduction

This chapter discusses the contribution of this study to the relevant body of literature, summarizes the main results, and provides recommendations for future work.

9.2. Contributions

The main contributions of this research work are the following:

9.2.1. Selection the best working fluid(s) and power cycle(s)

Selection of working fluids resulting in best performance (thermodynamic efficiency or net specific work output) of the simple and combined power cycles, such as Brayton, ORC, Brayton/ORC, and Rankine/ORC for the specified cycle operating conditions (maximum temperature and pressure, heat rejection temperature, and others) is typically a time-consuming and arduous task. The commonly used approach involves performing a large number of parametric calculations which are carried out over a range of operating parameters for a number of candidate working fluids for the power cycle under consideration.

A novel and systematic multi-step method was developed for the selection of best working fluids for the commonly considered power cycles. The first step involves development of a thermodynamic cycle model using the semi-perfect gas assumption (defined in Section 3.3 of Chapter 3) to develop theoretical expressions for thermal efficiency, heat input, and net specific work. The detailed models of the power cycles are developed in the second step using EBSILON Professional version 11 (EPV-11) power systems modeling code. The EPV-11 models are exercised over a range of operating

conditions and a multitude of working fluids to generate results on cycle performance. The statistical regression analysis is used in the third step to develop correlations for the cycle efficiency and net specific work of the same form as theoretical expressions developed in Step 1.

The last step in the process involves construction of performance maps, where performance parameters, such as thermodynamic efficiency and net specific work output are presented as functions of the cycle operating conditions. The performance maps are constructed by using an extremum seeking algorithm which, for the specified cycle operating conditions, identifies the working fluid resulting in the best cycle performance from the results generated by the EPV-11 power cycle models. The performance maps typically contain several zones and identify the best working fluid for each zone.

Finally, the performance (thermodynamic efficiency or net specific work output) and the cost of the single and combined cycles are compared to select the best power cycle(s) for a CSP-T plant. Using the best power cycle lowers the cost of a CSP-T plant.

9.2.2. Heat rejection

An improvement to the direct dry cooling, involving the cold energy storage system (CE-TES), has been proposed to improve the cooling efficiency and performance of the dry-cooled power plants. Two configurations of the CE-TES are proposed: the dry cooling, and the closed-loop hybrid cooling systems.

9.3. Summary of the Research

This study focuses on the CSP-T technology integrated with power cycles such as Rankine and Brayton. Selection of the power cycles, working fluids, and heat rejection

systems was analyzed with the objective to improve conversion (mirror-to-electric generator) efficiency and reduce the cost.

9.3.1. Selection of the best working fluid(s)

Thermodynamic performance (thermal efficiency and specific net power output) of power cycles was analyzed for different working fluids. To avoid safety issues and adverse effects of a working fluid on the environment, environmental and safety characteristics of working fluids, such as: GWP, ODP, toxicity, flammability and corrosiveness were considered during the fluid selection process. The expressions for thermal efficiency, net specific work output, and specific heat input are proposed based on the thermodynamic analysis and EPV-11 model results in terms of the relevant cycle parameters. Performance maps were developed for the analyzed power cycles as guides for the selection of the best working fluid(s) for the specified (selected or given) set of cycle operating conditions.

9.3.1.1. ORC

The results show that for all working fluids, thermal efficiency increases as the maximum pressure is increased. However, for high pressures (higher than critical), thermal efficiency becomes virtually independent of the maximum pressure. The effect of turbine inlet temperature (TIT) on thermal efficiency depends on the type of working fluid. The results show that for an ORC operating with a wet working fluid, thermal efficiency increases with an increase in the turbine inlet temperature (TIT) due to the divergence of the isobaric lines with temperature. Since for the dry fluids the isobars converge with temperature, thermal efficiency decreases as the maximum cycle temperature is increased in ORC applications with such fluids. For the isentropic fluids thermal efficiency is, however, relatively independent of TIT. The results show that efficiency of an ORC

operating with isentropic working fluids is higher compared to the dry and wet fluids; also working fluids with higher specific heat capacity provide higher cycle net power output.

For a subcritical ORC without the superheat, thermal efficiency is a linear function of the figure of merit (FOM). However, the coefficients in this linear function are quadratic functions of the ratio of evaporation and condensation temperatures. For the superheated subcritical ORC, the relationship between thermal efficiency and a modified Jacob number (Ja_t), proposed in this study, is also linear. For the supercritical ORC, thermal efficiency is a linear function of the dimensionless temperature and the ratio of evaporation and condensation temperatures.

9.3.1.2. Brayton cycle

The developed expressions show that real gases produce lower net work output for the same heat input in comparison to the perfect gases.

The analysis of a Brayton cycle shows that for the optimum pressure ratio outside the Critical Zone and maximum temperatures higher than 500°C, thermal efficiency is virtually independent of the working fluid properties. Regenerative Brayton cycle has higher efficiency compared to a simple Brayton cycle and, thus would be a better choice for the CSP applications.

However, for the optimum pressure ratio inside the Critical Zone, thermal efficiency of a Brayton cycle is a function of the working fluid properties. In this case, different working fluids give different values of thermal efficiency, with sCO_2 resulting in the highest thermal efficiency of all analyzed working fluids. This is because operation inside the Critical Zone in the “liquid-like” region results in a significant decrease in the

specific compressor work, leading to the higher net work output and higher thermal efficiency.

The performance map for efficiency shows that at the optimal pressure ratio, depending on the cycle operating conditions, either N_2 or CO_2 are the best working fluids. For high maximum temperatures and low maximum pressures, N_2 is the preferred working fluid, while for higher maximum pressures or lower maximum temperatures CO_2 gives the highest efficiency. The performance map for the net specific work output shows that helium is the best working fluid over the entire range of cycle operating conditions investigated in this study.

9.3.1.3. Combined Brayton/ORC cycle

In case of a combined regenerative Brayton/ORC cycle, the results show that CO_2 and air are the best working fluids for the topping cycle. Depending on the exhaust temperature of the topping cycle, Iso-butane, R11 and Ethanol are the preferred working fluids for the bottoming ORC cycle, resulting in highest efficiency of the combined cycle. However, for the maximum cycle temperature higher than 600°C, there is virtually no difference in performance of different working fluids.

9.3.1.4. Combined steam Rankine/ORC cycle

In a combined steam Rankine/ORC cycle ammonia followed by R11 and R141b is the preferred choice for a working fluid in the bottoming ORC. However, Ammonia and R11 are toxic and phased out, respectively. Thus, R141b is the best choice for a bottoming ORC in the combined steam Rankine/ORC cycle.

As the results show, adding an ORC to the Brayton cycle can increase thermal efficiency of the system around 15%-points, while adding an ORC to the steam Rankine cycle can increase the thermal efficiency by less than 2%.

9.3.2. Selection of the best power cycle(s)

The best power cycles giving the highest thermal efficiency or highest net power output for the low-, medium, and high maximum cycle temperature ranges were identified in Chapter 6 of this study

The results show that for the maximum cycle temperatures lower than 300°C, the ORC has the highest thermal efficiency. For the medium maximum cycle temperatures (300 to 800°C), the combined Rankine/ORC and the regenerative Brayton cycle with recompression (RBCR) are the best choices. For the maximum cycle temperature higher than 800°C, the combined Brayton/ORC cycle gives the highest thermal efficiency.

The results also show that for the low and medium maximum cycle temperatures, the regenerative steam Rankine cycle with reheat (RSRC) gives the highest specific net work output, followed by the combined Brayton/ORC cycle using Helium as the working fluid in the topping cycle and Ethanol in the bottoming ORC. For the maximum temperature of higher than 650°C, the combined Brayton/ORC cycle using Helium as the working fluid in the topping cycle and Ethanol in the bottoming ORC gives the highest specific net work output.

9.3.3. Techno-economic analysis of CSP-T plants

The results of the techno-economic analysis performed for a simple ORC, a regenerative Brayton cycle, a regenerative Brayton cycle with recompression, and a combined Brayton/ORC cycle are presented in Chapter 7.

As discussed in Section 6.3 of Chapter 6, information on the power cycle cost metrics, such as the total investment cost (C_{TCI}) and the levelized cost of electricity (LCOE) is needed in addition to the performance data to make an impartial and objective selection of the best power cycle for the given plant and power block operating parameters.

The results of techno-economic analysis are summarized as follows:

a) As the results show, for a specified (selected) cycle, higher thermal efficiency results in a lower capital investment and lower LCOE. Thus, for the selection of a working fluid for a power cycle, thermal efficiency is more important parameter than the specific net work output.

   The RBCR has higher thermal efficiency compared to the RBC. However, RBCR has higher capital investment cost and higher LCOE compared to the RBC.

b) The total capital investment cost and LCOE for the combined Brayton/ORC cycle are lower compared to the regenerative Brayton cycle (RBC).

c) For the analyzed CSP-T plant –power block configurations the cost of the power block is between 14 to 28% of the overall cost of the CSP-T plant, and increases as the maximum cycle temperature is increased. Also, the size of the solar field decreases as the maximum cycle temperature is increased because of the higher power block efficiency.

d) Although an increase in thermal efficiency of the power block generally increases the cost of the power block, it decreases the cost of the overall CSP-T plant because, the total cost of the solar field, tower/receiver, and TES is the dominant factor affecting the total CSP-T plant cost.

9.3.4. Heat rejection

An improvement to the direct dry cooling, involving the cold energy storage system (CE-TES), has been proposed to improve the cooling efficiency and performance of the dry-cooled power plants. Two configurations of the CE-TES are proposed: the dry cooling, and the closed-loop hybrid cooling systems.

The closed-loop hybrid system is more efficient in improving the power output and generation of the power block, compared to the dry cooling system.

For the analyzed CSP plant location (Ivanpah site), employing a CE-TES with the dry cooling system could increase electric energy (electricity) generation of the RSRC and simple ORC power block by 1 to 3%, respectively. The large overall temperature difference is, however, the main drawback of the CE-TES because the heat is exchanged between the air and the energy storage fluid twice.

In a closed-loop hybrid cooling system, the heat is exchanged only once, during the CE-TES charging. Thus, the overall temperature difference is equal to the HEX approach, resulting in a lower steam condensation temperature, lower turbine back-pressure, higher power output, and higher generation (up to 2.2% for the RSRC, and up to 7% of the ORC).

9.4. Recommendations for Future Research

The effect of using pure working fluids on thermodynamic performance of a power cycle was investigated in this work. It is recommended that analyzing the effect of a mixture of working fluids on the performance of power cycle be considered.

The working fluid and power cycle selection analysis (Chapters 4, 5, and 6) was performed by assuming constant ambient temperature. However, in a real operation, the ambient temperature changes throughout the day, seasonally and annually. The variation

in the ambient temperature results in the off-design operation of the power cycle, which impacts its performance and output. Thus, the effect of variation in ambient temperature should be considered in future research. It should be mentioned that the ambient temperature effect was included in the techno-economic analysis of a CSP-T plant (Chapter 7) and investigation of the effect of CE-TES system on performance of the power cycle (Chapter 8).

A closed-loop hybrid cooling system was proposed in this study and thermodynamic analysis of its performance was performed as described in Chapter 8. Although the proposed system increases the power output and generation, a techno-economic analysis needs to be performed to determine its actual economic benefits. Also, a more detailed modeling of the proposed modification to the ACC cooling tube design needs to be performed for a more precise determination of the reduction in the condensation temperature, turbine backpressure, and the associated thermodynamic and economic benefits.

REFERENCES

1. Ebsilon Professional Program Documentation. 2017; Available from: https://www.steag-systemtechnologies.com/ebsilon_professional+M52087573ab0.html.
2. World Energy Outlook 2011. 2011.
3. The Concentrating Solar Power: Advanced Projects Offering Low LCOE Opportunities (CSP: APOLLO). 2014.
4. Baharoon, D.A., et al., Historical development of concentrating solar power technologies to generate clean electricity efficiently – A review. Renewable and Sustainable Energy Reviews, 2015. 41(0): p. 996-1027.
5. Power, C.S., Integrated Solar Thermochemical Reaction System. 2013.
6. Xu, R. and T.F. Wiesner, Closed-form modeling of direct steam generation in a parabolic trough solar receiver. Energy, 2015. 79: p. 163-176.
7. 2015; Available from: http://www.volker-quaschning.de/index.php.
8. Zhu, G., et al., History, current state, and future of linear Fresnel concentrating solar collectors. Solar Energy, 2014. 103(0): p. 639-652.
9. Martin, C.L. and D.Y. Goswami, Solar energy pocket reference. 2005: Earthscan/James & James.
10. Babaelahi, M. and H. Sayyaadi, A new thermal model based on polytropic numerical simulation of Stirling engines. Applied Energy, 2015. 141: p. 143-159.
11. Collado, F.J. and J. Guallar, A review of optimized design layouts for solar power tower plants with campo code. Renewable and Sustainable Energy Reviews, 2013. 20: p. 142-154.
12. Bazilian, M., et al., Re-considering the economics of photovoltaic power. Renewable Energy, 2013. 53: p. 329-338.
13. Technology Roadmap: Solar Photovoltaic Energy - 2014 Edition. 2015.
14. Kolb, G.J., et al., Power tower technology roadmap and cost reduction plan. SAND2011-2419, Sandia National Laboratories, Albuquerque, NM, 2011.
15. Barigozzi, G., et al., Thermal performance prediction of a solar hybrid gas turbine. Solar Energy, 2012. 86(7): p. 2116-2127.
16. Tsiklauri, G., et al., Supercritical steam cycle for nuclear power plant. Nuclear Engineering and Design, 2005. 235(15): p. 1651-1664.

17. Forsberg, C.W., P.F. Peterson, and H. Zhao, High-temperature liquid-fluoride-salt closed-Brayton-cycle solar power towers. Journal of Solar Energy Engineering, 2007. 129(2): p. 141-146.

18. Wheeldon, J., Engineering and Economic Evaluation of 1300 F Series Ultra-Supercritical Pulverized Coal Power Plants: Phase 1. EPRI, Palo Alto, CA, 2008. 1015699.

19. First Quadrennial Technology Review (QTR 2011). 2011, U.S. Department of Energy.

20. Kosmadakis, G., D. Manolakos, and G. Papadakis, An investigation of design concepts and control strategies of a double-stage expansion solar organic Rankine cycle. International Journal of Sustainable Energy, 2015. 34(7): p. 446-467.

21. Freeman, J., K. Hellgardt, and C.N. Markides, An assessment of solar-powered organic Rankine cycle systems for combined heating and power in UK domestic applications. Applied Energy, 2015. 138: p. 605-620.

22. Desai, N.B. and S. Bandyopadhyay, Thermo-economic analysis and selection of working fluid for solar organic Rankine cycle. Applied Thermal Engineering, 2016. 95: p. 471-481.

23. Li, J., et al., Effect of working fluids on the performance of a novel direct vapor generation solar organic Rankine cycle system. Applied Thermal Engineering, 2016. 98: p. 786-797.

24. Calise, F., et al., Design and simulation of a prototype of a small-scale solar CHP system based on evacuated flat-plate solar collectors and Organic Rankine Cycle. Energy Conversion and Management, 2015. 90: p. 347-363.

25. Feng, Y., et al., Thermoeconomic comparison between pure and mixture working fluids of organic Rankine cycles (ORCs) for low temperature waste heat recovery. Energy Conversion and Management, 2015. 106: p. 859-872.

26. Liu, Q., A. Shen, and Y. Duan, Parametric optimization and performance analyses of geothermal organic Rankine cycles using R600a/R601a mixtures as working fluids. Applied Energy, 2015. 148: p. 410-420.

27. Chagnon-Lessard, N., F. Mathieu-Potvin, and L. Gosselin, Geothermal power plants with maximized specific power output: Optimal working fluid and operating conditions of subcritical and transcritical Organic Rankine Cycles. Geothermics, 2016. 64: p. 111-124.

28. Yang, M.-H. and R.-H. Yeh, Economic performances optimization of an organic Rankine cycle system with lower global warming potential working fluids in geothermal application. Renewable Energy, 2016. 85: p. 1201-1213.

29. Saleh, B., et al., Working fluids for low-temperature organic Rankine cycles. Energy, 2007. 32(7): p. 1210-1221.

30. Chen, H., D.Y. Goswami, and E.K. Stefanakos, A review of thermodynamic cycles and working fluids for the conversion of low-grade heat. Renewable and Sustainable Energy Reviews, 2010. 14(9): p. 3059-3067.

31. Shengjun, Z., W. Huaixin, and G. Tao, Performance comparison and parametric optimization of subcritical Organic Rankine Cycle (ORC) and transcritical power cycle system for low-temperature geothermal power generation. Applied Energy, 2011. 88(8): p. 2740-2754.

32. Lakew, A.A. and O. Bolland, Working fluids for low-temperature heat source. Applied Thermal Engineering, 2010. 30(10): p. 1262-1268.

33. Papadopoulos, A.I., M. Stijepovic, and P. Linke, On the systematic design and selection of optimal working fluids for Organic Rankine Cycles. Applied Thermal Engineering, 2010. 30(6): p. 760-769.

34. Stijepovic, M.Z., et al., On the role of working fluid properties in Organic Rankine Cycle performance. Applied Thermal Engineering, 2012. 36: p. 406-413.

35. Mazur, V.A. and D. Nikitin. Sustainable working media selection for renewable energy technologies. in Proceedings of the World Renewable Energy Congress. 2011.

36. Kalra, C., et al. High-Potential Working Fluids and Cycle Concepts for Next-Generation Binary Organic Rankine Cycle for Enhanced Geothermal Systems. in 37th Workshop on Geothermal Reservoir Engineering, Stanford, CA, Jan. 2012.

37. Roedder, M., et al., Systematic Fluid Selection for Organic Rankine Cycles and Performance Analysis for a Combined High and Low Temperature Cycle. Journal of Engineering for Gas Turbines and Power, 2016. 138(3): p. 031701.

38. Roy, J. and A. Misra, Parametric optimization and performance analysis of a regenerative Organic Rankine Cycle using R-123 for waste heat recovery. Energy, 2012. 39(1): p. 227-235.

39. He, C., et al., The optimal evaporation temperature and working fluids for subcritical organic Rankine cycle. Energy, 2012. 38(1): p. 136-143.

40. Wang, D., et al., Efficiency and optimal performance evaluation of organic Rankine cycle for low grade waste heat power generation. Energy, 2013. 50: p. 343-352.

41. Kuo, C.-R., et al., Analysis of a 50kW organic Rankine cycle system. Energy, 2011. 36(10): p. 5877-5885.

42. Zhang, J., et al., Performance analysis of regenerative organic Rankine cycle (RORC) using the pure working fluid and the zeotropic mixture over the whole operating range of a diesel engine. Energy Conversion and Management, 2014. 84: p. 282-294.

43. Algieri, A. and P. Morrone, Comparative energetic analysis of high-temperature subcritical and transcritical Organic Rankine Cycle (ORC). A biomass application in the Sibari district. Applied Thermal Engineering, 2012. 36: p. 236-244.

44. Mago, P.J., et al., An examination of regenerative organic Rankine cycles using dry fluids. Applied Thermal Engineering, 2008. 28(8): p. 998-1007.

45. Acar, H.I., Second law analysis of the reheat-regenerative Rankine cycle. Energy Conversion and Management, 1997. 38(7): p. 647-657.

46. Ying, Y. and E.J. Hu, Thermodynamic advantages of using solar energy in the regenerative Rankine power plant. Applied Thermal Engineering, 1999. 19(11): p. 1173-1180.

47. Wang, E., et al., Optimized performances comparison of organic Rankine cycles for low grade waste heat recovery. Journal of Mechanical Science and Technology, 2012. 26(8): p. 2301-2312.

48. Hung, T.-C., Waste heat recovery of organic Rankine cycle using dry fluids. Energy Conversion and Management, 2001. 42(5): p. 539-553.

49. Wang, M., et al., Thermodynamic analysis and optimization of a solar-driven regenerative organic Rankine cycle (ORC) based on flat-plate solar collectors. Applied Thermal Engineering, 2013. 50(1): p. 816-825.

50. Pei, G., J. Li, and J. Ji, Analysis of low temperature solar thermal electric generation using regenerative Organic Rankine Cycle. Applied Thermal Engineering, 2010. 30(8): p. 998-1004.

51. Kribus, A., et al., A multistage solar receiver: The route to high temperature. Solar Energy, 1999. 67(1): p. 3-11.

52. Ries, H., A. Kribus, and J. Karni, Nonisothermal Receivers. Journal of Solar Energy Engineering, 1995. 117(3): p. 259-261.

53. Angelino, G., Perspectives for the liquid phase compression gas turbine. Journal of Engineering for Gas Turbines and Power, 1967. 89(2): p. 229-236.

54. Dostal, V., P. Hejzlar, and M.J. Driscoll, The supercritical carbon dioxide power cycle: comparison to other advanced power cycles. Nuclear technology, 2006. 154(3): p. 283-301.

55. Moisseytsev, A. and J.J. Sienicki, Investigation of alternative layouts for the supercritical carbon dioxide Brayton cycle for a sodium-cooled fast reactor. Nuclear Engineering and Design, 2009. 239(7): p. 1362-1371.

56. Angelino, G., Carbon dioxide condensation cycles for power production. Journal of Engineering for Power, 1968. 90(3): p. 287-295.

57. Reyes-Belmonte, M., et al., Optimization of a recompression supercritical carbon dioxide cycle for an innovative central receiver solar power plant. Energy, 2016. 112: p. 17-27.

58. Ortega, J., et al., Coupled Modeling of a Directly Heated Tubular Solar Receiver for Supercritical Carbon Dioxide Brayton Cycle: Optical and Thermal-Fluid Evaluation. Applied Thermal Engineering, 2016.

59. Cardemil, J.M. and A.K. da Silva, Parametrized overview of CO2 power cycles for different operation conditions and configurations–An absolute and relative performance analysis. Applied Thermal Engineering, 2016. 100: p. 146-154.

60. Yu, S.-C., et al., A brief review study of various thermodynamic cycles for high temperature power generation systems. Energy Conversion and Management, 2015. 94: p. 68-83.

61. Cheang, V., R. Hedderwick, and C. McGregor, Benchmarking supercritical carbon dioxide cycles against steam Rankine cycles for Concentrated Solar Power. Solar Energy, 2015. 113: p. 199-211.

62. Chacartegui, R., et al., Alternative cycles based on carbon dioxide for central receiver solar power plants. Applied Thermal Engineering, 2011. 31(5): p. 872-879.

63. Iverson, B.D., et al., Supercritical CO2 Brayton cycles for solar-thermal energy. Applied Energy, 2013. 111: p. 957-970.

64. Garg, P., P. Kumar, and K. Srinivasan, Supercritical carbon dioxide Brayton cycle for concentrated solar power. The Journal of Supercritical Fluids, 2013. 76: p. 54-60.

65. Turchi, C.S., et al., Thermodynamic study of advanced supercritical carbon dioxide power cycles for concentrating solar power systems. Journal of Solar Energy Engineering, 2013. 135(4): p. 041007.

66. Alpy, N., et al. Gas cycle testing opportunity with ASTRID, the French SFR prototype. in Supercritical CO2 Power Cycle Symposium. 2011.

67. Angelino, G. and C. Invernizzi, Binary conversion cycles for concentrating solar power technology. Solar Energy, 2008. 82(7): p. 637-647.

68. Jeong, W.S., et al., Potential Improvements of Supercritical Recompression CO2 Brayton Cycle Coupled with KALIMER-600 by Modifying Critical Point of CO2. 2010.

69. Sarkar, J., Thermodynamic analyses and optimization of a recompression N2O Brayton power cycle. Energy, 2010. 35(8): p. 3422-3428.

70. Memon, A.G., et al., Thermo-environmental and economic analysis of simple and regenerative gas turbine cycles with regression modeling and optimization. Energy Conversion and Management, 2013. 76: p. 852-864.

71. Spelling, J., et al., Thermoeconomic optimization of a combined-cycle solar tower power plant. Energy, 2012. 41(1): p. 113-120.

72. Klimas, P.C. and M. Becker, Status of second-generation central receiver technologies. Solar Energy Materials, 1991. 24(1): p. 162-171.

73. Yamamoto, T., et al., Design and testing of the organic Rankine cycle. Energy, 2001. 26(3): p. 239-251.

74. Caresana, F., et al., Micro combined plant with gas turbine and organic cycle. Proceedings of the ASME Turbo Expo 2008, 2008. 1: p. 787-795.

75. Invernizzi, C., P. Iora, and P. Silva, Bottoming micro-Rankine cycles for micro-gas turbines. Applied Thermal Engineering, 2007. 27(1): p. 100-110.

76. Enviromental Impacts of Power Plants. Public Service Commission of Wisconsin, 2011.

77. Pihl, E., et al., Material constraints for concentrating solar thermal power. Energy, 2012. 44(1): p. 944-954.

78. Chien, J.C.-L. and N. Lior, Concentrating solar thermal power as a viable alternative in China's electricity supply. Energy Policy, 2011. 39(12): p. 7622-7636.

79. Holbert, K.E. and C.J. Haverkamp. Impact of solar thermal power plants on water resources and electricity costs in the Southwest. in North American Power Symposium (NAPS), 2009. 2009. IEEE.

80. Azoumah, Y., et al., Siting guidelines for concentrating solar power plants in the Sahel: Case study of Burkina Faso. Solar Energy, 2010. 84(8): p. 1545-1553.

81. REFPROP version 7.1, NIST standard reference database. The U.S. Secretary of Commerce.

82. McLinden, M.O., NIST thermodynamic and transport properties of refrigerants and refrigerant mixtures-REFPROP. NIST Standard Reference Database, 1998. 23.

83. El, W.M., Power Plant Technology. 1984, McGraw-Hill International.

84. Dunham, M.T. and B.D. Iverson, High-efficiency thermodynamic power cycles for concentrated solar power systems. Renewable and Sustainable Energy Reviews, 2014. 30: p. 758-770.

85. Wang, K., Y.-L. He, and H.-H. Zhu, Integration between supercritical CO2 Brayton cycles and molten salt solar power towers: A review and a comprehensive comparison of different cycle layouts. Applied Energy, 2017. 195: p. 819-836.

86. Seider, W.D., J.D. Seader, and D.R. Lewin, PRODUCT & PROCESS DESIGN PRINCIPLES: SYNTHESIS, ANALYSIS AND EVALUATION, (With CD). 2009: John Wiley & Sons.

87. Turton, R., et al., Analysis, synthesis and design of chemical processes. 2008: Pearson Education.

88. Pierobon, L., et al., Multi-objective optimization of organic Rankine cycles for waste heat recovery: Application in an offshore platform. Energy, 2013. 58: p. 538-549.

89. Ho, C.K., et al., Technoeconomic Analysis of Alternative Solarized s-CO2 Brayton Cycle Configurations. Journal of Solar Energy Engineering, 2016. 138(5): p. 051008.

90. Turchi, C.S. and G.A. Heath, Molten salt power tower cost model for the system advisor model (SAM). 2013, National Renewable Energy Laboratory (NREL), Golden, CO.

91. Toffolo, A., et al., A multi-criteria approach for the optimal selection of working fluid and design parameters in Organic Rankine Cycle systems. Applied Energy, 2014. 121: p. 219-232.

92. Trieb, F. Global potential of concentrating solar power. in Concentrating Solar Power and Chemical Energy Systems. 2009. Berlin, Germany.

93. Stekli, J., L. Irwin, and R. Pitchumani, Technical challenges and opportunities for concentrating solar power with thermal energy storage. Journal of Thermal Science and Engineering Applications, 2013. 5(2): p. 021011.

94. Blair, N., et al., System advisor model, sam 2014.1. 14: General description. 2014, National Renewable Energy Laboratory (NREL), Golden, CO.

95. Glatzmaier, G., Developing a cost model and methodology to estimate capital costs for thermal energy storage. 2011, National Renewable Energy Laboratory (NREL), Golden, CO.

96. Hung, T.-C., T. Shai, and S. Wang, A review of organic Rankine cycles (ORCs) for the recovery of low-grade waste heat. Energy, 1997. 22(7): p. 661-667.

97. Desai, N.B. and S. Bandyopadhyay, Process integration of organic Rankine cycle. Energy, 2009. 34(10): p. 1674-1686.

98. Chen, Q., J. Xu, and H. Chen, A new design method for Organic Rankine Cycles with constraint of inlet and outlet heat carrier fluid temperatures coupling with the heat source. Applied Energy, 2012. 98: p. 562-573.

99. Srinivasan, K.K., P.J. Mago, and S.R. Krishnan, Analysis of exhaust waste heat recovery from a dual fuel low temperature combustion engine using an Organic Rankine Cycle. Energy, 2010. 35(6): p. 2387-2399.

100. Walraven, D., B. Laenen, and W. D'haeseleer, Comparison of thermodynamic cycles for power production from low-temperature geothermal heat sources. Energy Conversion and Management, 2013. 66: p. 220-233.

101. Wright, S.A., et al., Operation and analysis of a supercritical CO2 Brayton cycle. Sandia Report, No. SAND2010-0171, 2010.

102. Breidenich, C., et al., The Kyoto protocol to the United Nations framework convention on climate change. The American Journal of International Law, 1998. 92(2): p. 315-331.

103. Secretariat, U.N.E.P.O., Handbook for the Montreal protocol on substances that deplete the ozone layer. 2006: UNEP/Earthprint.

104. IFA, GESTIS Information System on Hazardous Substances. 2014: Sankt Augustin, Germany.

105. Wang, E., et al., Study of working fluid selection of organic Rankine cycle (ORC) for engine waste heat recovery. Energy, 2011. 36(5): p. 3406-3418.

106. Lecompte, S., et al. Potential of Organic Rankine Cycles (ORC) for Waste Heat Recovery on an Electric Arc Furnace (EAF). in 13th International Conference on Heat Transfer, Fluid Mechanics and Thermodynamics. 2017.

107. Bao, J. and L. Zhao, A review of working fluid and expander selections for organic Rankine cycle. Renewable and Sustainable Energy Reviews, 2013. 24: p. 325-342.

108. Anderson, J.D., Modern compressible flow: with historical perspective. Vol. 12. 1990: McGraw-Hill New York.

109. Javanshir, A. and N. Sarunac, Thermodynamic analysis of a simple Organic Rankine Cycle. Energy, 2017. 118: p. 85-96.

110. Ebsilon Professional Program Documentation. 2014; Available from: https://www.steag-systemtechnologies.com/ebsilon_professional+M52087573ab0.html.

111. Javanshir, A., N. Sarunac, and Z. Razzaghpanah, Thermodynamic analysis of a regenerative organic Rankine cycle using dry fluids. Applied Thermal Engineering, 2017.

112. El-Wakil, M.M., Powerplant technology. 1984: Tata McGraw-Hill Education.

113. Javanshir, A., N. Sarunac, and Z. Razzaghpanah, Thermodynamic Analysis of ORC and Its Application for Waste Heat Recovery. Sustainability, 2017. 9(11): p. 1974.

114. Javanshir, A. and N. Sarunac. Effect of the Working Fluid on Performance of the ORC and Combined Brayton/ORC Cycle. in ASME 2017 11th International Conference on Energy Sustainability collocated with the ASME 2017 Power Conference Joint With ICOPE-17, the ASME 2017 15th International Conference on Fuel Cell Science, Engineering and Technology, and the ASME 2017 Nuclear Forum. 2017. American Society of Mechanical Engineers.

115. Javanshir, A., N. Sarunac, and Z. Razzaghpanah, Thermodynamic analysis and optimization of single and combined power cycles for concentrated solar power applications. Energy, 2018. 157: p. 65-75.

116. Javanshir, A., N. Sarunac, and Z. Razzaghpanah, Thermodynamic analysis of simple and regenerative Brayton cycles for the concentrated solar power applications. Energy Conversion and Management, 2018. 163: p. 428-443.

117. Peris, B., et al., Performance evaluation of an Organic Rankine Cycle (ORC) for power applications from low grade heat sources. Applied Thermal Engineering, 2015. 75: p. 763-769.

118. Neij, L., et al., Experience curves: a tool for energy policy assessment. IMES. 2003, EESS report.

119. Kheiri, A., M. Feidt, and S. Pelloux-Prayer, Thermodynamic and economic optimizations of a waste heat to power plant driven by a subcritical ORC (Organic Rankine Cycle) using pure or zeotropic working fluid. Energy, 2014. 78: p. 622-638.

120. Woods, M.C., et al., Cost and performance baseline for fossil energy plants. National Energy Technology Laboratory, 2007.

121. Turchi, C., et al. Current and future costs for parabolic trough and power tower systems in the US market. in Proceedings of the 16th SolarPACES Conference, Perpignan, France. 2010.

122. Air-Cooled Condenser Design, Specification, and Operation Guidelines. EPRI, Palo Alto, CA, 2005. 1007688.